The Institute of Paper Science and Technology

Atlanta, Georgia

Doctor's Dissertation

Fluid Dynamics of Short-Dwell Blade Coater Ponds and Their Relationship to Cross Directional Coat Weight Nonuniformities

Nicholas G. Triantafillopoulos

February, 1991

FLUID DYNAMICS OF SHORT-DWELL BLADE COATER PONDS AND THEIR RELATIONSHIP TO CROSS DIRECTIONAL COAT WEIGHT NONUNIFORMITIES

A thesis submitted by
Nicholas G. Triantafillopoulos
B.S. 1981, Western Michigan University, Kalamazoo, MI
M.S. 1985,Western Michigan University, Kalamazoo, MI

In partial fulfillment of the requirements
of the Institute of Paper Science & Technology
for the degree of Doctor of Philosophy
Atlanta, Georgia

FEBRUARY, 1991

TABLE OF CONTENTS

LIST OF FIGURES

LIST OF TABLES

NOMENCLATURE

d	Radiographic x-ray dosage in Roentgen.
d_x	Radiographic x-ray dosage measured at distance x away from the source.
D	Width of the cavity in cm (i.e., dimension along the machine direction).
Gö	The dimensionless Görtler number of flow in curved streamlines.
H	Depth of the cavity in cm.
H*	Height (from bottom boundary) of downstream secondary vortex in cavity flow, in mm.
h	Depth of short-dwell pond in meters.
I	Intensity of radiographic x-ray radiation.
K	Coefficient in the power-law model for fluids. It corresponds to the zero-shear-rate viscosity of the fluid and is also known as consistency index. Its units are in milliPascals seconds (mPa sec).
L	Width of a single cellular flow structure near an end-wall (i.e.,corner vortex) in cm.
m	mass flow rate through the cavity in Kg/sec per unit spanwise length.
M	Volumetric through-flow rate in a cavity per unit span length in cm^2/sec.
N	Dimensionless coefficient in the power-law model for fluids. It is commonly referred to as the flow behavior index. (N<1 shear thinning, N=1 Newtonian, and N>1 shear thickening fluids.)
Q	Volumetric through-flow rate in mL per second through the cavity.
P_c	Cavity pressure in kPa. It is actually measured in the feeding line of the cavity.
P_h	Hydraulic pressure in kPa that keeps the cavity in contact with the roll. It is the air pressure of the hydraulic cylinders.
r	In flow visualization studies, the radius of curvature (in cm) of the irrotational flow inside a vortex. In flash x-ray radiography, the distance of an object from the radiographic source.

Re	Cavity Reynolds number. It is based on cavity width, roll peripheral speed, the density and viscosity of the fluid. Corresponds to laminar flow and a Newtonian fluid.
Re*	Reynolds number for through-flow. It is based on the through-flow rate, the density and viscosity of the fluid. Corresponds to laminar flow and a Newtonian fluid.
Re_a	Apparent Reynolds number of coating colors based on Brookfield (@ 100 rpm) viscosity.
S	Spanwise length of the cavity in cm.
U	Tangential velocity of fluid elements in flow streamlines. (Assumed one third of roll speed at the interface between the primary and secondary cavity flows.)
V	In flow visualization experiments is the peripheral roll speed in meters per second. In numerical simulations it represents machine speed.
W	In computer modeling is the width of the pond in cm, i.e., the distance between the tip of the stiff blade and the overflow baffle.
x	Thickness of a material penetrated by x-rays along the direction of beam travel.

GREEK SYMBOLS

γ	Shear rate in reciprocal seconds.
λ	Wavelength of unstable flow structures in cm as observed visually.
μ	Fluid viscosity in mPa sec or Kg/m sec. The viscosity used for calculations is measured with a Brookfield viscometer (100 rpm, mostly with spindle no. 3).
μ_l	Linear x-ray absorption coefficient of a material in reciprocal centimeters.
μ_α	Apparent Newtonian viscosity of coating colors in numerical simulations.
μ_B	Apparent Newtonian (Brookfield) viscosity of coating colors in pilot-plant trials.
ν	Kinematic viscosity; the ratio of shear viscosity and density of fluid.
ρ	Fluid density in in g/cc or Kg/m^3.

ABBREVIATIONS

CMC	Carboxymethylcellulose
DAR	Depthwise aspect ratio of the cavity, D/H
DSV	Downstream secondary vortex in cavity flow. The small vortex formed in the corner of the bottom boundary and the downstream sidewall of the cavity
FDM	Finite differences (numerical) methods
FEM	Finite elements (numerical) methods
FTSD	Film-to-source distance in flash x-ray radiography
FXR	Flash x-ray radiography
LWC	Lightweight coated paper
OTSD	Object-to-source distance in flash x-ray radiography
TGL	Taylor-Görtler-like vortices of the centrifugal instability
SDC	Short-dwell coater
SAR	Spanwise aspect ratio of the cavity, S/D
USV	Upper secondary vortex in cavity flow. The small vortex formed at the corner between the lid, which drives the flow, and the upstream vertical sidewall

ABSTRACT

Although short-dwell blade coaters have increased productivity and imparted desired sheet properties, especially in the manufacturing of lightweight coated papers, the trend to increase machine speed while minimizing coat weight is hindered by the difficulty of maintaining a uniform coat weight profile across the machine. Periodic and random coating thickness nonuniformities produce a patterned surface characterized by CD variations in coat weight, i.e., streaks running along the machine direction. This is particularly true when applying formulations containing delaminated clays which provide superior print quality but whose runnability is not conducive to high machine speeds and solids content. The main objective of this thesis was to explore the possibility that nonuniform CD profiles originate from, and hence correlate with, three-dimensional flow patterns developing in the pond upstream of the blade. Evolving flow structures in the pond may provide the mechanism for nonuniform fluid transfer and solid particles concentration gradients along the span of short-dwell coaters by affecting the distribution of hydrodynamic pressure, mass and momentum into the blade nip.

The methodology comprised of visualization experiments in a laboratory facility, numerical simulation of the two-dimensional flow in the pond, and pilot-plant trials. The pond hydrodynamics resemble the flow in a lid-driven cavity with finite dimensions, hence short-dwell ponds were experimentally simulated as lid-driven rectangular cavities (i.e., with square cross sections having a span-to-width aspect ratio of 3:1) with a small through-flow. Qualitative features were visually studied by altering the control parameter of flow, i.e., the cavity Reynolds number, Re, based on roll speed and Brookfield shear-viscosity of the fluid. The core of information was collected using the suspended-particles and direct dye-injection techniques in transparent Newtonian fluids (i.e., glycerol solutions in water). In addition, a novel flash x-ray radiographic technique was developed to record stop-motion images of patterns through opaque coating fluids.

Flow visualization in a lid-driven rectangular cavity with through-flow and finite dimensions reveals previously unknown aspects of such flows. The primary steady state of flow at low speeds ($100<Re<400$) competes with at least three other stable secondary states featuring three-dimensional cells. A number of counter-rotating recirculating cells appear with the same scale as the cavity depth and rotational axes parallel to the principle direction of flow. The flow becomes unstable at high speeds ($Re>500$) when three-dimensional spanwise structures of centrifugal instability appear in the form of Taylor-Görtler-like

vortices. These evolving cellular structures take the system from time-periodic to oscillatory and, eventually, unsteady states as Re progressively increases above 1100. The critical ranges of the values of Re for occurrence of each state are reported, but only for square lid-driven cavities having a 3:1 spanwise aspect ratio. Visualization studies with flash x-ray radiography revealed similar flow structures with transparent and coating fluids.

Numerical simulations of the laminar two-dimensional steady flow in ponc s reveal that, under conditions of practical interest, the flow in the pond is controlled by the moving web. Two circulating vortices were identified: a large intense vortex driven by the web occupying most of the cavity, and a counter-rotating weaker vortex close to the lower stagnation corner. The curvilinear streamlines of such flows can induce three-dimensionality because they are susceptible to centrifugal instabilities.

Correlations of expected flows in the pond - using the cavity Reynolds number as the control parameter - with the results from pilot-plant trials suggest a qualitative agreement between the hydrodynamic instability characteristics in the pond and the appearance of streaks on lightweight coated papers. Visual observation of streaks coincides with onset of instability in the pond when the machine speed raises the Reynolds number above its critical range. However, streaks appear only when the color shear viscosity (i.e., Brookfield at 100 rpm) exceeds 9 Pascal seconds (900 cps).

There is little doubt that similar flow phenomena observed in the experimental cavity appear in the pond of short-dwell coaters and other confined-flow geometries of size press equipment. The existence of multiple operating states under the same conditions at comparatively low machine speeds can explain the difficulty observed in practice for predicting coater runnability. The results from this study do not provide enough information to completely pinpoint the origin of streaks and to explain the physics involved. In general, hydrodynamic instability in the pond constitutes an adequate condition for development of uneven coat weight profiles, but it is also coupled with a comparatively high shear-viscosity of the color. This study, however, increased the understanding of the problem and has proven, with concrete evidence, the existence of some new flow instability issues which may influence the operation of short-dwell coaters and other equipment for web modification with similar hydrodynamic characteristics.

CHAPTER ONE

INTRODUCTION

BACKGROUND

Coating with a trailing blade is the most common process used to continuously apply a uniform thin layer of mineral suspensions or polymeric fluids to moving webs such as paper and paperboard. Demand for higher productivity and lower coat weight has prompted continual upgrading of blade coating methods. The short-dwell coater is an application system where the flexible blade itself acts both as a boundary that keeps the fluid in contact with the substrate and as a metering device (Fig. 1). Excess fluid is usually fed under pressure into an application chamber, the pond, that sits against a rotating roll to maintain adequate hydraulic pressure and prevent air entrainment. The pond is bounded by the blade on the one side and an overflow wall, the baffle, on the other. The baffle terminates near the backing roll and leaves a small overflow gap for flow opposite to the direction of the moving web.

Short-dwell coaters (SDCs) have gained popularity over the past ten years due to their compactness, operational efficiency, and increased productivity. In contrast to systems with an applicator roll (Fig. 2), color penetration into the sheet prior to metering is minimal and, all other parameters remaining constant, a given coat weight can be attained with lower blade pressure. Today SDCs are popular in producing a wide variety of value-added grades, on- or off-machine, with a bevelled blade configuration. They are extensively utilized, for example, in the production of surface-treated and lightweight coated papers (LWC), grades with a rising demand whose production was limited before by poor machine runnability.

Coating with a SDC has limitations which restrict its wide acceptance in the industry. First, unpredictability appears to be a problem as differences in runnability and coating quality exist between identical coating heads or from day-to-day under the same operating conditions. Second, and most importantly, the trend towards increasing machine speed while reducing coat weight has been hindered by difficulty in maintaining uniform coverage of the substrate. When the machine exceeds a certain speed, the coat weight profile in the cross-machine direction (CD) becomes uneven, with variations outside statistically acceptable limits and larger by several orders of magnitude than the microroughness or formation variations of the base stock. Spatially and temporally periodic, sometimes even random, wet-film thickness

nonuniformities generate a patterned coated sheet of paper which, when viewed under transmitted light, appears dark with many narrow bright stripes. These distinct opacity variations are the result of differential coverage arising from wet streaks running along the machine direction. The streaky (sometimes also called patchy or blotchy) appearance of paper and paperboard makes them aesthetically unacceptable and results in uneven ink coverage during printing. Practical experience has shown that the streaks become easily visible to the naked eye when utilizing coating formulations with large amounts of delaminated clays. Although these pigments are preferred because they provide superior print quality, their runnability is problematic at high speeds and solids content.

The characteristic defect described above is exclusively associated with short-dwell bevelled blade coating, i.e., it does not occur in systems with an applicator roll. It is macroscopic in the sense that the wet streaks are from one to several centimeters wide, a scale much larger than the roughness of the base sheet or the size of pigment particles. Preliminary experience with pilot-plant trials[1] indicates that the streaks become visible when both the (simple shear) viscosity of the coating suspension and the machine speed are comparatively high. Streaking patterns are visually more profound when using large portions of delaminated clays. For example, streaks appear when formulations containing more than 80% delaminated clays at solids contents above 58% or having Brookfield shear-viscosities (@ 100 rpm) above 1000 milliPascal seconds (mPa sec) are used to apply anywhere from 6 to 10 g/m^2 (per side) coat weight at speeds above 1000 m/min. This implies that there may be a coatability limit so that, for a given set of operating conditions and fluid viscosity, a maximum coating speed exists above which streaks appear. Although the streaks are only visible in light weight coating grades, where coat weight is usually in between 6 and 13 g/m^2 per side, they may also set in for heavier coating thicknesses. Coating film thickness nonuniformities are becoming more critical as the trend in the industry is for lower coat weights, higher machine speeds, and consistently superior print quality.

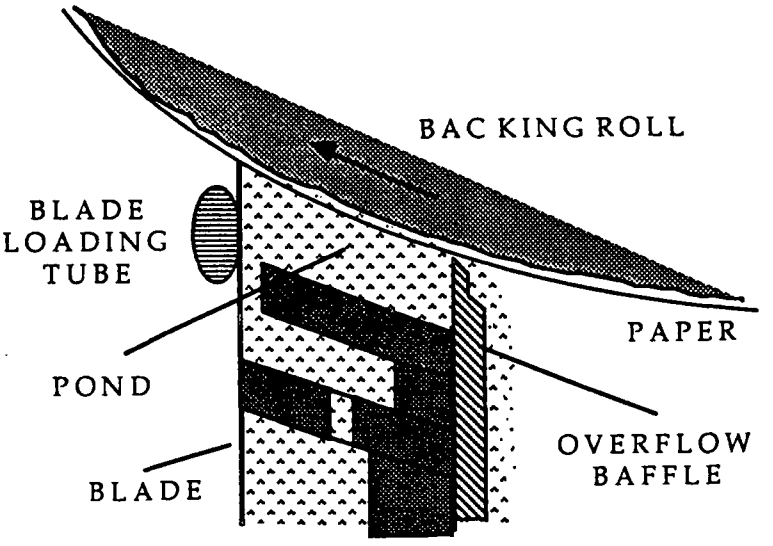

Figure 1. Schematic of a bevelled blade coater with a short-dwell applicator.

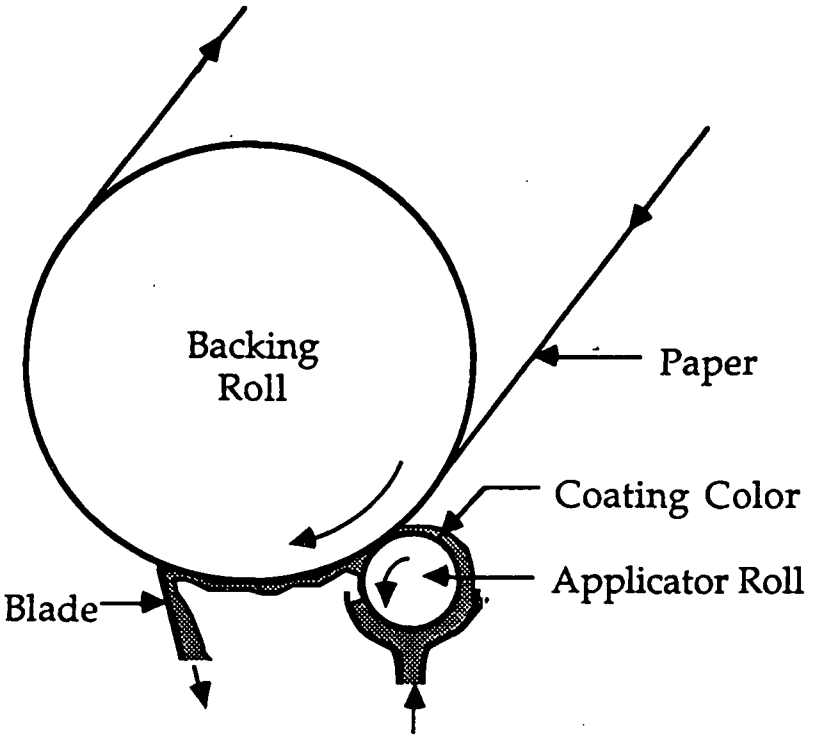

Figure 2. Schematic of a bevelled blade coater with an applicator roll.

The origin of nonuniform profiles in blade coating with a short-dwell coater has been the subject of some investigation and much speculation, but it has not yet been systematically studied. Popular opinion ascribes the problem to "turbulence" upstream of the blade. Eklund, et al.,[2-3] have demonstrated with flow visualization experiments that "two-dimensional" circulating vortices prevail inside SDC ponds. These authors suggested that such flows could generate an uneven distribution of coat weight due to centrifugal forces inside the pond which, in turn, can induce concentration gradients. Consequently, a plethora of articles[4-10] appeared in the literature that put the maximum operational speed limit to approximately 1000 m/min due to "turbulence" in the pond. Concentration gradients referred to by Eklund, et al., however, are in a plane parallel to the machine direction and cannot generate coat weight nonuniformities in the cross machine direction, the problem considered here. More recent numerical simulations[11-13] verified, at least qualitatively, the visualization results by Eklund, et al., and gave a more complete picture of the flow phenomena involved. Characteristically, the flow is driven by the movement of the web, while there are always two

counter-rotating recirculating vortices in SDC ponds under laminar flow conditions; this describe the primary steady state of flow (Fig. 3). In contrast to these two-dimensional treatments, incomplete experimental work by Higgins[14] was the first to indicate the existence of three-dimensional recirculating eddies along the span of a puddle-type coater, i.e., a blade coater similar to the modern short-dwell coater. These three-dimensional cells had axes parallel to the principle direction of flow and appeared at a steady state for speeds even lower than 200 ft/min (for a 75% by volume solution of glycerol in water). The cells were reported to oscillate and eventually become unsteady as the velocity of flow increased. Higgins explicitly suggested that flow instabilities in the puddle can lead to "streaking" defects in the coating film. Nevertheless, there is no published experimental data or other systematically documented evidence to connect pond flows with nonuniform coating thickness profiles.

Motivated by the need to discover the origin of the coat weight nonuniformities discussed above, a fundamental study was undertaken to systematically investigate the hydrodynamic flows in SDC ponds. Although there may be complex interacting mechanisms which contribute to such nonuniformities, the present study concentrated only in one aspect of the physics involved. In particular, it was suggested that three-dimensional hydrodynamic instabilities inside the pond might indirectly be responsible for, and hence correlate with, wet-film thickness variations across the machine line direction. Disturbances in the pond would be transported, influencing the mass and momentum transfer into the blade nip and, consequently, affecting coat weight and its uniformity. Not only is it possible for various forms of hydrodynamic instabilities to set in, but the system may also have multiple stable states. Such phenomena could induce three-dimensional patterns in the pond, which eventually would convect into the blade nip and cause coat weight variations. Central to this hypothesis is the thickness and uniformity (along the span of the doctoring blade) of the coating color layer which travels with the moving web and is eventually delivered into the blade nip (Fig. 4). In systems with an applicator roll and absence of film splitting at the application nip, this layer is well-defined.

A fundamental difference exists between the characteristics of the layer entering the blade nip of a SDC compared to the nearly irrotational layer in a roll applicator system.[15] In the case of a SDC, a viscous layer forms near the dynamic contact line upstream of the blade. This layer is susceptible to hydrodynamic instability and interaction with the dynamic contact line or the three-dimensional patterns forming when the nearly irrotational eddies in the pond destabilize. In general, flows with curvilinear streamlines are susceptible to centrifugal hydrodynamic instabilities, as the control parameter of the flow increases, which can give rise to three-dimensional patterns and eventually unsteady behavior that may lead to chaotic flows.[16] Thus, such interactions generate a nonuniform wavy layer entering the blade nip,

which could convect into the blade nip and produce adverse consequences in terms of coat weight profile. Revealing the rich nature and forms of these flows contributes to an appreciation of the differences observed in practice between systems with an applicator roll and short-dwell coaters. In addition, understanding the physics involved will lead to better control of the process. Finally, information on the fluid flow aspects provides the basis for the design of the future generation of coaters.

A logical first step towards understanding SDC pond flows is to study an idealized flow which incorporates the essence of the relevant physics, but has a simpler geometry with well-defined boundary conditions. The geometry in the pond of a SDC is similar to a narrow rectangular cavity, hence the viscous flow is induced by the shear stress imposed on the fluid by the moving upper boundary (or web) of the cavity. Thus the flow in a lid-driven cavity of square cross section was selected with "through-flow", as a relatively small flux of fluid continuously passes through the enclosure. This type of isothermal viscous flow resembles the recirculating flow in an enclosed shear-driven cavity, a benchmark problem used extensively at low Reynolds numbers to validate computer codes and used experimentally to study complex recirculating flows existing in the industry and geophysical environment. Although the previous studies have covered a range of Reynolds numbers - the control parameter that describes the viscous flow as defined in the next section - ranging from 100 to 10,000, the interest here concentrates in flow phenomena occurring in the range of 100 to 2000 which represents a typical range of practical interest in coating with a short-dwell. In the following sections the general goals of the work are outlined and the approach taken in achieving these goals is described. This introduction is concluded with an outline of the organization of the rest of the dissertation.

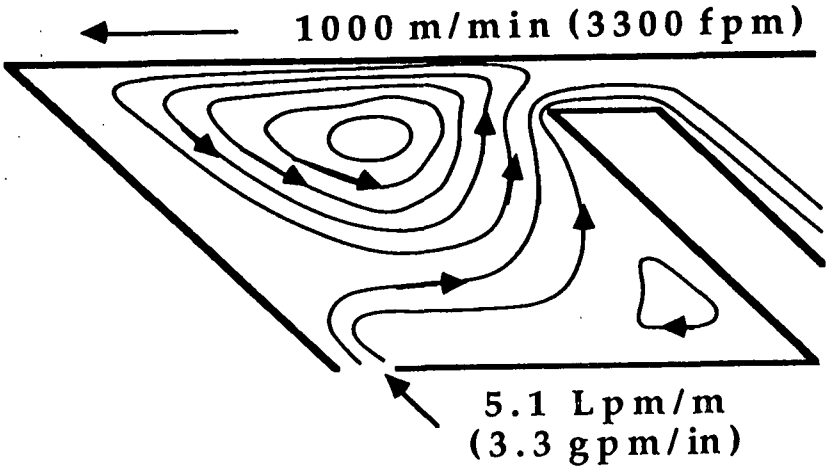

Figure 3. Contour of streamlines of the two-dimensional, laminar, steady flow in a short-dwell pond from numerical simulations.

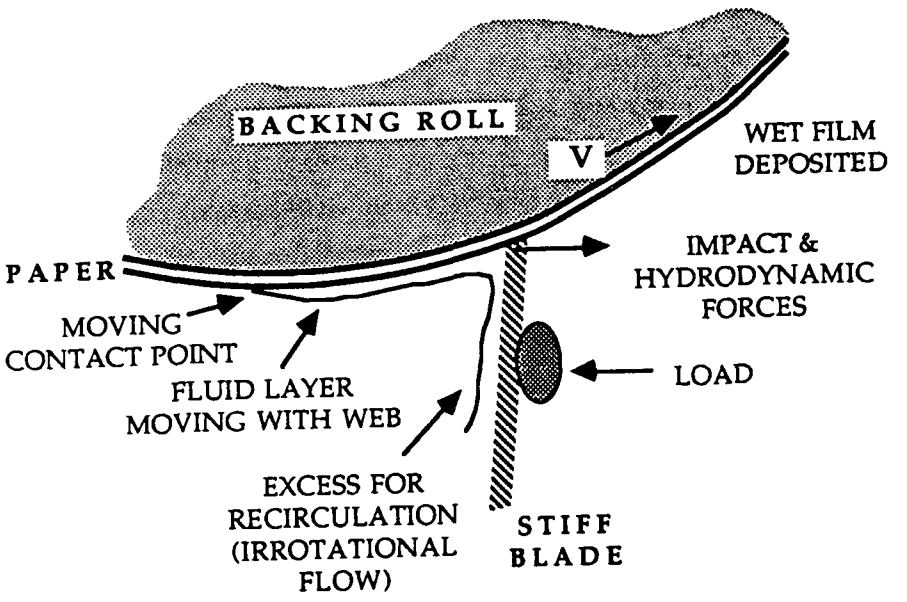

Figure 4. Schematic of conceptual understanding of phenomena in a SDC pond. Dimensions not to scale.

RESEARCH GOALS

The principle objective of the research work was to qualitatively explore flow phenomena inside the pond and investigate their possible connection to the appearance of visible wet streaks on a coated web. To achieve this (a) the fluid dynamics in a geometry similar to a short-dwell pond were studied, and (b) the onset and appearance of wet streaks were systematically documented with pilot-plant trials. As stated above, the pond was experimentally simulated as a narrow rectangular lid-driven cavity with small through-flow. Because of the finite dimensions of the cavity, the side endwalls induce three-dimensionality. The scope was to visualize flow patterns developing into cavities of a specific size as the control parameter(s) of the flow changed. Accordingly, experiments were deviced with the following specific objectives:

1. To document the appearance and form of steady and unsteady flow features as the lid speed progressively changes;

2. To determine the control parameter(s) of the flow and their critical ranges for onset of the various modes of flow in the cavities of the specific size;

3. To document flow structures which exist with optically opaque non-Newtonian fluids (i.e., typical coating suspensions);

4. To identify stability features of a three-dimensional driven cavity flow.

It is worth noting that the last goal led to an additional set of visualization experiments after the research program was underway. This was a result of preliminary observations which indicated that the apparently basic steady state of flow in cavities of finite span competes with other three-dimensional steady states.

Since no systematic pilot-plant data have been published with respect to the occurrence of wet streaks, the task of our work was to collect evidence that could connect visually observed wet streaks on LWC paper with expected transitions on the pond flow. Trials, under conditions similar to the ones common in industrial practice, were motivated by two primary needs. First was the need to determine as precisely as possible the exact conditions under which streaks appear. Second was to establish a data base for evaluating the nature of streaks on a paper web.

As part of this research, limited numerical experiments were conducted with a commercially available computational fluid dynamic code. Although the computer model of SDC pond flows considered only the two-dimensional equations for the laminar steady-state

flow, it was developed to confirm previous works and gain some new insights of the flow characteristics. Specific goals of numerical experiments were:

1. To verify flow visualization results from earlier work appearing in the literature;
2. To resolve the principle features of the two-dimensional, laminar, steady flow in the pond of a short-dwell coater;
3. To determine the effect of machine speed, fluid rheology (only power-law fluid model) and feeding flow rate on the basic flow.

APPROACH

The methodology implemented for realizing the objectives of this research incorporated flow visualization experiments, pilot-plant trials with a short-dwell coater, and numerical experiments using a commercially available code. A facility was built to conduct flow visualization experiments. The flow in short-dwell coater ponds has been simulated experimentally as a shear-driven flow in a rectangular cavity. Furthermore, to consider the fluid deposited onto the web, a relatively small flux of fluid was allowed to pass through the cavity. Enclosed lid-driven cavities constitute a relatively simple geometry to study recirculating flows in fluid dynamics and have been used extensively, at least in their two-dimensional form, as a benchmark problem to test numerical codes.The flow is characterized by a Reynolds number (Re) defined as:

$$Re = \frac{\rho V D}{\mu}, \tag{1}$$

where V is the velocity of the lid and D is the depth of the cavity. For cavities with through-flow, however, an additional dimensionless parameter is required to define the flow. This is the Reynolds number (Re*) based on the net volumetric flow rate through the cavity (Q) and the spanwise length of the cavity, S:

$$Re^* = \frac{\rho Q}{\mu S}, \tag{2}$$

Flow visualization studies performed during the course of this research were for Re between 100 and 9200, while the range for Re* varied from 0.01 to 2.40. Within this range, the through-flow cavity has flow characteristics similar to an enclosed lid-driven cavity. Cavities with the same aspect ratios, i.e., span-to-width (SAR) and depth-to -width (DAR) ratios of of 3:1 and 1:1 respectively, but different sizes were used, while machine speed and fluid viscosity were the parameters varied to alter the Reynolds numbers.

Several flow visualization techniques were utilized and a novel radiographic technique was developed to obtain quantitative information about the state of flow. Most of the experiments were performed with a transparent Newtonian fluid continuum and a suspended-particles technique using a sheet of light, although direct-injection of a dye was used occasionally. Still and video photography was employed to record the experiments, but also some qualitative data was obtained by visual estimation and direct measurement of sizes. A flash x-ray radiographic technique was developed to create stop-motion images of the flow through non-Newtonian opaque fluids, like the concentrated mineral suspensions used in paper coating. Direct-injection of an x-ray absorbant fluid, otherwise having similar properties as the bulk fluid, allows for recording the flow non-intrusively.

ORGANIZATION OF PRESENTATION

The remainder of the report includes details of the literature review, numerical simulations of pond flows, experimental program, methods and procedures, visualization and pilot-plant results, discussion and interpretation of results, and conclusions. The first section briefly reviews the principles of blade coating, different theories on the factors affecting the deposition of coat weight, operational features of short-dwell coating and its problems. This section also includes a review of the state of knowledge of the flow in a lid-driven cavity, the geometry used here for experimentally simulating SDC ponds. Both experimental and numerical works are being reviewed. Following is a presentation of results from computer modeling, and discussion of their significance. The next section outlines the procedures followed in the experimental design, describes the experimental facility, flow visualization methods and procedures used, and presents the viscometric measurements technique and an uncertainty analysis. Appendices A and B provide supplemental details on the facility and the flash x-ray radiographic technique, used in first-time visualization of the flow through opaque fluids such as coating colors. Appendix C has details on the uncertainty analysis.

The results section comprises of two parts. Results from flow visualization experiments in the lid-driven cavity with through-flow are presented first, followed by data from pilot-plant trials. The first part of the results section includes a description of flow phenomena and their characteristics, important factors influencing the flow, the control parameter and its critical ranges, and concludes with interpretation of results and discussion. The second part presents characterization of problematic coating colors and systematic documentation of the

appearance of streaks on LWC paper coated in a pilot machine. Supplemental information on the laboratory and pilot-plant results are included in Appendices D and E. The final section contains a discussion and implication of results, in addition to a summary of the results, recommendations for further work, and conclusions.The final Appendix F contains the literature cited on flash x-ray radiography.

CHAPTER TWO

REVIEW OF RELATED LITERATURE

OVERVIEW

The literature review section is divided into two distinctively independent parts. In the first part (blade coating), a summary is provided of the factors controlling coat weight and of the short-dwell blade coating process. In the second part (driven cavity flows), the state of knowledge on shear-driven cavity flows is reviewed with emphasis on the three-dimensionality of the flow. Although seemingly unrelated, the two parts formulate the background to build on the concept that what is going on in the pond of a short-dwell coater may be important when considering the uniformity of the coating film across the machine line direction.

The section on blade coating summarizes the state of knowledge about the mechanism(s) which determine coat weight on paper webs. It highlights the two mainstream theories and establishes the connection between film thickness downstream and the upstream fluid delivered into the blade. It also points out the key features of a short-dwell coater which differentiate it from previous generations of blade coaters. This information is relevant because it helps to conceptualize the more complex physics involved in this new type of coating machines, or more specifically the influence of the fluid dynamics in the pond, a recirculating bounded flow driven by the moving web. The purpose, therefore, of the discussion in this part is to outline the basis for choosing the experimental flow of interest, i.e., a lid-driven cavity flow with through-flow.

The section on driven cavity flows describes the flow characteristics from previous experimental and computational results. Because there is a large number of references regarding this type of flow, due to its relative simplicity and use as a benchmark problem to evaluate numerical codes, only important issues relevant to the present work are reviewed. The features of the basic steady flow - which we call primary as it corresponds to the "two-dimensional" state appearing in the literature - are presented, but the focus is on three-dimensional flow phenomena which are responsible for transport processes along the span of the cavity. The goal here is to highlight missing information, or more specifically aspects of the evolution of flow, which led to formulating the experimental program.

BLADE COATING OF PAPER

There are various ways to use blades as the metering device for depositing thin films of coating colors, a waterbased blend of mineral suspensions and polymeric additives, onto a moving paper or paperboard web. The blade configuration of interest here is that of a stiff blade, also called trailing or bevelled type, where the blade tip is resting parallel to the traveling web and is tangent to the backing roll surface, to differentiate it from the low-angle configuration of the bent or flexed blades. Such relatively straight blades have typical tip (or bevelled) angles between 20° and 50°, the 45° blade angle being most commonly used and chosen as a reference. To control coat weight, the blade is often loaded by a pressure hose, where air pressure within the hose can be used to control coat weight, but it can also be point-loaded by a metallic bar in the mode known as S-matic™. It is worth noting that coat weight control with blade pressure is strikingly different between the bent and bevelled blade configurations.[17]

In the bevelled mode and when the blade tip remains parallel to the web surface, experience has shown that coat weight is reduced continuously with increasing blade-loading (mechanical) pressure and eventually approaches the pressure axis asymptotically. Blade nip geometry is important because, as Kuzmak[18] has shown, slight variations by running on blade heel or toe can effectively alter this relationship and generate unsteady conditions.When the viscous layer of fluid which moves with the web enters the converging nip under the blade it accelerates and, consequently, deflects the blade. The deflection of the blade is counter-balanced by the externally applied mechanical pressure, the blade load. Most of the fluid approaching the blade is being decelarated away and only a relatively small amount (i.e., about 2%) passes into the blade nip. The physics involved are complicated because inertia, pressure, and viscous forces interact to cause most fluid elements to decelerate, and some to accelerate or even rotate. Assuming that a bevelled blade is indeed running on its bevel (i.e., steady condition), the question is: what factors influence coat weight deposition?

Coat Weight Deposition

Many theories have been proposed and semi-empirical models developed over the years to explain bevelled blade coating of paper, mainly in an attempt to predict and control

operating parameters which influence coat weight. These theories have considered three fundamental phenomena: (a) the filling-in of pores in the compressible and rough substrate (the paper or paperboard web), (b) the pressure and capillary penetration before and during metering, and (c) the fluid mass and momentum transport phenomena in the vicinity and under the blade nip. From the standpoint of short-dwell blade coating, the first two are of lesser importance because of the low hydraulic pressure prevailing in the pond and the short period of time for contact between the fluid and web before metering that do not allow for liquid penetration or dewatering to occur.[7,19] The third mechanism plays an equal or more important role in short-dwell coating, as in previous systems with an applicator roll.

Most analyses are based on the argument that coating deposition onto paper is determined by the hydrodynamic phenomena under the blade and is somewhat influenced by absorption of the coating fluid into the substrate. According to this approximation, the flow under a bevelled blade is a combination of drag flow driven by the moving substrate and a pressure gradient acting along the direction of the web movement. Consequently, the pressure force exerted by the fluid tends to lift the blade which is taken as a purely linear elstic solid. Thus, by approximating the blade nip geometry as a converging [20-26] or parallel wedge,[27-32] blade coating can be analyzed with the hydrodynamic lubrication theory for a rotating slider (or journal bearing) and the blade considered as a cantileved beam. The characteristic pressure gradient is proportional to the volumetric flow rate per unit width, Q, as depicted in the following relationship:

$$\frac{dP}{dx} = \frac{6\mu}{h_y^2}\left(V - \frac{2Q}{h_y}\right) \tag{3}$$

where h_y is the distance of the blade pressure from the web in the blade nip. Considering the blade as a cantilever beam, the hydrodynamic lift should then be equal to the applied load (mechanical pressure) on the blade under steady conditions. Thus the flow rate, and therefore the wet-film thickness of the coating, is given by the equation:

$$Q = \frac{2}{3}\left(\frac{\mu\, t\, V^3}{P\, \sin 2\alpha}\right)^{1/2} \tag{4}$$

where t is the blade thickness and α is tha blade angle, i.e., the angle formed by the blade and by the tangent to the web at the blade nip.

Results from numerous pilot-plant trials correlated this analysis with operating parameters which affect coat weight, such as fluid viscosity, machine speed and blade thickness.[25,26,27,29] Parameters like liquid penetration into the substrate,[33-36] surface

microroughness,[37-38] blade flexibility,[29] and viscoelasticity[39] have also been considered.The fundamental assumption in lubrication approximation is that a two-dimensional flow field can be represented by a one-dimensional model. Once this has been accepted, solution of the fluid flow equations is trivial, at least for the case of a Newtonian fluid.[40,41] Attempts to introduce rheological effects have also had some success.[43-46] Based on this simplified model, coat weight is directly proportional to the volumetric flow rate passing through the nip, hence the wet film thickness at the exit of the blade nip.

According to the lubrication model, the flow under the blade is a combination of a velocity-driven (Couette) and pressure-driven (Poiseuille) flows. In addition to the pressure gradient that drives fluid into the blade nip, another pressure gradient opposite to the moving web direction develops causing a backflow upstream of the nip. This gradient deflects excess fluid carried by the moving web away from the nip into the recirculation loop. Modrak [25] was the first to suggest that unstable conditions at the edge of this backflow may be responsible for non-symmetrical particles (i.e., clay platelets) to ‹‹... flip end over end...›› and cause blade coating defects ‹‹... due to disruption and disintegration of the laminar film of color supporting the blade.›› However, two major disadvantages of lubrication model are that (a) it does not account for the finite but unknown location of free surfaces across the blade nip, and (b) it cannot differentiate between possible two- or three-dimensional flows in the upstream pond - the centerpiece of the proposed hypothesis here for short-dwell blade coating. Because this model does not take into account the boundary conditions upstream of the blade nip, it does not consider the momentum change of the excess fluid which exerts an impact pressure force onto the blade. Furthermore, the uniformity of both the momentum change and pressure gradient across the width of the blade are not an issue.

More generalized approaches are taking into account hydrodynamic phenomena upstream as well as free contact lines, i.e., the moving contact line upstream and the static contact line at the blade exit. Guzy and Higgins[46] illustrated theoretically the effect of hydrodynamic pressure drop across the nip, thus accounting for the flow in the upstream pond and the developing free contact line. They demonstrated that wet-film thickness is influenced by the pressure level in the upsteam pond of a puddle-type coater (a coater with an application zone similar to SDC where the pond is confined between an inverted blade and the backing roll). Because the upstream pressure, inside the pond and before the blade, is above atmospheric,[14,47] there is always a viscous pressure drop across the nip and the final wet-film thickness deposited is greater than the gap under the blade tip. An interesting observation from this analysis is that if the pressure in the pond becomes subatmospheric, e.g., due to suction induced by a recirculating eddy in the SDC pond before the nip, there is an

In an attempt to better correlate operating and design parameters with coat weight in bevelled blade coating, several analyses consider the impact of excess fluid carried by the web. Kuzmak [31-32] takes into account the force (F_m) externed by the coating striking the underside of the blade, hence the wet coating thickness is proportional to:

$$\left(\frac{6\, k\, \mu\, (t / \sin\alpha)^2\, V \cos\alpha}{(k'\, P - F_m)} \right)^{1/2} \tag{5}$$

where k and k' are empirical constants. This work shows that, in order to maintain a constant coat weight, there is a need for a steadily increasing blade load when running a bevelled blade on the heel and decreasing load when running the blade on its toe. From a different point of view, Windle and Beazley[48] suggest that the blade should be making contact with the paper by assessing from experience that «... when one treats the blade as a simple cantilever beam, the hydrodynamic force required to deflect the blade by a distance equal to the thickness of a typical coating is almost one thousandth of the force generated [as this was measured from the necessary blade load to attain a certain coat weight].» Then, it is the web compressibility that lets fluid to fill-in the blade gap. Advancing this concept a step further, Kahila and Eklund[49-51] have developed a theory based on the impulse approximation which suggests that the inertia of the fluid layer delivered to the blade influences coat weight by deflecting the blade and modifying the compressive force acting onto the web. In addition to the hydrodynamic force, H_Z, from the lubrication approximation, two more forces are acting on the blade: the impulse (R_Z) and pressure (P_Z) forces. Both originating from the momentum change under the blade, they are calculated, respectively, from the following relationships:

$$R_z = \dot{m}\, V\, (1 + \cos\alpha)\, \sin\alpha \tag{6}$$

and

$$P_z = \frac{1}{2}\, \dot{m}\, V\, \frac{\pi}{\alpha}\, f(\pi, \alpha, h_2, h_o) \tag{7}$$

where h_2 and h_o are the film thicknesses of the fluid reaching the blade and passing under the nip, respectively. Thus, the compressive force acting on to the web and backing roll is defined as the difference between blade load and the impulse, pressure, and hydrodynamic forces. According to this approximation, although blade load controls the nip gap, it is the surface roughness of the web under the blade which determines the coat weight pickup. Under conditions of practical interest (i.e., bevel angles greater than 27°) and speeds in excess of 900 m/min, impulse forces are two orders of magnitude greater than the hydrodynamic

Under conditions of practical interest (i.e., bevel angles greater than 27°) and speeds in excess of 900 m/min, impulse forces are two orders of magnitude greater than the hydrodynamic force calculated from the lubrication approximation. The process therefore is assumed to be stable only when the blade makes contact with the paper (although there is probably always a monolayer of fluid between blade surface and web) and, therefore, coat weight can be controlled. Because impact forces are proportional to the mass flow rate (m) and velocity of the fluid entering the convergent nip between blade and web, momentum transfer into that region and its uniformity would play an important role in coated film thickness and its cross web uneveness.

Ongoing research by The Coating Flows and Coating Rheology Group at the University of Minnesota is utilizing theoretical and computational calculations in a supercomputer to unveil the mechanisms and parameters affecting blade coating. Considering the viscous and pressure forces exerted by the fluid and the elastic forces that deform the blade together in an elastohydrodynamic model, researchers from this group have simulated bevelled blade coating of deformable[15,52] and porous[53] substrates. The elastohydrodynamic analysis takes into consideration two-dimensional inetial effects, the free surface upstream as well as downstream of the blade nip region, the compressibility and permeability of the substrate. It is basically a force balance which incorporates elastic, pressure and viscous forces. Computational results from two-dimensional models using a finite element code have provided interesting details of the different flows at various regions in the vicinity and under the blade, as well as of the effects occuring when changing operational parameters. Of particular interest to our work is the observation that a thicker incoming layer (into the convergence of blade and web) would increase the amount of inviscid fluid deflected away from the blade, increase blade loading, and yield a thicker coated film. All numerical experiments, however, concentrated on blade coating systems with an applicator roll, assuming a two-dimensional steady state where there is a uniform delivery of the fluid layer into the blade across the machine line direction.

A common assumption in all of the above theories (i.e., lubrication approximation, impusle approximation, and elastohydrodynamic analysis) is the delivery of a uniform layer of fluid travelling with the web into the convergent nip close to the blade. Spatial and temporal uniformity of this layer, however, cannot be assumed *a priori* , especially in the case of a SDC where inherent system behavior upstream and close to the blade is different from systems with an applicator roll - the prototype used in all of the analyses discussed above. Although similar physics are probably involved in the blade nip of both systems, this may not be necessarily true for the 'approaching the nip' fluid flow. There are two important issues which deserve observation. First, the velocity profile of the fluid entering the blade nip may

not be uniform across the blade due to hydrodynamic instability upstream which features three-dimensional cellular structures. Second, this velocity profile may vary with time so that instead of the simple momentum term mV, the expression

$$\dot{m} \int_{t_1}^{t_2} V \, dt \tag{8}$$

needs to be used. The next section highlights differences in the application zone of the two types of coaters to elucidate dynamic phenomena which may dramatically alter the mass and momentum transfer into the nip of a SDC.

Short-dwell Blade Coaters

Blade coating has been extensively used in the paper industry for more than a quarter of a century, the most common type of coater being the flooded nip with an applicator roll (Fig. 2). Coat weights deposited vary between 4 and 32 grams per square meter (gsm) per side of paper, corresponding to approximately 10-60 μm of wet film thickness.[23] Several problems are associated with such coaters. The relatively high hydraulic pressure applied at the nip of the applicator roll, i.e., 100-300 kPa,[10] and the prolonged time of contact between the color and the web before metering, i.e., about 30 milliseconds,[4] cause excessive dewatering of the color through the web. Because of extensive capillary and pressure penetrations, the solids content of a color traveling towards the blade nip increases and, therefore, raises the required blade load to attain a certain coat weight. High pressures not only induce penetration of color components into the web, an undesirable phenomenon that reduces some strength properties of paper, but also reduce productivity because of frequent web breaks.

The short-dwell coater was developed to effectively solve these problems and to reduce coat weights, primarily of light basis weight grades, to 4-10 gsm.[54] With SDC it is possible to apply a given coat weight at a lower blade load than with an applicator roll,[55] and lower loads are required with SDC to maintain a constant coat weight when the machine speed increases.[56] Although the term "short-dwell" was established because of the limited period of time that the fluid remains in contact with the web before metering , i.e., 2-8 msec, a more appropriate term is "low-pressure" applicator since hydraulic pressures as low as 2-5 kPa are applied onto the web before metering.[18] The key component of such a coater is the application pond that is open upstream towards the backing roll, bounded by the blade

machine direction width and 4-7 cm in depth (Fig. 5). Fluid is supplied from a distribution chamber through a feeding slot that extends across the operating width of the machine. By feeding the coating fluid into the pond at sufficiently high volumetric flow rates and maintaining a certain hydraulic pressure, an overflow is established in the gap between the roll and the baffle with flow opposite to the direction of web traveling. The overflow gap can be adjusted to 2-10 mm to avoid penetration of ambient air into the pond. Thus, the pond serves a dual purpose; to bring the coating fluid in contact with moving web and to exclude inclusion of air. It is similar to the pool of a puddle-type coater, i.e., an earlier version of blade coaters, confined by the web and the blade at the bottom, while the top remained open to the atmosphere.

The popularity of short-dwell coaters has increased over the past ten years mainly due to their compactness, operational efficiency, reduced web breaks and low water penetration into the web.[57-59] However, their effective operation at speeds above approximately 1000 to 1200 m/min and coat weights below 10 gsm has been plagued by uneven cross directional coat weight profiles and wet streaks.[7,9] This problem has been attributed to "turbulence" in the pond, which subsequently can also destabilize or dettach the moving contact line upstream to cause coated film thickness nonuniformities. However, there is no documentation yet to support such an argument. Thus, an interesting question that remains unanswered concerns the characteristic flows in the pond as web (or machine) speed increases and the system is driven from its basic (primary) steady state to more complex modes of flow. The latter would not only affect the thickness of the boundary layer impacting the blade and its spanwise uniformity, but also could have a detrimental effect on the uniformity of the moving contact line upstream the pond.

The flow in a SDC pond is an isothermal, bounded recirculating flow induced by the moving boundary on the top which, due to the no-slip condition, imposes shear stresses onto the fluid. The rigid blade bounds the flow downstream, while the overflow baffle confines it upstream. Characteristically, a "rotating roll of coating [fluid]" has been seen in the pool of a puddle coater as web speed increases, which causes poor mixing and separation of coating fluid components due to centrifugal forces.[9] Although the SDC pond is enclosed, it is fundamentally similar to the pool of a puddle coater having recirculating flows. These were shown experimentally and computationally by Eklund ,et al.,[2,3] and computationally by the author, et al.,[11,12] and others.[13] Furthermore, the SDC pond flow is a variation of the classic lid-driven flow in a rectangular cavity, one of the simplest examples of flows exibiting closed streamlines and used extensively as a benchmark problem to evaluate computational codes. The only difference is that there is a relatively small (compared to the amount of fluid recirculating) flux of fluid continuously passing through a SDC pond, and therefore this

recirculating) flux of fluid continuously passing through a SDC pond, and therefore this system can be experimentally simulated as a lid-driven flow in a rectangular cavity with "through-flow".

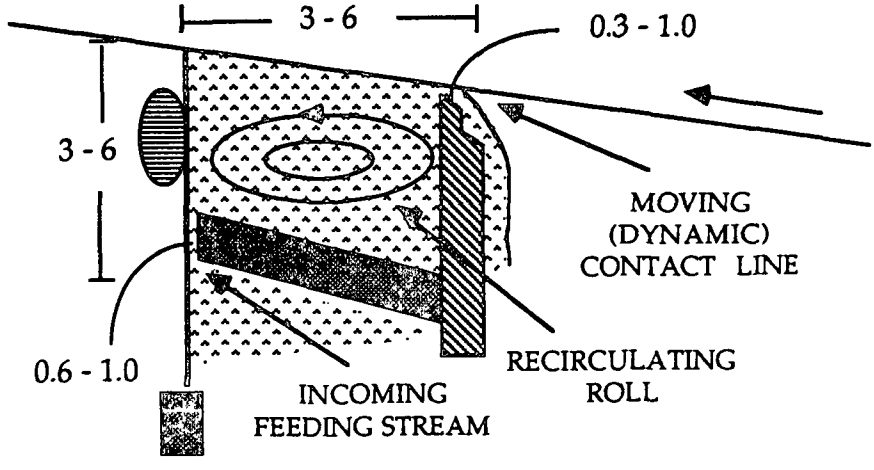

Figure 5. Definition sketch of the geometry in a short-dwell blade coater pond.

The Problem Associated with Short-Dwell Blade Coaters

Although "turbulence" in the pond has been suggested in the literature as the cause of wet streaking on paper, there is no published data to support such an argument. The scope in this

preliminary evaluations and previously unpublished data from pilot and laboratory coater trials.[1]

Uncontrollable coat weight profiles appear in the form of wet streaks running along the machine line direction immediately downstream from the blade nip. After drying and when a sampled sheet of paper is viewed under transmitted light, the streaks look as bright ribbonlike strips on a darker background (Fig. 6). Not to confuse these streaks with the blade coating defect known as skips - where air entrapment causes total depletion of coating fluid from certain spots [60] - opacity differences here represent uneven coverage of the web, i.e., the bright areas having lower coat weight than the dark. Microscopic analysis of the coated sheet surface indicates that the region within a streak comprises of pigment particles, in cocntrast to skips where there are no particles deposited, but in numbers substantially lower than in adjusted regions. In practice wet streaks are being readily differentiated from skips, at least in their conventional appearance. At first streaks are discontinuous with variable length and intensity, but become continuous strips of low coat weight at higher speeds, thus creating a striated pattern onto the paper. The width of the streaks is usually between 1 and 8 cm and, therefore, the streaks are considered large-scale inhomogeneities, i.e., their spatial scale is many orders of magnitude larger than the basestock microroughness and basis weight variations. Streaks are usually moving across the machine direction, although occasionally they have been observed to be stationary.

The problem becomes more profound when attempting to deposit relatively thin films of viscous coatings beyond a certain machine speed. Film thicknesses in the range from 4 to 12 gsm are common nowdays for LWC publication papers having basis weight of 40-60 gsm.[7,8] Because minimum thickness with optimum coverage of the substrate inhomogeneties are desired, flat kaolin platelets (i.e., delaminated clays) are the preferred pigments for better smoothness, gloss, brightness, and opacity. Such clays are comprised of laminar particles with large diameter-to-thickness aspect ratios, i.e., 4:1 to 8:1 and 14:1 to 20:1 for Georgia and English China clays, respectively. Although these clays provide superior print quality, their runnability is poor due to high shear viscosity,[61] probably arising from the the large size and, therefore, orientability of the particles. Above a certain speed, which depends primarily on the solids concentration by weight, CD uneveness appears in the form of a heavily striated film. For example, streaks can be visually identified with the naked eye when a rotogravure formulation containing more than 80% delaminated clays at total solids contents above 58% or having Brookfield viscosity (100 rpm) above approximately 1000 mPa sec is utilized to apply 6-10 gsm at machine speeds above 1000 m/min. Interestingly, a similar pattern can be reproduced when the "problematic" coating color is applied directly onto the rubber covered

backing roll (Fig. 7), which indicates that streaks are independent of base stock formation characteristics.

In summary, empirical observations of the cross directional coat weight profile problem in SDC coating show several trends. For a given set of operating conditions and fluid viscosity, a maximum coating speed exists above which, for a slight increase in machine speed, the CD coat weight profile is uncontrollable. This is a phenomenon which does not relate to the porous substrate but rather to the dynamic processes occurring in the application zone of the coater. Profile variability may or may not be observed visually, but when it does it appears in the form of wet streaks or striations running along the machine direction. In the case of viscous fluids, i.e., highly concentrated suspensions of delaminated clays, the streaks become more intense and are visible to the naked eye. Also worth noting is the observation that at speeds where a streaky coated paper is produced the overflow above the baffle many times becomes unstable by pulsating unevenly across the machine, hence indicating an irregular moving contact line upstream. However, it is possible to get streaking while the overflow seems to be uniform and maintaining contact with the web across the machine. Remedies like decreasing the overflow gap or increasing the feeding flow rate though helping to reduce the intensity of the problem did not provide permanent solutions, i.e., pushing the operating speed limitation substantially higher.

The next section gives an overview of the state of knowledge on lid-driven cavity flows, the topic being relevant to the present thesis since this ideal type of recirculating flow was utilized to experimentally simulate SDC pond flows.

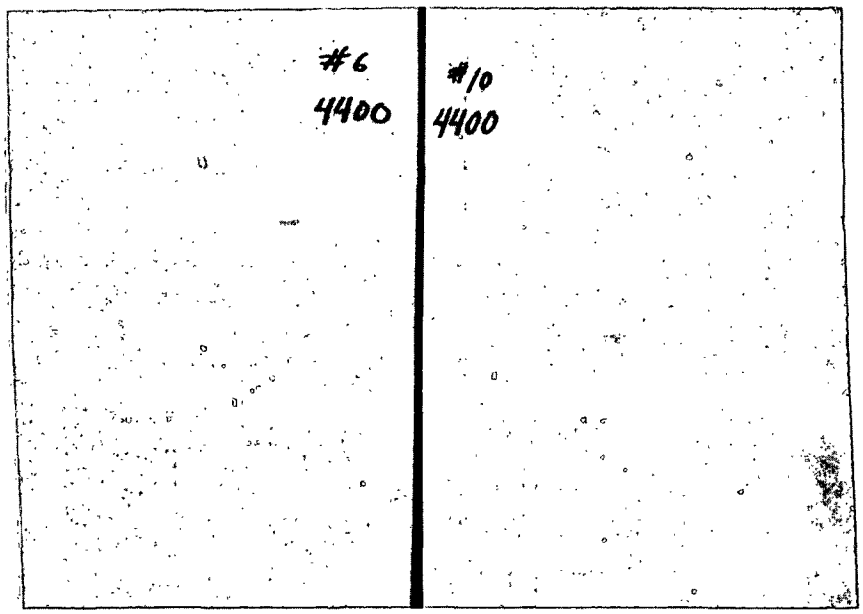

Figure 6. A characteristic example of wet streaks appearring on LWC paper coated in a pilot-plant at machine speed of 1340 m/min.

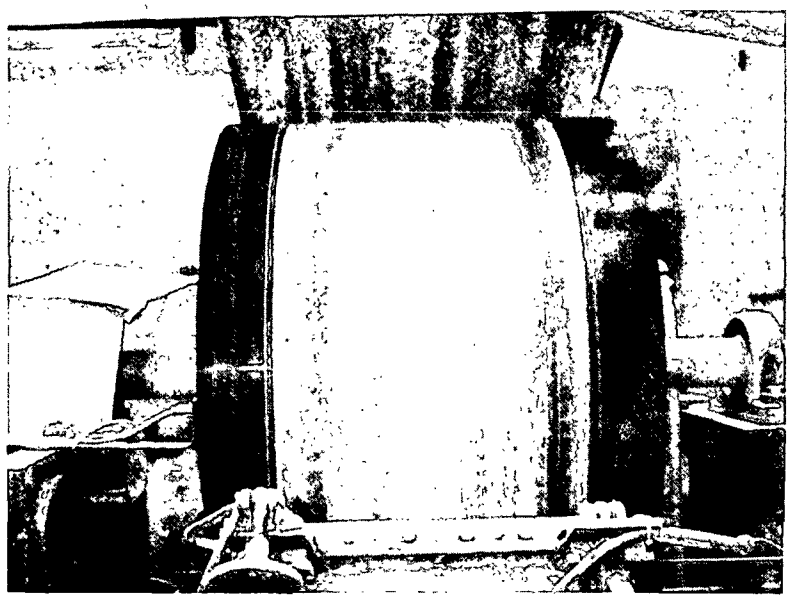

Figure 7. Patterns appearring when the same coating color as in Fig. 6 is applied directly on to the rubber covered backing roll (1070 m/min speed).

SHEAR-DRIVEN CAVITY FLOWS

The shear-driven cavity flow of a viscous incompressible fluid has been a classic problem in fluid mechanics due to its simple geometry and straightforward boundary conditions. The literature contains a plethora of papers on experimental studies and numerical simulations. Although at comparatively low Reynolds numbers (Re<400) the flow is steady and thereby both experimental and numerical results are in good agreement, substantial differences occur at higher Re due to inaccuracy of the numerical techniques employed and increased complexity of the flow. The flow becomes unsteady at higher Re because of edge (or end-wall) effects and hydrodynamic instability. Comprehensive lists of the most important studies are presented in tabular form in Tables 1 and 2. The first Table outlines previous experiments in channel cut-outs (i.e., where the flow in a cavity is driven by an outer or external stream) and in enclosed lid-driven cavities, while Table 2 presents three-dimensional simulations up to date. Dicussion in the following sections concentrates on major features of the flow with particular emphasis to recent discoveries regarding three-dimensional flow phenomena. Numerical results are discussed only for three-dimensional simulations. The scope is to define the flow features at low-to-moderate Reynolds numbers, describe implications of previous studies, and demonstrate areas where lack of knowledge might be important to the problem on hand.

Previous Experimental Works

Experiments have been performed in rectangular cavities with finite dimensions and for a wide range of depthwise and spanwise aspect ratios. Cavities have been either open at the top (as in a channel cut-out) or enclosed, while flow features have been studied for a wide range of Reynolds numbers - the Reynolds number as defined in Eq. 1. In a channel cut-out the flow is usually driven by an outer stream of air or water in wind and water tunnels for low and high Reynolds numbers (see Table 1). High Reynolds number experiments have been performed by Maull and East,[62] Mills,[63] Haugen and Dhanak,[66] Roshko,[68] Fox,[69] and Orlandi and Ianetta.[70] Low Reynolds number experiments have been conducted by Johnson and Dhanak,[64]Reiman and Sabersky,[65] Weiss and Florshein,[67] and Rockwell and Knisely.[71]

Flow visualization experiments by Maull and East[62] illustrated for the first time the three-dimensionality of the flow in open channels and its dependence on the span-to-width (SAR) aspect ratio. Both visualization of oil patterns and spanwise pressure measurements illustrated development of surface waves, pressumably originating from the outer stream,

and edge effects. Separation of the two effects, however, remained incomplete and the effect of Re was not investigated. Rockwell and Knisely[71] revealed longitudinal vortices appearring on the top of the cut-out next to the driving stream for high Reynolds numbers (Re>10,000). Weiss and Florshein[67] reported two vertical recirculating vortices present in a channel with depth-to-width (DAR) aspect ratio of 3:1, but only one cell for DAR=1:1.

In review, the laminar flow in open cavities is characterized by the appearance of one or two circulating cells, depending on the depth of the cavity. Experiments have also demonstrated the strong dependence of the flow on the incoming boundary layer on the top that drives the flow. It is possible, for instance, that the flow may become periodic with waves at relatively low Reynolds numbers (Re <200) due to a turbulent shear layer driving the flow.[65] At even higher Re, the frequency spectra of oscillations are more complicated, the destabilizing effect becoming more predominant in shallow cavities.[72] In contrast, the recirculating flow where an impermeable moving (top) boundary of the cavity induces the motion is a physical situation more representative of the problem considered here.

Fewer excperiments have been run with enclosed cavities and are mostly three-dimensional. The flow in an enclosed lid-driven cavity constitutes a simple and controlled problem because there are few external factors influencing its state. For low Reynolds numbers (Re<400) the flow may be considered as two-dimensional, at least at the symmetry plane of the cavity. At higher Reynolds numbers, however, the flow field becomes unsteady, demonstrating substantial movement in the third direction (i.e., the span of the cavity) which is perpendicular to the primary direction of flow. Three-dimensionality in a rectangular cavity arises from end-wall effects and the curved streamlines of the flow. Although the spanwise ratio plays a role in determining the magnitude of these effects, the development of structures of hydrodynamic instability at moderate Re precludes the possibility of two-dimensional flow, however large the ratio. More details from these experiments are discussed in the next few paragraphs.

The basic lid-driven flow at low Reynolds numbers (Re<400) as revealed from previous flow visualization experiments is sketched in Fig. 8, hence characteristic planes are defined. The inviscid primary recirculating roll exists due to the shear-induced motion of the fluid near the lid and circulates clockwise, in the same direction as the lid which defines the principle direction of flow. Fluid from lip E flows down along the vertical downstream wall EF to separate from it at some distance. The downstream secondary vortex (DSV) is formed as a result of frictional losses and stagnation pressure. Similar vortices appear at the corner upstream (hence the upstream secondary vortex, USV) and at the top of the upstream vertical wall AG. These are secondary flows in the sense that they are weaker than the primary roll,

which essentially dominates the cavity flow, and form due to interaction of the viscous fluid with the rigid boundary walls.[75] Therefore, although the core is inviscid, shear layers are formed close to the walls.

The schematic appearing in Fig. 8 has been widely accepted now as representative of the fully developed lid-driven cavity flow and has also been verified by numerous two-dimensional numerical simulations [see Koseff[77] pp. 17-21 for a thorough review]. However, experimental results indicated that the flow is more complicated. The experiments by Mills,[73] using different depthwise aspect ratios of 0.5:1, 1:1, 2:1 and Reynolds numbers from 100 up to 100,000, demonstrated that for DAR=1:1 there exist both primary and secondary circulating cells (DSV and USV) but with a measured strength one third of that expected theoretically. He attributed the weakening of the flow to adjustment of the cells to the no-slip conditions at the end-walls. Relevant to the work here are also the experiments performed by Pan and Acrivos[74] using a rotating cylinder at the top of a rectangular cavity filled with oil. Depthwise aspect ratios up to 10:1 and a spanwise aspect ratio of 1:1 were investigated up to a maximum Reynolds number of 4000. The flow remained steady featuring the primary cell and the two secondary cells in the whole range of Re investigated. For the case of a cubic cavity, they found that the size of the secondary vortices increased with Re up to 500 and then decreased. These results are limited because, as the cylinder protruded into the cavity to about 17% of the cavity depth, vertical components of velocity were introduced at the upper boundary. [85] Additionally, they identified three-dimensional motions in the spanwise direction which, they assessed, did not extend into the mid-section, i.e., the symmetry plane, where they observed the flow. Thus Pan and Acrivos did not study three-dimensional features of the shear-driven cavity flow.

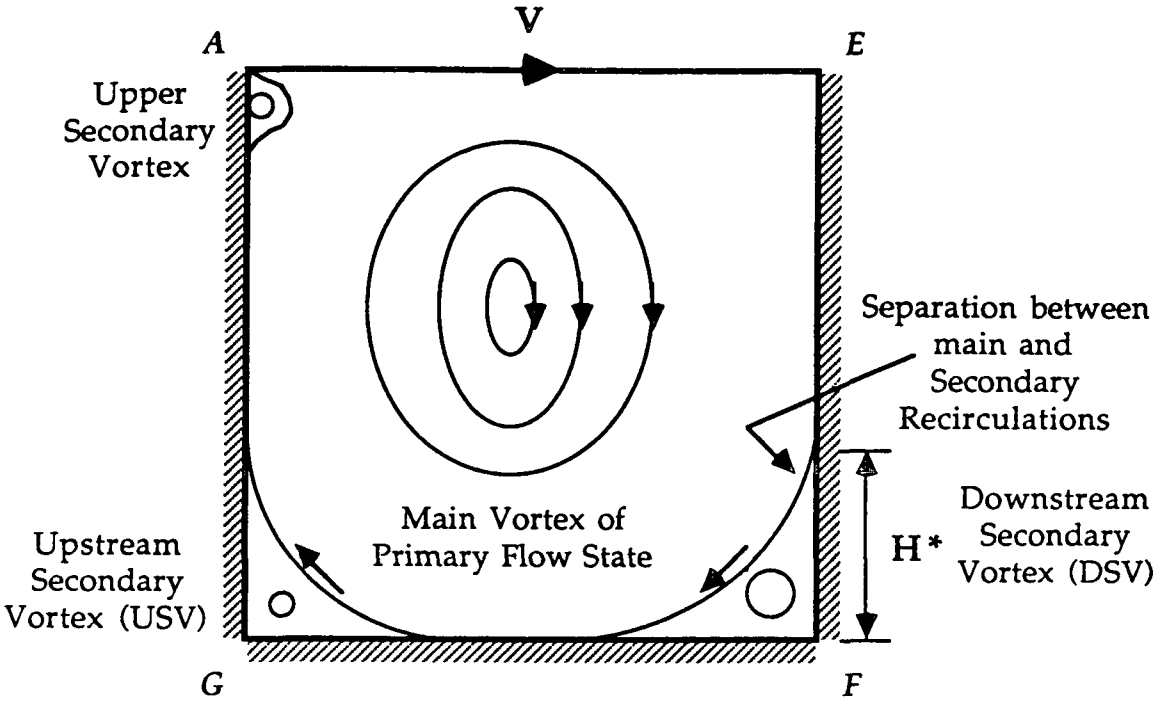

Figure 8. Definition of the primary two-dimensional flow in a lid-driven enclosed cavity.

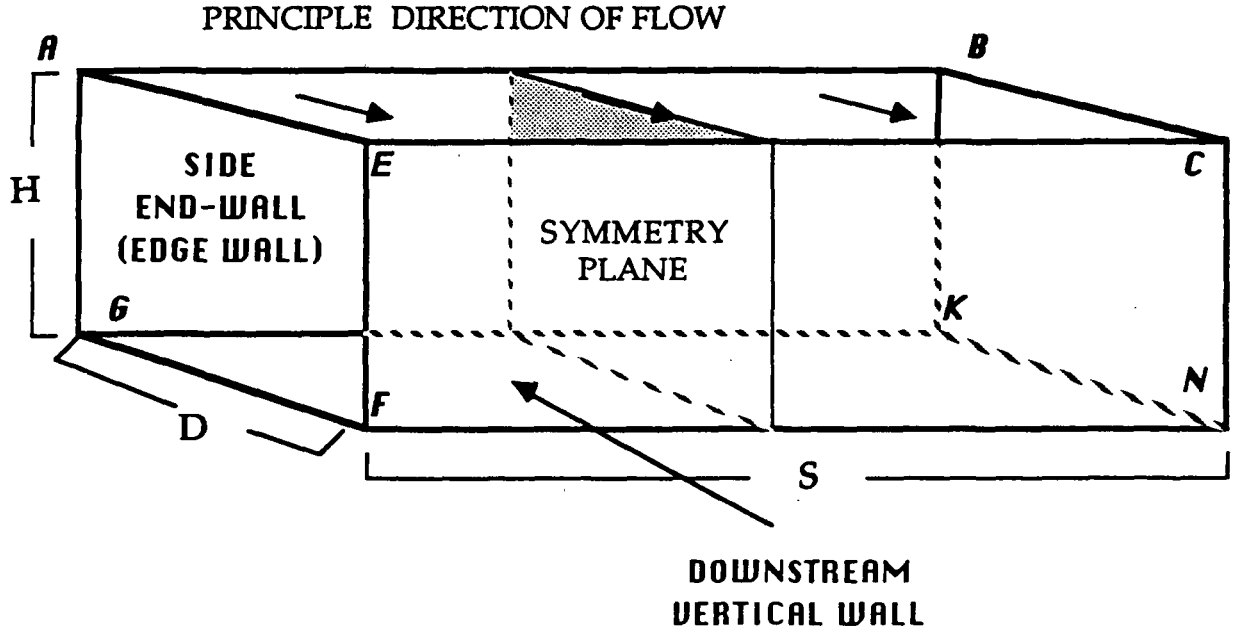

Figure 9. Schematic and definitions of geometical features in a (three-dimensional) rectangular cavity.

Recent experimental studies of impulsively started flows in a lid-driven cavity (DAR =1:1 and SAR=3:1) at moderate Reynolds numbers are by Koseff, et al.,[76-80] where the initial and fully-developed flows are studied for discrete Reynolds numbers between 1000 and 10,000. The three main conclusions from these works are:

1. The presence of bounding walls gives rise to substantial movement of fluid in the transverse plane of the lid motion, thus manifesting three-dimensionality,

2. For Re greater than 2000, centrifugal instabilities induce three-dimensional flows in the form of Taylor-type vortices during startup and Taylor-Görtler-like (TGL) structures when the flow is fully developed.

3. Turbulence occurs for Re above 6000.

Thus shear-driven cavity flows are, in general, unsteady and posses three-dimensional flow structures. These structures appear due to viscous damping of the primary cell with the side endwalls and the instability of the concave separation line between the primary and the DSV. In a global scale, three-dimensional effects weaken the two-dimensional flow due to the adjustment of the primary circulation to the no-slip condition at the endwalls. In the local scale, corner vortices appearing next to side endwalls and TGL vortices inside the DSV interact with the primary circulation and, therefore, influence the momentum transfer within the entire cavity.[80] The observed TGL spanwise structures are similar to the ones developed from the centrifugal instabilities in flows with curved streamlines, like the ones recorded by Taylor [81] and Görtler [82] for Couette flows and boundary flows over a concave wall, respectively. Most of the activities take place in the vicinity of the DSV which led Koseff and Street[78] to suggest that these centrifugal instabilities arise from destabilization of the boundary layer between the primary and secondary recirculating rolls which is effectively a concave wall (a thorough description of these phenomena is included in the works by Freitas[83,84]). The TGL vortices were recorded in pairs, meandering along the cavity span for Re of 2000, 3300, and 6000. It is noteworthy that existence of these vortices does not indicate turbulent flow, which was reported to appear only for Re between 6000 and 8000.[76]

In addition to the Reynolds number, the SAR also affects the flow by influencing the intensity and distribution of the TGL vortices and thereby the whole flow domain.[80] At Re values of 2000 and 3200, an increasing SAR raises the viscous drag from the end walls which reduces the flow velocity over most of the flow domain. Under these conditions, flow velocity fluctuations inside the cavity are caused by the TGL vortices. At higher Re, the peak velosity observed close to the lower cavity boundary increases with decreasing SAR.

Table 1. Review of previous experiments on lid-driven cavity flows.

	Fluid	Two /Three dimensional	Reynolds Number Range	Cavity Dimensions DAR	SAR
		Open Cavities (Channel cut-outs)			
Maul and East [a,62]	air	three	274,000-380,000	0.5-3.4	9.0-4.73
Mills[b,63]	air	two	62,300	1.0	1.0
Johnson and Dhanak[b,64]	air	two	10-10,000	1.0	--
Reiman and Sabersky[a,65]	water	two	8-200	1.0	14
Haugen and Dhanak,[b,66]	air, water	two	50,000-100,000	1.0-3.0	10
Weiss and Florshein[67]	water/glycerin	two	150	1.0-3.0	--
Roshko[b,68]	air	two	150,000	--	--
Fox[b,69]	air	two	163,000	--	--
Orlandi and Ianetta[b,70]	water	two	3340/5080	--	--
Rockwell and Knisely[a,71]	water	two	13,250	--	--
Neary and Stephanoff[a,72]	water	two	11,300-33,500	3.5	--
		Enclosed Lid-driven Cavities			
Mills[a,b,63,73]	air	two	54,700-100,000[c]	1.0	4.0
Mills[b,73]	oil	two	100-1000	0.5-2.0	0.5-4.0
Pan and Acrivos[a,74]	oil	two	20-4000	0.5-10	1.0
Chashechkin[a,b,75]	water	two	2700-26,000	2.6	2.0
Koseff[a,b,76-80]	water	three	1000-10,000	1.0-5.0	3.0

[a] Visualization studies.

[b] Velocity measurements.

[c] Mills used sometimes one third the lid velocity to calculate the Reynolds number (see text for explanation).

Although the work by Koseff shed new light in the physics of shear-driven cavity flows, the concentration was in flow phenomena during startup and the fully-developed flow for Reynolds numbers above 2000. In all of the experiments the lid started impulsively to a preselected Reynolds number and, therefore, TGL vortices appeared shortly after startup. The transitional mode of these evolving structures as a function of Re has not been systematically

studied yet. For example, little is known about the sequence of destabilization phenomena which take the system from its steady state at low Re to unsteadiness at moderate-to-high Re.

Numerical Simulations

Shear-driven flows in a closed rectangular cavity has been used as a benchmark problem to test new numerical codes and compare various schemes because it is geometrically simple, with comparatively minor singularities, and easily defined boundary conditions. There is a plethora of publications regarding the two-dimensional case and, in general, numerical results compare well with experimental observations at low Reynolds numbers (Re<400). Good reviews of these are given by De Vahl Davis and Mallinson[85] and Tuann and Olson.[86] At high Reynolds numbers (i.e., Re greater than 400), only a few models could predict the recirculating flows observed experimentally. The reason for the limitation of numerical simulations is insufficient accuracy. First, calculations become more intensive and computer time-consumption and cost increase dramatically as a relatively large number of nodes is required to unveil interesting details of the flow when the flow becomes three-dimensional, especially for cavities with a relatively short longitudinal dimension.[87] Second, discretization schemes with central differencing for the convective terms which have been used extensively are numerically unstable.[85,86] First-order accurate (i.e., the HYBRID scheme) differencing has also been proven equally unsatisfactory because of numerical diffusion.[84] Only third-order accurate schemes such as the QUICK (quadratic upstream interpolation for convective kinematics) for convective differencing have been successful. [83] Incorporating turbulence models is not always necessary since turbulence occurs at Re greater than 6000.[76] The next few paragraphs review attempts to perform three-dimensional simulations and discuss their results in lieu of the newly discovered structures by Koseff.[77] Table 2 presents an overview of important features from each work.

Most of the early three-dimensional simulations reproduced only the most general features of the flow and identified the endwall effects. De Vahl Davis and Mallinson[85] essentially simulated a two-dimensional cavity with a finite differencing (FDC) scheme, but illustrated the three-dimensionality of the flow by releasing a particle at the symmetry plane (Fig. 9). For Re up to 400, numerical results suggest that two-dimensional models overestimate the strength of the motion in that plane. Particles released from a point near one end wall and close to the center of the primary recirculating roll traveled towards the symmetry plane, gradually spinned outwards, and eventually returned to the end wall via the boundary layer. Motion along the spanwise length of the cavity was attributed to the

interaction of the stationary end wall and the rotating fluid elements. Thus, the side endwalls, and therefore the spanwise ratio SAR, determine the degree of weakening of the the flow. Gresho, et al.,[83] solved the primitive velocity and pressure equations with a modified finite element method (FEM) for increased speed and simplicity but no three-dimensional structures were revealed, probably due to the low Re. Also, early simulation work by Koseff[84] was unsuccessful in revealing the structures this author observed experimentally due to the low refinement of the grid and inadequate numerical accuracy. The work of Ku, et al.,[93] in a cubic cavity for Re=100,400, and 1000, illustrated that three-dimensional effects appear even at low Re due to the boundary layers on the side endwalls. The effect became more important closer to the walls and at higher Re, its contibution mainly being the weakening of the flow as compared to the two-dimensional simulation. However, these simulations did not resolve the TGL cells for Re=1000. As pointed out by Freitas and Street,[84] discrepancies between numerical solutions and the observed therr-dimensional flow result from the absence of a mechanism for energy redistribution in the spanwise direction.

Among the limited number of numerical simulations that have, up to date, resolved the spanwise TGL vortices are the works by Freitas, et al.,[84,90] Kim and Moin,[91] Hwang and Huynh,[92] and Iwatsu, et al.,[94] The first work constitutes the earliest successful attempt to numerically generate the experimental results by Koseff at Re=3200. Flow structures were reconstructedcomputationally using a higher-order accurate scheme without introducing a random perturbation of the velocity fields, but let the presence of the endwall instigate the TGL vortices. The strength of these vortices depends on their proximity to the downstream wall, i.e., appearing larger or more fully developed at further distances away. On the other hand, Kim and Moin[91] introduced random disturbances in the spanwise direction and periodic boundary conditions to resolve TGL cells at Re greater than 900. Hwang and Huynh[92] reported three pairs of vortices in a cubical cavity at Re equal to 2000. Finally,Iwatsu, et al.,[94] resolved TGL vortices for discrete values of Re ranging from 100 to 4000. Onset of unsteadiness in the form of TGL vortices did not appear but only in the neighborhood of Re=2000-3000. Endwall effects, however, persisted close to the walls even at comparatively low Re.

The most complete work have been the analysis presented by Freitas and Street,[84] who used a REMIXCS code (recirculating mixed convection simulator) of high-order accuracy to study three-dimensional shear-driven flows for Re=3200. The dominant phenomena under these conditions are TGL vortices which, are intimately coupled with the primary circulation. Thus spanwise flow variations are not solely due to endwall effects, but also to the complex interaction of a spanwise pressure gradient inside the DSV, the radial pressure gradient and centrifugal forces in curved streamlines of the flow, and the no-slip (i.e., the viscous

damping) velocity boundary condition. As a result, the intensity and size of all features depend on the spanwise location and time. These authors have studied both the wavelengths and time scales of these phenomena at Re=3200.

Table 2. Review of previous three-dimensional numerical simulations of viscous flow in a lid-driven cavity.

Authors	Numerical Scheme	Grid	Reynolds Number	Comments
de Vahl Davis & Mallinson[85]	FDC scheme; upwind differencing	25x25	100-2000	Essentially simulated 2-D. Used solenoidal vector potential to study 3-D effects via particles tracking.
Goda, K.[87]	A MAC method	20x20x20	100,400,1000	Side endwalls effects.
Gresho , et al.,[88]	A FEM technique for primitive equations	500 nodes for half a cavity	100	No 3-D structures.
Koseff , et al.,[89]	FDC (REBUFFS) and hybrid FEM	Rectangular cavity; half span 23x23x23	1000-2000	Longitudinal vortices could not be simulated.
Freitas , et al.,[90]	FDC (REBUFFS) with modified 3-D QUICK scheme; a higher-order upwind FDC	32x32x45 per half cavity	400-2,000	Taylor-Görtler-like vortices resolved in spanwise length of downstream wall.
Kim & Moin[91]	Method based on a fractional-step approximate-factorization.	32x32x32	5000	Weak spanwise TGL cells.
Hwang & Huynh[92]	First-order FDC. Upwind differencing for velocity; central differencing for other terms	Cubic cavity 30x30x30	100-2000	Side walls formed a pair of secondary vortices moving towards the symmetry line. Three pairs of Taylor-like vortices close to bottom wall.
Ku,Hirsh, Taylor[93]	Chebyshev pseudospectral	25x25x25 31x31x31	100,400 1000	3-D endwall effects; Flow weaker than 2-D.
Freitas and Street[84]	REMIXCS FDC (advanced QUICK-type)	32x32x45 Half cavity	3200	TGL and corner cells ; particles tracking.
Iwatsu et al. [94]	MAC scheme	81x81x81 Cubic cavity	100-2000 2000,3000,4000	3-D endwall effects 3-D unsteady TGL

SUMMARY

Analyses of the blade coating process for the deposition of coating colors on a moving paper web indicate that, in addition to other parameters, the impulse (inertial) forces acting on the blade and arising from the momentum of incoming fluid control film thickness. It has also been recognized, at least practically, that there are outstanding differences between bevelled blade coating with a short-dwell coater and a system with an applicator roll. Appearance of coat weight-profile uneveness, which hinders operation of a SDC at high speeds and low film thicknesses, has been attributed to "turbulence" in the pond. However, there is no systematic documentation of film nonuniformities and there has not been a study of pond-type flows and their stability to justify such an argument.

The hypothesis in this investigation is that hydrodynamic phenomena in SDC ponds, more specifically three-dimensional instabilities, may convect through the blade nip and generate wet-film thickness nonuniformities. This maybe achieved by variations of the hydrodynamic pressure and velocity profiles inside the SDC pond as the machine speed increases. Such an argument challenges the assumption made by all theories and models so far that the fluid (viscous) layer entering the blade is, at all times, uniform across the machine line direction. Of interest in this work are therefore transport phenomena which influence the distribution of momentum within geometries similar to the SDC pond.

By experimentally simulating the flow in a SDC pond as a shear-driven cavity with through-flow, this study concentrates in three-dimensional features occuring at comparatively low to medium values of the control parameter, i.e., the cavity Reynolds number based on cavity width. Lid-driven flow in a rectangular cavity is a classic problem in fluid dynamics which has been studied extensively, both experimentally and numerically. Results demonstrate that recirculating flows in an enclosed cavity depend on the Reynolds number and geometry, i.e., the spanwise aspect ratio. In channel cut-outs, the flow is also dependent on the characteristics of the outer stream which drives the flow.

Although both experiments and two-dimensional simulations are in agreement at low Reynolds numbers, in reality the flow is always three-dimensional because of the bounding rigid walls where the no-slip conditions need to be satisfied. In addition, hydrodynamic instability makes the picture more complicated as the Reynolds number increases. Recent experimental results for impulsively started flows have documented the existence of three-dimensional structures in the form of Taylor-Görtler-like vortices for Reynolds numbers above 2000. These structures are generated from a centrifugal hydrodynamic instability in the

separation between the primary and secondary circulations in the cavity and interaction with endwall, their existence also confirmed numerically. It should be emphasized, however, that in the experiments by Koseff[77] the flow was always impulsively started at a selected series of Reynolds number above 2000 where the fully-developed flow was already unsteady.

Although the endwall cells and TGL vortices have been documented at Re=3200, there is no systematic study of the transitional modes of flow from its basic steady state to time-periodic and unsteadiness. For example, little is known about flow features and their evolution at low-to-moderate Reynolds numbers (i.e., 100<Re<2000) where the state of flow has **always** been considered steady and unique. Essentially there is no experimental investigation of the stability of the flow in the region of the parameter space where, due to the viscous nature of applied fluids or suspensions, most pond-type hydrodynamic systems for paper web modification operate.

Motivated by the need to improve characterization of the hydrodynamics upstream the blade and the desire to show how computational fluid dynamics codes can be practically utilized, we have modeled SDC ponds and numerically simulated the two-dimensional, laminar flow therein. The scope of the first series of simulations was to verify the applicability of the model by comparing numerical solutions with flow visualization experiments conducted by Eklund, et al..[3] Then, cases of practical interest were simulated to illustrate the effect of machine speed, feeding flowrate, and color viscosity on pond flow characteristics. Although the model is limited by certain approximations, key features of the numerical results provide an indication of the three-dimensional picture of the flow.

CHAPTER THREE

NUMERICAL SIMULATION OF SHORT-DWELL POND FLOWS

MODELLING OF SHORT-DWELL COATER PONDS

The isothermal, steady-state, laminar two-dimensional flow of a homogeneous viscous fluid upstream the blade nip and in the pond of a SDC coater has been simulated using a general-purpose computational fluid dynamics (CFD) code [FLUENT,©Trademark of Creare, Inc., Hannover, NH]. Simulation of this physical system involved four basic steps: (a) the development of a model based on the geometry of interest in practice, (b) discretization of the flow domain, (c) application of a computational (numerical) method to solve the system of governing equations, and (d) analysis of the numerical results in lieu of the current understanding of theory and experimental data. Specific goals of modeling the fluid flow in the pond were (a) to verify previous experimental results from flow visualization studies, (b) to unveil details of the flow which are not readily available from visualization experiments, and (c) to attempt to qualify the effect of machine speed and fluid rheological model on to the flow characteristics.

The family of codes under the name FLUENT comprises CFD computer programs for fluid flow modeling. In general, these codes can be applied to a wide variety of engineering problems including laminar or turbulent flows, steady or transient flows, reacting flows, combustion, heat transfer, etc. In the simulations of interest here, the governing partial differential equations for conservation of mass and momentum were solved.[95-98] These equations, written in tensor notation, take the following forms (for mass and momentum conservation, respectively):

$$\frac{\partial \rho}{\partial t} + \frac{\partial (\rho u_i)}{\partial x_i} = 0 \tag{9}$$

$$\frac{\partial (\rho u_j)}{\partial t} + \frac{\partial (\rho u_i u_j)}{\partial x_i} = \frac{\partial}{\partial x_i}\left[\mu\left(\frac{\partial u_i}{\partial x_j} + \frac{\partial u_j}{\partial x_i}\right)\right] - \frac{\partial p}{\partial x_j} + \rho g_j + F_j \tag{10}$$

where the left portion of the momentum equation represents the convection term, the first part on the right hand side represents the diffusion term, and the remaining terms representing pressure, gravity and body forces. After the domain has been subdivided into a number of control cells, the governing equations are reduced to finite difference equations (FDE) by integration over the computational cells in which the domain of flow is divided, in addition to implicit integration in time. While the velocity components lie on the cell boundaries by means of a "staggered" grid, the scalar quantities (such as pressure) are calculated and stored at the grid (nodal) points which surround these cells. The program provides options for increasing the density of nodal points in regions where the flow changes direction or steep gradients are expected. A power-law differencing scheme is used for interpolation between nodal points and for calculating the derivatives of velocities and pressure. A third-order accurate scheme (QUICK-type) can also be used which introduces an additional node upstream between two grid points and, therefore, improves accuracy. Inlet boundary conditions are specified ahead, while outlet conditions are stipulated by the program to maintain overall continuity. In regions near walls, wall functions are matched with the FDE by cutting the link between the boundary and the near wall nodes and inserting the wall effects by means of linearized source terms. The set of simultaneous algebraic equations is solved by a semi-implicit iterative scheme (SIMPLE),[88-89] starting from the initial conditions imposed and converging to the solution which satisfies the FDE after a number of iterations. The velocity equations are solved first using an arbitrary pressure value, but then are adjusted by solving a pressure-corrective equation which locally satisfies mass continuity. In general, these steps are repeated until the error has becoming consistently smaller than a certain value. The fluid is regarded as a continuum, and is solved in an Eulerian frame of reference. More about criteria for convergence of a solution will be discussed with the results from the numerical simulations.

The work discussed below is restrained by limitations of the version of the software program used(version 2.82), and by limitations of the computer hardware available. The most important of these are:

(a) version used does not have the recently-released body-fitted coordinate capabilities that permit smooth modeling of sloped or curved boundaries. Thus, nonorthogonal boundaries resemble irregular or jagged shapes.

(b) This version is only capable of handling steady-state models, while updated versions are capable of modeling dynamic (unsteady) systems.

(c) Representation of coating color rheology is confined to only the power-law model. In practice, coating mineral suspensions demonstrate more complex rheology which requires constitutive equations with at least three parameters, e.g., yield-power-law (the Herschel-Bulkley) model, or models considering fluid "memory" and elasticity.

(d) The program cannot simulate free-surface flows.

Hardware limitations were related to the limited memory allocation available for this work. Such costraints reduce the maximum number of nodes which can be used and, consequently, confine the numerical problem to only two-dimensional. It should be emphasized that two-dimensional simulations cannot resolve three-dimensional flow features and unsteadiness.

The analysis presented here has modeled a typical SDC pond as a two-dimensional diagonal cavity, represented by a parallelogram with a 45° angle of inclination (Fig. 10), and simulated the bounded flow therein. The top boundary of the model is defined as a moving surface by assigning appropriate boundary conditions to simulate the backing roll. Overall dimensions of the model are 4.34 cm (1.71 in.) by 1.80 cm (0.71 in.), thus replicating commercial SDC ponds, while the inlet opening is dimensioned to be 0.318 cm (0.125 in.) and the baffle gap is set at 0.337 cm (0.133 in.) by properly designing the grid. Twenty-two nodes are specified as being the output on the left vertical boundary, upstream of the overflow baffle. The most important geometric approximations of the model are:

(a) the roll curvature is very small in comparison to the length of the pond, and the top boundary, therefore, can be assumed as a straight line. This boundary is not absorbant or compressible.

(b) There is no outlet in the point where the downstream inclined wall meets the top boundary, which in the actual case is the position of the blade nip, because having two outlets will not guarantee a unique solution for overall mass conservation.[99]

(c) The downstream inclined wall is not flexible, although it simulates the blade.

Although these factors play an important role in the operation and performance of the system under the blade tip, they are not expected to substantially alter the macroscopic picture of flow in the pond, the important issue under consideration here. Numerical results are limited to qualitative information about the flow in the pond, which is essentially an irrotational flow with dominating inertial effects, rather than quantitative data.

The program has a built-in grid generator that automatically generates a uniform computational grid. However, nonuniform grids can be created by expanding or contracting the spacing of nodal point for high resolution in regions where steep gradients are anticipated. For the SDC pond model the geometrical domain is discretized with a nonuniform 41 by 100 Cartesian grid (Fig. 11) with the location of the grid points carefully selected to concentrate in regions of abrupt flow changes. Through much trial-and-error, this grid has been designed to contain the largest number of grid points possible for the desired nonorthogonal geometry with the version of code being used here, while keeping the

distance between nodes as small as possible to avoid grid dependency. It should be noted that the total number of active nodes is less than 4100 because some nodes are within regions defined as stationary walls.

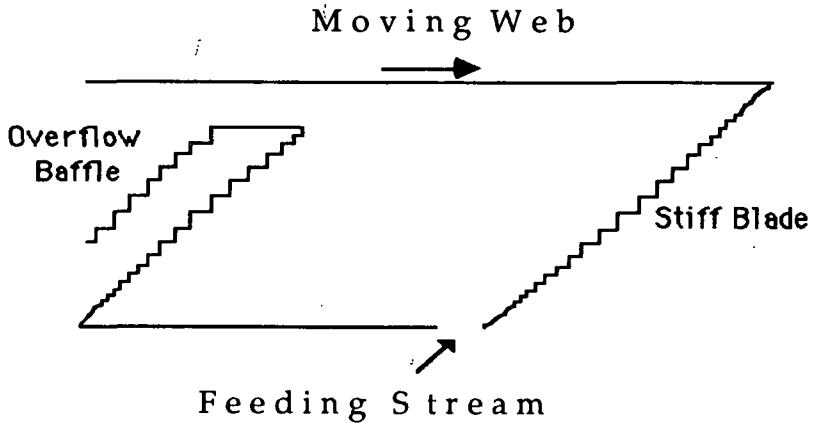

Figure 10. The geometry of the flow domain in the SDC pond model used in numerical simualtions.

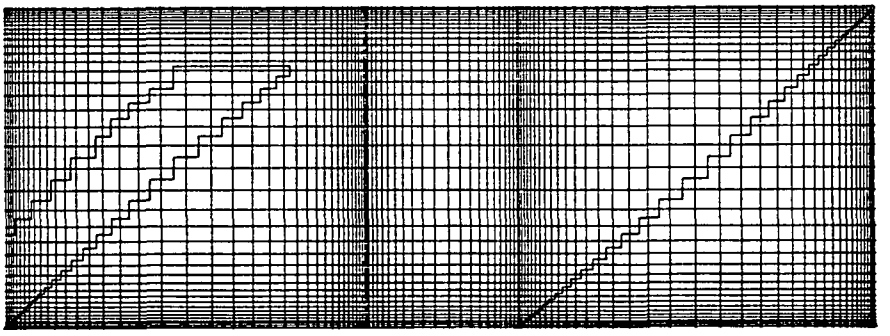

Figure 11. The nonuniform grid arrangement superimposed upon the solution domain. The origin of the Cartesian coordinates is placed at the lower left corner.

Location of the grid points is also important. A nonuniform grid is utilized to place more nodes in regions where intense activity or steep gradients are expected, such as close to the blade nip and in the corners, especially near the moving boundary representing web or backing roll. The distribution of grid lines must be also balanced by the requirement for symmetry about the center point of each of the diagonal walls in order to maintain constant slope of the 45° walls. Thus, the entire domain is composed of three symmetric subregions - the two end regions which are symmetric about the diagonal walls, and the center region which is symmetric about the vertical center line of the domain.

The side endwalls of a SDC pond are approximated by diagonal boundaries with a 45° angle of inclination. Because the current version of the program works only with simple orthogonal coordinate systems (i.e., Cartesian or polar), these boundaries are established by a stair-step approximation. Stepped, or jagged, boundaries can impact the accuracy of a flow simulation, if the flow is not strongly influenced by shear stresses in the vicinity of the boundary.[100] In the case of interest here, attention is concentrated on qualitative features of the pond flow where the flow is not dominated by wall stresses.

In addition to supplying information about the geometry, system boundary conditions and input variables that drive the flow field are required. Input variables are the speed of the top boundary, which is equal to the machine speed, and the velocity of the entering flow which is modeled with a parabolic profile along the inlet opening. The flow at the inlet is assumed fully-developed, with its mass flow rate per unit width attaining values of practical interest. Although input boundary conditions are introduced by the user, output conditions are calculated internally by the program to maintain overall mass and momentum conservation.

The laminar flow in the domain depicted in Fig. 10 is similar to flow in a lid-driven cavity with flow through where numerical solutions of the two-dimensional Navier-Stokes equations are obtained at steady state. The cavity flow is characterized by a Reynolds number which varies with the speed V of the top boundary (i.e., the machine speed) and the apparent (Brookfield @ 100 rpm) viscosity, μ_α, of the fluid:

$$Re = \frac{\rho V W}{\mu_\alpha} \tag{11}$$

where ρ is the fluid density and W is the width of the pond, i.e., distance between the baffle from the blade. Estimation of Re, however, is not trivial because the apparent viscosity of coating colors is primarily a function of shear rate which varies widely from one location to another inside the pond. It is noteworthy that, although the shear rate in close proximity to

the moving top boundary is comparatively high due to steep velocity gradients, the average shear rate throughout the bulk of the pond does not exceed about 1000 sec^{-1}. For the numerical experiments, the Reynolds number is calculated based on the value of the zero-shear-rate viscosity; the latter calculated analytically from data obtained with typical viscometric measurements used in the industry (i.e., using a Brookfield and a Hercules® Hi-shear viscometers). The fluid, therefore, is assumed to be homogeneous and isotropic while its viscosity depends on the shear rate (γ) in accordance to the power-law fluid model:

$$\mu_\alpha = K \gamma^{N-1} \tag{12}$$

where K is the consistency index (or zero-shear-rate viscosity) and N a dimensionless coefficient termed the flow behavior index. Mineral suspensions, such as coating colors, can be represented for simplicity with this type of constitutive equations.[101] In general, however, coating colors are non-Newtonian fluids with more complex rheology exhibiting yield stress, thixotropy, and/or elasticity, hence are described more accurately with equations having three parameters.[103] The values for K and N were calculated from data obtained with the Brookfield and Hercules® viscometer using the procedure outlined by Hyman,[103] as will be discussed later in the section on experimental procedures.

Generally, converegence of a numerical solution in FLUENT is expressed in the form of residuals that define the degree to which each equation is satisfied throughout the flow field. Residuals for each flow variable, which give a measure of the magnitude of the correction made at each iteration, are normalized by dividing by the residual from the second iteration. In particular, normalized residuals of the order of 10^{-3} are considered adequate for representing a converged solution.

Numerical simulations of the flow in SDC ponds were executed on a Digital Equipment Corp. Micro VAX 11/780 computer where accuracy of the solution rather than execution time was the issue. In a sensitivity analysis of the SDC pond model, repeated simulations and evaluation of the results from 1000 to 4000 iterations indicated that the optimum number of iterations was 2000 for all the cases investigated, corresponding to an execution time of approximately 10 to 11 hours CPU time. After these many iterations, the normalized residuals for the velocity components were between 10^{-5} to 10^{-6} and pressure residuals varied from 10^{-3} to 2×10^{-2}, depending on the simulation case. These values, which decreased monotonically for the last 300 iterations, were determined to be sufficient for convergence of the numerical solution. Changing from the power-law to the higher order QUICK scheme did not appreciably change the residuals. This suggested that the power-law solution was accurate and

that numerical diffusion was not a problem in these simulations. Such results also imply that the solutions are grid independent.

NUMERICAL RESULTS AND DISCUSSION

The scope of the first series of simulations was to verify the applicability of the model by comparing numerical solutions with flow visualization experiments conducted by Eklund and Norrdahl.[3] Then, cases of practical interest were simulated to illustrate the effect of machine speed, feeding flowrate, and color viscosity on pond flow characteristics. These numerical experiments were arranged according to the 2^3 factorial design depicted in Fig. 12. The values of the variables studied, presented in Table 3, were selected based on previous experience in a pilot coater.[1] Essentially, both shear-thinning and -thickening colors were simulated for comparatively low and high machine speeds at two feeding flow rates. The Base Case corresponds to the best simulation which provided results similar to the visualization experiments. It is characteristic that, although Cases 1 through 6 produced a satisfactory coating film, Cases 7 and 8 were problematic in the sense that wet streaks were visually observed. These were running along the machine direction, both when coating on to a LWC paper and directly onto the rubber covered backing roll of a laboratory coater. The results from the simulation cases are discussed below.

Numerical experiments provide a unique piece of information which, to date, has not been possible to obtain experimentally. Since numerical solutions yield velocity distributions, numerics give information about the fate of individual particles, placed anywhere in the flow domain. In confined flows, fluid particles move in an ordered or sometimes disordered manner depending on the balance of the forces acting upon them and the effect of possible hydrodynamic instabilities. The system becomes more complicated in the case of two-phase fluids, like the pigmented suspensions for paper coating. In flow fields where viscous forces are predominant, like the flow considered here where the ratio of viscous to gravity forces under conditions of practical interest is greater than 45, small particles precisely follow the streamlines of the flow. Thus, computational fluid dynamics can show the discrete, detailed microscale behavior of high-speed particles by revealing the characteristic streamlines of the fluid based on the numerical solution. However, numerical calculations cannot predict possible complications arising from viscosity and density stratifications due to concentration gradients in flow fields with strong centrifugal forces. In this context, simulation results

presented in the following subsections serve the purpose of revealing general features of the two-dimensional, steady-state, laminar flow in the pond.

Table 3. Characteristic prameters and results of the Cases simulated.

Case	Speed m/min	Feeding flowrate Lpm/cm width	K mPa sec	N	Re [a]	Ψ Range[b] m^2/sec
Base	1000	22.7	800	1.80	525	–
1	300	1.67	250	1.95	510	-18.2 to 3.35
2	300	1.67	500	1.95	255	-18.2 to 3.35
3	300	1.67	500	2.40	255	-19.5 to 3.35
4	300	1.67	250	2.40	510	-19.5 to 3.35
5	1340	1.67	250	1.95	2251	-82.2 to 4.00
6	1340	1.67	500	1.95	1126	-82.3 to 3.99
7	1340	1.67	500	2.40	1126	-82.3 to 4.45
8	1340	1.67	250	2.40	2251	-87.1 to 4.45
9	1340	5.17	250	2.40	2251	-85.7 to 11.0

a The Reynolds number Re is based on the zero-shear rate viscosity.

b Ψ represents flow rate per unit width.

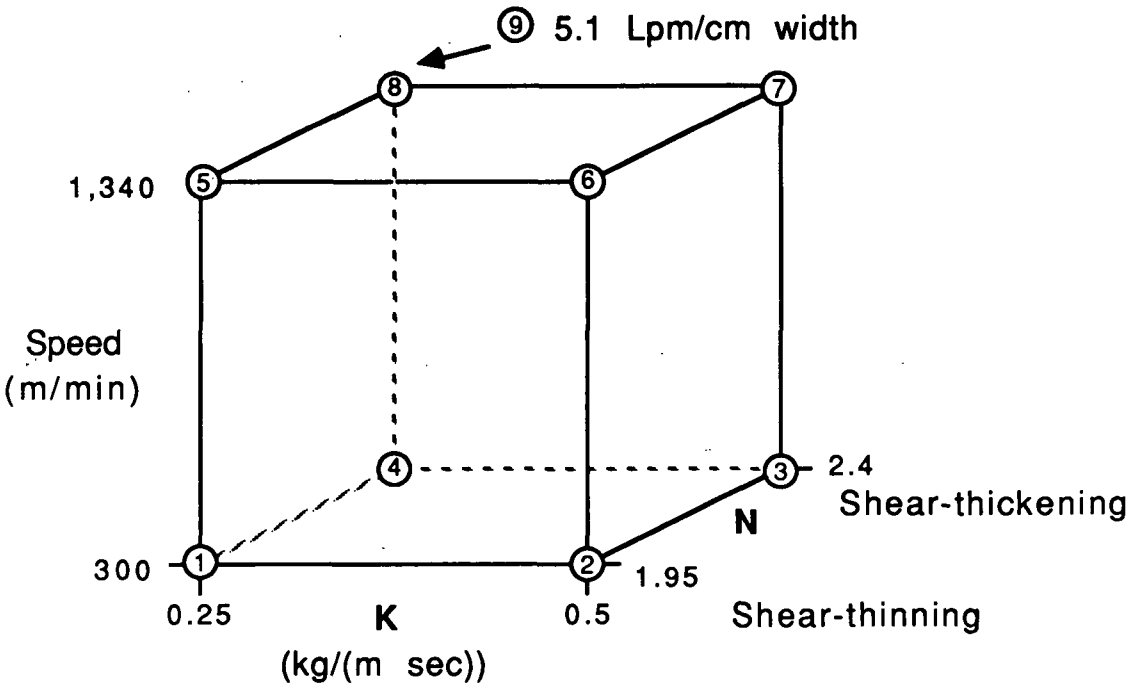

Figure 11. Factorial design of numerical experiments. Cases 1 through 8 are based on a feeding flow rate of 1.67 Lpm/cm width.

Model Verification

Results of the numerical simulation of the "Eklund's" Case (i.e., the Base Case) compare qualitatively well with observed flows. Contours of streamlines appearing in Fig. 13 through 15 reveal recirculating flows in the lower portion of three types of ponds commercially available. These flows are also evident in the photographs obtained from the videotape of the dye-injection studies.[3] The numerical solution for the Base Case was obtained with a shear-thinning fluid for a machine speed of 1000 m/min and for the three different inlet stream positions available commercially. However, the high feeding flow rate is unrealistic but necessary to match the optical image of flow. Unfortunately, the feed flow rate was not monitored during videotaping.

It is interesting, but not surprising, that a noticeable recirculating eddy exists on the upper right corner of the pond which was not clearly visualized in the videotape, probably due to poor contrast as dye diffused in that region. This eddy, termed the upper-corner vortex, is driven by the top surface and is influenced by the inlet stream. The converging flow in this region is slightly more intense than that in the lower portion of the cavity. This recirculating flow is expected to be of primary importance in practice because, being close to the blade nip, it is the prime suspect for (a) disrupting the fluid (boundary) layer reaching the blade, and (b) can cause misalignment of pigment particles at the entrance to the blade nip.

Good correlation between the computational solutions and the flow visualization experimental results demonstrates the validity of the SDC pond model and the numerical simulation, which provides a measure of confidence in using the model to study typical SDC conditions. Nevertheless, the feeding-the-pond flow rate in all of these cases was, at least numerically, artificially high. It is important to recognize that, under industrially interesting conditions, this flowrate is approximately from five to thirteen times lower. Thus, the rest of the numerical experiments (cases 1 through 8) were based on 1.7 liters per minute per centimeter width (Lpm/cm) except for Case 9 where a flow rate of 5.1 Lpm/cm was used.

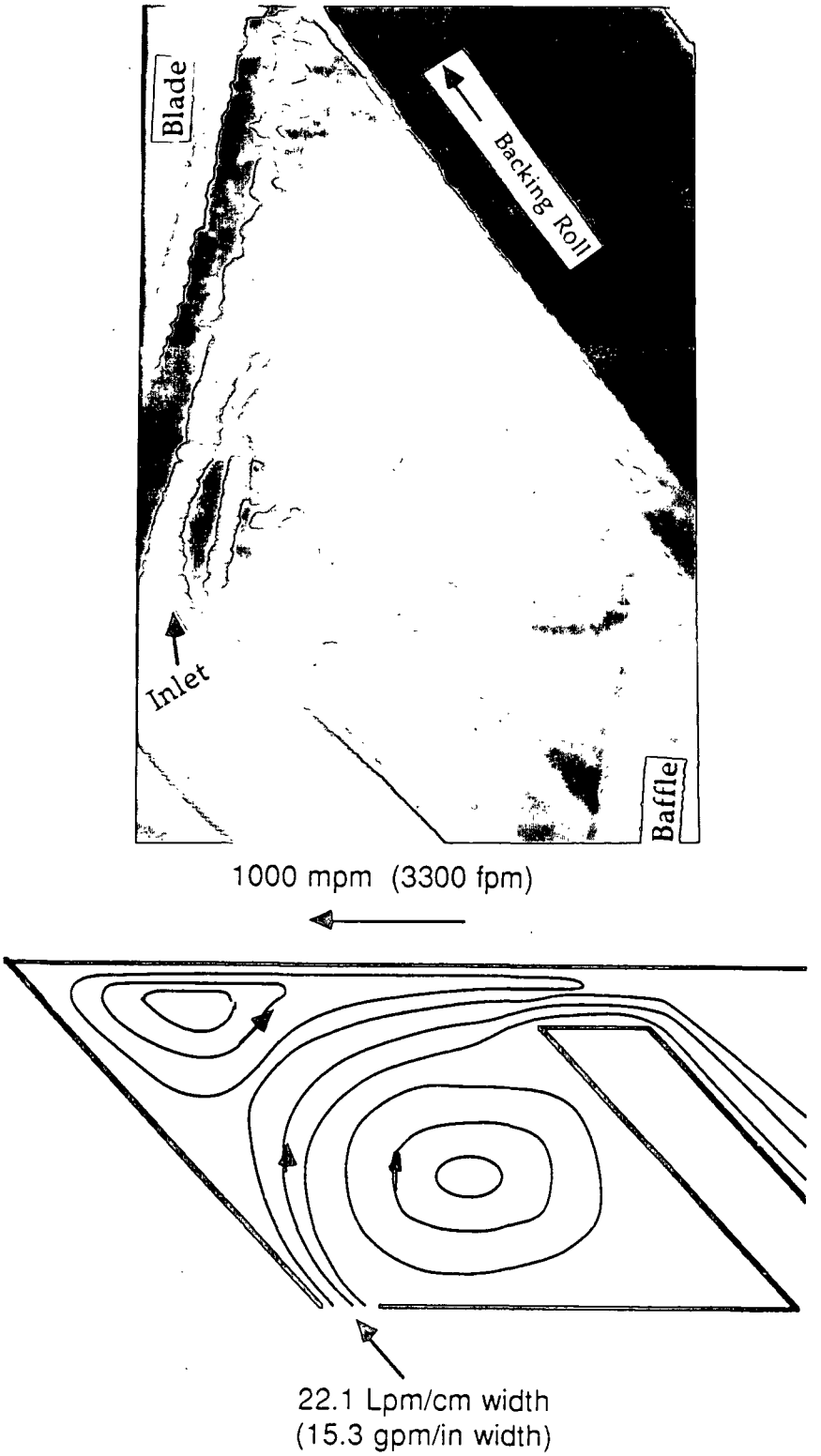

Figure 13. Flow visualization of streamlines after the experimental work by Eklund & Norrdahl[3] (top); contour of streamlines from numerics (bottom). Design A.

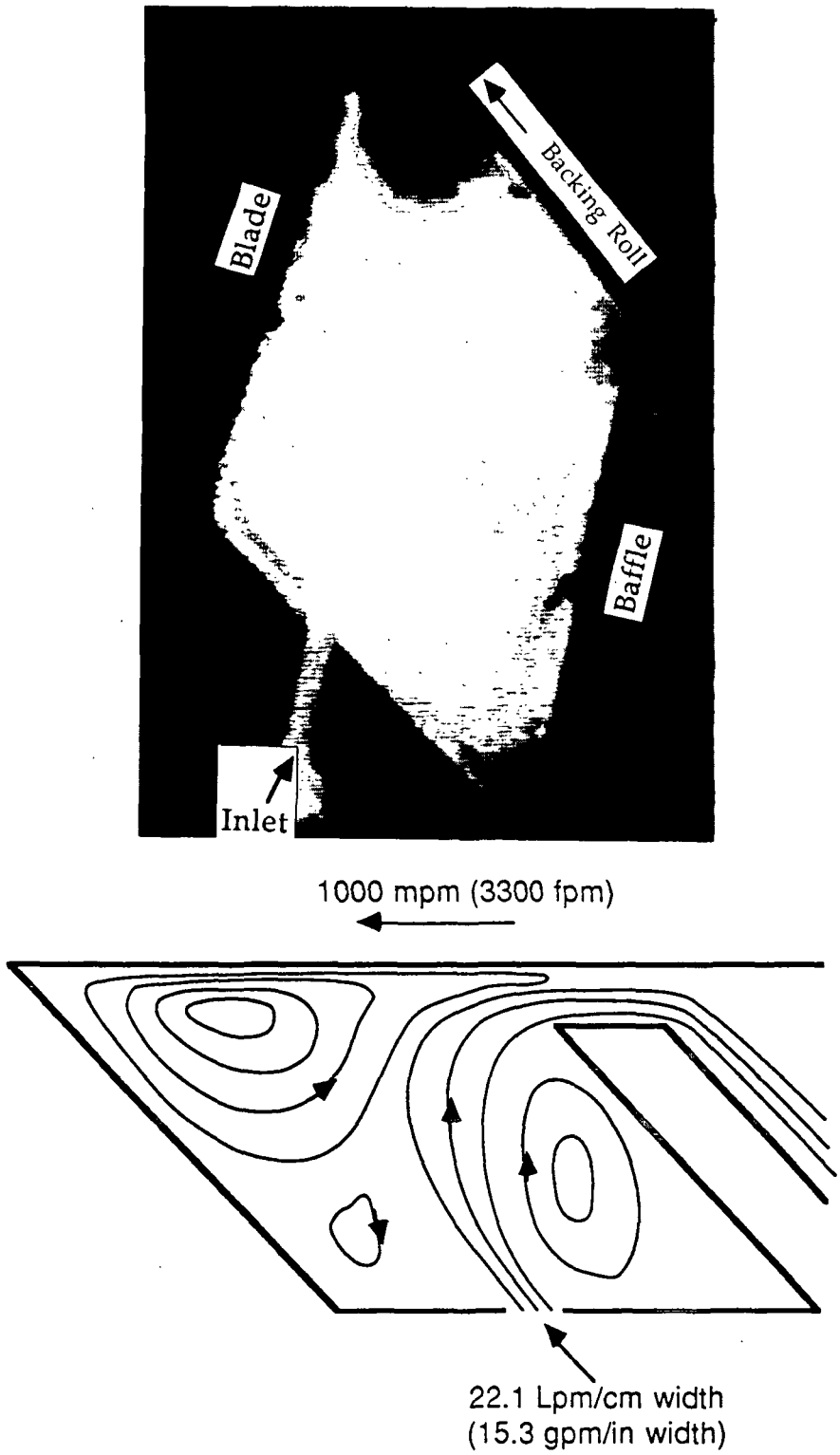

Figure 14. Flow visualization of streamlines after the experimental work by Eklund & Norrdahl[3] (top); contour of streamlines from numerics (bottom). Design B.

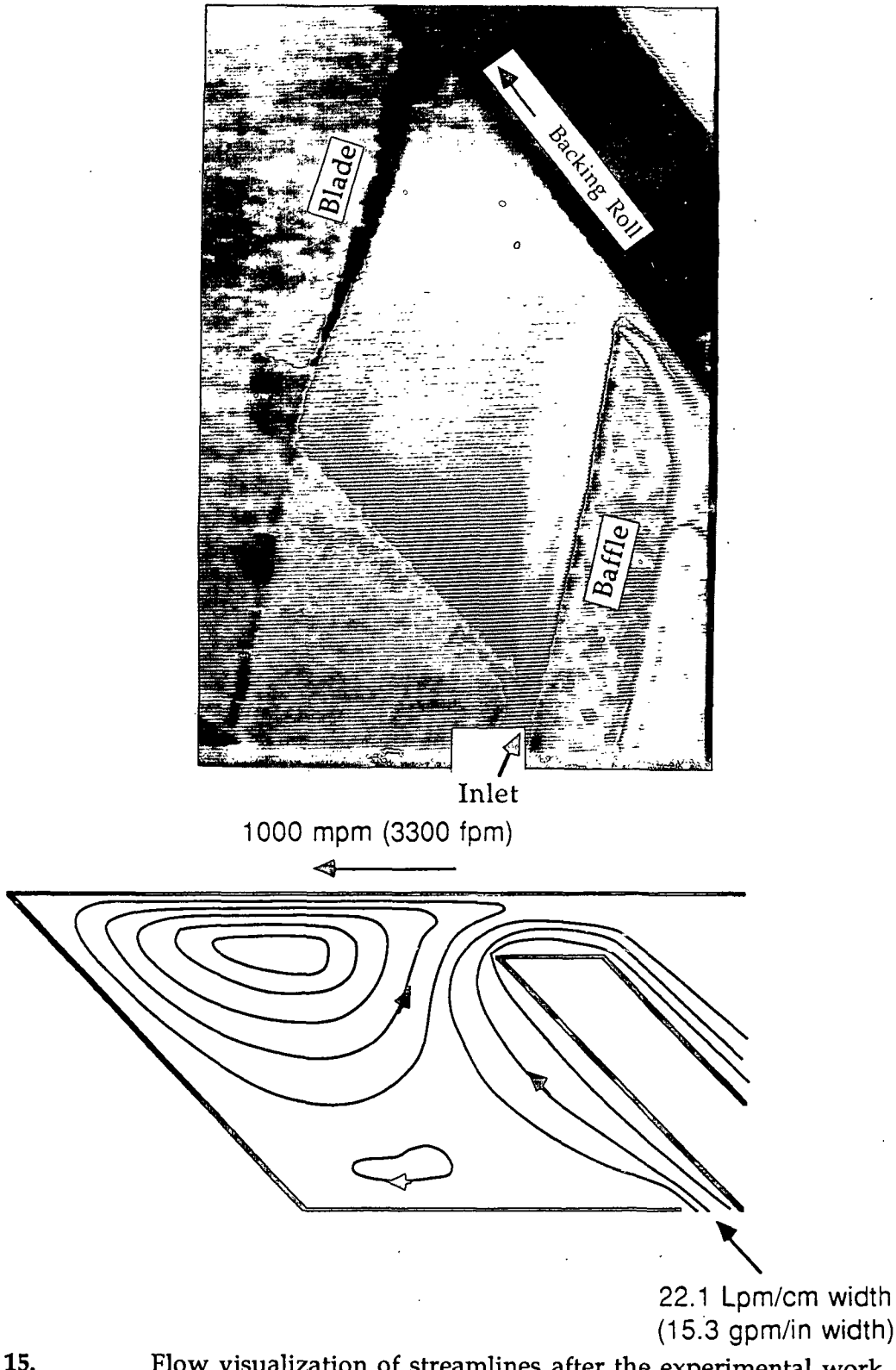

Figure 15. Flow visualization of streamlines after the experimental work by Eklund & Norrdahl[3] (top); contour of streamlines from numerics (bottom). Design C.

Numerical Experiments

At the comparatively low feeding flow rates which are common in practice, the machine speed always dominates the characteristic confined flow in the pond. As illustrated in Fig. 16 and 17 for two different speeds, the upper-corner vortex expands over most of the domain of interest. Therein flow is induced by the shear stress imposed onto fluid elements from the movement of the top boundary. The streamlines of this vortex have negative values of Ψ, the flow rate per unit width, which, depending on speed, are from one to two orders of magnitude greater than those in the lower portion of the cavity, hence streamlines have positive Ψ. Although, in general, qualitative features of the flow are independent of machine speed, the upper vortex is slightly smaller and flatter at low speeds (Case 1 in Fig. 16) than at comparatively high speeds (Case 5 in Fig. 17) because in the former case the inlet stream penetrates further into the cavity. The size of the upper-corner vortex, which dominates the flow pattern in the pond, is determined by the balance of the force imposed by returning fluid at the bottom of the vortex and the force of the incoming flow.

Similar trends are observed when increasing the feeding the pond flow rate, a corrective action commonly taken in practice when raising machine speed while coating with relatively viscous colors. Higher inlet velocities (but not as high as in model-verification cases) allow for the inlet stream to penetrate deeper into the cavity, but the flow is still governed by machine speed (Fig. 18). It is noteworthy that Case 9 should be compared to Case 8 which, however, gave the same results as Case 5 (Fig. 17). In general, an increased feeding flow rate does not change the qualitative picture of the steady two-dimensional flow, but substantially increases the recirculation rate of the corner vortex (see Table 3, case 9).

Various cases were simulated by altering rheology through changes of the coefficients in the power-law fluid model (Eq. 4), as illustrated in Table 3. The scope of these numerical experiments was to attempt to identify changes in flow characteristics which may depend on the zero-shear-rate viscosity (K) and the flow behavior index (N). It was hoped that these results could be related to differences observed during pilot-plant trials, hence K represents the low-shear viscosity and N the shear-thinning or -thickening flow behavior in intermediate shear rates.[104] In practice, the conditions represented with cases 7, 8, and 9 have been proven to be problematic in the sense that uncontrollable wet streaks lead to development of a nonuniform coat weight profile and therefore inferior product quality. In contrast, Case 6 produces a uniform coating film at speeds even greater than 1300 m/min. Contour plots of streamlines from cases with different K an N (Fig. 16, 19 and 20), however,

depict similar qualitative pictures of the flow. Like in the cases discussed earlier, machine speed dominates the pond flow characteristics but, somehow, the role of rheology is underestimated. Altering coefficient N from 1.95 to 2.4 does affect the results quantitatively, but rarely is the change dramatic except in regions of compratively high shear rates. Also during this sensitivity analysis, doubling the zero-shear-rate viscosity does not have any effect on the solution. A similar situation occurs in the case of using a Newtonian fluid model with viscosity equal to K. The only variation occurs in the velocity gradient next to the moving boundary which is a high shear zone, i.e., the profile of the horizontal velocity component is steeper in the case of a shear-thinning fluid.

It is difficult to assess the exact reasons for not been able to simulate the magnitude of rheological effects on the flow, as these are evident from practice. However, certain speculative reasons can be offered. One maybe the inability of the steady two-dimensional model of laminar flow to consider unsteadiness which originates from the dynamic three-dimensional nature of flow. In addition, the power-law model cannot accurately describe constitutive equations of practical paper coating fluids undergoing viscous flows with a wide range of shear rates where, from the theory, N becomes important only in regions of high shear rate. This can possibly be attributed to the fact that there are some regions in the solution domain where shear rate is extremely low and others where it is very large. Because moderate changes of N only affect the flow in intermediate shear rates, such changes may not be sufficient to substantially alter the results of numerical solutions. This suggests that perhaps a more sophisticated fluid model would be required, like the Carreau model which has three parameters, to simulate the behavior of paper coating fluids in confined flows such as the one considered here. Furthermore, it would be interesting to consider how viscoelastic effects, the relaxation time, and elongational viscosity of the fluid at the strains experienced in practice may alter flow structures and the relaxation of the thin film applied onto a web. Such a study can be carried out with the aid of a perturbation analysis similar to the one described by Aidun[105] for steady isothermal spinning of a viscoelastic liquid film.

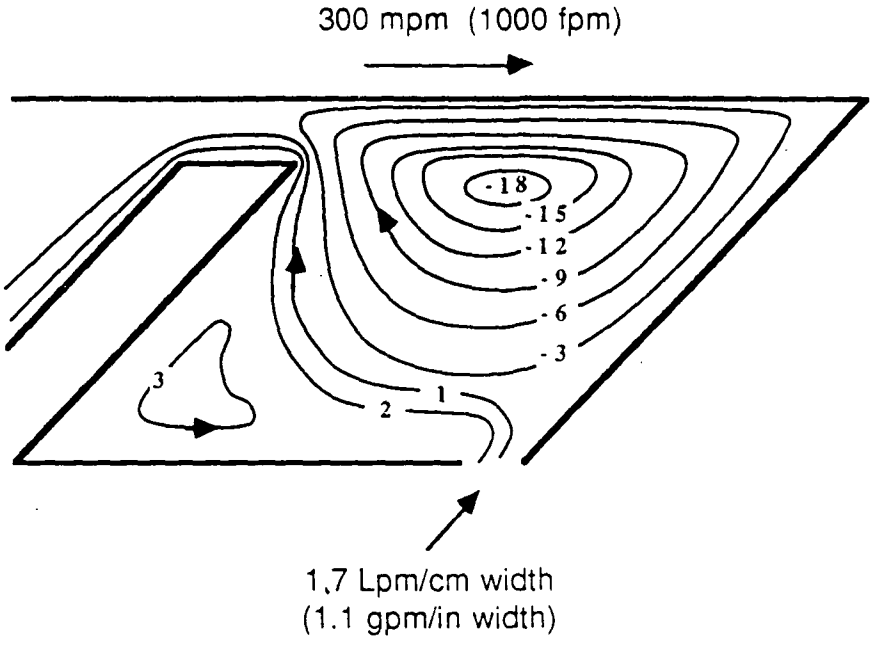

Figure 16. Contour of streamlines from numerical solution at comparatively low machine speed (K=250 mPa sec, N=1.95; Case 1).

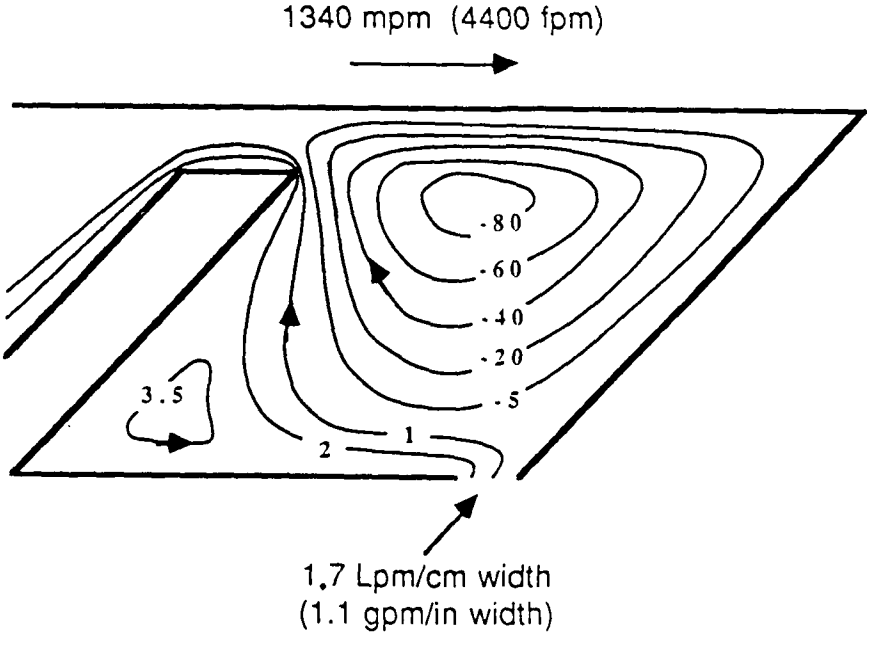

Figure 17. Contour of streamlines from numerical solution at comparatively high machine speed (K=250 mPa sec, N=1.95; Case 5).

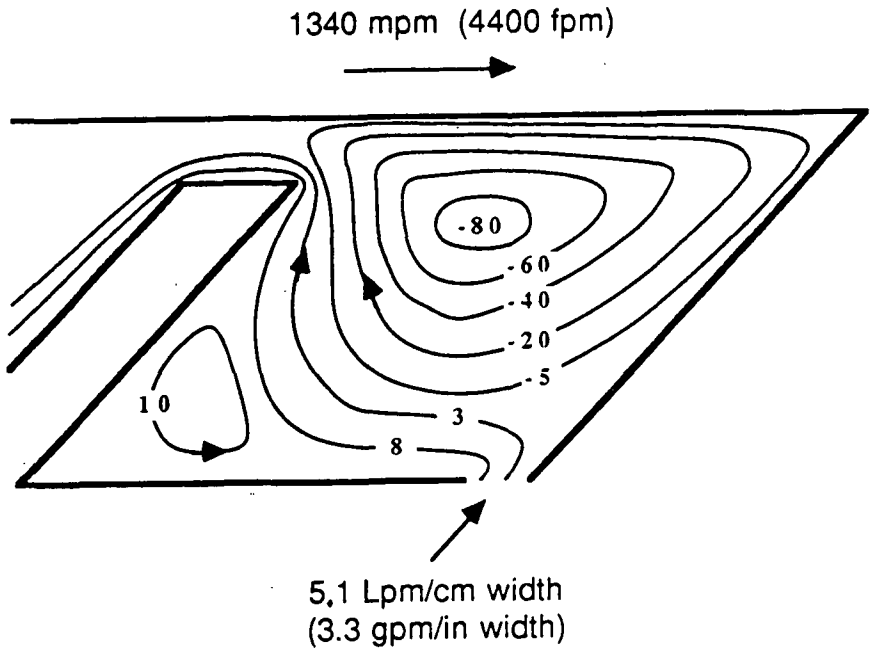

Figure 18. Contour of streamlines from numerical solution with comparatively high feeding flow rate for a viscous fluid (K=250 mPa sec, N=2.40; Case 9).

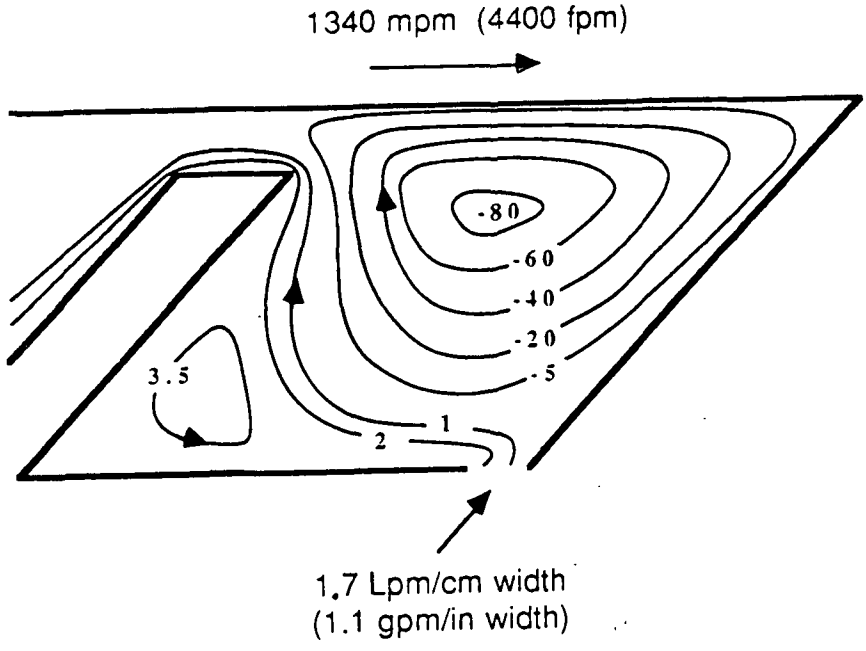

Figure 19. Contour of streamlines from numerical solution for a shear-thinning (pseudoplastic) model fluid (K=500 mPa sec, N=1.95; Case 6).

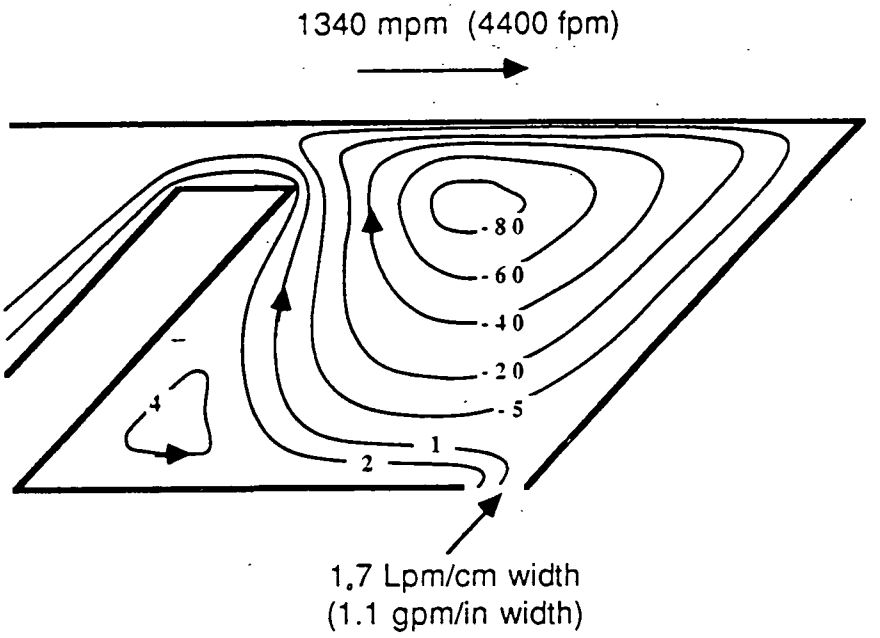

Figure 20. Contour of streamlines from numerical solution for a shear-thickening (dilatant) model fluid (K=500 mPa sec, N=2.40; Case 7).

Implication of Numerical Results

The numerical experiments indicate that the two-dimensional laminar flow in SDC ponds is featuring at least two counter-rotating vortices. The more intense one is rotating clockwise and it is located close to the blade nip, thus creating the danger of separating the viscous boundary layer traveling with the moving surface and, therefore, destabilizing the momentum transfer into the nip. The second is a weaker counter-clockwise rotating one located near the bottom boundary in the region diagonally opposite to the first. These two vortices are separated by a streamline with the characteristic value equal to zero (Ψ=0) which forms an effective concave surface, hence the imbalance between centrifugal forces and the pressure gradient can destabilize the flow. The key conclusion from these results is that, for the feeding conditions of practical interest, the flow in SDC ponds is dominated by the

recirculating vortex induced from the movement of the web (or backing roll), something which was also observed in the numerical simualtions by Conlisk, et al.[13]

The overall picture of flow, under the assumptions of the model, indicates that most fluid elements entering the pond exit by flowing over the baffle. Only elements within few millimeters of the moving boundary (representing the web or backing roll) translate parallel to the direction of motion, thus forming the viscous layer which enters the convergent region under the blade. Particles further away from the moving boundary are subjected to rotation as they are entrapped into the recirculating vortex. The closed zones of recirculating flows induce efficient mixing, but feature indefinitely long residence times as particles entrapped in rotating motion cannot escape[14] unless three-dimensional disturbances destabilize the vortices, causing them to discharge their contents from time to time. Another problem is that the two-dimensional vortex upstream from the blade nip causes a (hydrostatic) pressure drop which, considering the relatively low pressure in the pond, may induce detrimental air entrainment. The minimum pressure inside the pond corresponds to the location of the center of the recirculating vortex. Furthermore, if the pressure in the SDC pond becomes subatmospheric, there is a positive pressure drop across the blade nip, a condition which can generate an unstable film thickness according to the lubrication theory.

Although the simulations in this study are limited to two-dimensional flows, the significance of two counter-rotating vortices should not be underestimated. Their existence indicates, both from the theoretical and experimental points of view, that the hydrodynamic system is susceptible to instabilities due to internal or external disturbances as the control parameter of the flow increases. For example, transitions to three-dimensional structures due to infinitesimal disturbances (absolute instability) can be sustained by the system, the transitions analyzed with linear stability theory. It is well established that flows with curved streamlines develop centrifugal-force driven instabilities due to the competition between the centrifugal force and the radial pressure gradient. The unstable structures appear in the form of Taylor-Couette vortices in flow between concentric cylinders,[81] and as Görtler vortices in boundary layer flow over a concave wall.[82] Furthermore, such instabilities have been observed in lid-driven cavity flows, hence the geometry and two-dimensional features of flow are similar to the ones prevailing in SDC ponds. Numerical results demonstrate that (a) the requirements for occurrence of three-dimensional centrifugal instabilities exist in SDC pond flows, and (b) unstable flow structures along the span of the blade can dramatically influence the uniformity of momentum transfer along the cross machine line direction. The latter effect can be realized by variations in the spanwise velocity profile arising from the cellular type of flow close to the high-shear zone of the blade. Such variations could convect through the nip and be responsible for the wet streaks. Although purely centrifugal

instabilities have not been related directly to ribbing of thin coating films like the ones appearing in slide coating flows,[106] they could generate density and viscosity gradients which would change the flow in SDC ponds and, eventually, influence coat weight uniformity in blade coating of paper. In addition, unstable flows may cause undesirable orientation of pigment particles prior to entering the blade nip. Strongly asymmetric particles in coating suspensions (e.g., delaminated clays which are desirable for good printability) with a high solids content may not have enough time and/or space to achieve proper orientation in order to pass under the blade and attain optimum packing in the crevices of a paper web surface.

In summary, numerical experiments have shown that computational modeling is a useful tool for acquiring new insights into fluid dynamics problems of practical interest. Numerical solutions can provide detailed results on flow characteristics which are not always possible to obtain experimentally. Simulations performed during the course of this study verified, at least qualitatively, results from flow visualization experiments in ponds of short-dwell coaters. Numerical results, however, determined that the flow is always dominated by machine speed, which induces an intense recirculating flow in the vicinity of the blade nip. This was the primary characteristic in all the two-dimensional cases investigated under laminar, steady state conditions. Altering the speed or the inlet flowrate affected the size of the vortex sharply but not its location. Three-dimensional phenomena cannot be assessed from this kind of simulations, therefore limiting the usefulness of the results.

Certain limitations of the SDC pond model and the version of *FLUENT* available for this work became evident during this study. The power-law fluid model is not sufficient to unveil the significance of rheology in viscous SDC pond flows. A more sophisticated rheological model may show the variable behavior between different coating formulations observed in practice. In addition, steady-state two-dimensional simulations cannot predict onset of flow variations originating from three-dimensionality or undamped pertubations. Three-dimensional free-surface flow simulations with dynamic contact line capabilities are required to locate the unknown moving boundary upstream of the pond and to incorporate two outlets, one downstream and the second over the baffle.

CHAPTER FOUR

EXPERIMENTAL DESIGN, METHODOLOGY, AND TECHNIQUES

The research program of this study has been divided into two major parts. The first involves flow visualization experiments to qualitatively examine the flow in a geometry similar to the one in SDC ponds. The second deals with the pilot-plant trials to characterize the appearance of wet streaks on LWC paper. Before proceeding it is worth outlining the conceptual steps taken to plan and complete this work:

1. Choose a bounded flow field to simulate SDC ponds because visualization of flow within a SDC pond is physically restricted by small geometrical dimensions and the fact that actual coating colors are optically opaque. After reviewing the literature, the choice of flow to study was the lid-driven cavity flow because this has been an "ideal"problem in fluid dynamics and has similar physics as the pond. However, in order to resemble a SDC pond there must be a flux (relatively small) of fluid passing through the cavity. A lid-driven cavity facility was designed with adjustable through-flow rate.

2. Define the specific goals for visualization studies after reviewing the previous experiments on enclosed lid-driven cavities.

3. Develop a technique based on flash x-ray radiography for visualizing the flow of opaque coating fluids.

4. Establish experimental procedures for data collection and manipulation. Uncertainty analysis was performed to define the limits of the experimental techniques.

5. Characterize the lid-driven flow in a cavity with through-flow to establish interrelation of its operational parameters, and define the optimum conditions to simulate flow in a SDC pond using dimensionless parameters.

6. Identify and document evolving features of the flow as the control parameter of the flow changes.

7. Identify the range(s) of the control parameter for which substantial qualitative changes of flow features occur. Also, document the exact conditions under which specific flow patterns prevail.

8. Design pilot-plant trials to document the specific conditions for visual observation of wet streaks and document their appearance on a LWC paper.

In the present study, the SDC ponds have been simulated as lid-driven cavities with small through-flow. Visualization experiments provided mainly qualitative information on flow

patterns. The experiments primarily concentrated on the effect of changing the lid speed, and secondarily the fluid viscosity, on to the evolution of flow. Most of the work was done with a Newtonian viscous fluid, but a few experiments were performed with actual (opaque) coating colors. The presentation in this section concentrates on the experimental program implemented for flow visualization. Background information, the design of the pilot-plant experiments, and results from trials are included under a separate section. Descriptions of the experimental facility for the cavity experiments and the techniques used follows, both supplemented by Appendices. An extended discussion of the flash x-ray radiographic technique is included since this is a new application of this technique. However, details on system selection and choice of tracers are contained in an Appendix. The following subsections include characterization of the flow, experimental procedures, measurements, and uncertainty analysis.

METHODOLOGY

A facility was constructed which incorporated a fluid loop for supplying and recycling fluid into a rectangular cavity (Fig. 21). The flow is driven by a cylindrical rotating roll, which rests onto the cavity, so that the flow inside the cavity is of the shear-driven recirculating type. Some fluid was always escaping as a thin film onto the roll. The facility, therefore, is essentially a lid-driven cavity with through-flow and in this sense it resembles the short-dwell pond.

A suspended-particle technique was first utilized to obtain photographic and video images of the flow by illuminating areas of interest with a sheet of diffused light. Direct dye-injection techniques were also used to obtain streaklines of the flow and its structures. For most of the visualization studies, a transparent Newtonian fluid was used (i.e., glycerol in water) to establish knowledge of the major flow structures occurring in the cavity. Next, a flash x-ray radiographic technique was developed and used to record representative stop-motion images of the same flows but through optically opaque coating colors. X-rays have the ability to penetrate through intervening material and therefore are ideal for an application where direct injection of an x-ray absorbant tracer can form streaklines of the flow patterns. In the

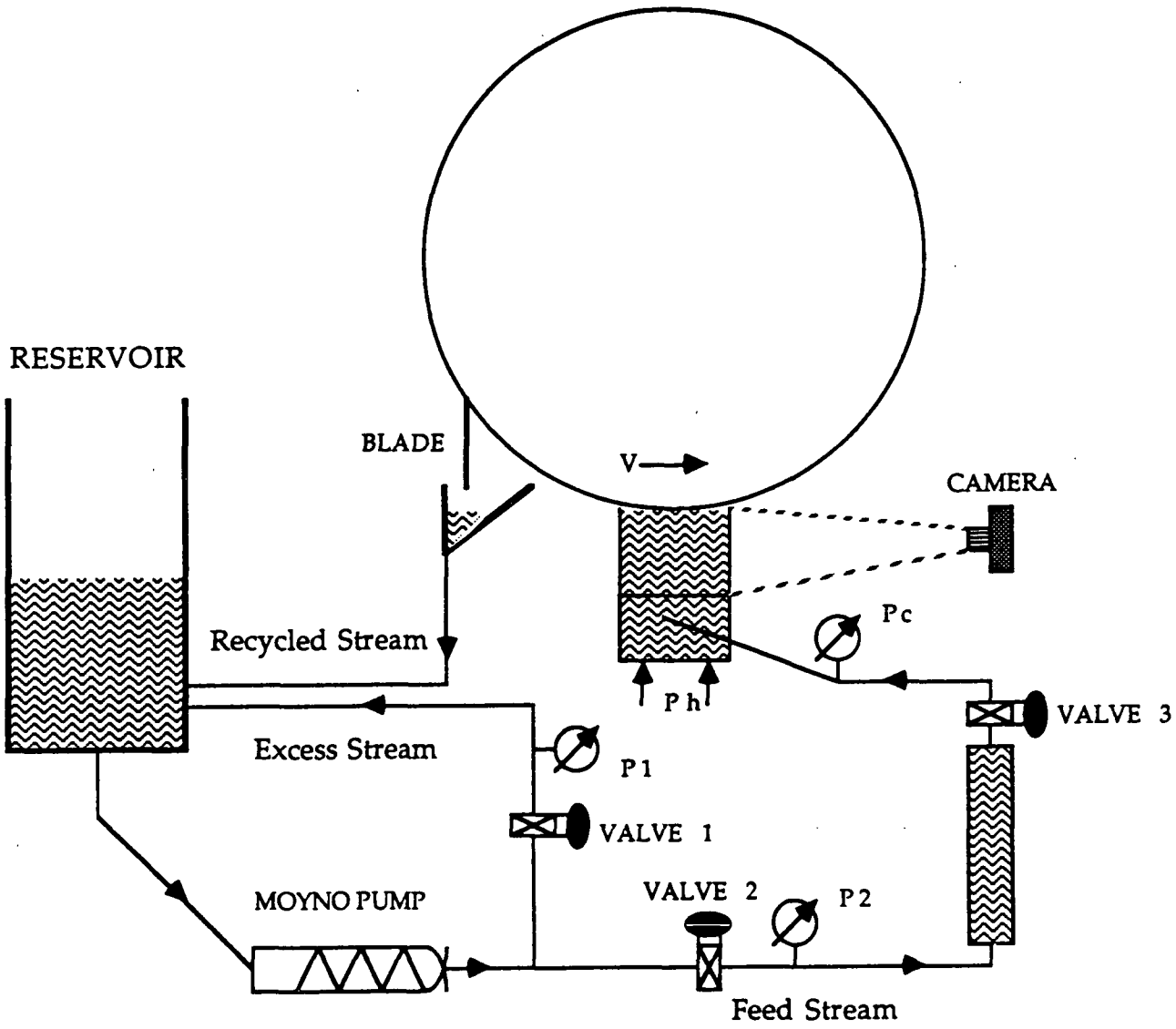

Figure 21. Schematic of experimental setup for flow visualization.

next subsections the facility and its features are presented first, followed by more detailed description of the visualization techniques.

The Facility for Flow Visualization and its Features

In this subsection the discussion concentrates on the design and basic features of the experimental setup for flow visualization, supplemented by Appendix A. Characterization of the flow will be described more extensively in a following subsection. Before proceeding, however, it is essential to define the primary parameters and dimensionless numbers defining the flow of interest. The set of dimensionless parameters which parametize the flow in the experimental cavities are:

(a)	the cavity Reynolds number,	$Re = \rho VD/\mu$,
(b)	the Reynolds number of through flow,	$Re^* = \rho V S/\mu$,
(c)	spanwise (span-to-width) aspect ratio of the cavity,	SAR,
(d)	depthwise (depth-to-width) aspect ratio of the cavity,	DAR,

where ρ and μ are the density and viscosity of the fluid, respectively. Although many variables affect flow conditions, it was only possible to vary a select few in this experimental program:

(a)	the peripheral speed of the roll that drives the flow,	V
(b)	the net volumetric flow rate of fluid passing through the cavity, (which, as it will be shown later, depends on a number of operational parameters),	Q
(c)	the size of the cavity, i.e., spanwise length but constant spanwise aspect ratio,	
(d)	fluid shear viscosity (which is constant only in the case of Newtonian fluids)	μ

To accurately simulate the flow conditions in SDC ponds requires that the values of certain characteristic dimensionless parameters be matched in the laboratory facility. It is necessary to have geometrical, kinematic, and dynamic similarities between the experimental model and the flow of interest. Consideration of boundary and inertial conditions, required to fully define the dynamic problem, may introduce additional nondimensional groups. Complete simulation of the pond, therefore, becomes a difficult task because, in addition to

incoming and outgoing constraints, the characteristic flow contains moving and static contact lines. However, since the interest in the present work concentrates on the hydrodynamic flows inside the pond, only the geometric and dynamic similarities were kept in mind when designing the experimental facility and choosing appropriate test fluids. First, the scale of geometric and kinematic parameters was selected to be similar to the operating conditions common in practice. For example, the depthwise ratio of the cavities was selected such as to represent dimensions typical of a SDC pond. All cavities used in this work had equal width and depth so that the width could be the characteristic unit length scale which also enters into the equation of the (cavity) Reynolds number, Re. The spanwise ratio was chosen based on practical criteria and the requirement to match an aspect ratio used in the experiments by Koseff,[76] who was the first to report three-dimensional structures in cavity flows. The only scale difference between the experimental cavities and the ponds used in practice is the spanwise length, the latter being several meters long in production machines and about 10:1 in pilot-plant machines. Thus, the effect of geometry on the flow was not investigated as both the SAR= 3:1 and DAR=1:1 remained constant. In addition to geometric, the kinematic scale was the same as the one common in industrial applications; i.e., the maximum peripheral speed of the unloaded roll was 1500 m/min.

Second, the main effort in experimental design was to simulate dynamic parameters that describe the flow, namely the cavity and the through-flow Reynolds numbers Re and Re*, respectively. The Reynolds number Re was altered in visualization experiments by adjusting mainly the roll speed and secondarily the fluid viscosity. The Reynolds number in SDC ponds can attain values from several hundred to a couple of thousand, e.g., Re=1400 for 1200 m/min machine speed, blade tip-to-baffle distance of 5.00 cm, ρ=1.40 g/cc, and μ=1000 mPa sec. (This value of viscosity is realistic considering that the bulk of the fluid inside the pond experiences relatively low shear rates, a few hundred reciprocal seconds.) Therefore, the cavity Reynolds number, Re, in visualization experiments varied between 100 and 9200, although most of the studies were conducted in the range of 100 to 2000. The other Reynolds number, Re*, which essentially defines a boundary condition, was varied between 0.006 and 0.86 in visualization tests and attained values as high as 2.5 during experiments for characterizing the flow. Considering a typical pumping rate used in industrial applications, such as 200 L/min per meter pond span length and the fluid properties listed in the example above, Re* should be equal to 2.3. However, it was not possible to obtain such high values consistently in the laboratory due to the limited power of the pump and the relatively high viscosity of the test fluids. In most of the experiments, therefore, Re* maintained between 0.1 and 0.8.

The principal component of the experimental equipment is the cavity area upon which a rotating cylindrical roll supplying the driving force rests. A typical cavity box consists of two

rectangular compartments (Fig. 22). The upper one, the observation cavity, makes contact with the roll and has a width of 5.08 cm parallel to the direction of roll motion, a depth (H) of 5.08 cm, and a span (S) of 15.24 cm perpendicular to the direction of roll motion. The lower compartment, the feeding chamber, has a depth of only 2.54 cm (but otherwise identical dimensions with the cavity) and serves the purpose of feeding fluid uniformity into the cavity. Fluid is supplied to the feeding chamber via a 1.00 cm pipe tap on one of the side endwalls. All endwalls of the cavity are 12.5 mm thick, fabricated from Plexiglas. A second cavity was also utilized which had the same dimensions as the first but thinner walls (3.2 mm), to better facilitate visual observation, and a metal frame for support. Finally, a third cavity with dimensions H=D= 2.54 cm and S=7.62 cm was used where the fluid supplied in to the feeding chamber entered from the upstream endwall.

An important feature considered in the design of the cavity assembly is that of allowing a uniform film of fluid to escape downstream when the roll, which drives the flow, was rotating. This is achieved by mounting each cavity box on a adjustable support plate which is pivoted on two removable screw pins, one on each of the opposite sides of the plate. The adjustable plate sits on a support frame which is hydraulically pressurized with two air cylinders. The box is held in contact with a 59.7 cm diameter chrome-plated roll (Fig. 21) by applying hydraulic pressure P_h on the support frame. A 1.0 cm thick Teflon collar around the cavity lip (ABCE in Fig. 22) allows for contact between the cavity and the roll surface with minimum friction. The inner edge of the collar is sharp and forms a 90° angle with roll surface. The curvature of the roll along the width of the largest cavity is 0.12% and 1% in the case of the smaller cavity. Therefore, the penetration of the roll into the cavity is considered negligible. The thin film of fluid deposited on to the roll is removed by a plastic doctoring blade upstream from the cavity and the collected fluid is recycled back in to the reservoir. Details of the facility design and other supporting equipment are included in Appendix A.

Figure 21 shows the assembled form of the experimental facility. Up to 0.15 m^3 of a fluid can be accommodated in the reservoir tank and pumped with a progressive cavity (Moyno) pump into the feeding line. Only a part of pumped fluid, however, enters the feeding line; the excess is recirculated back into the tank. Because valve 2 remains all the way open during operation, the flow rate of the feed stream is controlled by opening or closing valve 1. Therefore, this valve monitors the pressure P_c in the feeding line before the entrance to the chamber and, by controlling the feeding flow rate, affects the through-flow. Before entering the chamber, the feeding fluid passes through a cylindrical container which dampens any pulsations originating from the pump. Valve 3 also remained totally open during operation. Although a detailed description of the operational parameters and their influence on the

character of the flow in the cavity, is discussed in a following section, it is appropriate to close this section by listing these parameters:

(a) hydraulic cavity pressure, P_h
(b) pressure of feeding stream, P_c
(c) valve 1 setting,
(d) motor (which drives the roll) output setting.

In the context described above, the experimental cavity with through-flow simulates practical conditions accurately flows in SDC ponds. The isothermal confined flow in the lid-driven rectangular cavity with through-flow, like the flow in SDC ponds, is induced by the shear stress imposed on the fluid by the moving top boundary. The difference in the geometry between the pond and the cavity is not expected to have a substantial influence onto the large flow picture since the basic physics remain unchanged. Two differences worth noting are the flexible blade that forms the metering boundary and the finite opening over the baffle; both characteristics of SDC ponds which were replaced with a stiff wall and essentially no overflow in the experimental cavity. However, the essence of the relevant hydrodynamic phenomena is preserved as consideration is given only onto the flow features in the bulk of the pond.

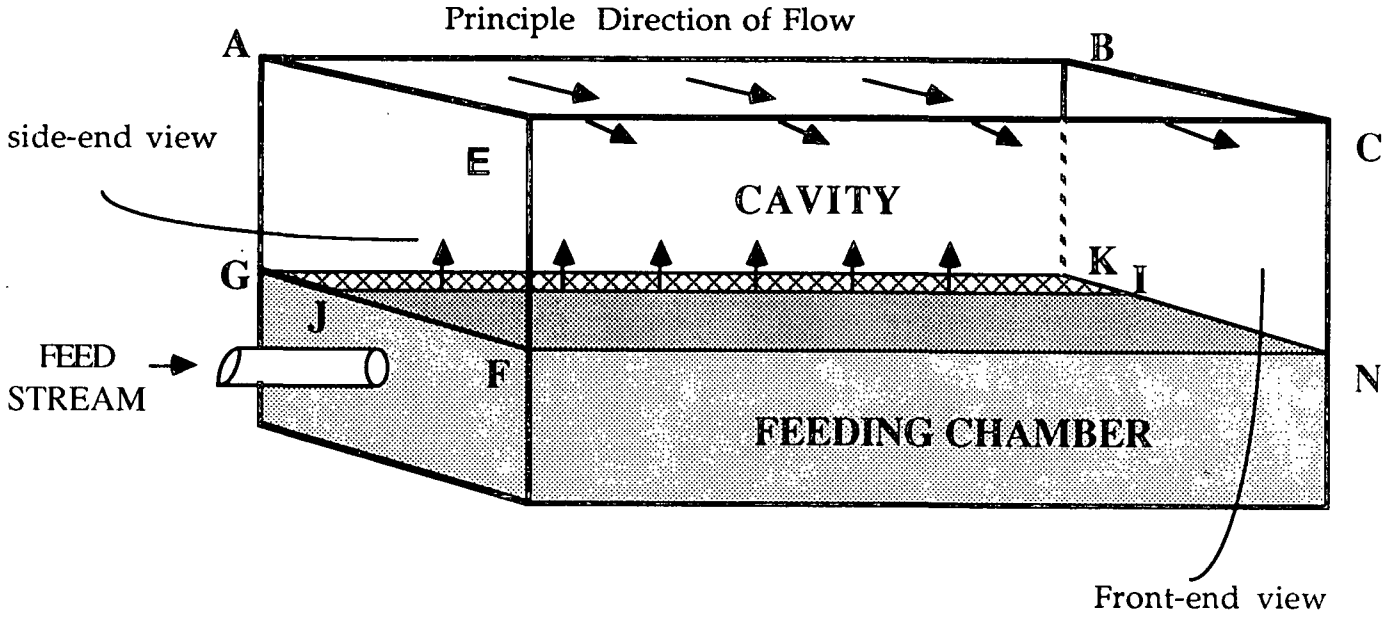

Figure 22. Schematic of a cavity box showing the through-flow cavity for flow visualization and its feeding chamber.

Cavity with Through-flow: Characterization of the Flow

The purpose of this subsection is to describe the operational variables and their interrelation as they can affect the flow in the roll-driven, rectangular cavity with through-flow. The flow in the facility described above is much more complicated than that cited in the literature because of the additional boundary conditions introduced from through-flow. The next few paragraphs present and discuss experimental results from a series of preliminary runs in the experimental facility for flow visualization. The first goal of these tests was to determine how operational variables relate to each other and affect the value of the nondimensional parameters. The two Reynolds numbers Re and Re*, which have been identified as the nondimensional numbers describing the flow of interest here, are manifested by various combinations of the operational parameters. Furthermore, principle requirements are that the fluid inside the cavity makes physical contact everywhere with the roll surface and that there is a constant feed all across the span of the cavity. The second goal, therefore, of the preliminary experiments was to select the appropriate combination of operational parameters which, within the range of fluid velocities tested, can satisfy the above condition. At the same time it is desirable to keep the hydrostatic pressure inside the cavity (P_c) and the volumetric through-flow rate (Q) as low as possible to avoid disturbance in the cavity flow. In fact, proper balance of the operational variables provides an example in which the flow in a lid-driven cavity with through-flow has features remarkably similar to those appearing in an enclosed cavity. The discussion that follows is based on data collected with the cavity having a span of 15.24 cm using a 80/20 glycerol solution in water; the transparent Newtonian fluid which was mainly used in these experiments with a Brookfield viscosity between 140 and 155 mPa sec, depending on temperature. (Details of the viscometric measurements are included in a following subsection.)

Characteristics of the operation of the experimental facility were documented visually as a function primarily of the cavity Reynolds number, Re, and secondarily of the through-flow Reynolds number, Re*. The Reynolds number Re was altered by gradually increasing the peripheral speed of the roll, V, in small increments. An overview of different parametric changes that can influence the operation of the experimental facility is presented in Table 4. This Table illustrates how each one from the six operational parameters can be altered when another one is changing. (The underline indicates the manual change implemented while maintaining at least another variable constant.) For example, speed V depends on a number of variables, in addition to the output of the variable-speed motor that drives the roll. It is inversely proportional to hydraulic pressure P_h, which could be varied stepwise in discrete

values between 207 and 510 kPa, as frictional losses between the cavity collar and the roll tend to slow down the roll. Under constant hydraulic pressure and motor setting. Under constant hydraulic pressure and motor setting, fluid in the clearance between the collar and the roll surface acts as a lubricant assisting the rotation of the roll. Consequently, both the through-flow rate (Q) and cavity pressure (Pc) determine the exact value of speed attained during an experimental run. The peripheral roll speeds investigated ranged from 15 to 670 m/min, although most of the flow visualization experiments were performed in between 24 and 240 m/min. Experimental uncertainty in these measurements was variable, depending on the exact value of speed. characteristically, it was 15% at speeds of 18 m/min, and less than 1% for speeds higher than 60 m/min.

Table 4. Operational variables for through-flow cavity and their interrelationships.[a].

Hydraulic Pressure (P_h)	Cavity Pressure (P_c)	Valve 1 % Opening	Motor Output Setting	Roll Speed (V)	Through-flow rate (Q)
Constant	Increase	Closed	Constant	Increases	Increases
Decreases	Constant	Closed	Constant	Increases	Increases
Constant	Increases	Constant	Increases	Decreases[b]	Decreases
Increases	Increases	Constant	Constant	Decreases	Decreases

[a] Underlined action indicates the operation performed manually.
[b] Except for P_h=414 kPa, hence V remained constant while P_c increased.

The relationship between the Reynolds number Re and Re* is illustrated in Fig. 23 and 24 for different sets of pressures P_h and P_c. The range over which the cavity Reynolds number Re was varied corresponds to the range over which most visualization experiments were conducted. At constant hydraulic pressure P_h, the through-flow Reynolds number Re* increases with rising Re because higher roll speeds raise the rate with which fluid is being removed from the cavity (Fig. 23). In addition, higher cavity pressures give larger Re* because they increase the through-flow rate Q. Similar trends were also observed with other values of the hydraulic pressure tested. In contrast, Re* is inversely proportional to hydraulic pressure for a constant cavity pressure (or pressure in the feeding chamber) as depicted in Fig. 24. This is because lower hydraulic pressures allow for thicker films to be deposited into the roll and,

consequently, increase the through-flow flux of fluid. Thus, the combination of P_h=207 kPa and P_c=10 kPa provides a balance between relatively substantial through-flow without excessive inlet flow into the cavity. This set up, therefore, was used as a standard for most visualization experiments.

One issue of concern was the spanwise uniformity of the feeding stream from the lower (feeding) chamber due to the fact that fluid is fed into the chamber from one of its side endwalls. A perforated plate was used to equally distribute the incoming flow into the cavity, illustrated schematically as area GKIJ on wall GKNF in Fig. 22. The obvious alternative to change the position of the feeding stream was implemented but with the smaller dimensions cavity (having the same spanwise aspect ratio as the previous one). In that case, the fluid was introduced from a tap at the middle of the upstream vertical wall. No differences in the cavity flow, however, were observed between the different arrangements at the same Re. In addition, utilization of a 3-mm open slot (i.e., no perforation) and a gradually widening insert at the bottom of the chamber (i.e., a tapered chamber) did not have any substantial impact on flow features. Details of this and other modifications of the original design of the facility are described in Appendix A. For the case of a slot with perforations - the setup with which most of the flow visualization experiments were performed - visual inspection from the upstream vertical wall indicated that all the fine jets enamating from the holes of the perforated plate are symmetrical around the line of symmetry in the middle of the cavity. Thus, it was assumed that the effect of any pressure differential across the cavity onto the flow was negligible.

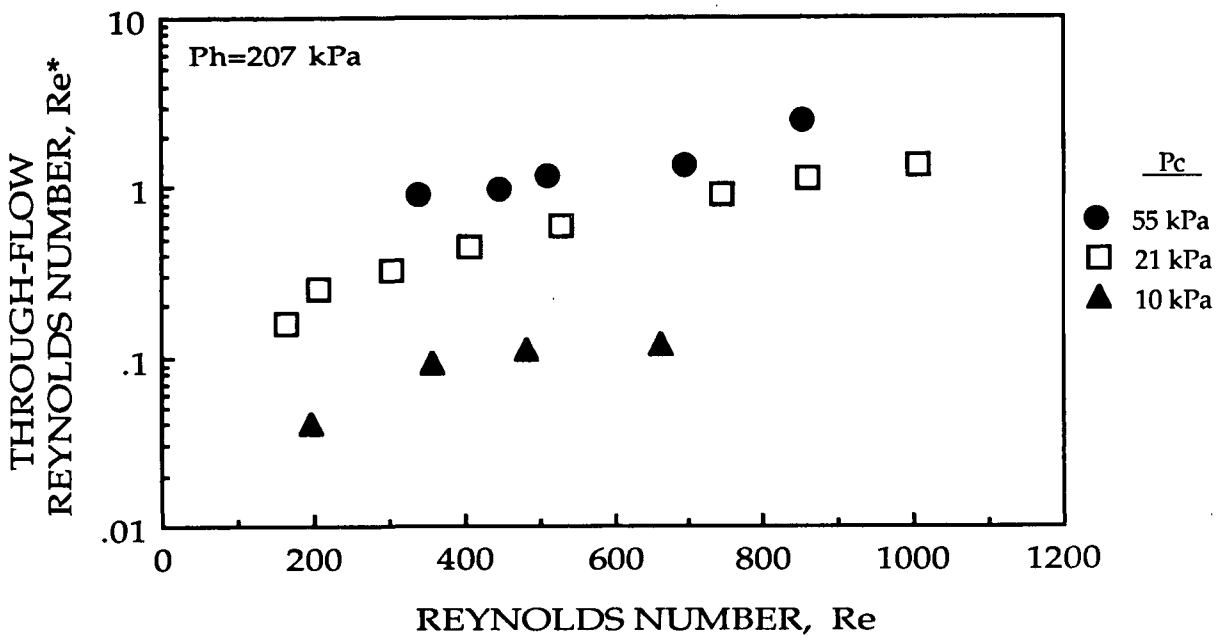

Figure 23. The relationship between the two Reynolds numbers in a lid-driven cavity with through-flow at constant P_h for a series of different P_c.

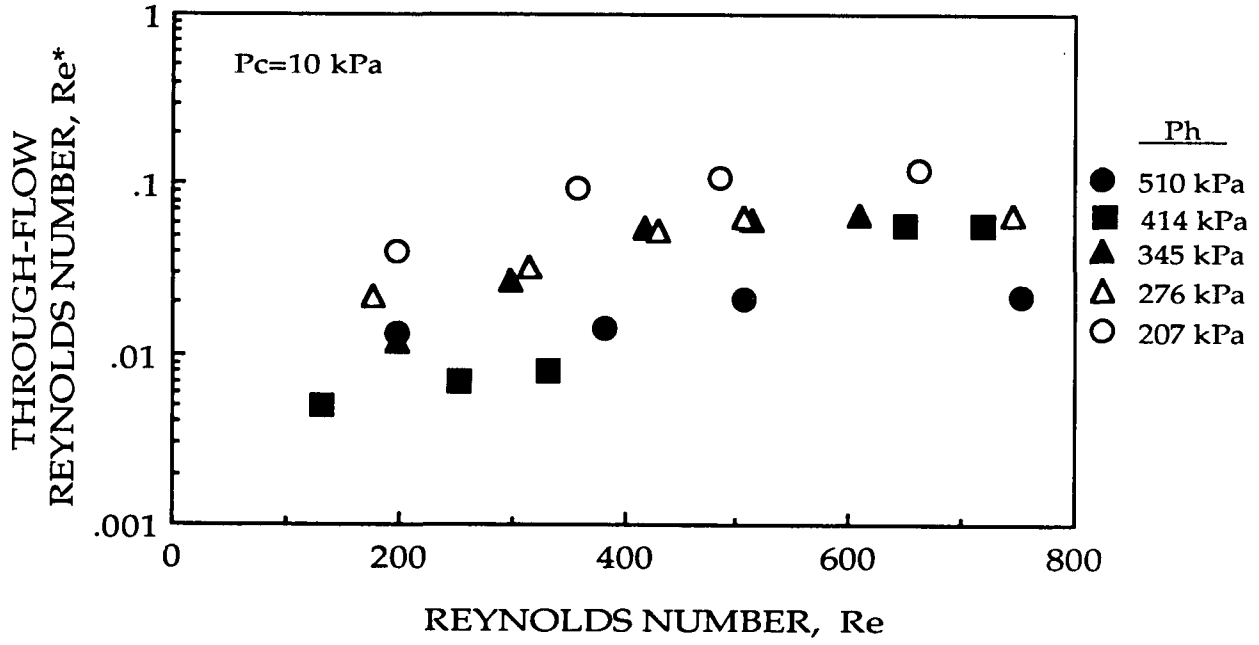

Figure 24. The relationship between the two Reynolds numbers in a lid-driven cavity with through-flow at constant P_c for a series of different P_h.

Flow Visualization: Optical Methods and Techniques

Two different types of fluids and techniques were utilized to visualize the flow in rectangular cavities with through-flow. Newtonian liquids and coating suspensions, usually shear thinning, consisted the test fluids that filled the cavity. The primary visualization technique was based on a suspended-particle technique, a standard fluid-marker method for revealing flow structures.[107] This technique gives pictures of planes of the flow next to end walls, documented with photographs and video. Both steady state and transient flow characteristics were observed with this method. In addition, direct dye-injection techniques[108] were also used to obtain patterns of the flow at selected conditions which, in general, represent streaklines. A novel technique of this type was developed to resolve, for the first time, structures appearing in the flow of opaque fluids (such as mineral suspensions utilized in paper coating). In the next few paragraphs these techniques are described in details.

Glycerol mixtures in deionized distilled water were used as a Newtonian, transparent fluid. Typical proportions by weight comprising 80% glycerine (99.9% pure chemical grade) and 20% water produced a glycerol solution having a viscosity of 148 to 165 mPa sec, depending on temperature and ambient conditions as glycerol is highly hydroscopic. (The method of measuring viscosity is with a rotating spindle-type instrument, e.g., a Brookfield viscometer, under standardized conditions as will be discussed in a later section.) Fluid viscosity during visualization experiments was varied within the range from 77 to 165 mPa sec by adjusting the water content of the glycerol solution. Other physical properties of the test fluid were its density, 1.26 -1.28 ± 0.04 g/cm^3 (measured with a pychnometer), and surface tension, 62.3±0.4 dynes/cm (measured with a Cenco-duNoüy tensiometer). A few experiments was conducted using a shear thinning polymeric solution, i.e., approximately 4% by weight solution in water of a low molecular weight sodium alginate (Kelgin ™ XL, Kelco Inc.). Its physical properties were: μ=95 mPa sec (Brookfield viscometer @ 100 rpm), and ρ=1.1 g/cm^3.

The major criterion for selecting a testing fluid was the requirement for dynamic similarity, with respect to Re, between the experimental cavities and practical SDC ponds. Due to their relatively high solids content and the presence of polymeric additives coating colors, especially the ones that have runnability problems at high machine speeds, are highly viscous with shear viscosity between 800 and 2000 mPa sec (e.g., measured with a Brookfield® instrument at 100 rpm). However, such high viscosities would be difficult to process consistently in a laboratory scale, requiring high pumping rates. Also, as the dynamic contact angle is mainly dependent on viscosity,[109] high viscosity fluids limit the maximum roll

speed above which air entrainment from the upstream edge causes inclusion of air into the cavity and eventually loss of contact between the fluid and the roll surface. (A similar mechanism may also destabilize the flow upstream the blade nip in a short-dwell coater, but this phenomenon is not studied here.) In general, difficulties arise when processing a fairly high viscosity (385-400 mPa sec) Newtonian fluid mainly because of air entrainment and pumping power limitations. It was therefore beneficial in visualization experiments to scale viscosity down by an order of magnitude. This allowed for obtaining characteristic Re values at reduced roll speeds and, by adjusting operating parameters accordingly, to avoid detrimental air entrainment.

Several types of particles were investigated as markers for seeding the flow. Initially glass fibers, 50 microns in diameter and approximately 1 mm long, were dyed with methylene blue and suspended (0.7% by weight concentration) in the fluid continuum for the purpose of visualizing its motion. Although they resolved the major patterns of flow, they had the tendency to slowly float as soon as motion of the roll ceased. Disk-shaped, high reflectance aluminum flakes (300 mesh, manufactured by Atlantic Equipment Engineers, Bergenfield, NJ) on the other hand acted more like neutrally buoyant markers, probably due to their small size (i.e., at the most 42 microns in diameter and few microns thick with typical dimensions of 6x42x0.1 microns), large surface area, and relatively high density of the suspending medium. This was also confirmed experimentally by observing no appreciable sinking or floating of the particles, even after the motion of the roll ceased and the fluid inside the cavity was left to rest. Under the influence of flow, small aluminum flakes are assumed to align in the direction of the three-dimensional shear stress in the flow field and rapidly reorient themselves due to changes in the flow.[108] Thus, they are ideal for obtaining single images of the instantaneous state of flow and, by utilizing a video camera, for observing the development and evolution of periodic and unsteady phenomena. The concentration of the aluminum flakes in all experiments was less than 0.1% by weight.

Direct dye-injection techniques were also used with both transparent and opaque fluids. In the case of transparent fluids, superchrome black TS (Pharmaceutical Laboratories, NY) was mixed at 0.7% by weight into a portion of the fluid to form the tracer. For visualizing the flow through coating fluids, a liquid tracer which absorbs x-rays had to be developed (more details given in the next subsection). These techniques are, in general, more difficult to implement than the suspended-particle techniques but they have the advantage that a single photograph can present the accumulated results of all the various transport processes that carry the injected fluid, whether or not these processes are still active.[110] Not only must the injected stream have a similar density and viscosity as the rest of the fluid, but also the point and velocity of injection have to be carefully selected.[107] Also, the tracer should have low

miscibility to avoid instantaneous diffusion into the bulk liquid. Taking these considerations into account, a series of exploratory experiments were designed to select optimum injection points in the field and set-up. Details on the direct-tracer injection system are included in Appendix A and on the selection of x-ray tracers in Appendix B.

Implementation of flow visualization techniques and interpretation of results require caution. As pointed out by Gad-el-Hak,[111] qualitative data from a dye-injection technique should be interpreted with caution, especially in the case of unsteady flows; hence visualization provides the time history of the tracer in the form of streaklines rather than the local flow characteristics. (To briefly review, pathlines represent curves traversed by a particular fluid element in a flow field as a function of time; streamlines are curves that are tangential to the instantaneous velocity vector at all points in the flow field; and a streakline is the instantaneous locus of all fluid elements which pass through a fixed point in the flow field. All three lines coincide only in the case of a steady flow.) The suspended-particles technique provides snap-shots of whole planes of the flow and reveals flow patterns existing at an instant in time. Dye-injection techniques, on the other hand, give pictures which represent a Langragian view of the flow because they depict evolution of fluid elements. The aluminum-flake technique was used in the major part of flow visualization because it can be applied for steady, time-periodic, and unsteady flows. The dye-injection, as well as the flash x-ray radiographic, techniques were only used to supplement the information obtained with the suspended-particles technique by revealing the form of developed flow patterns.

Illumination of the cavity was achieved with a light sheet emerging from a slide projector utilized as tangential light to illuminate the downstream vertical wall of a cavity. The sheet was created by loading a slide frame having two razor edges coming together at its middle which, in turn, leave a sharp 1-mm wide slot opening. A laser point source was also utilized, the sheet created by using glass rods, to illuminate the cavities from a side end-wall (i.e., transverse to the plane of observation). However, due to the laser's relatively low power, i.e., less than 1 mW, the penetrating ability of the sheet generated was limited and only patterns few centimeters from the wall were visible.

Flash X-ray Radiographic Techniques

Flow visualization of opaque fluids and suspensions is not possible with optical techniques based on light transmission, scattering, or reflectance. This is because light beams are disturbed by either the fluid itself or the suspended phase, due to refractive index

variations and particle-particle interferences. Such phenomena would constrain application of high-speed photography to dense dispersions containing particles with relatively high refractive indices, such as the pigments used for paper coating. The limitations of optical techniques can be overcome by moving up the electromagnetic spectrum and using x-ray radiography. X-rays can easily penetrate fluids which are opaque to light, are not substantially affected by the concentration of solid particles, and generally are not obscured by interposing matter. In particular, non-intrusive flash x-ray radiographic methods have been used to study high-speed dynamic events which are formidable to photographic techniques.[112] Originally developed almost forty years ago to look at ballistic events, flash x-ray radiography today is being applied to image low density media in processes such fuel injection,[113] kraft black liquor spraying,[114] and recently for visualizing coating flows.[115]

Flash x-ray radiography (FXR) utilizes pulses of 10 to 100 nsecs to produce intense bursts of radiation, thus providing the capability of freezing high speed phenomena. The added capability of time resolution carries, however, certain limitations.[112] First, relatively high tube voltages are required to obtain adequate x-ray intensities during the very short period of a pulse. Second, very fast film and screen combinations must be used to achieve sharp images, since the intensity per pulse is limited and image enhancement cannot be adjusted during the exposure. Third, a large focal spot-size is required, since effective cooling of the x-ray generating target is impossible during a pulse, adversely affecting both spatial resolution and radiographic image sharpness. Thus the effectiveness of FXR depends upon (a) selection of a system with x-ray energy appropriate for the specific application, (b) x-ray absorption properties and density of the object to be radiographed, and (c) optimization of radiographic variables, as these are interrelated in obtaining a high contrast, sharp image. FXR systems comprise the pulsed beam generating unit and some kind of a detector which transforms x-rays into visually observable images. Details on technical aspects of their design and setup for radiography are included in standard texts on radiography.[112,116] Appendix B includes details on feasibility studies and preliminary experiments performed to optimize the FXR technique for the specific application of interest. The next few paragraphs highlight important results from these studies relevant to visualizing the flow of coating colors in a lid-driven cavity for the first time.

Selection of FXR source is based on availability and the requirement for a low energy x-ray beam, since the interest here is in visualizing internal phenomena through low density matter. (Preliminary investigation indicated that coating colors have an x-ray absorption similar to water.) The unit (Hewlett-Packard, McMinnville Division, OR) used for radiography produced a 150-KeV beam with a wide spectrum, focal spot of 3 mm, and pulse duration of 70 nsec. This relatively low energy beam allows for better image contrast on the

film, but limits the maximum thickness of the absorbant which can be penetrated. Spatial resolution on the film is primarily limited by the focal spot size. Resolution of tungsten, a material with high mass x-ray absorption coefficient, is confined to 50-and 100-microns thick wires through 8 and 10 cm of coating color, respectively. However, there is a tradeoff between contrast and resolution.

Selection of other radiographic variables is based on a series of experiments performed with the purpose of identifying: (a) best film and screen combination, (b) optimum combination of geometry, such the distances of the object and film from the source, and (c) an appropriate x-ray fluid tracer to be injected like a dye. Because it is impossible to optimize all these parameters simultaneously, priority was given to radiographic contrast and an x-ray tracing fluid with density and viscosity similar to typical coating colors. Best images are obtained with an industrial radiographic film (Kodak XAR™) backed by a rare earth screen sensitive to blue (MCI Optonix, Rarex™III). Keeping the object-to-film distance as short as physically possible, the optimum film-to-source distance is estimated to be between 110 and 130 cm. Thus, although screens generally reduce resolution and definition, they are required here because of the large distances and low beam dosages. After investigating a series of compounds containing tungsten, lead and silver (Appendix B), liquid tracers containing sodium tungstate ($Na_2WO_4 \cdot 2H_2O$) were the most effective. Solutions of approximately 3-4% low-molecular weight carboxymethylcellulose (CMC) have similar density and viscosity as typical colors. Thus, the tracer used in the FXR experiments performed with the cavity was a 50% by weight sodium tungstate solution in a 3% by weight solution of CMC (XL™ Hercules, Inc.). Density values for such solutions are 1.40-1.45 g/cc, while viscosity (Brookfield @ 100 rpm) is in the range of 500-1000 mPa sec depending on exact percentage of CMC and temperature. Figure 11 illustrates, as an example, the axisymmetric streamlines of laminar Couette flow in a radiograph obtained by injection of the tracer from the outer (stationary) wall.

The method used for flash x-ray radiography for visualization of the cavity flow with through-flow is, in principle, similar to the dye injection technique. The setup of the injection system in the cavity is described in Appendix A. Only the front view was observed with radiography. The film with the screen were placed in a 18x5 cm protective cassette which was set next to the upstream vertical wall, ABKG. Experiments were performed in a lead shielded room, for radiation protection, where the injection system was activated remotely with a solenoid valve. Coating colors utilized in flow visualization experiments with flash x-ray radiography were based on typical formulations for LWC papers to be printed by rotogravure. Principle ingredients were 80-100% parts per hundred (based on total dry solids) delaminated clay, 20-0 parts of a no. 2 grade of predispersed Georgia kaolin, 3-6 parts synthetic

binder (i.e., polystyrene butadiene or acrylic latex), and a few tenths of a percent thickeners such as an alkali-swellable (acrylic) latex or sodium alginate. The types of pigments used represent typical grades of clays which are desirable for their print quality but their shear-viscosities are not conducive to high solids content and machine speeds - the current trend in the industry. It is exactly this kind of formulation which has limited utilization with SDC due to poor runnability.

Flow Visualization: Procedures

Flow visualization studies were performed over a wide range of speed, that induced the flow, and a limited range of through-flow conditions. Development and evolution of the flow in the cavity with through-flow were visually observed as a function of the cavity Reynolds number Re under isothermal conditions. The Re was varied between 100 and 9000, although most of the visualization studies were conducted within the range of 100 to about 2000. The through-flow Reynolds number Re* was varied in between 0.1 and 0.8 for visualization experiments. In this range, changes in Re* do not change the qualitative features of the flow, and the flow inside experimental cavities had similar features with the flow in enclosed lid-driven cavities with finite dimensions. The primary suspended-particles technique gave a view of whole planes of the flow and, therefore, documented flow patterns existing at an instant in time. The injection techniques, on the other hand, gave pictures which depict the evolution of fluid elements.

The Reynolds number Re was varied by changing primarily the peripheral speed of the roll and secondarily the fluid viscosity. A certain Re was attained in three different manners: gradual increase, sudden start up, or gradual decrease of the roll speed. The more commonly used procedure was to slowly increase the speed in small increments and observe the transition of flow (with the aluminum-flake technique). The steps followed during the flow visualization experiments can be categorized under three phases. In the first phase the fluid and the visualization technique are prepared for the experiment. In the second phase the machine is set up to the desired conditions the flow is established, and in phase 3 the experiment is started and flow features are documented.

In phase 1 appropriate amounts of glycerol and water were mixed to get fluid shear viscosity within a desirable range. The fluid was then introduced into the reservoir. This phase was simpler for the aluminum-flake visualization experiments as aluminum flakes

were suspended by mixing in a sample of about 1 L removed the from the reservoir. After good wetting and dispersion of the flakes, the sample was added back into the reservoir, the pipelines connected, and the Moyno® pump started to bring fluid into the cavity. Fluid samples were obtained for testing viscosity and surface tension. In the case of the dye-injection and flash x-ray radiographic techniques, the tracing fluid was placed into its 500-ml and pumped up to the injection tube before filling the cavity with fluid.

Phase 2 started by loading the cavity so that the roll surface made contact with the cavity lip. Valve 1 was maintained partially closed to allow for fluid to slightly pressurize the cavity and avoid air entrainment. At this point the hydraulic pressure P_h was also selected. The motor was turned on and its output adjusted to obtain a preselected speed. When the desired range of speed was reached -this took a little of time since the roll inertia prohibits instantaneous increase from zero to maximum rpm - the opening of valve 1 was adjusted to maintain contact of the fluid in the cavity with the roll surface and to obtain a uniform film onto the roll. These requirements were monitored with visual inspection. Finally, the speed was checked with a tachometer. At that time also Re and Re* were calculated; the latter manipulated from measurements of the flow rate in the pan underneath the doctoring blade upstream the cavity.

In phase 3, flow features were documented after the flow in the cavity was allowed to develop for at least 15 minutes under steady state conditions (aluminum-flake technique). Next, the speed of the roll was gradually raised and any changes of flow features were recorded, using the same procedure, as Re was continually increased. In most cases, the opening of valve needed not to be adjusted during an experiment. In some experiments, however, the fluid inside the cavity lost contact with roll over a period of time or visible air bubbles were entrained inside the cavity. This happened when the speed exceeded 150 m/min, and the experiment was interrupted and started again from the beginning with a larger percent opening of valve 1. Trial and error was the only way to develop an assessment of the required pressure inside the cavity, which also depends on the viscosity of the fluid.

In experiments with the injection technique, phase 3 was slightly different. After attaining the precise experimental conditions and the photographic or radiographic hardware was prepared, the pneumatically controlled valve of injection was opened for 1 to 5 seconds (in most cases it was 3 seconds). Streams of the tracer were injected at 45° angle to the primary (two-dimensional) flow close to top edge of the lip on the downstream vertical wall. Trial and error established the combination of roll speeds, fluid and tracer viscosities, and injection times for optimum utilization of these techniques. All results obtained with injection techniques were also verified with the aluminum-flake technique. After each injection it was

important to stop the machine, unload the cavity and clean its contents because of contamination from the injected fluid. Then, new fluid was introduced into the cavity and the experiment continued.

Similar procedures were followed for start up of the roll at a preselected speed and the gradual decrease of speed. Steady flow structures were left to fully develop, while transient phenomena were recorded on videotapes. The exact conditions selected for observation with the injection technique were first documented with the aluminum-flake method to verify the existence of structures of interest. All experiments were conducted under ambient conditions (i.e., room temperature) and, because the maximum temperature rise measured during an experiment was 1°C, the flow was considered isothermal.

In general, two different views of the cavity were observed; a side-end view parallel to wall AEFG and the front-end view parallel to the downstream vertical wall, ECNF (Fig. 22). The latter was the main view of interest in flow visualization experiments, while a limited number of photographs obtained from the side-end view only served the purpose of confirming similarities with the enclosed lid-driven cavity. In both views the region near the roll surface is obscured by the Teflon collar that makes the contact between the cavity and the roll.

Flow patterns in each experiment were photographed using 35 mm still film and high resolution professional videocassettes. A Yashica FR-I camera was used with 28/80 mm and 85/120 mm macrolenses for still photography, the still photographs taken using black-and-white KODAK TMAX and TRI-X PAN (ASA 400) films. Short exposures of 125 and 250 shutter speeds were taken at f-stop settings of 3.5 to 8 for most pictures. A few long exposures were taken at f-stop of 22 and shutter speeds varying from 0.5 to 30 seconds. A Panasonic SuperVHS industrial camera having high resolution was used for videotaping.

The question of repeatability is raised because the experiments were performed over different sessions. In this instance, repeatability means that similar flow features were recorded under the same conditions for each individual session. To achieve this, care was exercised to ensure that both the initial and boundary conditions remained constant, or at least varied within a reasonable uncertainty. It should be pointed out, however, that the macroscale features of interest here were inherent to the type of flow rather than sensitive to initial conditions. Thus, the qualitative results indicate that the degree of repeatability in the flow visualization experiments was very good. Estimates of quantitative data such as the critical Re for transitions of flow, on the other hand, have comparatively large uncertainty because they were exclusively based on visual inspection.

Viscometric Measurements

A Brookfield laboratory viscometer (RVT model, serial no. 17776, replenished on February 1989) was used to determine the steady shear viscosity of all fluids in this work. This is a simple instrument whose single-point measurement comprises a standard in the paper coating industry. Therefore, calculations based on this measurement can be conveniently carried out or related to the pilot-plant and industrial environments. The instrument is of the rotational type where the torque required to rotate an immersed element (the spindle) in a fluid is measured. When the spindle is driven by a synchronous motor through a calibrated spring, the spring deflection is indicated by the pointer on a dial. The viscous drag is proportional to the spindle's rotational speed and depends to the spindle's size and shape (geometry). The shear rate, for a given viscosity fluid, varies with the distance from the spindle's surface but, generally, it is comparatively low, i.e., from one to about ten reciprocal seconds. It is, therefore, preferable to use the same spindle for comparative studies using a series of similar fluids.

Measurements with the Brookfield viscometer were mostly carried on with spindle no. 3, but spindles no. 2 and 4 were also used occasionally. Unless otherwise indicated, all data reported was based on measurements with the no. 3 spindle. Every fluid sample was placed in the same 600-ml beaker (filled up to the 500-ml line), the thermostatic fluid temperature was measured, and the dial displacement was recorded after three minutes had elapsed from when the spindle started rotating. The instrument was calibrated with various Newtonian fluids of known viscosities (i.e., silicone oils having viscosities of 10 and 100 mPa sec, respectively). For spindles no.3 and 4, and a fluid of nominal viscosity of 100 mPa sec, the estimated uncertainty was up to about 7 percent. More details of the estimated standard and random errors of measurements are listed under the uncertainty analysis section.

The primary torque-speed data obtained with the Brookfield viscometer were converted to viscometric shear stress-shear rate relationships. For this purpose a computer program, developed by the Research & Development of Beloit Corp., Beloit, Wisconsin, was used. The program is based on the computational technique listed by Hyman[103] which allows for determining the two coefficients of the power-law fluid model. This procedure was used to calculate all the data presented in both numerical experiments and pilot-plant sections. It should be pointed out, however, that the shear rates attained with this instrument were in the range of 10 to 100 sec^{-1}.

UNCERTAINTY ANALYSIS

This section contains details on the sources of errors and the precision associated with the experiments in this thesis, and discusses the methods used to determine uncertainty. The procedures implemented for estimating uncertainty comply with ASME/ANSI standards.[117-119]

Values of a parameter in science and engineering are subjected to uncertainty because no measurement is perfectly accurate. Generally, inaccuracy comprises two components: a fixed or systematic error and a random component, usually referred to as precision. The first expresses the difference between the true and the recorded value, and it is termed bias error. It cannot be sampled but it has to be estimated, hence calibration helps, and remains the same within certain procedures and/or apparatus. The second is a statistical quantity that can be estimated by repeating a measurement many times, thus it is related to a certain probability level quantified through the standard deviation. Although repeatability of a measurement or procedure refers to precision only, reproducibility denotes the total uncertainty (precision plus bias).

Moffat[118] describes three different kinds of uncertainty associated with experiments: interpolation uncertainty, unsteadiness, and instrument calibration. Interpolation uncertainty, also known as "zeroth-order" error, arises from the inability of an observer to ascribe a certain numerical value to a phenomenon with absolute certainty. (Here bias and precision cannot be distinguished.) Examples of this, pertaining to the experiments on hand, are the uncertainty in measuring the density of a fluid and in estimating high-shear viscosity from rheograms. Unsteadiness, a "first-order" level of uncertainty, describes variations due to unsteadiness in an instrument or apparatus observed when a measurement is repeated as time runs forward. It also includes possible information on instrument calibration. The uncertainty in the roll speed, which is variable depending on speed level, is a good example of this. Instrument calibration, the "Nth order" level of uncertainty, represents variability obtained over long periods of time when a certain apparatus is shut down and started again, or a procedure is repeated by resetting nominal values. The reproducibility (± 6%) in measurements with the Brookfield viscometer is a good example of this; reproducibility here means day-to-day variation with the same instrument and operator. This type of "reset" uncertainty is important in the fluid dynamics experiments performed during this research. This is because small alterations in the setup may introduce finite disturbances which may

influence not only the state of flow but also the critical range of the control parameter over which transitions occur.

Table 5 contains a summary of the estimated uncertainties for measured and calculated data. More details and the methods used to determine the uncertainty of the calculated data are included in Appendix C. Total uncertainty is based on 95% confidence level, and t-values have been obtained from statistical Tables. Errors in viscosity measurements with the Brookfield instrument are reported for all the different spindles utilized during the course of this research. † Repeatability of measurements with the same spindle was, in general, better than 1%. Precision indices vary because a different multiplication factor is used with each spindle for obtaining viscosity. Reproducibility from one day to the next was about 6%, which also includes variation in temperature of the fluid sample by less than ±1 °C. The numbers reported for the two Reynolds numbers were primarily influenced by fluctuations in the peripheral speed of the roll which, all other variables constant, was varying within a narrow range. In general, it was steadier at relatively high speeds. It is noteworthy that the numbers reported for Re* represent maxima. These values were mostly influenced by variations in the flow rate of the fluid deposited onto the roll surface, e.g., exiting the cavity downstream.

---

† Additional viscometric measurements, after completion of the experiments in this study, indicated a larger bias error than the one reported initially for the Brookfield instrument. When measurements of standard viscosity (Newtonian) fluids were conducted with a rotational coaxial-cylinders viscometer, the values obtained were from 30 to 60 percent lower than the estimates with the Brookfield viscometer; the exact difference depending on fluid viscosity and spindle type (used with the Brookfield instrument). In the useful range of viscosities for flow visualization, Brookfield overestimated the viscosity of glycerol by about 60 percent. As a result, all the calculated dimensionless numbers in the following experiments have been overestimated by the same amount.

Table 5. Uncertainty of measured and calculated data.

Parameter	Instrument	Bias (B_{P_X})	Precision (S_{P_X})	Uncertainty (α=0.05)
		Specifications		
Cavity dimension (width)	--	0.05 cm	--	±0.05
		Measured Data		
Fluid density	Pychnometer	0.04 g/cm^3	--	±0.04
Temperature	Thermometer	--	0.20 °C	±0.40
Fluid viscosity	Brookfield (100 rpm, 20.8±0.2°C)			
	Spindle #2	1.00 mPa sec	0.23 mPa sec	±1.11
	#3	2.50 mPa sec	0.55 mPa sec	±3.11
	#4	5.00 mPa sec	1.00 mPa sec	±7.04
Roll speed	Tachometer			
	low (18 m/min)	0.30 m/min	1.00 m/min	±2.69
	medium (46 m/min)	0.30 m/min	0.90 m/min	±1.93
	medium high (73 m/min)	0.30 m/min	0.20 m/min	±0.39
	high (270 m/min)	0.30 m/min	0.40 m/min	±0.66
		Calculated Data		
Reynolds number, Re				
	low roll speed	0.03	0.08	±17%
	medium roll speed	0.03	0.04	±10%
	medium high speed	0.03	0.03	±8%
	high roll speed	0.03	0.03	±8%
Reynolds number, Re*	(maximum)	0.013	0.015	±0.043

CHAPTER FIVE

EXPERIMENTAL RESULTS FROM FLOW VISUALIZATION STUDIES

OVERVIEW

The basic steady-state pattern of the fully developed flow in a cavity with through-flow is depicted schematically in Fig. 25. For the low through-flow rates considered here, the rotation of the metal roll causes the fluid flow in the cavity. Fluid dragged downstream reaches edge E where most of the fluid follows wall EF and only a relatively small amount exits the cavity as a thin film deposited on to the roll surface. Thus the primary recirculation is induced. Separation of the viscous flow occurs along the wall EF because of friction, which decelerates the fluid, and the stagnation imposed by the corner F. As the pressure gradient that opposes fluid motion cannot be overcome, the flow separates resulting in the formation of a secondary recirculation in the vicinity of corner F. This is the so termed downstream secondary vortex, DSV, which counter-rotates with respect to the primary recirculation and it is similar to the structure appearing in the enclosed lid-driven cavity flow (Fig. 8). In contrast, the upstream secondary vortex does not exist in the through-flow cavity due to positioning of the feeding stream, while the upper secondary vortex is not visible due to the Teflon collar.

The above simplistic description refers to the fully developed steady "two-dimensional" flow - the basic laminar state of flow. In three dimensions, the main and downstream secondary circulations of the steady flow comprise cylindrical rolls extending along the span of the cavity, while the line separating the two rolls is an interface. Endwalls of a cavity induce spanwise motions so that, in the practical case of experiments, the flow is three-dimensional. Furthermore, the concave separation interface between the primary and the secondary rolls destabilizes.[77,84] Using the "two-dimensional" picture of the flow as a reference, the interest in our work concentrates on three-dimensional features, both stationary and time-dependent, which appear when the parameter that controls the flow changes. As mentioned earlier, flow visualization experiments were performed for Re within the range of 100 and 2000, while Re* varied between 0.1 and 0.8. Most of the results corresponds to standard conditions of P_h=207 kPa and Pc=10 kPa. Flow phenomena and structures described in the next few pages were reproducible in the sense that they could be

obtained irrespectively of the size of rectangular cavity, fluid used, or the specific point in time a visualization experiment was performed (assuming that initial and boundary conditions remained practically the same). The first and major part of the qualitative results is based on photographs obtained with the suspended-particles technique. The second part includes stop-motion images of flow structures obtained with the dye-injection and radiographic techniques. Appendix D describes in detail selected flow visualization experiments and reports the corresponding conditions under which various phenomena occurred. Observations in the present study focus on the vicinity of the downstream secondary vortex, DSV, which traditionally is the point of interest in experimental and computational studies of cavity flows. In addition, it seems that flow instabilities set in first in this region and interesting flow structures were formed. Finally, it should be pointed out that the phenomena observed refer to fully developed flow and its transitional modes.

As estimated from repeated visual observations, the control parameter that describes the flow is the cavity Reynolds number, Re. Gradual increase of the peripheral roll speed takes the system from its basic steady state (i.e., the primary stable state) to time-periodic and unsteady states featuring three-dimensional cellular structures. Torroidal eddies in the form of Taylor-Görtler-like vortices meander along the spanwise direction of the cavity with their axes parallel to the principal direction of flow. These structures are centrifugal instabilities inherent to the system's dynamics and are relatively weak (secondary) flows which are superimposed on the base flow. Similar structures are obtained during sudden start-up of the flow. The only requirement is that the value of Re is above a certain critical range. When the cavity Reynolds number is below approximately 500, the primary state of flow is steady featuring the main and downstream secondary rolls. For Re in the range of 500 to 600, vertical spikes are generated at the centerline and start traveling toward both side endwalls (edges). At higher Re, the separation line becomes wavy with the waves subsequently engaged in a complex spanwise oscillatory motion up to Re of about 1100. At this point, spikes grow small crowns at their tops which give them a mushroom-like form. As the speed slowly increases, the flank and stem of mushrooms first oscillate in-phase and eventually fluctuate causing the flanks to alternatively jump from left to right rapidly, thus giving the appearance they are disappearing into their neighbors and reappearing a short while later. These phenomena are considered to indicate an unsteady state.

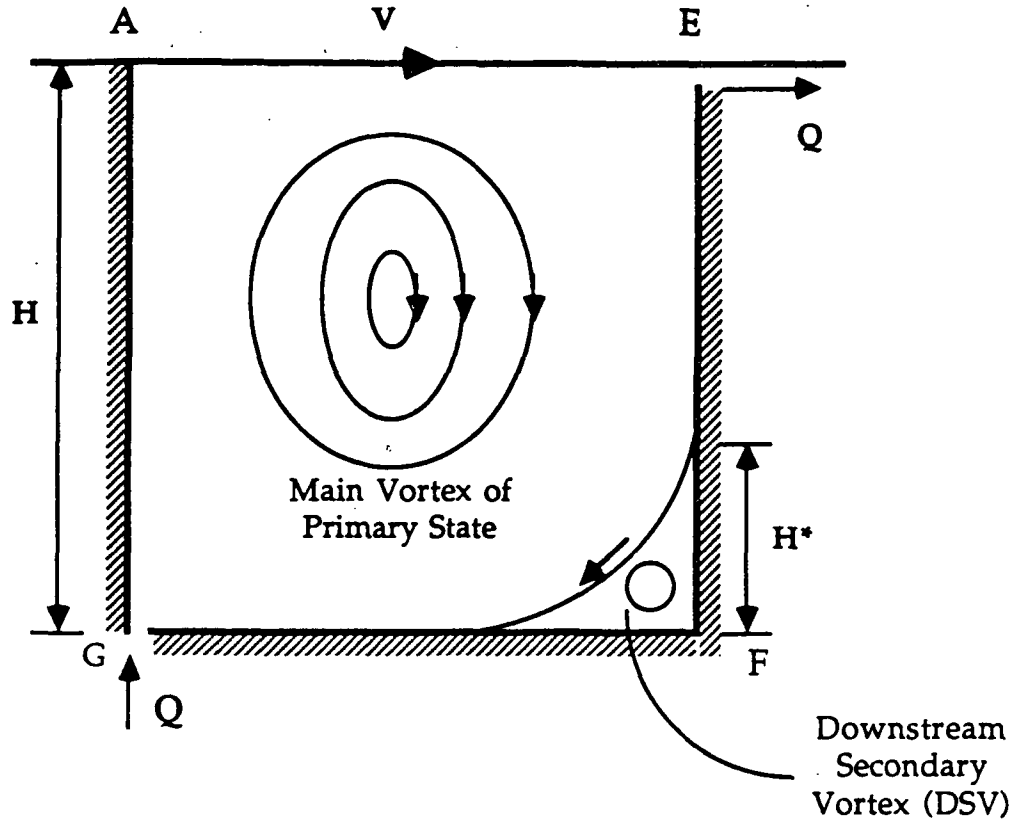

Figure 25. Schematic of "two-dimensional" flow features in a cavity with through-flow. Side end-view only.

The following section describes observations from flow visualization experiments and qualitative changes of the flow as Re changes with roll speed and, secondarily, fluid viscosity. Some quantitative data are presented with the emphasis on critical ranges of the control parameter under the geometries considered. Important influences on the flow are also discussed. All this phenomenological data assist in describing a more complete picture of the flow, including its instability forms and multiple stable states.

DESCRIPTION OF FLOW PHENOMENA AND THEIR CHARACTERISTICS

Visualization with Suspended Particles

Data described in this section are based on photographs obtained with a particle-laden fluid. This technique allows for pictures of the instantaneous state of flow and it is independent of flow type, i.e., steady, time-periodic, or unsteady. It gives snap shots of entire planes parallel to the walls bounding the flow field. Assessment of time-dependent phenomena is obtained with motion pictures (video). Except for two photographs of the side-end view presented in the immediately proceeding section, where glass fibers were used for tracers, the tracing particles were aluminum flakes.

The Basic Primary Steady State

Figure 26 illustrates the main and downstream secondary vortices on visualization photographs taken from the side endwall AEFG in Fig. 9. The tracing particles were colored glass fibers and the flow field was illuminated from the side opposite to the one used for observation. The main and downstream secondary vortices, as well as the concave (as seen from the center of the cavity) interface between the two vortices, are resolved in both cases. Because the secondary eddy is weaker than the main recirculation its visualization is possible only when the roll speed is comparatively high (i.e., Re greater than 200). Both the separation

as well as the reattachment points of the flow on the front and bottom walls, respectively, remain stationary within the Re range from 100 to 490. The distance of the separation point from the bottom wall of the cavity, determined by scaling lengths on photographs, is 40% and 36% of the total depth for the large and small cavities, respectively. Assuming an ideal two-dimensional steady flow in an enclosed cavity having same dimensions as the large cavity in the experiments and fluid properties similar to the ones of the experimental fluid (ρ=1.28 g/cm^3, μ=161 mPa sec), numerical simulation for Re=500 gave a height representing 44% of the cavity depth. This value is close to the one obtained experimentally. The agreement suggests that, within the low range of through-flow rates (or Re*) investigated, the flow in lid-driven cavities with small through-flow is qualitatively similar to the flow in enclosed cavities. In other words, the roll movement dominates the flow because the ratio Re/Re* is of the order of magnitude of 10^4. (The ratio of Reynolds numbers is equal to the product of roll speed with the cavity width divided by the through-flow rate, and therefore it is independent of fluid properties.) The 4 % difference between the experimental and numerical results may be attributed to the fact that laminar two-dimensional simulations usually overestimate the strength of the flow, especially close to endwalls.[84,85] Differences observed experimentally between the two cavities in Fig. 26 could also be explained with edge effects which, under the same flow conditions, are more dominant in the smaller size cavity.

The steady primary flow pattern persists for Re up to approximately 500 irrespectively of the specific way in which the final Reynolds number was approached; e.g., by gradual acceleration, deceleration, or sudden startup of the roll. In addition, relatively small amplitude disturbances do not influence the flow characteristics. Variation of the Pc, for example, from 8 to 70 kPa (P_h constant at 207 kPa) did not change the qualitative picture of the flow, although it did influence the size of the DSV, as it will be discussed later under factors influencing the flow.

Flow structures such as the ones described above can also be observed from the front-end view of a cavity with through-flow using a fluid laden with aluminum flakes (Fig. 27). A dark horizontal line appears along the span of the cavity which is the separation line between the main and the secondary downstream rolls. The line is straight and almost parallel to the lower boundary everywhere except from regions in the vicinity of the side endwalls where a steep positive slope exists. To confirm that this line represents the demarcation between the two recirculating rolls, the growth of its characteristic length scale (height H*) is compared with results from studies appearing in the literature.

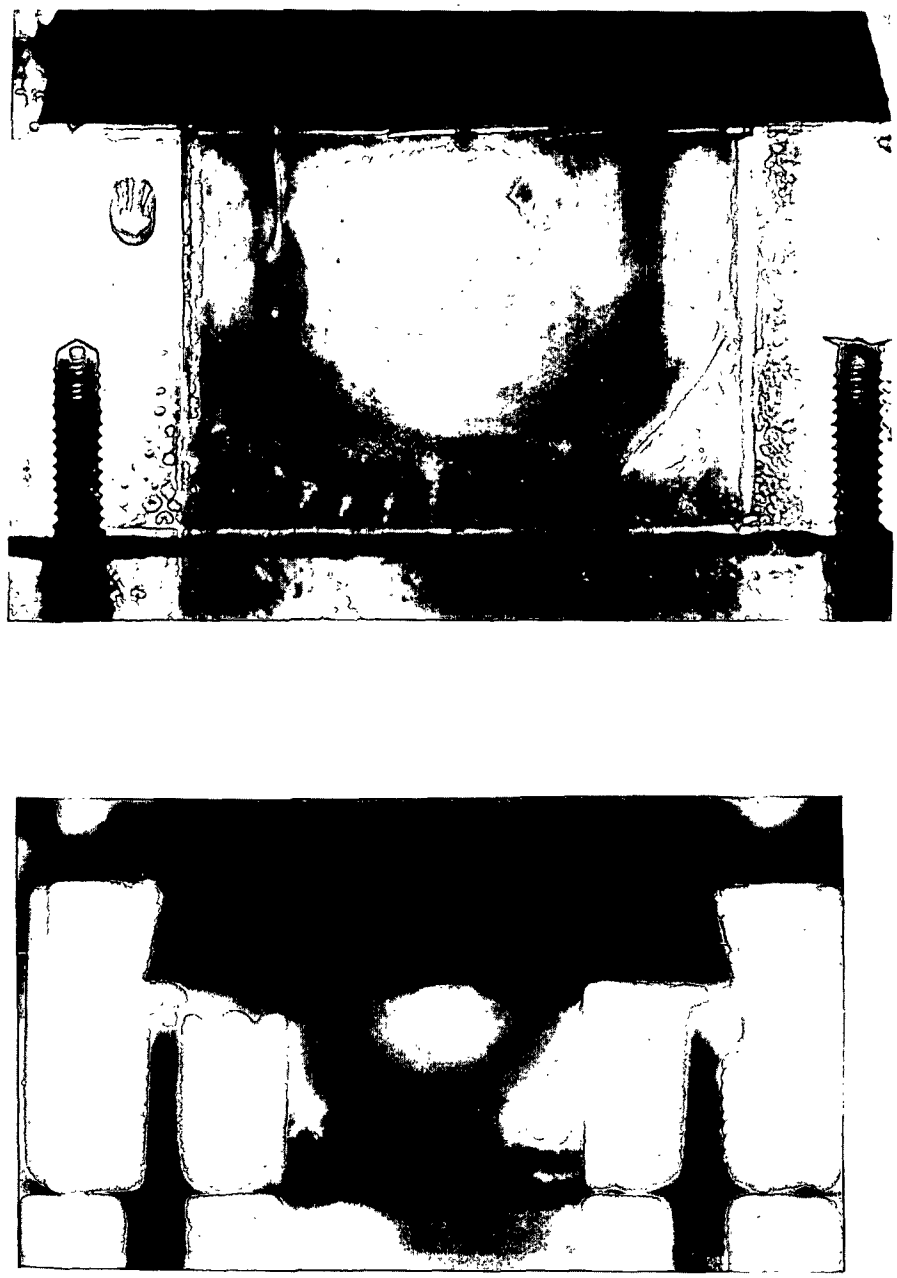

Figure 26. Photographs illustrating the main and secondary (DSV) vortices of the basic state of flow (side end-view only). Top: large cavity, Re=470; bottom: small cavity, Re=490. Re^*=0.01, P_h=207 kPa, P_c=10 kPa. Principle direction of motion is from the left to the right.

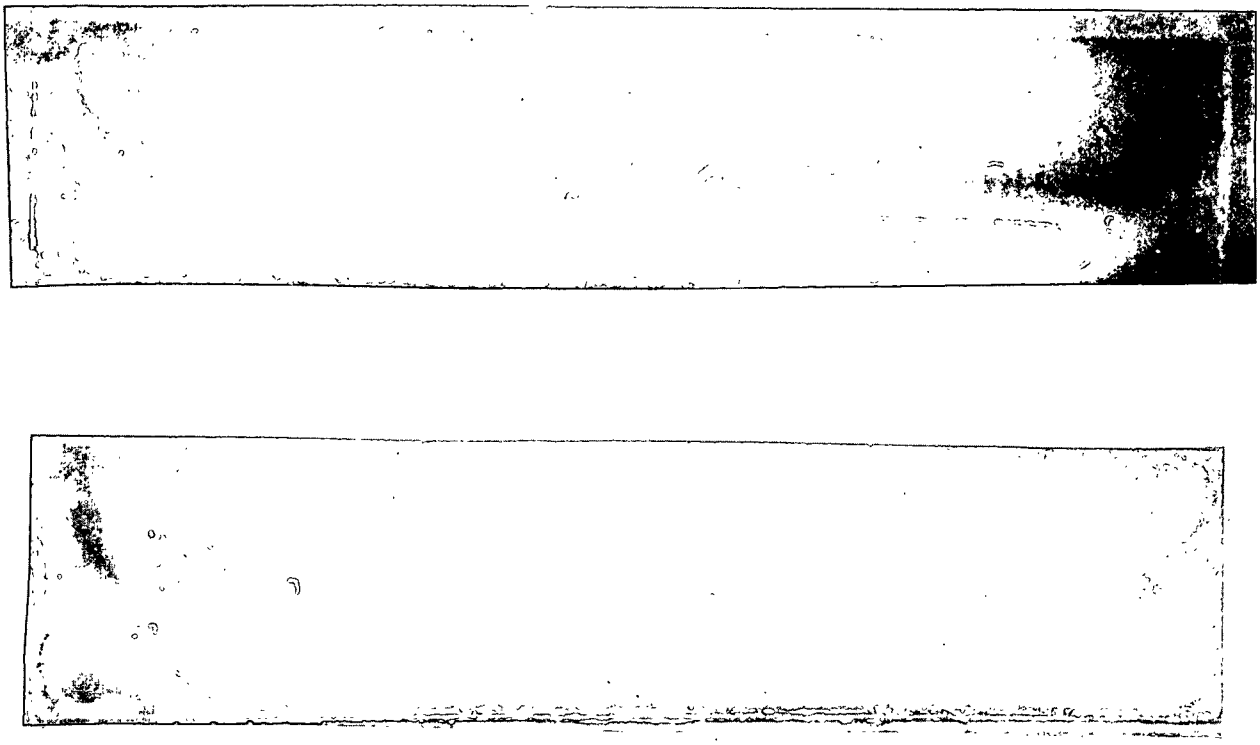

Figure 27. Photograph of the separation line between the main and the downstream secondary vortices. Basic state of flow (front end-view only). P_h=207 kPa, P_c=10 kPa. Top: gradual speed increase, Re=390, Re*=0.40-0.50; bottom: gradual speed decrease, Re=370, Re*=0.40.

Size of the Downstream Secondary Vortex

The characteristic height H* of the observed line is comparable to the size of the DSV in enclosed lid-driven cavity flows reported in previous numerical and experimental studies. The value of H* was visually estimated by measuring the distance of the separation line from the edge of the bottom wall at the vertical centerline (see Fig. 27). This dimension is divide by the cavity depth, H, and plotted as a function of Re in Fig. 28. In the case of the large cavity, typical values of H* are 14 and 19 mm for Re equal to 250 and 500, respectively. The height H* increases sharply with Re up to 400, thereafter its rate of growth reducing substantially as its value reaches a plateau. For Re greater than 600, the flow is already three-dimensional, as will be shown later, and the separation line is no longer uniform along the span of the cavity. Under the standard conditions of experimentation (i.e., P_h=207 kPa, Pc=10 kPa), the trend observed here is in good agreement with the numerical results of Burrgraf,[120] Bozeman and Dalton,[121] and Nallashamy and Prasad[122] for the size of the DSV in enclosed lid-driven cavities. This evidence implies that height H* can be interpreted as representing the size of the DSV. In general, the experimental data presented give sizes about 4 percent of the cavity depth different from the numerical estimates. This difference could be attributed to the fact that simulations were carried out for two-dimensional flows in unbounded cavities with infinite span and without outflow. In contrast, the experiments were performed for confined flow in a bounded cavity with through-flow. Additionally, the flow in the experimental cavity is three-dimensional due to endwalls.

Our results also compare well with the experimental data from Pan and Acrivos[74] but only for Re around 500. For values below that level, their data are approximately 17% lower than the H* distances measured here. It should be noted, however, that these authors used a cubic cavity where the roll penetrated in to the cavity by about 17 percent of its depth, as compared to approximately 1% in our experimental facility. Differences therefore between the work here and that of Pan and Acrivos[74] maybe attributed to these geometrical differences. Putting these disagreements aside, the general trend of the DSV size as a function of the Reynolds number is similar to the one depicted for height H*. This indirectly implies that, within the experimental conditions considered, the picture of the flow observed from the front-view here is similar to the flow in an enclosed lid-driven cavity.

Visual inspection reveals interesting phenomena in the vicinity of the side endwalls, AEFG and BCNK in Fig. 9. The separation line develops a steep positive slope near these walls indicated by the linear growth of the characteristic height H* (Fig. 27). The value of H*,

measured directly on the various cavities used for flow visualization, raises by about 30 to 40% next to the side endwalls as compared at the centerline. In contrast, if one compares the value of H^* at the centerline (front-end view) with the size of the DSV extrapolated from the side-end view AEFG (i.e., photo in Fig. 26) there is only a 10% increase. This difference can be explained from variations in the type of lower boundary between the two sets of photographs. The whole boundary in side-end view photographs is a perforated plate, while in front-end view photographs the lower wall has a perforated slot next to the upstream vertical wall. Thus, although the two views qualitatively depict the same patterns under similar flow conditions, there are quantitative differences due to variable feeding geometries.

Such differences, however, cannot underestimate the effect that the side endwalls have on the flow, especially in close proximity to the walls. The recirculating path of fluid elements in these regions, and therefore the size of the DSV, increases linearly with decreasing distance from the wall.The distance from the walls, where such a phenomenon occured, was estimated visually to be 5 and 12 mm for the small and large cavities, respectively. The apparent DSV growth can be attributed to weakening of the flow next to the side endwalls, where the no-slip condition is satisfied, so that separation of the main recirculation from the downstream vertical wall occurs closer to the edge EC (Fig. 9) and consequently H^* increases. This observation is consistent with velocity measurements taken by Koseff[77] who found that endwalls weaken the flow next to them as compared to the purely "two-dimensional" flow due to shear stresses that cause local reduction in the mean kinematic energy of the fluid in the endwall region. An additional phenomenon which manifests three-dimensionality due to the presence of side endwalls is discussed next.

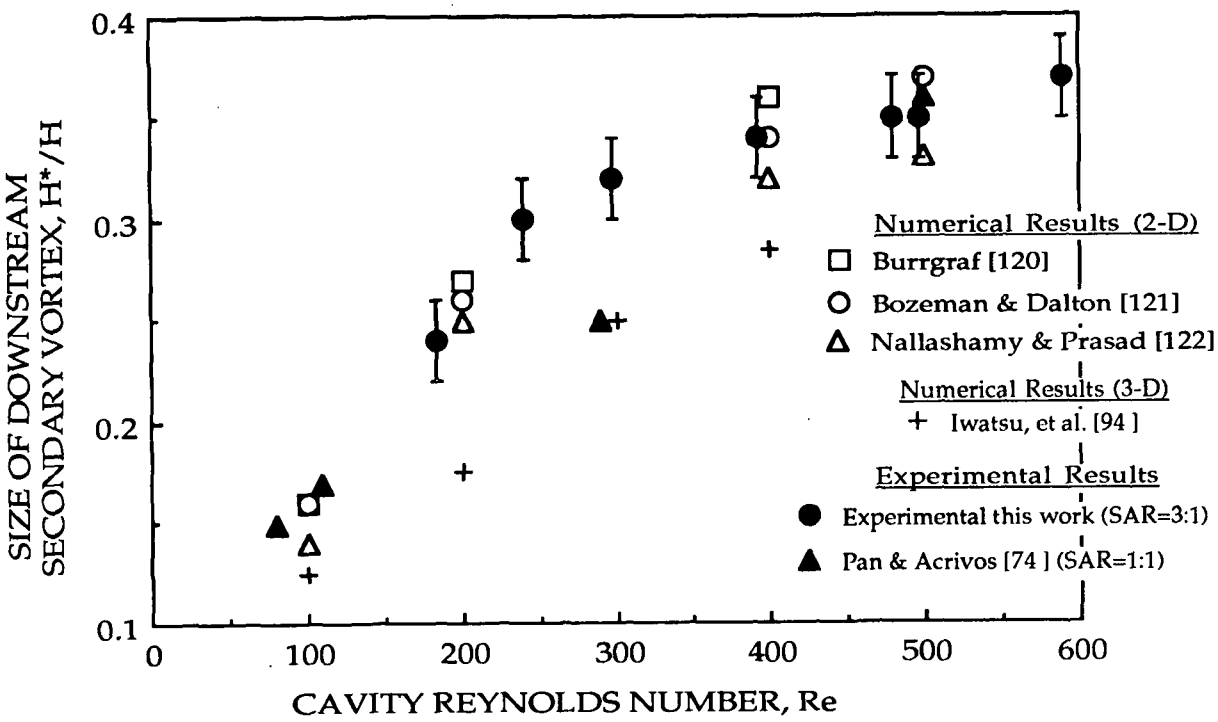

Figure 28. The size of the downstream secondary vortex as a function of the Reynolds number Re (or machine speed). Re^*=0.22-0.35, P_h=207 kPa, P_c=10 kPa.

Corner Vortices

Another interesting structure, seen only from the front end-view, is a recirculating cell appearing next to side endwalls at comparatively low Re. The example depicted in Fig. 29 is a long-exposure (5 seconds) photograph taken with a sheet of laser light illuminating the cavity along the spanwise direction. In this picture the flow is parallel to wall ECNF in Fig. 9. A similar cell existed at the same time next to the other side endwall of the cavity. In fact, the two cells recirculate in opposite directions, i.e., the cell next to the right edge wall counter-clockwise, and the one next to the left edge clockwise. Such cells, which are termed "corner vortices", appeared upon gradual increase, decrease, or sudden startup of the flow for Re greater than 130, and remained stationary up to Re equal to about 350. No corner vortices were observed above this value of the Reynolds number. The flow became time-periodic at about Re=500. Corner vortices were not influenced by changes of the Re* within the range of 0.01 to 0.40, and of the Pc from 8 to 83 kPa. However, their size depended on Re, as will be discussed in a later section.

Corner vortices are a local in the sense that they are confined next to the side endwalls. In fact, they are manifesting three-dimensionality in the flow due to edge effects, similar to the ones described by Koseff.[77] These vortices originate from the adjustment of shear and pressure forces, acting on fluid elements in the primary recirculation, to the no-slip condition imposed by the presence of lateral bounding walls in the cavity. Because the centrifugal acceleration is balanced by a radial pressure gradient, fluid particles in the vicinity of endwalls follow paths of smaller radius of curvature to maintain mass balance. Thus the no-slip condition generates an Eckman-type viscous layer at the endwalls which induces a radially inward motion of the fluid, i.e., towards the center of the main recirculation. Consequently, viscous damping of the primary recirculating flow generates corner vortices next to endwalls. The existence and development of corner vortices can be responsible for perturbing the flow and inducing spanwise motion in enclosed lid-driven cavities.[84]

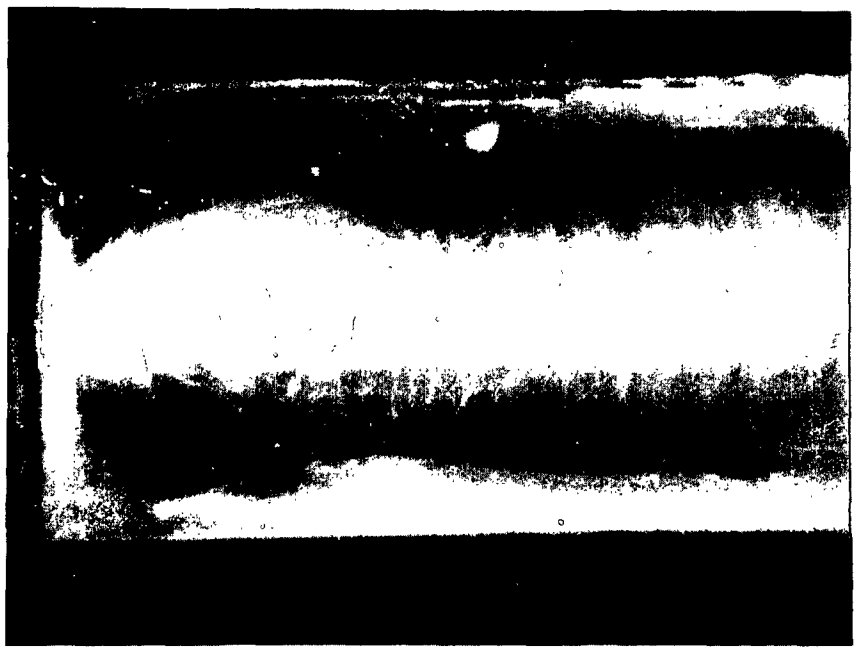

Figure 29. A corner vortex appearing next to the side endwall of the cavity (front end-view). Re=340, Re*=0.30. P_h=207 kPa, P_c=28 kPa.

Time-Periodic Flow

Upon progressively increasing speed of the roll so that the Re exceeds 500, visual observation reveals that the the flow inside the DSV destabilizes. A time-periodic flow sets in as pairs of streaks, oriented vertically inside the DSV, appear which are brighter than the rest of the fluid (Fig. 30). These streaks are generated at the centerline and each member of a pair accelerates outwards (i.e., net flow from the center of the cavity towards the side endwalls is defined as outflow.) As soon as a pair convects to an edge of the flow, another pair is generated at the middle of the cavity to assume the same motion. In general, streaks move faster as roll speed rises and with increasing distance from the center of the cavity. Observation indicated that the time required for a single streak to travel the distance of half the cavity span (76 mm) decreased with increasing Re, at constant viscosity. For example, it took 15 seconds to travel this distance at Re=620, but only 7 seconds at Re=820 (μ=95 mPa.s, P_h=207 kPa, Pc=10 kPa). Consequently, the frequencies of this motion were 67 and 140 mHz for the low and high Reynolds numbers, respectively. In a case where viscosity was reduced to 77 mPa sec, the characteristic period of time measured was 15 seconds at Re=655, and 10 seconds at Re=700. Thus, it seems that viscosity also affects this type of fluid motion and its acceleration.

The present evidence suggests that a small-amplitude flow disturbance superimposes a time-periodic motion on to the basic steady state of the system. Dynamic flow visualization experiments indicated that the movement of bright streaks inside the DSV resembles trajectories with a helical flow path. Such a path would be induced by the momentum of the disturbed flow which tends to drive the spanwise outflow, and the curvature of streamlines forces centripetal acceleration around the DSV.

The time-periodic flow observed in our experiments is similar to phenomena described in the literature. In the case of an enclosed lid-driven cavity, Koseff[77] observed a counter-clockwise spiralling motion inside the DSV. He attributed such fluid motions, and hence three-dimensionality, to the rigid endwalls and the finite span of the cavity. According to Freitas and Street,[84] this pressure-driven flow is generated and maintained by the interaction of the primary recirculation and the effect of the endwall viscous damping. Fluid elements from the center of the main recirculating flow next to the side endwall travel towards the vertical centerline and eventually flow radially outwards to complete a loop, therefore maintaining mass balance. This path is similar to the tracking of fluid particles as appearing in the numerical work by DeVahl Davis and Mallinson.[85] However, the exact mechanism

that causes destabilization of the basic primary state cannot yet be identified with any degree of certainty strictly from flow visualization.

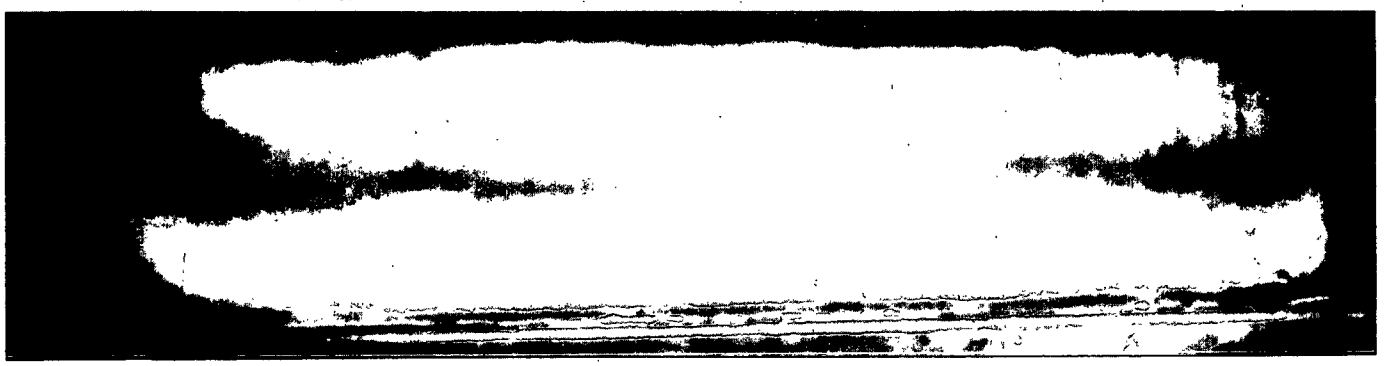

Figure 30. Onset of time-periodic flow inside the DSV (front end-view). Re=580, Re*=0.40, P_h=207 kPa, P_c=10 kPa.

Irregular Separation Line and Unsteady Flows

As the speed of the roll continues to rise and Re increases from 500 to about 1000, the separation line between the main and secondary recirculations becomes irregular featuring wavy patterns like the ones depicted in Fig. 31 and 32. Simultaneously, discrete vertical spikes appear inside the DSV and in the middle of the crest of a wave which have a darker color than the rest of the fluid. It is characteristic that waves start to slowly travel outwards, from the centerline towards both side endwalls of the cavity. Irregularity and the number of waves along the cavity span increases with the Reynolds number Re, as shown at the sequential snapshots in Fig. 31 and 32. At Re approximately in the range of 900 to 1100, traveling waves start a rapid movement which visually appears as an oscillation of wave crests along the span of the cavity (Fig. 33).

Spikes inside the DSV approach the side endwalls and seemingly bounce back, thus generating the perception of a complex spanwise oscillatory movement throughout the whole cavity. Characteristic frequencies of this time-periodic spanwise motion are given in Fig. 34 as a function of the Reynolds number. These were visually estimated from frames of videotapes. The reported numbers represent averages of twelve estimates from different experiments, while the total error is 10 percent. In general, frequency increases linearly with roll speed.

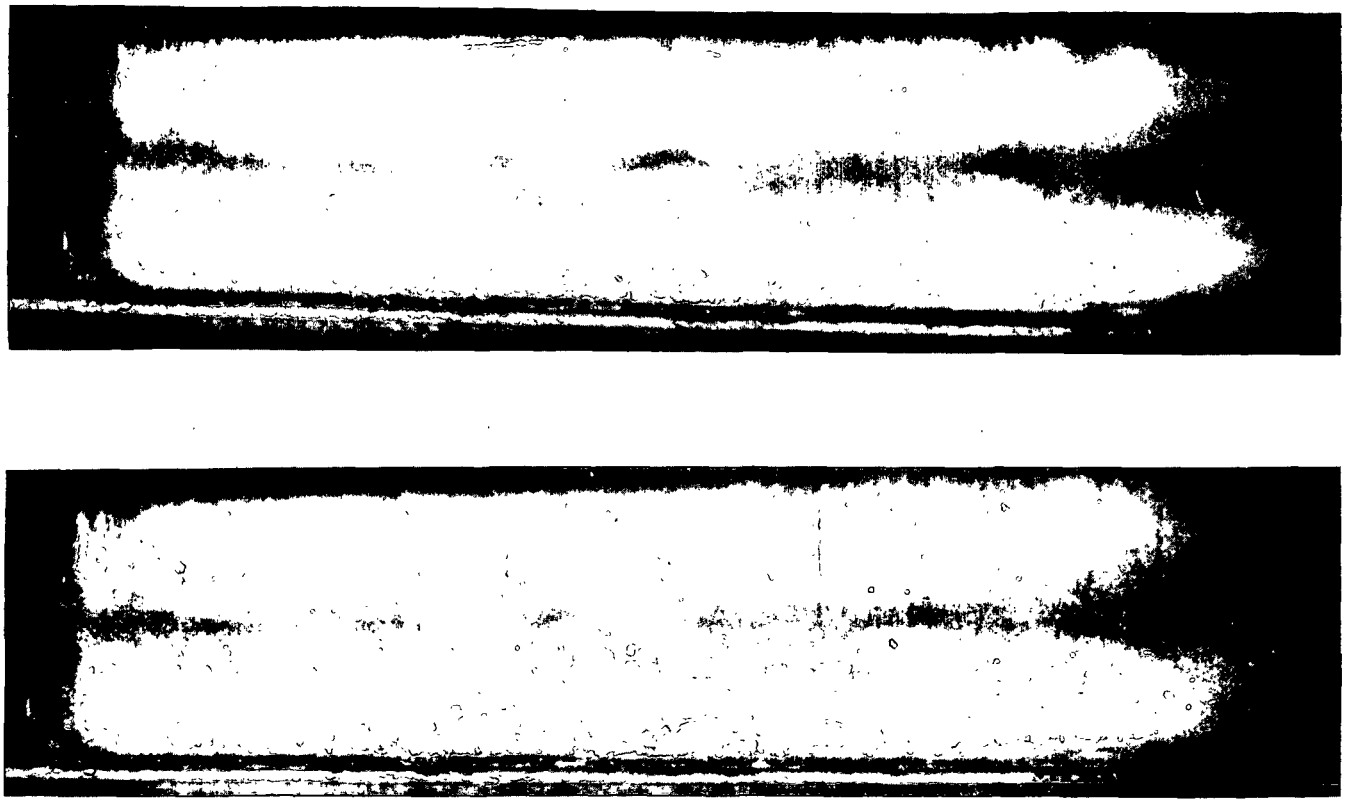

Figure 31. Sequential pair of photographs depicting evolution of waves from the centerline towards the side endwalls inside the DSV (front end-view). Re=650, Re*=0.40, P_h=207 kPa, P_c=10 kPa.

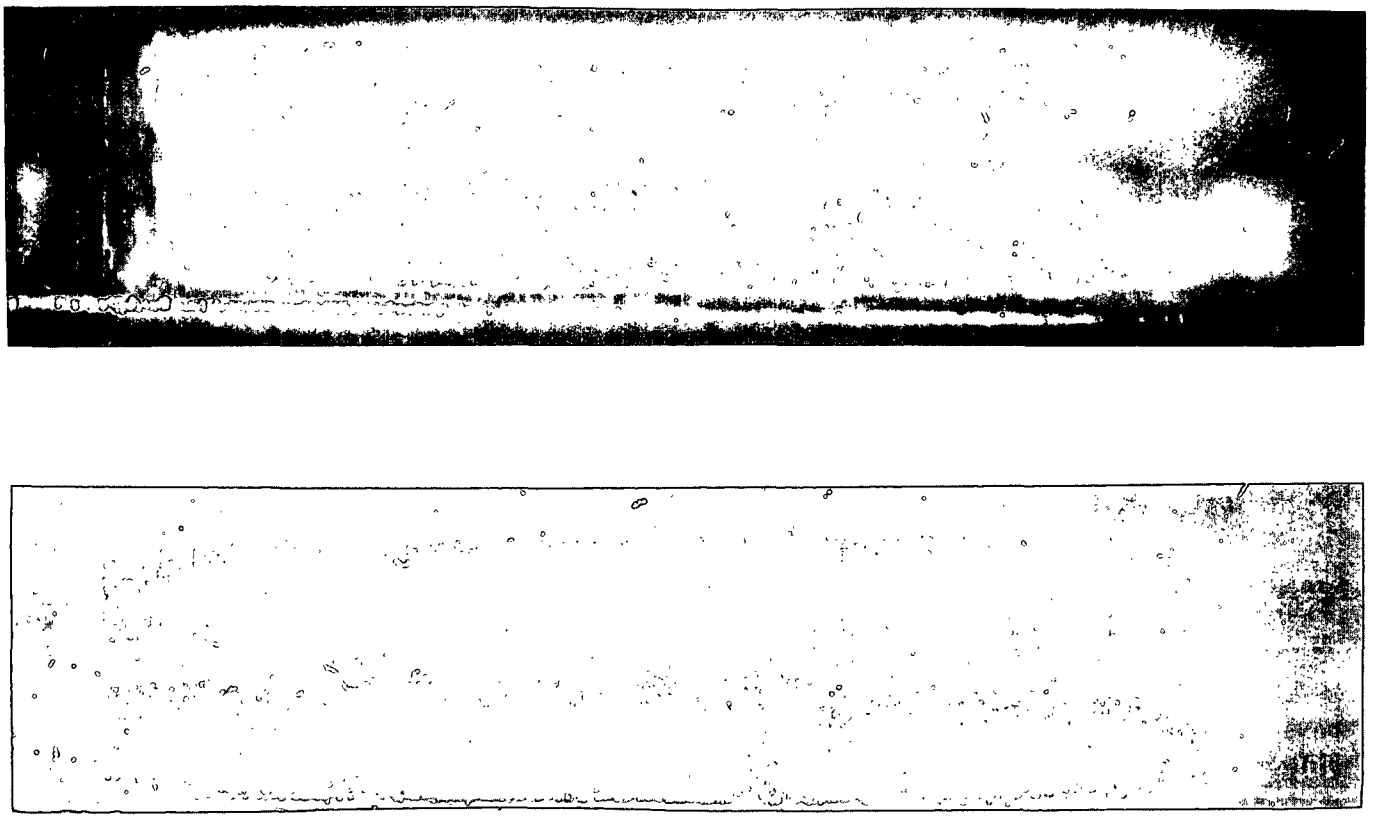

Figure 32. Sequential pair of photographs depicting evolution of waves from the centerline towards the side endwalls inside the DSV (front end-view). Re=700, Re*=0.40, P_h=207 kPa, P_c=10 kPa.

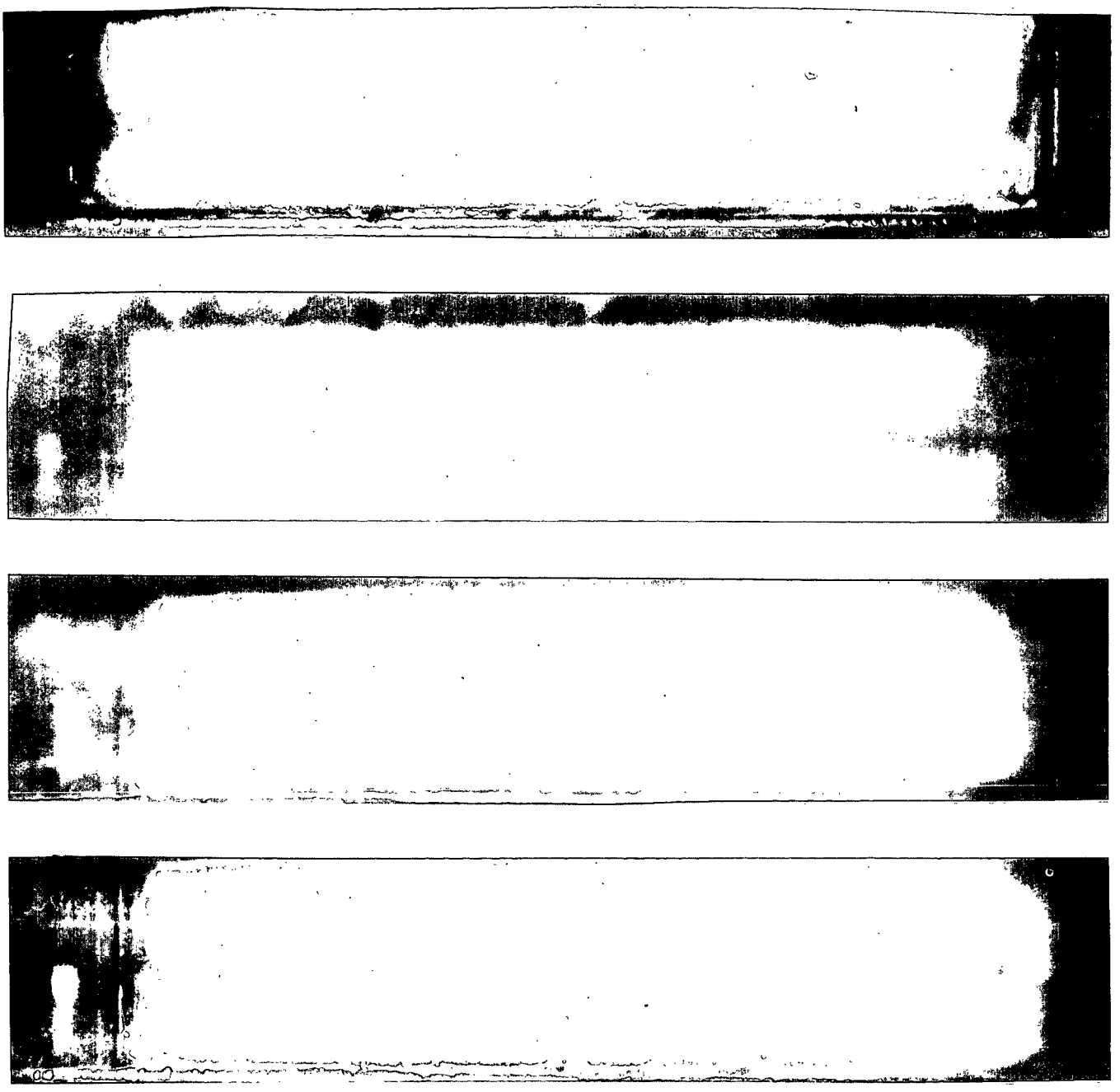

Figure 33. Sequential photographs depicting oscillation of waves along the cavity span inside the DSV (front end-view). Re=1000, Re*=0.57, P_h=207 kPa, P_c=10 kPa.

Upon continuous increase of the roll speed, the spikes grow small crowns at their tops which give them a mushroom-like form, like the one depicted in Fig. 35 for Re=1430. Originally mushrooms move about a stationary position keeping their points of contact with the bottom wall fixed. At this point, the structures in the DSV interact with the main recirculation by creating vertical ribs between mushrooms which extend in the full depth of the cavity. As the speed slowly increases, the flank and stem of the mushrooms first oscillate in-phase (Fig. 36) for Re=1620 and eventually fluctuate, causing the flanks to alternatively jump from left to right rapidly, thus giving the appearance that they are disappearing into their neighbors and reappearing a short while later. An example of such flows is illustrated in Fig. 37 with a series of photographs taken sequentially at Re of about 2500, each shot being approximately 3-4 seconds apart. The frequency of fluctuation of mushroom-like structures is linearly proportional to the Reynolds number in the range of 1100 to 1600, as depicted from visual estimates and illustrated in Fig. 38

As the speed increases to reach Re of several thousands, the qualitative picture of flow does not change, dominated by violent spanwise movement and higher frequency of mushrooms' appearance/disappearance in the vicinity of the DSV. Mushroom-like structures could be visually identified even at the maximum Reynolds number investigated, i.e., approximately 9000.

Movement of the wavy patterns is interpreted as a higher transitional mode of flow, while onset of the violent fluctuations is interpreted as an unsteady nonperiodic state. In general, mushrooms were nonuniform in size and had irregular spacing, and no stationary structures were recorded with the aluminum-flakes technique for Re greater than about 500. The size shrank slightly with raising roll speed (or Re) but their number did not change. Eight mushroom-like structures were counted across the cavity in the whole range of Re tested, thus giving a characteristic wavelength of λ=19.05 mm.

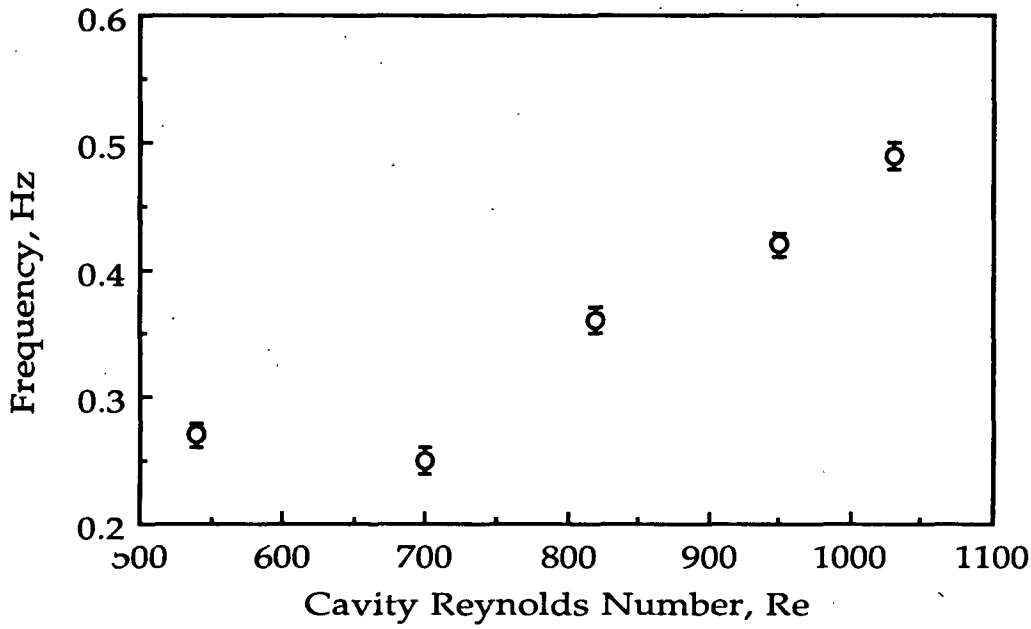

Figure 34. Frequency of spanwise movement as a function of the Reynolds number for the range of 500 to 1000. P_h=207 kPa, P_c=10 kPa.

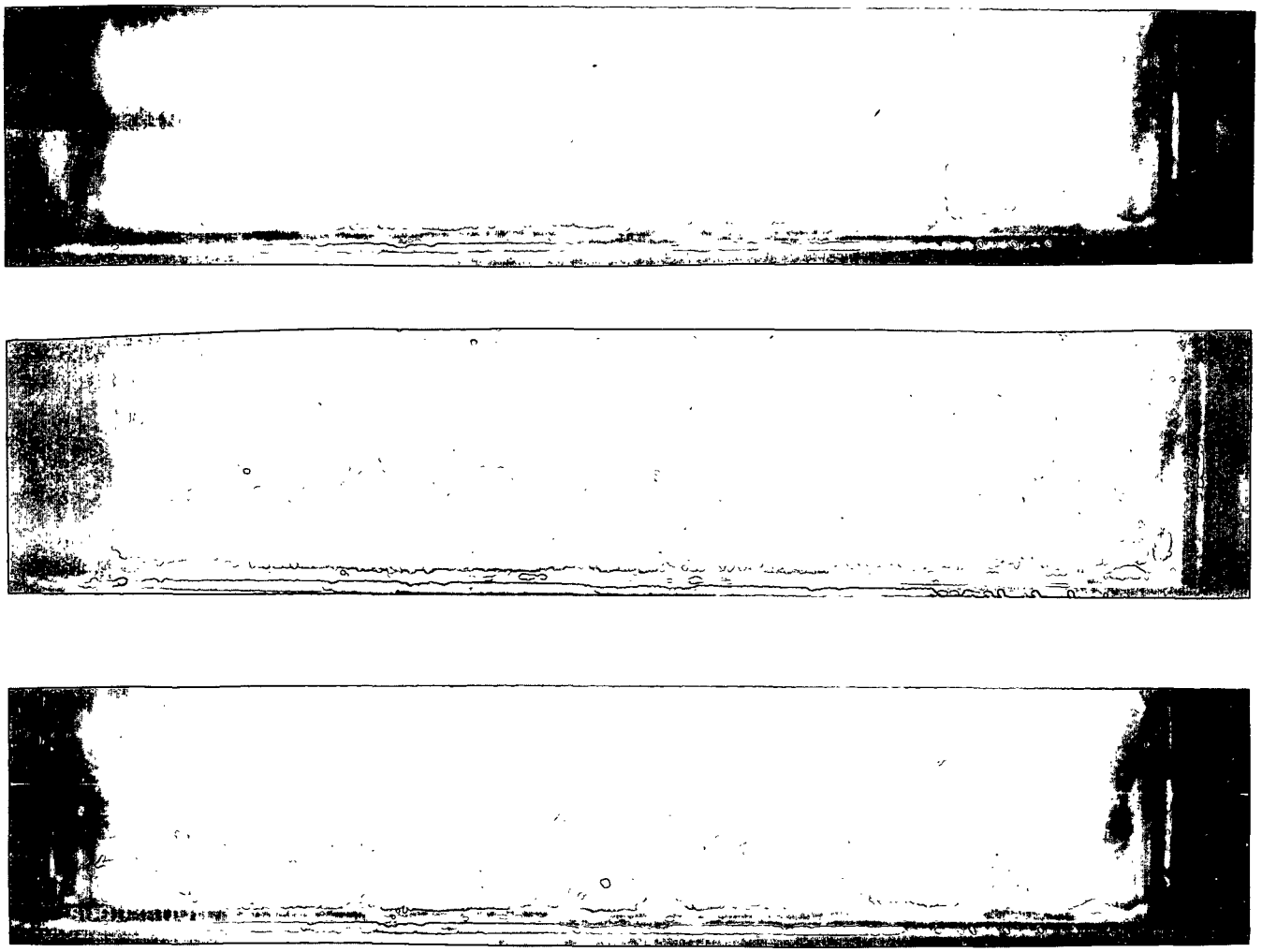

Figure 35. Sequential photographs illustrating growth of mushroom-like structure (front end-view). Re=1430, Re*=0.57, P_h=207 kPa, P_c=10 kPa.

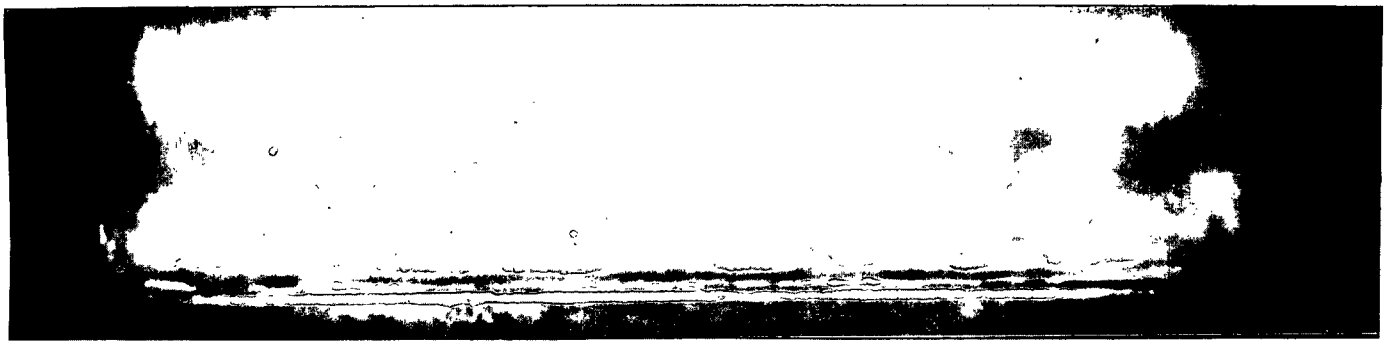

Figure 36. Photograph illustrating moving mushroom-like structures inside the DSV (front end-view). Re=1630, Re*=0.57, P_h=345 kPa, P_c=10 kPa.

Figure 37. Sequential photographs depicting violently fluctuating motion of mushroom-like structures inside the DSV (front end-view). Re= 2530, Re*=0.10, P_h=414 kPa, P_c=21 kPa.

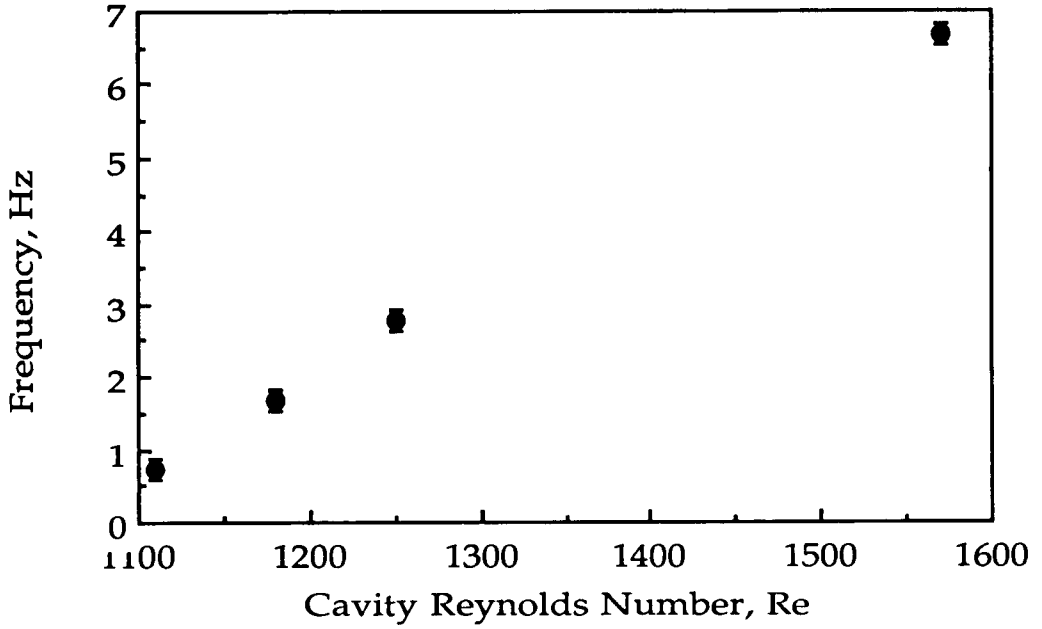

Figure 38. Frequency of spanwise movement as a function of the Reynolds number for the range of 1000 to 1600. P_h=207 kPa, P_c=10 kPa.

Multiple Stable States at Low Reynolds Numbers

A more intriguing feature of the flow in a lid-driven cavity with small through-flow is the appearance of large scale three-dimensional structures at low to moderate Re which compete with the basic state of flow. Our work indicates for the first time that the basic primary flow is not the only stable state, but it competes with several other secondary steady states with complex large-scale patterns where the recirculating main and downstream secondary rolls do not exist. Instead, the flow comprises three-dimensional structures which appear in the form of counter-rotating boxlike cells having axes parallel to the principle direction of flow. These cells represent comparatively weak recirculations of the secondary disturbed flow.

At least three alternative secondary states have been observed (Fig. 39) in cavities with SAR=3:1 which can be potentially reached through gradual deceleration of the flow. These states appear irrespectively of the cavity size (Fig. 40) and for Reynolds numbers in the range of 100 and 300; the lower value set by the limitation of the motor that drives the roll. Above 300, the flow structures oscillate along the span of the cavity and subsequently break up to form the three-dimensional structures of the unstable flow as described above for Re greater than 500. The number of cells observed varies between 2, 3, and 4 without any significance of flow history, although the state with four cells was the one most commonly encountered. In most cases the cell arrangement is symmetric with respect to the centerline of the cavity. Once established, three-dimensional structures remain stable over long periods of time (several hours) and upon variation of the cavity pressure, P_C. In other words, all alternative states of flow are stable to infinitesimal flow disturbances.

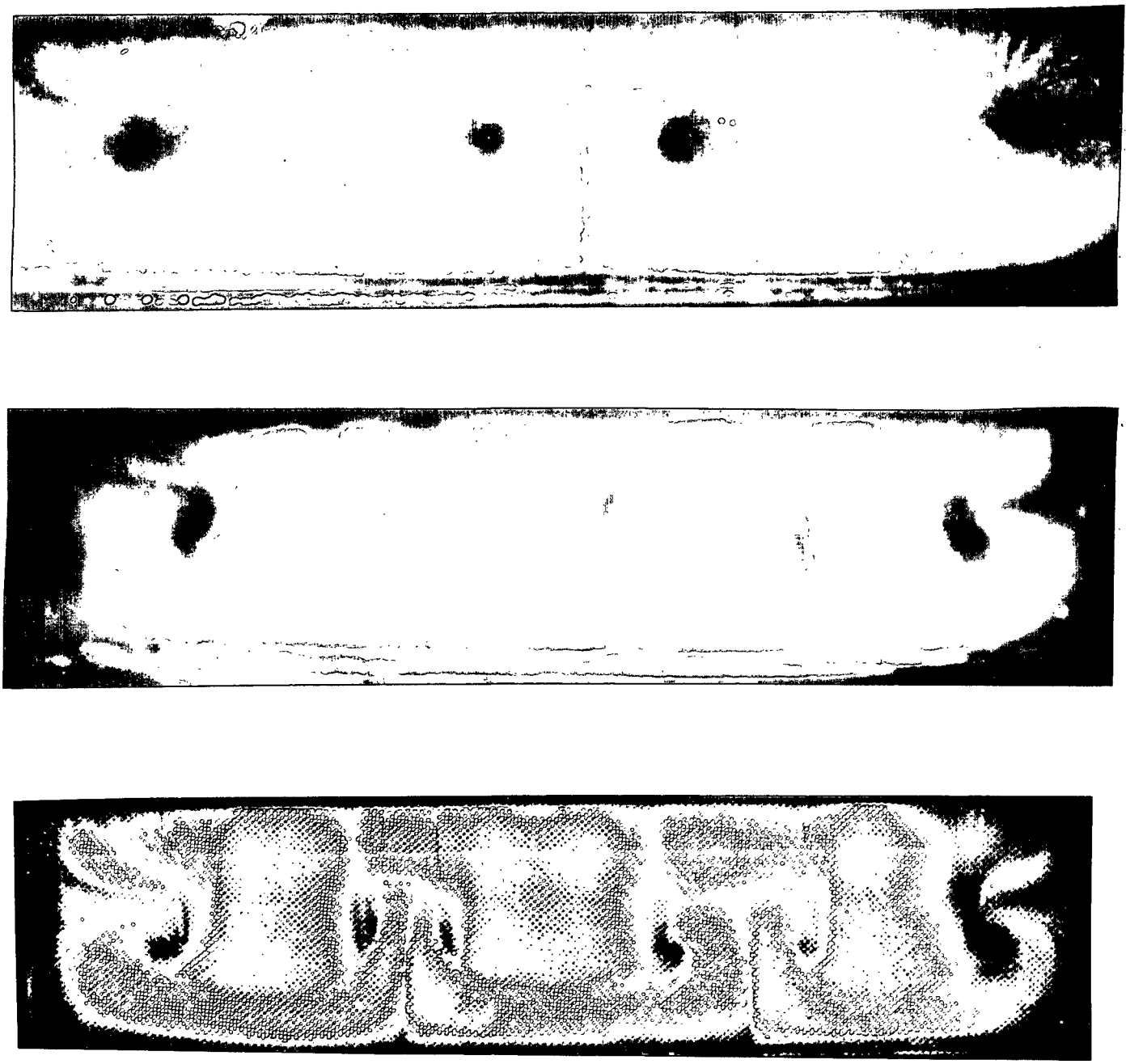

Figure 39. Various three-dimensional stable structures recorded upon gradual decrease of the roll speed. (a) Re=300, (b) and (c) Re=180-300. Re* was changed between 0.02 and 0.35.P_h=207 kPa, P_c=10 kPa.

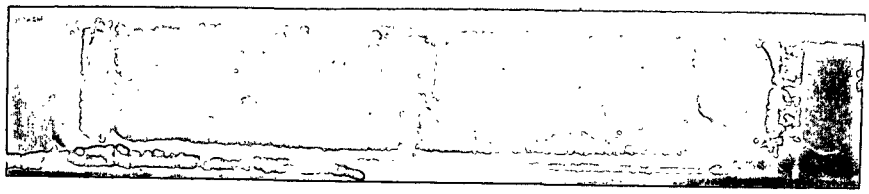

Figure 40. A three-dimensional stable structure recorded upon gradual decrease of the roll speed (small cavity). Re=145, Re* minimal, P_h=207 kPa, P_c=10 kPa.

Different spatial states were obtained by approaching the final Reynolds number from higher speeds. The possibility of attaining the basic primary state was equally probable with the appearance of three-dimensional flows. However, onset of the later flows required the separating interface between the main and downstream secondary vortices to be disturbed, i.e., become irregular before lowering the roll speed. This could be achieved, for example, by gradually reducing the speed of the roll starting at Re=1000 where the flow with three-dimensional structures was left to develop for a certain period of time, e.g., five minutes. A snapshot of the instantaneous (periodic) state of the irregular interface at Re=570 obtained during such a procedure is depicted in Fig. 41. Below Re of 300, the flow developed as illustrated in Fig. 39. The four large-scale cells were variable in size; e.g., the two in the middle having a width of 26 mm, while the ones close to the sides were 46 and 52 mm for the right and left edges of the flow, respectively. The cause of this asymmetry is not known, but it might have originated from a slight imbalance between the roll and the cavity. It is worth noting that repeating the same procedure after a while yielded the basic primary state of flow for any Re in the range of 170 to 300. Additionally, changing the pressure P_h did not influence the state of flow, whichever this may be from all the possible ones, in the range of 207 to 345 kPa (at constant roll speed). This suggests that once established each one of the multiple three-dimensional states of flow are stable.

Figure 41. Transient form of an irregular interface between the main recirculation and the DSV. Re=570, Re*=0.62, P_h=207 kPa, P_c=10 kPa.

Visualization with Direct Dye-Injection

These tests were based on injection of streams of the same fluid as the one inside the cavity but which contained a dye for easy visualization. Tracing streams were injected close to the centerline of the cavity along the vertical wall ECFN and a few millimeters below edge EC (see Fig. 22). Details of the remotely controlled injection system are included in Appendix A. This technique provided the opportunity to photograph three-dimensional structures of the flow which were not easily identifiable from planar pictures obtained with suspended-particles techniques. The interest of the work here concentrated in revealing the shape of structures appearing in the vicinity of the downstream secondary vortex at Re greater than 500, e.g., when the separation line has become irregular with a wavy pattern. However, because under these conditions the flow is time-dependent, results obtained with injection techniques should only be interpreted in conjunction with the observations presented above. Before presenting qualitative information at high Re, a photograph at lower Reynolds

number is included as a reference corresponding to the basic steady state of flow. All photographs show the front end-view of the large cavity or sections of it, hence the boundary in the bottom of pictures is the lower rigid wall of the cavity.

The photograph in Fig. 42 demonstrates the appearance of five dye streaks entrapped in the main circulation of the basic primary state of cavity flow (Re=305). The fluid was a 95% glycerol solution in water (μ=385 mPa.sec), hence the high viscosity delayed diffusion of the injected stream into the bulk fluid. Consequently, both hydraulic and inlet pressures had to be comparatively high to avoid air entrainment. Similar paths of injected streams were observed with lower viscosity fluids at lower pressures, but clear observation was hindered because the dye streaks mixed in the fluid fairly rapidly. Visual observation from a slightly oblique view to the front wall, indicated that the streaks do not enter the region in the vicinity of the downstream corner, the location of the secondary vortex. Because the flow is steady, the injected streams follow the curvilinear streamlines of the main cylindrical roll of the basic primary state of flow.

When the Reynolds number exceeds approximately 500, the flow becomes three-dimensional. A good example of three-dimensionality is the funnel-like structure resolved in Fig. 43 which forms a horseshoe-shaped vortex at its lower end. This vortex appears about 1 cm away from the centerline of the cavity and a few millimeters above the lower boundary. Its existence indirectly suggests that there is a mechanism which allows for transporting fluid from the main recirculation into the downstream secondary. It is not a necessary requirement for this mechanism to always be present, but it is sufficient to exist at some point in time between injection and photographing (e.g., about 3-4 seconds). The fluid which enters the DSV forms the horseshoe-type structure, even before coming in contact with the lower boundary. This and the repeatability with which this structure could be obtained, minimize the possibility that its appearance is an artifact arising from the shear layer formed next to the downstream wall by the injected stream. In addition, similar structures were recorded by Kossef[77] in an enclosed lid-driven cavity flow using a different technique, but for Re above 2000. Because the flow at Re=580 is time-dependent, however, not all injections provide the same results. In contrast to the above, the stream on the right of the photograph in Fig. 43 shows essentially a streakline similar to the case of the primary state of flow. A possible explanation for this is that, during its lifetime, the stream injected from that point did not encounter any transport processes which could transfer it into the secondary vortex. In general, unless the injected stream finds itself in the right time at the right location, it would never enter the DSV to form the characteristic three-dimensional structure. The state of flow therefore could erroneously misinterpreted as that of the basic primary state. However, in accordance to previous observations with the suspended-particles technique, at Re greater

than about 500 streaks are time-periodic and waves appear on the separation line in the spanwise direction.

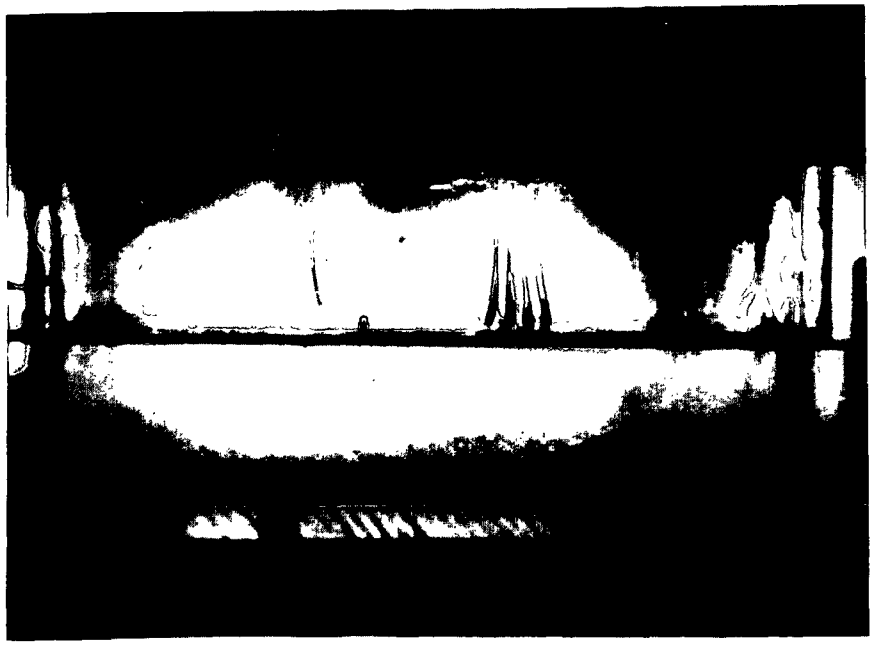

Figure 42. Front end-view of the cavity showing injected streams in basic primary state of flow. Re=305, Re*=0.08, P_h=482 kPa, P_c=138 kPa.

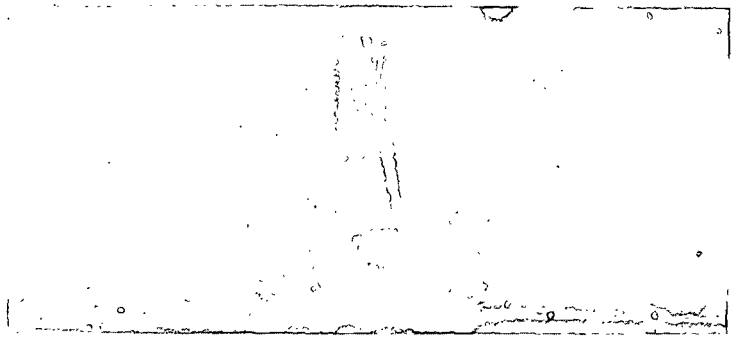

Figure 43. Funnel-like structure with a horseshoe-shaped vortex at its end. Re=580, Re*=0.10, P_h=207 kPa, P_c=10 kPa.

Visualization with Flash X-ray Radiography

Information about the form of three-dimensional structures can also be obtained with the flash x-ray radiographic technique. Initially the technique was applied to the flow of glycerol solutions, since the behavior of this fluid has already been documented. Then the technique was used to obtain stop-motion images through opaque coating suspensions, like the ones in practice. The goal is to show that similar flow structures occur irrespective of the type of fluid. The tracer stream, described previously in the section on experimental techniques, is injected along the streamlines of the main recirculation next to the downstream wall. When it enters the region of the downstream secondary vortex, i.e., at high Re, it tends to take the shape of characteristic three-dimensional flow structures. These structures appear darker than the background in radiographs (shadowgraphs) because the tracer absorbs more x-rays than the any other fluid.

Figures 44 and 45 present funnel-like structures from selected radiographs obtained through glycerol at Re=580 (front end-view only). The position of injection is exactly the same as the one depicted on the left of Fig. 43. The tracer is a diluted (about 2% CMC by weight) x-ray absorbant like the one described in an earlier section. Interesting is the photograph in Fig. 45 because it illustrates the concept of how a horseshoe-type vortex at the lower end of a funnel rides onto a pair of Görtler vortices. The two oval-shaped structures shown are conjectured to represent cross sections of neighboring Görtler vortices, hence flow in between the two vortices moves away from the lower boundary. This radiograph was taken at a later stage of a funnel-like structure development, as can be seen from the different injection times between Fig. 44 and 45. When the roll speed increases, new shapes appear like the unsteady mushroom structure captured in Fig. 46 for Re=1280. The injected stream actually entered the DSV from a point at the left of the picture but the formed structure moved onto the right, indicating spanwise movement inside the secondary vortex. This structure is similar to the mushroom-like structures observed with the particle-laden fluid (Fig. 35 and 36).

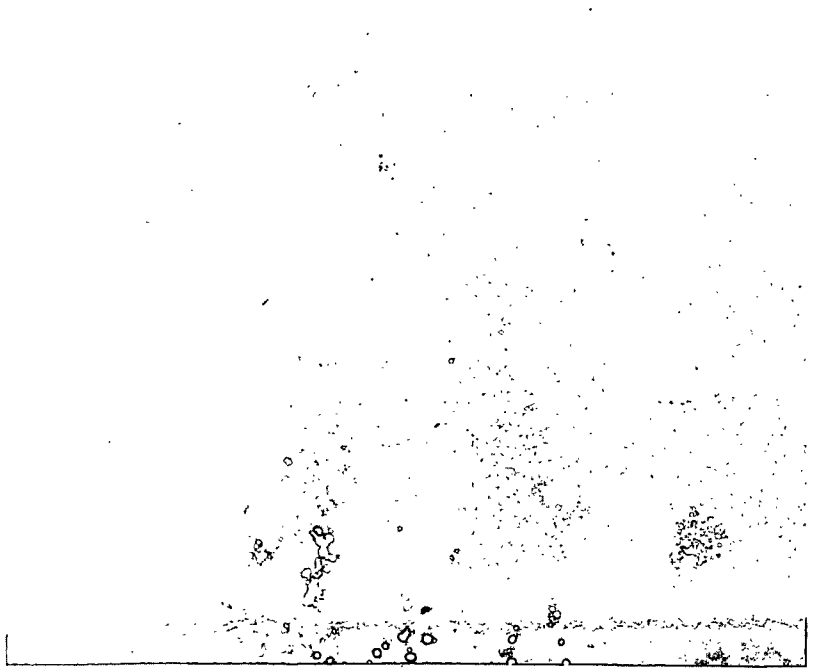

Figure 44. Funnel-like structures in a flash x-ray radiograph.Fluid: glycerol/water. Re=580, Re*=0.11, P_h=207 kPa, P_c=35 kPa, FTSD=105 cm, injection time = 3-4 sec, injection pressure = 103 kPa.

Figure 45. A horseshoe-shaped vortex obtained with FXR at the lower end of a funnel. The vortex is riding on a pair of Görtler-like vortices. Re=580, Re*=0.11, P_h=207 kPa, P_c=35 kPa, FTSD=105 cm, injection time = 6 sec, injection pressure = 103 kPa.

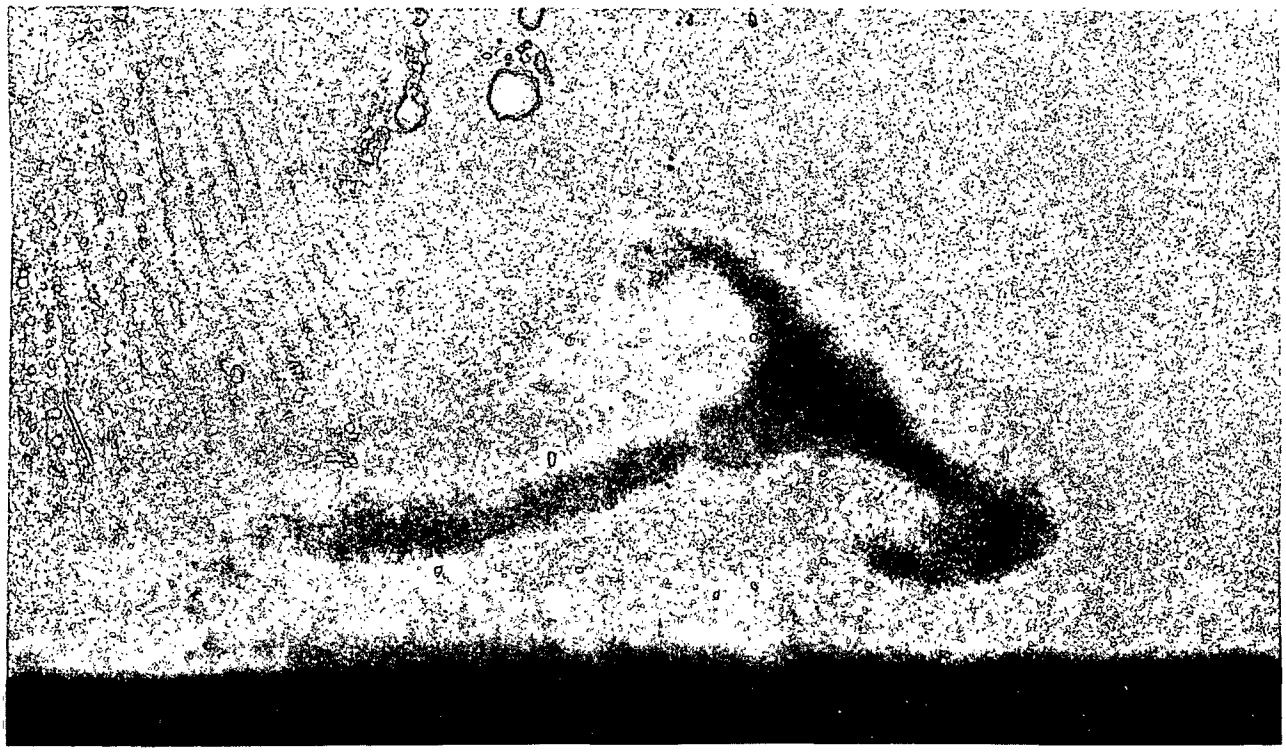

Figure 46. A FXR image of a mushroom-like structure appearing inside the DSV. (Picture magnified to show details.) Re=1280, Re*=0.54, P_h=207 kPa, P_c=138 kPa, FTSD=150 cm, injection time =3 sec, injection pressure=104 kPa.

Application of the flash x-ray radiographic technique to study the flow of coating colors is demonstrated in Fig. 47 and 48. The background (bulk) fluid was basically a clay mineral suspension (61% by weight) and the tracer a CMC solution saturated with sodium tungstate, both of them having properties like the ones presented in Fig. 70 (Appendix B). Figure 47 presents the shadowgraph of a funnel-like structure at Re=450, while Fig. 48 illustrates the lower end of such a vortex (at Re=465) at a later stage of its development, hence a horseshoe-shaped vortex is riding on two Görtler vortices. Also, the sense of rotation of the spiral-like cross sections of the two Görtler vortices indicates these flow structures translate toward the downstream vertical wall. These pictures of flow patterns are similar to the ones obtained with the transparent Newtonian fluid above, therefore suggesting that the three-dimensional flow structures exist independently of the type of fluid. In other words, characteristic features of the flow in a lid-driven cavity with through-flow remain the same even in the case of suspensions with a relatively high solids content, such as coating colors. However, a note of caution is worth mentioning here. Because coating colors are non-Newtonian fluids, i.e., their shear viscosity is both time- and shear-dependent, it is not easy to determine with confidence their viscosity in complex flow fields, like the one considered in this study. The value of flow parameters therefore, such as the Reynolds number, Re, can only be approximated based on a single-point viscometric measurement. This may explain differences in the critical values of Re for observation of three-dimensional flows between glycerol and coating colors, as these will be presented later.

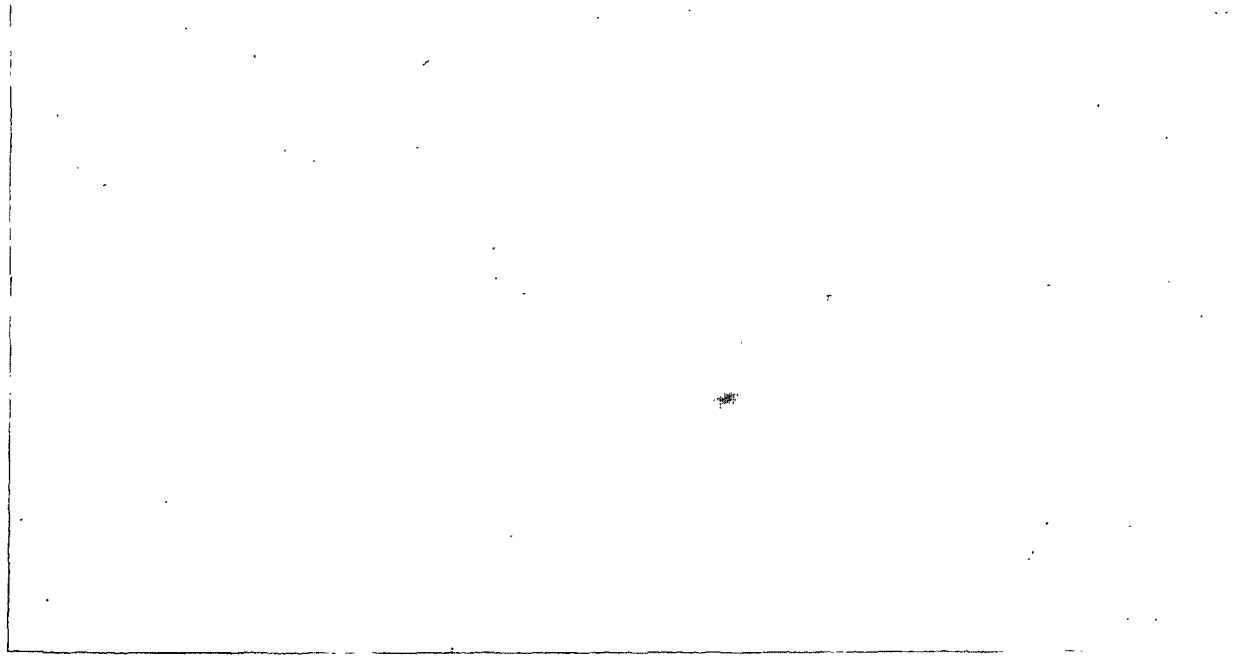

Figure 47. A FXR image of a horseshoe-shaped vortex through an opaque coating color.(Picture magnified to show details.) Formulation: LWC for rotogravure, 62% solids content. Re_a=450, Re^*=0.54, P_h=345 kPa, P_c=138 kPa, FTSD=150 cm,injection time = 4 sec, injection pressure = 275 kPa.

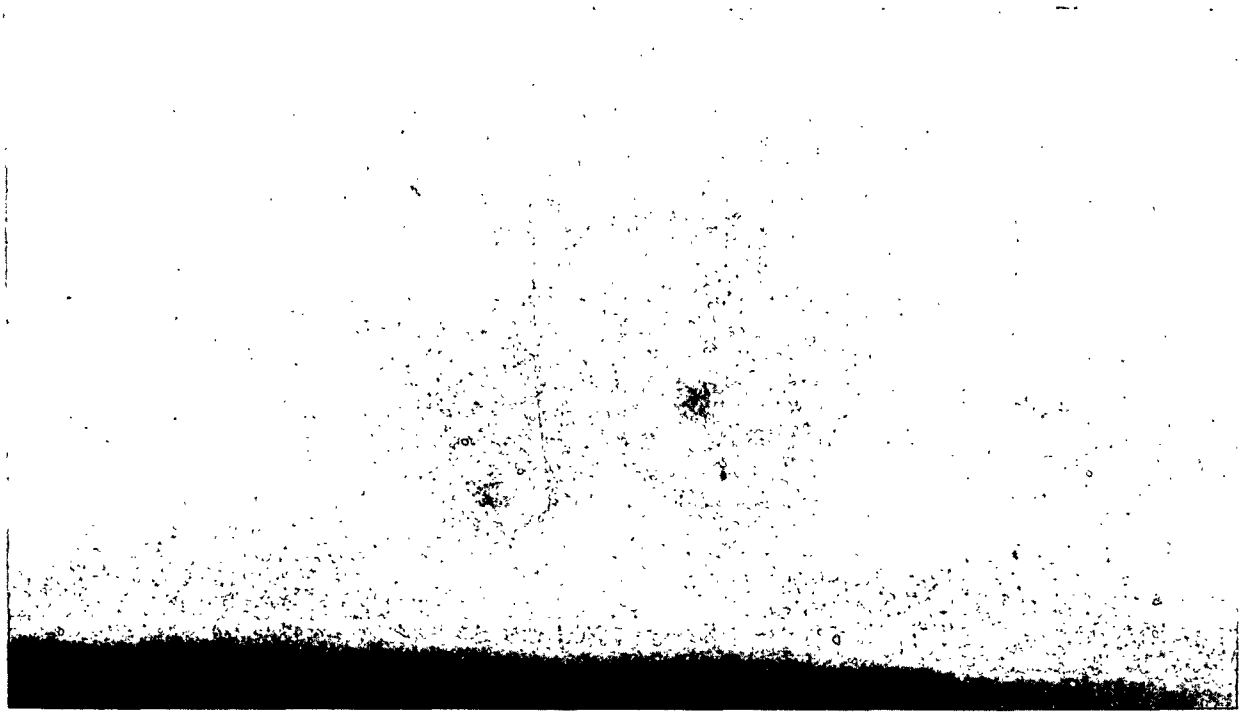

Figure 48. A FXR image of a horseshoe-shaped vortex riding on to a pair of Görtler-like vortices. (Picture magnified to show details.) Formulation: LWC for rotogravure, 62% solids content. Re_a=450, Re*=0.54, P_h=345 kPa, P_c=138 kPa, FTSD=150 cm, injection time = 5 sec, injection pressure = 275 kPa.

IMPORTANT INFLUENCES ON THE FLOW

Endwall (Edge) Effects

Edge effects from solid walls parallel to the principle direction of flow influence the flow in their close proximity. This was documented with (a) the increase in size of the downstream secondary vortex, and (b) the existence of corner vortices rotating with axes parallel to the principle direction of flow. The second, which is a comparatively weak secondary flow, provides evidence of how these walls can affect the flow in the cavity and induce three-dimensionality. The following is a brief description of how these phenomena may come in to existence.

As pointed out by Koseff and Street,[77-78] and Freitas and Street,[84] one of the reasons that lid-driven cavity flows are three-dimensional is the existence of endwalls. Pao[123] has also determined that, in confined flows like the one in a rectangular cavity, boundary layers developing on the walls induce motions perpendicular to these walls. Relevant is the work by de Brederoede and Bradsaw,[124] who studied with experiments the three-dimensional flow over a rearward-facing step, a flow similar to the one encountered here because it is bounded by endwalls and characterized by separation. These authors discovered recirculating cells (with axes of rotation parallel to the principle direction of flow) in the vicinity of the endwalls and next to the step which they named corner vortices. They offered the explanation that these originate from the adjustment of the shear and pressure forces acting on the recirculating fluid to the no-slip condition imposed by the side endwalls, or edges of the flow field. Koseff[77] used the same concept to explain observation of corner vortices in enclosed cavities, hence he attributed spanwise variation of flow to the complex interaction of spanwise pressure gradient, radial pressure gradient (from the primary recirculation), centrifugal force and the no-slip velocity boundary condition. Furthermore, he suggested that the DSV near an endwall turns downstream in its entirety and enters the corner vortex, so that the spanwise spiralling motion observed inside the DSV is actually driven by a corner vortex. The hypothesis put forward is that corner vortices, in combination with endwall viscous damping, initiate the Taylor-Görtler-type vortices which will be discussed later.

Similar phenomena, but with some differences, were observed in the lid-driven cavities with through-flow considered in the present visualization experiments. The apparent increase of the DSV size next to endwalls (Fig. 28) is an example of how shear stresses from

viscous damping next to the wall can alter the flow. In fact, the shape of the separation line in the vicinity of endwalls could be illustrating the velocity profile, i.e., shear gradient, of the viscous boundary layer in that region. The shear velocity of the fluid, being zero at a rigid wall in accordance to the no-slip condition, progressively increases with the distance from the wall to attain a maximum (constant) velocity which is proportional to roll speed. The shape of the separation line is linear, as expected for the velocity profile of a Newtonian fluid in a shear or boundary layer. Thus the distance from an endwall over which the slope of the separation line increases may be interpreted to represent the thickness of the viscous boundary layer (or boundary-layer-type velocity profile) on that wall. For cavities with spanwise ratio of 3:1, stress-induced viscous effects are confined in regions next to endwalls which represent less than 10% of the cavity span. Interestingly, the ratio of the apparent boundary-layer thickness to the cavity span increases with larger cavities.

Another phenomenon recorded in the visualization experiments is the appearance of corner vortices which were the first indication of three-dimensionality of the flow. These were recorded in both corners next to the two (side) edges of the cavity when this was properly illuminated with a sheet of laser light from the side. Based on the discussion presented earlier, these vortices are initiated from the adjustment of the recirculating fluid forces to the no-slip condition on the wall, and the complex interaction of pressure and centrifugal forces. Thus it is the viscous damping of the primary recirculation next to the side endwalls which is responsible for generating the corner vortices.[84] The observed vortices here were qualitatively different from the ones reported by Koseff[77] in that they were boxlike cells, occupying the whole depth of the cavity at Re from 120 to 350, and therefore have a more global character. In contrast, the ones observed by Koseff were smaller, confined to the size of the DSV for Re=5700. However, it should be noted that all of his flow experiments were impulsively started at comparatively high Reynolds numbers, i.e., exceeding 2000.

The sense of rotation of the corner vortices indirectly implies a spanwise outflow, like the spiralling motion of bright streaks. In other words, as also suggested by Koseff and Street,[78] the corner vortices eventually induce spanwise movement in the flow by driving fluid from the centerline toward the side endwalls. A detailed explanation of the progressive development of spiral motion is included in the work by Freitas and Street,[84] where the spanwise flow was attributed to forces arising from the endwall boundary layer, the corner vortex, and pressure gradients. However, no corner vortices were observed in the present experiments for Re above 350, while the spiralling motion was documented only for Re greater than 500. Insufficient experimental evidence is therefore available to speculate on the effect corner vortices might have on the flow for moderate Re (i.e., from approximately 100 to 1000).

Qualitative Changes of Flow Structures

This section illustrates how, besides the roll speed and fluid viscosity, operational parameters of the cavity with through-flow affect the flow. Essentially these effects are qualitative in the sense that major features of the flow are preserved, with changes occurring only in the size of the large scale cellular structures.

Size of the Downstream Secondary Vortex

The size of the DSV at the vertical centerline, as observed with the aluminum-flake technique in a cavity with through-flow, is a function of the hydraulic pressure P_h. The vortex size H* grows linearly with hydraulic pressure P_h (Fig. 49) for constant speed of the roll and feeding pressure Pc. (The latter two parameters were maintained constant by adjusting the motor output, that drives the roll, and valve no. 1 in Fig. 21.) Progressive change of the value of P_h from 207 to 480 kPa at constant Re (equal to about 330) causes the ratio H*/H to grow by 25 percent, reaching a maximum value equal to 0.375. Maximum size of the DSV is obtained when, for all practical purposes, the cavity is enclosed. This is illustrated in Fig. 49, hence the through-flow Reynolds number Re* remains constant up to P_h=414 kPa, but thereafter drops by an order of magnitude. These results suggest that changes in hydraulic pressure rather than through-flow rate affect the size of the DSV. On the other hand, altering pressure Pc from 8 to 30 kPa does not induce any measurable variation in size.

The dependence of H* on P_h does not underestimate the results shown in Fig. 28, where the DSV size is plotted as a function of Re. Although generally the trend in the present data is similar to the one observed in previous works, variations maybe attributed to through-flow. It is characteristic that when the hydraulic pressure is high, i.e., corresponding to operating the cavity like an enclosed unit, the DSV size attains higher values. The DSV size increases with Re until a maximum value is attained, the size remaining constant thereafter. Under all experimental conditions investigated, the ratio H*/H levelled off at the value of 0.375.

Size of Corner Vortices

The size of corner vortices decreases with increasing roll speed. The referenced size is the distance of the separation point (on the lower boundary) of a recirculating vortex from the

side endwall. This distance is divided by the span of the cavity and plotted in Fig. 50 as a function of the Reynolds number Re. The size of the DSV progressively increases as the roll speed, and therefore Re, gradually decreases. A possible explanation for this behavior may be that the size of the rotating cell next to the wall increases to compensate for the lower angular velocity, occuring at low speeds, so that the system can conserve angular momentum. Thus edge effects are a function of Re in the range of 100 to 500. Above Re equal to about 500, the flow becomes three-dimensional and the weak corner recirculation ceases to exist.

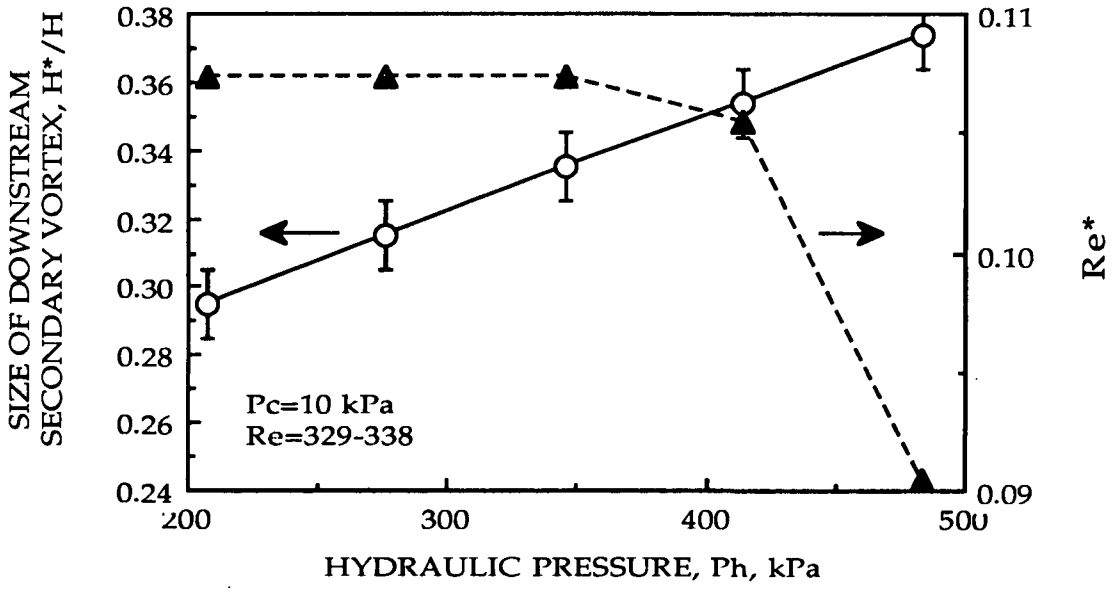

Figure 49. The effect of hydraulic pressure on the basic primary state of flow. P_C=10 kPa, Re=329-338.

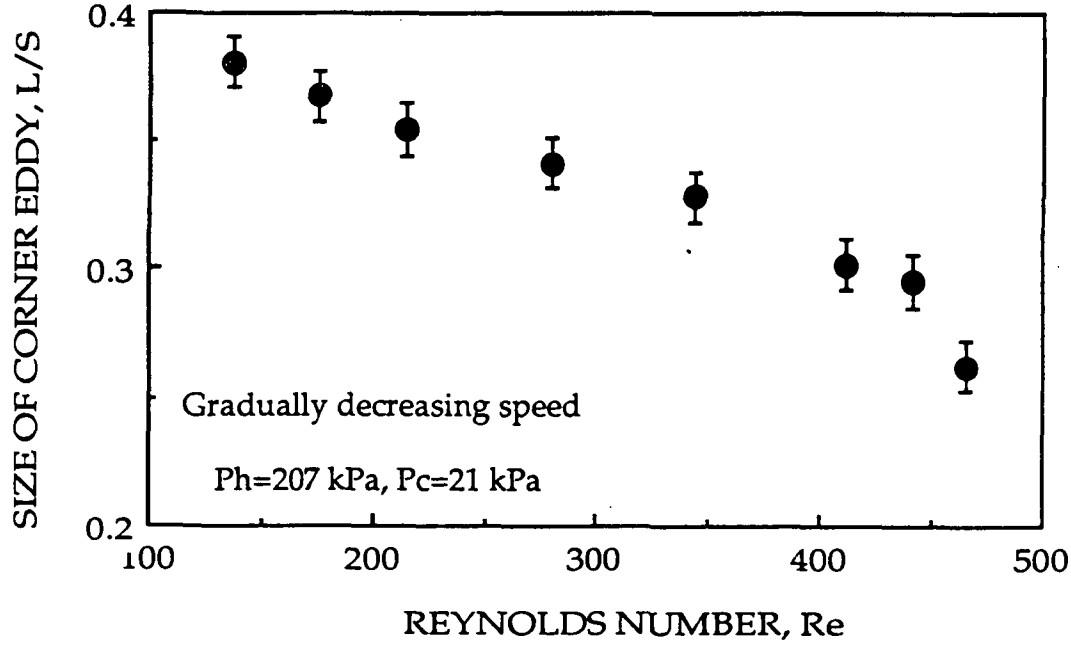

Figure 50. The effect of roll speed on the size of a corner vortex. Gradually decreasing speed. μ=145 mPa.s, P_h=207 kPa, P_c=21 kPa.

THE CONTROL PARAMETER AND ITS CRITICAL RANGES

Repeated and randomized visual observations indicated that qualitative reorganization of the flow in a lid-driven cavity with through-flow depends on the cavity Reynolds number Re. This is important when considering the transitions from steady to time-periodic, and the evolution of flow structures preceding the establishment of unsteady states. Results from aluminum-flake visualization are presented in tabular form (Tables 8 and 9) to illustrate that, irrespective of other factors, the control parameter of the flow is Re. Quantitative data corresponds to square cavities with spanwise aspect ratio 3:1. Table 6 points out selected cases where the spiralling motion, hence three-dimensionality, inside the DSV was observed for the first time. Independently of fluid viscosity, inlet type, hydraulic and feeding pressures, the downstream secondary vortex destabilizes in the range of Re from 470 to 620. A trend also implies that greater Re* values raise the critical Re. However, observations in a wider range of through-flow Reynolds numbers are required to better assess the effect of this dimensionless number on the flow.Table 7 presents representative data which illustrates that (a) onset of violent spanwise fluctuations occurs for $930<Re<1040$, and (b) unsteady mushroom-like structures appear for Re greater than 1100. It is noteworthy that unstable flows and their corresponding structures appear when the Reynolds number Re exceeds a certain critical range, no matter how the final Re was attained, i.e., gradual increase or decrease of roll speed, or sudden start up of the roll. (Although the roll can be put into motion suddenly, it takes a while for the flow in the cavity to reach its maximum speed.) Table 8 presents a review of the rough estimate of the critical ranges and corresponding observations from flow visualization experiments using square cavities with a SAR of 3:1.

It should be pointed out that the critical phenomena observed are dependent on the cavity span-to-width aspect radio (SAR) and the Reynolds number of the flow. Because three-dimensionality arises from edge effects, cavities with larger SAR would be expected to illustrate changes on the global picture of flow at higher Re. The values of Re presented here correspond to the specific cavities used in flow visualization experiments. Uncertainty analysis (in previous section) indicated that the value of fluid shear viscosity has the most influence. Therefore Re values are dependent on the measurement of viscosity , more specifically the accuracy of determining the absolute viscosity of the fluid. In general, absolute viscosity is difficult to measure accurately due to fluid temperature variations and dependency on the geometry of the instrument. Measurements taken for this work were done in a calibrated spindle-type instrument (i.e., a Brookfield viscometer), as discussed previously.

In addition to the accuracy of viscosity determination, the estimated critical Reynolds numbers depend on the sensitivity of the detection method. Flow visualization experiments relied on the unaided eye to detect the onset of unstable flows and the form of evolving flow structures. As the roll speed was changed in the experiments, the gradual transition from two- to three-dimensional flow, as well as the evolution of transitional flows, were observed. The origin of the uncertainty in determining the critical values of the control parameter lies in the subjective nature of the discrimination between one state of flow and another. However, because in general the amplitude of the disturbed flows is initially small, visual observation overestimates the critical value of Re for onset of flow instabilities or transition to the different modes of flow. Flow disturbances may exist before (their visually estimated) appearance of their influence on the state of flow.The maximum experimental error in determining Re is ±40, while the uncertainty in estimating a critical Re with the naked eye is about 20 percent. Therefore the accumulative error is about 30 percent.

Table 6. Visually estimated onset of time-periodic cavity flow (DAR=1:1, SAR=3:1).[a]

Viscosity (mPa.sec)	Cavity Size	Type of Inlet Opening	P_h (kPa)	Pc (kPa)	Re	Re*
385	Large	Perforated	482	83/193	470-505	0.02-0.08
160	Large	Perforated	345	14	520	--
140	Large	Perforated	276	138	500	--
95	Large	Perforated	207	10	530	--
85	Large	Perforated	207	10	530-590	0.57
77	Large	Perforated	207	8	510	0.10
95	Large	Slot	207	10	620	0.97
80	Large	Slot	207	10	520	0.10
77	Large	Slot	482	8	515	0.06
140	Small	Perforated	207	10	530	0.14
95	Small	Perforated	207	10	530	0.01

[a] Viscosity is being overestimated by 40-60% due to bias error in measurements.

Table 7. Visually estimated instability modes of the lid-driven cavity flow with small through-flow (DAR=1:1, SAR=3:1). Viscosity overestimated by 50-60%.

Viscosity (mPa.sec)	Cavity Size	Type of Inlet Opening	P_h (kPa)	Pc (kPa)	Re	Re*
		Spanwise fluctuation of flow				
160	Large	Perforated	345	55	1030	–
140	Large	Perforated	276	138	990-1015	–
80	Large	Slot	207	10	940	–
85	Large (IPST)	Slot	207	10	1030	–
95	Large	Slot	207	10	1020	0.97
95	Large	Perforated	207	10	940	–
95	Small	Perforated	207	10	930-960	–
85	Small	Perforated	207	10	1040	0.01
77	Large	Perforated	207	10	930	–
		First appearance of unsteady mushroom-like structures				
80	Large	Perforated	207	10	1140	–
77	Large	Perforated	207	10	1100	–

Table 8. Estimated critical Reynolds number ranges from flow visualization experiments (Lid-driven cavity with small through-flow, Re*<2.0, DAR=1:1, SAR=3:1). Numbers underestimated by about 60% due to bias in viscosity measurements.

Re (±30% uncertainty)	Observations
Above 500	A time-periodic, three-dimensional instability is superimposed on the DSV of the basic primary state.
600-700	Separation line between the primary (main) recirculation and the DSV becomes wavy; waves travel in spanwise direction starting from the centerline.
900-1000	Violent spanwise oscillation of waves.
1100 and up	Unsteady mushroom-like structures fluctuate violently inside the DSV. Whole flow regime becomes unstable.

INTERPRETATION OF RESULTS AND DISCUSSION

Although only limited information can be obtained through flow visualization experiments, results from this investigation shed some light on large-scale spanwise structures occurring in lid-driven cavity flows, the cavities having finite dimensions and small through-flow. In particular, there is for the first time evidence of the stability properties of this type of confined recirculating flows as the cavity Reynolds number progressively changes. The dominant phenomena that govern this flow are (a) three-dimensional recirculating structures, which affect the global state of flow at low Reynolds numbers, (b) Taylor-Görtler-type vortices which appear locally in the DSV as the velocity of flow increases and Re is above a critical range, and (c) corner vortices which form locally next to side endwalls.

The basic stable two-dimensional flow is characterized by two counter-rotating recirculating rolls - the primary and secondary - which expand throughout the full span of the cavity. This describes the steady primary state of the system. At a cavity Reynolds number Re greater than about 500, the interface between the two rolls becomes unstable, featuring a wavy pattern and spikes which appear to designate onset of periodic flow. Because the main roll seems to be unaffected by this motion, the time-periodic state can be described as having small oscillation amplitude. The perturbation which causes this flow is probably originating from the viscous damping next to the side endwalls. Although not rigorously proven yet, transition from the stable to the periodic state is most likely to be through a Hopf bifurcation.[125] At Re values greater than 1100, the flow features mushroom-like structures which are conjectured to represent cross-sections of a pair of Taylor-Görtler-type vortices appearing inside the DSV. Such structures were observed with both a Newtonian fluid and a coating color. As the flow develops a violent complex behavior at even higher values of Re, it demonstrates similarities with higher order transitional flows. The next few paragraphs attempt to compare structures observed in the present experiments with recorded flow structures appearing in the literature. In addition, there is discussion on interpretation of the observed phenomena.

The qualitative results presented above demonstrate that the flow in a lid-driven rectangular cavity with small through-flow is susceptible to three-dimensional centrifugal instabilities as the Reynolds number Re increases. These instabilities arise from imbalances induced by competing centrifugal forces (due to curvilinear streamlines of recirculating rolls) and the pressure gradient, created in a manner similar to the Taylor vortices appearing in

Couette flow,[81] and the Görtler vortices appearing in boundary layer flows over concave walls.[82] Interestingly, the sequence of evolving structures described above is reminiscent of the instability of a laminar boundary layer flowing over a concave wall.[126-130]

The visualized flow structures describing transitional and unstable modes of flow as the cavity Reynolds number progressively increases are reminiscent of flow patterns found in transitional and turbulent boundary layers near walls. Such viscous layers develop streamwise counter-rotating vortices which have axes parallel to the principle direction of flow. Only in the case of a boundary layer over a concave wall is the mechanism of instability known, as a centrifugal force-driven instability arises from the competition between the centrifugal force and radial pressure gradient.[126] In particular, the curvature of streamlines generates a centrifugal force acting on the fluid particles which is counterbalanced by a pressure gradient normal to the wall. As the velocity of fluid particles increases, imbalances between the centrifugal and pressure gradient forces give rise to unstable flow structures. These are the three-dimensional structures which are widely known as the Taylor-Görtler-type vortices. Development of such vortices has been extensively studied, both theoretically and experimentally, for Couette flows and flows over concave boundaries. Interestingly, similar structures have been observed recently in transitional and turbulent bounded shear flows next to a wall.[128-130] However, only in the case of the boundary layer flow over a concave wall has the destabilizing mechanism been established and understood.

Flow structures isolated with aluminum flakes in the vicinity of the DSV for Re greater than 500 appear to be similar to the ones visualized by Peerhossaini and Wesfreid[127] in their experimental study of the Taylor-Görtler instability over concave walls. These authors used the laser induced fluorescence technique to visualize the flow of water with a solution of fluorescent dye as a tracer. The spikes observed in our experiments at Re above 500 (Fig. 51) appear similar to the spike configuration conjectured by these authors to represent the cross-section of the vertical interface between two neighboring Görtler vortices. Characteristically, the spikes signify fluid being pumped away from the wall. A pair of such vortices is more descriptively captured on a later state of its development (Re=940), hence the spike has grown an umbrella shape on its top giving a mushroom-like configuration which overrides the centers of two counter-rotating vortices (Fig. 51). Thus, spikes can be interpreted as the outgoing, i.e., away from the bottom wall, boundary between a pair of vortices. Eight pairs of such vortices appear along the span of the cavity for Re in between 600 and 1000. Above Re of 1100, fluctuations of the flow make it difficult to identify the exact number of vortices.

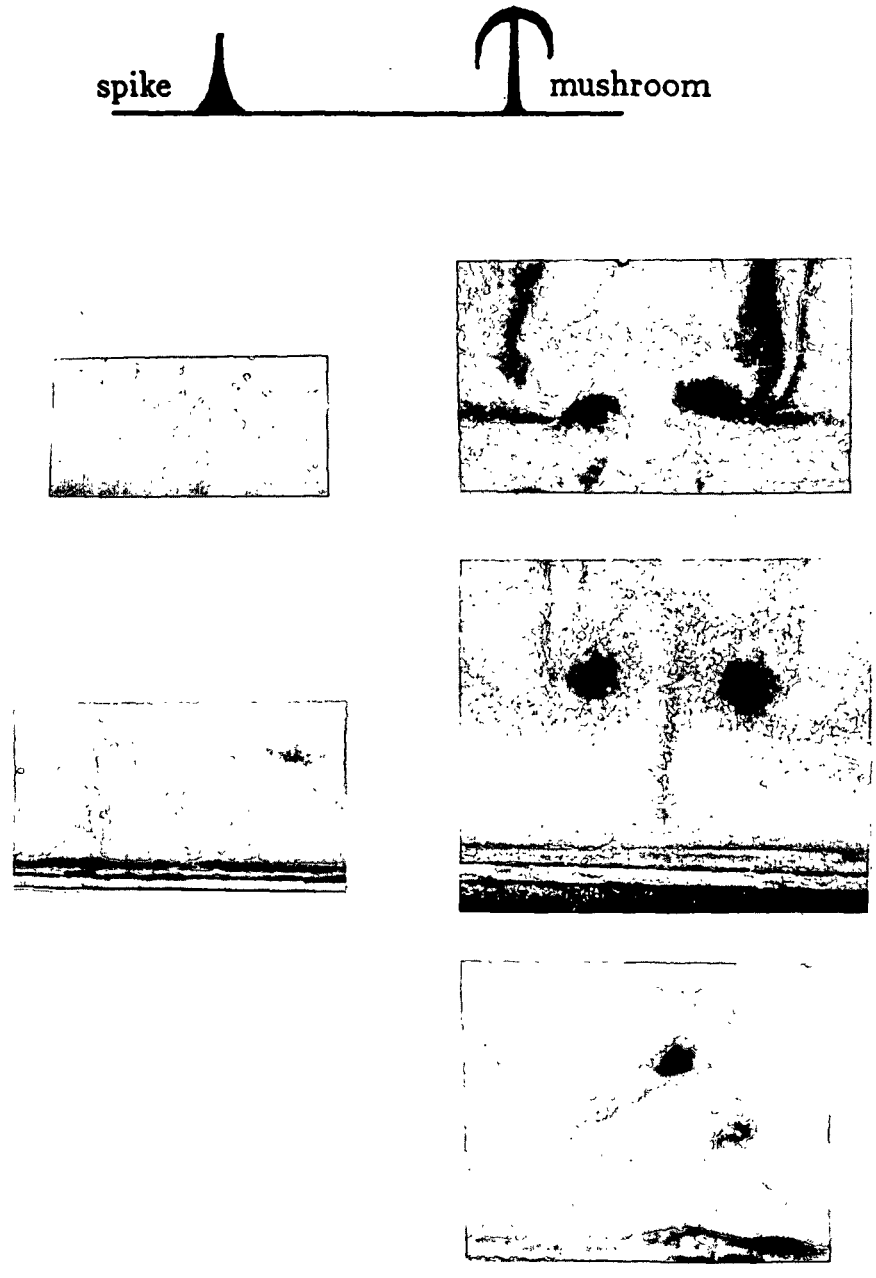

Figure 51. Comparison of flow structures between the experimental work by Peerhossaini and Wesfreid[127] (schematics on top) and the present work.Photographs on the left: Re=870, Re*=0.44, P_h=207 kPa, P_c=10 kPa,on the right (top):.Re=940, Re*=0.62, (bottom): Re=1440, Re*=0.37, P_h=207 kPa, P_c=10 kPa.

Similarities between the system considered here and the Taylor-Görtler instability developing over concave walls extend to evolution of more complex states as the control parameter of the flow continues to increase. Oscillation of vortices in the transverse plane (parallel to spanwise direction of the cavity) constitutes a higher order mode of the Görtler instability along concave walls.[128] In the same manner, the author has observed spanwise oscillation of the mushroom-like structures. Dynamical structures photographed by Peerhossaini and Wesfreid[127] at amplified states of the Taylor-Görtler instability were also isolated in the present work. In fact, the shape depicted at the bottom of Fig. 52 for Re=1400 is identical to the one presented by these authors as designating the "jump-and-stay" motion (top), a term used to describe alternating rapid jumps of flanks from one side to another with a long residence time at each side. At even higher instability modes vortices start to interact with each other and, as phrased by these authors, "... one pair is intermittently attracted and then swallowed by its neighbor, only to reappear in its place after an extremely short delay." Similar processes were observed in the lid-driven cavity flow with through-flow for Reynolds numbers above 1100 ± 30% (Fig. 35-37). Furthermore, the violent fluctuation of the flow, and perception of disappearance/reappearance of mushroom-like structures are reminiscent of transition to turbulence in boundary layer flows over concave walls.[129]

Patterns observed with direct-injection techniques illustrate the existence of phenomena similar to the ones described above. As an example, the structure appearing in the radiograph depicted in Fig. 53 is similar to the form which represents a cross section of Görtler vortices in a transitional boundary layers (see Fig. 3 in Ito[129]). In general, horseshoe-shaped vortices are riding on a pair of Görtler vortices formed inside the downstream secondary vortex. It is characteristic that such structures do not appear when the Re is smaller than approximately 500, hence the injected stream remains coherent and never enters the region of the downstream secondary vortex DSV (Fig. 42). Vortical structures in the DSV prevail only at higher Reynolds number Re. In visualization experiments with aluminum flakes the onset of this state can be assumed upon appearance of a wavy interface and observation of spikes. Their occurrence suggests that there exists a transport mechanism to transfer fluid from the main into the downstream secondary vortex and, consequently, the interface between the two recirculating flows has been destabilized.

The vortices observed here are also similar to the TGL vortices prevailing in fully-developed flow inside an enclosed lid-driven cavity, as visualized by Koseff,[77] and Koseff and Street.[78] These authors observed the appearance of TGL vortices in impulsively started flow for Re greater than 1000. Because they were interested in studying the onset of turbulence, they did not determine the minimum Re value at which these vortices appear. These authors also suggested that the TGL vortices are formed because the surface of separation between the

main and the secondary recirculations of the primary state is effectively a concave "wall", as depicted schematically in Fig. 54. If this was the case, then TGL vortices would be moving towards the upstream vertical wall of the cavity and away from the downstream corner. This is not supported by the visualization experiments in the present work. Findings with both the suspended-particles and direct-injection techniques lead to suggestions that the movement of TGL vortices is towards the downstream vertical wall and not away from it. It seems probable that as fluid is been transferred from the the main to the secondary recirculations the TGL vortices are formed inside the DSV under the influence of its curved streamlines.

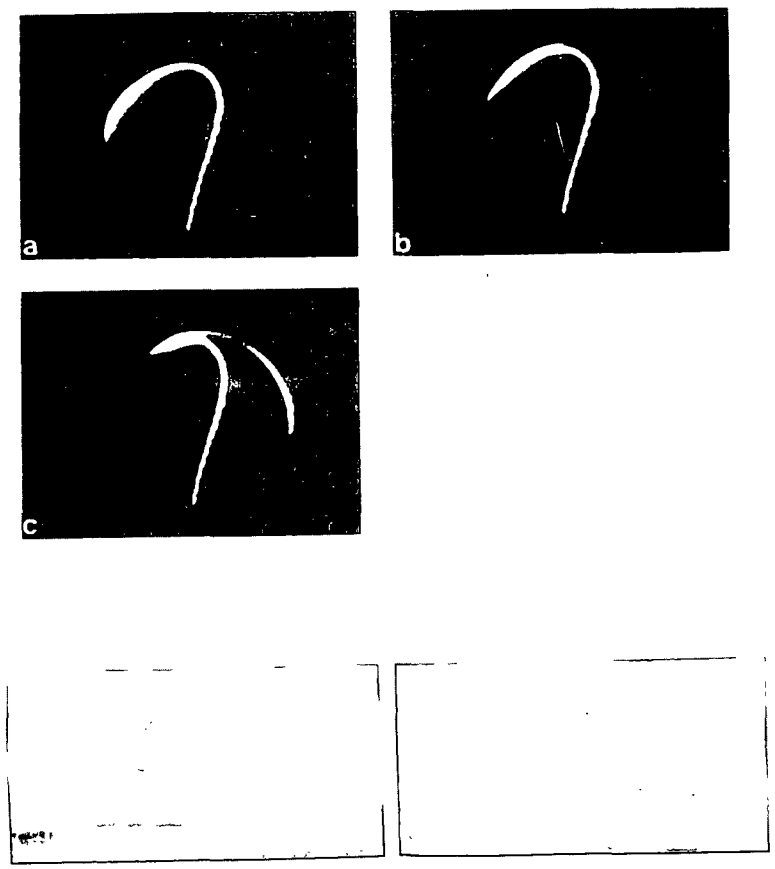

Figure 52. Comparison of flow structures between the experimental work by Peerhossaini and Wesfreid[127] (schematics on top) and the present work. The jump-and-stay motion. Photograph on the bottom: Re=1400, Re^*=0.64, P_h=207 kPa, P_c=21 kPa.

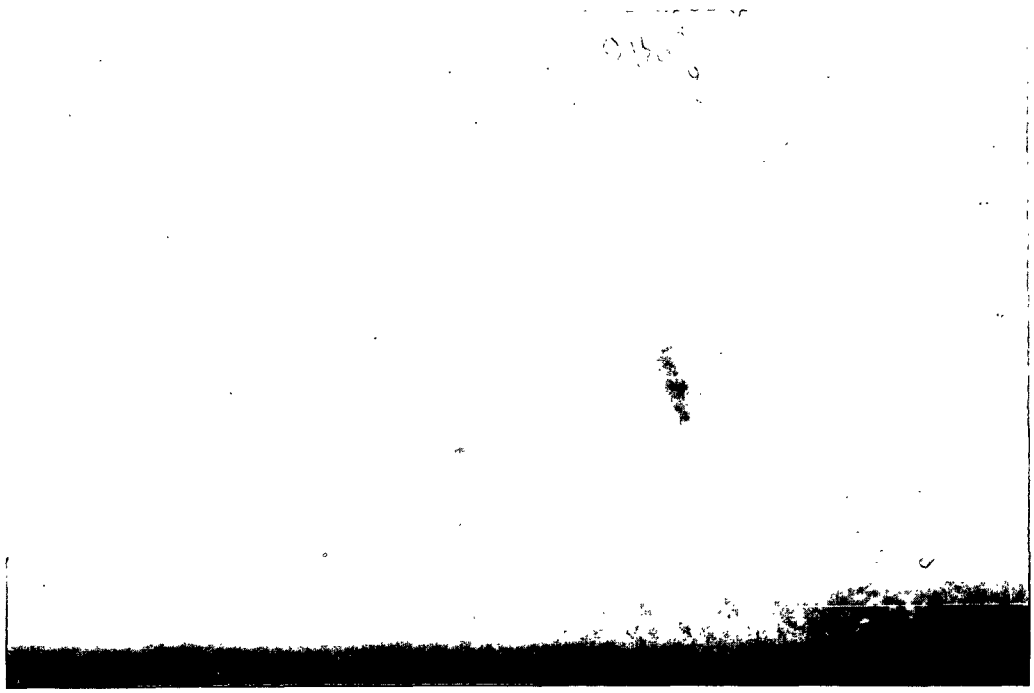

Figure 53. A horseshoe-shaped vortex obtained in the vicinity of the DSV with FXR. Fluid: glycerol/water. Re=1280, Re*=0.35, P_h=207 kPa, P_c=138 kPa. (Image magnified to show details.)

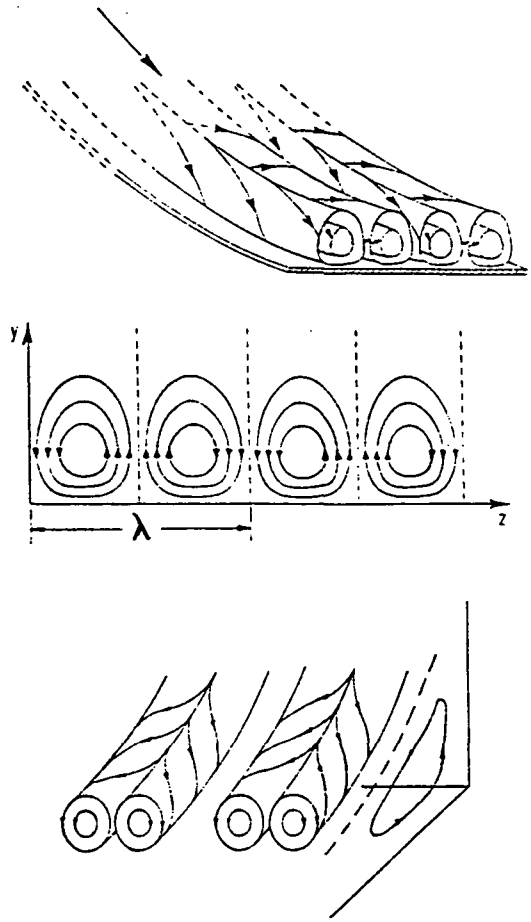

Figure 54. Schematic representation of Görtler vortices (top), Taylor boxlike vortices (middle) and the TGL vortices in an enclosed lid-driven cavity flow (Koseff, 1984).[77]

An important aspect of edge effects in the flow is the introduction of imperfect, or perturbed, bifurcations.[16] Here bifurcation, meaning forking, designates qualitative reorganization of the flow resulting from changes of the parameters on which it depends. An example of this is the observed transition from the basic primary to the three-dimensional states with Taylor-Görtler-type vortices as the roll speed increases above a critical range. However, imperfection is introduced by the presence of the side endwalls which have the tendency to break a bifurcation, so that the basic primary flow (referred to as the "two-dimensional" cavity flow in the literature) is not the only solution to the real problem at low Re. The finite distance of the side boundaries induces a destabilizing effect, not only in the vicinity of the walls, but throughout the whole flow field. Thus, the local event of the presence of corner vortices eventually destabilizes the global pattern of flow. It should be pointed out, however, that the appearance and establishment of TGL vortices along the span of the cavity - when the control parameter exceeds a critical range - indicates destabilization of the whole irrotational core rather than just the viscous boundary-like layers next to the walls.

The TGL vortices develop along the reattaching separation surface on the downstream wall. Their appearance is associated with a critical range of the control parameter of the flow, Re. However, the unstable condition which describes the onset of these vortices depends on the the fluid velocity at the separation surface (between the primary roll and the DSV) and the radius of curvature of the surface. As identified by Görtler,[82] the onset of vortical flow can be correlated to a certain critical value of a parameter that is now known as the Görtler number (Gö). The requirement for vortical flow through the thickness of a boundary viscous layer flowing over a concave wall is given by:

$$G\ddot{o} = \frac{U\lambda}{\nu}\sqrt{\frac{\lambda}{r}} > 50 \qquad (13)$$

where U is the stream velocity, ν the kinematic viscosity of the fluid, λ the wavelength of the unstable flow (i.e., the width of a pair of Görtler cells), and r is the radius of curvature. In the case of flow in a cavity, U represents the tangential velocity of the fluid at the separation surface, [84] while the radius of curvature can be taken as equal to half the depth of the cavity (or the radius of the primary recirculating roll). Assuming that U is equal to about 42% of the lid speed, as measured by Koseff,[77] λ = 1.91 cm (visually estimated for eight pairs of vortices across the span of the large cavity), and r = 2.45 cm, characteristic values of Gö are approximately in the range of 47 to 86. These correspond to conditions at the downstream wall where fully developed TGL vortices are observed from flow visualization experiments in the present study. In particular, onset of vortical flow in the case of progressively

increasing roll speed is identified for Gö in the range from 47 to 62. Upon sudden startup, the flow destabilizes at Gö=86. Under these conditions, the TGL vortices not only dominate the local flow at the DSV, but also influence the global picture of the flow as they are further amplified by the centrifugal instability.

The present evidence suggests that the flow state at cavity Reynolds numbers in the range of 100 and 300 is not a unique function of the Reynolds number and boundary conditions. The nonuniqueness of flow is in contrast to the traditionally accepted view that the the lid-driven cavity flow is always "two-dimensional" within this range of Reynolds number. For a cavity with finite dimensions and within the range over which the parameters of the flow were varied, alternative stable states do not connect with the basic steady state or with each other. Once established, different flows, corresponding to different integers of cells, cannot change from one to another set of integers without discontinuity, i.e. by breaking down the previous set. However, we cannot exclude the possibility that these flow states might be connected, representing bifurcation branches in the stability diagram of the flow, something which we have not yet detected because experimental Reynolds numbers below about 100 could not be attained. It is possible that at very low Reynolds number the basic steady (primary) state flow always prevails. Within the range of low Re values tested, alternative states competing with the basic steady state of flow is an example of imperfect bifurcation. Because of this, the confined flow in a lid-driven cavity with finite dimensions can be considered as locally stable but globally unstable.[125]

Of interest to the problem considered here is the axial (i.e., vertical to the principle direction of flow) distribution of the mass transfer along the span of the cavity in the presence of three-dimensional flow structures. In the case of Couette flow between two cylinders, where the inner rotates while the outer remains stationary, Kataoka[131] has illustrated that the mass-transfer coefficient on the outer cylinder has a distribution with axial periodicity. Furthermore, he has shown that the coefficient reaches a maximum in between the members of a pair of Taylor vortices and a minimum in between two pairs. The peak-to-peak distance of the axial distribution of the mass-transfer coefficient on the wall of the outer cylinder was found to be equal to the spacing of a vortex pair. This suggests that a similar distribution may develop in the experimental cavity, hence the outflow on to the roll surface may be influenced by the periodicity of the mass-transfer coefficient across the cavity.

The physical characteristics of structures and cells not only reflect the dynamics of the flow but also the transport processes in the vicinity of the wall. When the flow field becomes streaky or banded due to the development of TGL pairs, alternate regions of low- and high-velocity fluid exist in the cavity. As pointed out by Freitas and Street,[84] the major effect of

TGL vortices is to redistribute energy from the primary flow direction into a direction normal to the primary flow. Thus the flow appears streaky as the spanwise velocity field varies both in space and time, and the momentum transfer uniformity varies across the span of a cavity. It is exactly this mechanism that has been hypothesized to control the momentum transfer and mass flowrate, and eventually influence the cross directional profile of the wet-film deposited on the web in blade coating with a short-dwell coater.

CHAPTER SIX

PILOT COATER TRIALS

BACKGROUND

Since no systematic pilot plant data have been published regarding the occurrence of wet streaks, the task was to collect evidence that could connect visually observed wet streaks on LWC paper with expected transitions of the pond flow. Qualitative information was obtained by inspecting the coated paper with the naked eye. The hydrostatic pressure profile (along the machine direction) normal to the roll was also measured to compile quantitative data which indirectly relate to hydrodynamic phenomena in the pond. Details of the pilot plant trials are included in Appendix E.

Pilot-plant trials were based on actual production practices, the only difference being the effective span of the coater which was only 40 cm, i.e., depthwise ratio 1:1 and spanwise ratio 10:1. In all trial runs, operating conditions were adjusted to control coat weight, while the temperature of both the sheet and the color were maintained at about 27°C. Two series of trials were performed under well-controlled conditions using a 60 g/m^2 base stock for LWC in the first series of trials and a 50 g/m^2 stock in the second series. An outstanding difference between the two series was the type of delaminated clay used in otherwise similar formulations, i.e., typical of papers printed with rotogravure. English China and Georgia delaminated clays were used in the first and second series, respectively. In general, because coating colors are non-Newtonian fluids, it is difficult to determine with confidence the value of the Reynolds number in complex flow fields, such as the one inside the pond. Here, to be consistent with the flow visualization experiments, we have arbitrarily chosen to base the Reynolds number on the Brookfield (100 rpm) viscosity μ_B. Therefore, the parameter which defines the flow in the pond is given by an "apparent" Reynolds number Re_a as:

$$Re_a = \frac{\rho V D}{\mu_B}, \tag{14}$$

where V is the machine speed, and D the characteristic length that defines the distance between the blade tip and the baffle. The value of μ_B was controlled by maintaining high solids levels (56-59%) to keep it from falling below approximately 900-1000 mPa sec which,

from previous experience in the pilot plant,[1] has resulted in visible streaks. Before proceeding with trial results, it is worth noting certain rheological properties of the coating colors under consideration, namely the formulation with problematic machine runnability.

The efforts concentrated on formulations containing pigments with relatively high aspect ratio particles, i. e. above 15:1, such as English delaminated grades (type B) which are composed of particles which are platier than those in domestic delaminated grades of clay (type A).[61] In addition to delaminated clay, the rotogravure formulation contained 3.0-4.5 pph acrylic latex and 0.3 pph alkali-swellable thickener; its total solids content was approximately 58% by weight based on dry pigment. Practical experience in both a production facility and pilot-plant trials has shown that colors with the type B pigment are susceptible to wet streaking, which becomes visible to the naked eye at machine speeds above 1000 m/min.

Measured properties of both the respective pigments and their colors appear in Table 9. Density was determined by measuring the weight of a known volume of fluid and surface tension with a Cenco-duNoüy tensiometer. Both procedures were calibrated with water. The tensiometer is a sensitive balance which applies a slowly increasing upward force to an accurately constructed platinum-iridium ring in contact with the surface of the liquid under measurement. The amount of the upward force is indicated upon a circular graduated scale which, when calibrated, gives readings in dynes of force. During testing with the color type B, a problem was that the results varied depending on the depth of immersion of the ring into the fluid probably because of viscous drag contributing extra resistance. The problem was eliminated by precautiously ensure that the ring was first wetted by the color at the surface of a container and then was slowly pulled upwards. The MALVERN Zetasizer was used to measure (a) electrophoretic mobility, from which one can deduce the zeta potential from Henry's law, and (b) particle size (by determining the diffusion coefficient one can deduce size using Stoke's law for spheres). An advantage of this instruments is that the reported values represent averages from measurements on a large number of particles.

Table 9. Measured properties of reference (type A) and problematic (type B) coating colors.

	Type A	Type B
Total solids (%)	61.37 ± 0.01 %	58.61±0.09%
pH	8.6 (17.2°C)	8.1 (17.4°C)
Density (g/cm^3)	1.608	1.571
Surface tension (dynes/cm)	51.4 ± 0.7	66.9 ± 2.7
Zeta potential (mV) - pigments	-14.9 ± 0.9	-24.3 ± 1.3
Zeta potential (mV) - colors	-10.0 ± 1.2	-12.1 ± 0.9
Relative sediment volume - pigments	–	1.648

Certain observations from the data give an indication of the differences between colors A and B. First, the particle size distributions of the two types of pigments are substantially different. Figure 55 shows the accumulative percentage of particles below a certain size. It illustrates that type B contains more particles of larger size than type A. This is expected because that specific color contains English delaminated clays with nominally coarser particles than the ones comprising domestic grades of clay (i.e., Georgia kaolin) - characteristics which give superior print quality for gravure but worse rheology of colors. Second, zeta potential data indicates (a) substantial differences between the two pigments, and (b) a stronger pigment-binder interaction in the case of color B than A. The absolute value of zeta potential increases with the addition of a synthetic binder in a clay suspension as the electrophoretic double layer surrounding a particle depresses because of reduction of surface charge density mainly through charge neutralization or screening. The results imply comparatively high shear-viscosity for coating colors with type B pigment due to its large particle size and strong clay-binder interactions.

Figure 56 demonstrates the relationship between apparent shear-viscosity and shear rate for eleven decades of shear using four different viscometers. Here again, data of a type B formulation is being compared to a reference color (type A) which had no runnability problems for machine speeds up to 1200 m/min (4000 fpm). A pressurized-gas driven capillary viscometer (stainless steel capillaries, 100 mm in length, 1.03 mm in diameter) was used to collect data at shear rates of several hundred thousand reciprocal seconds, the raw

data corrected for all pertinent effects influencing the measurement. Hercules® measurements were taken with the instrument on its 'SET RPM' mode, thus minimizing the ramp time to attain the maximum shear rate (i.e., 500 msec) and avoid temperature buildup during a test. The scattering of this data is probably due to fact that all three annular gaps (with bobs A, E, and F) have been used. Brookfield data represent measurements at four different rotational speeds of the no. 3 spindle and calculation of the corresponding shear rates based on the procedure by Hyman.[103] The Carimed® instrument was a controlled stress rheometer (cone-and-plate geometry) with a logarithmic stress mode. Uncertainty in the measurements with all instruments was about 10%.

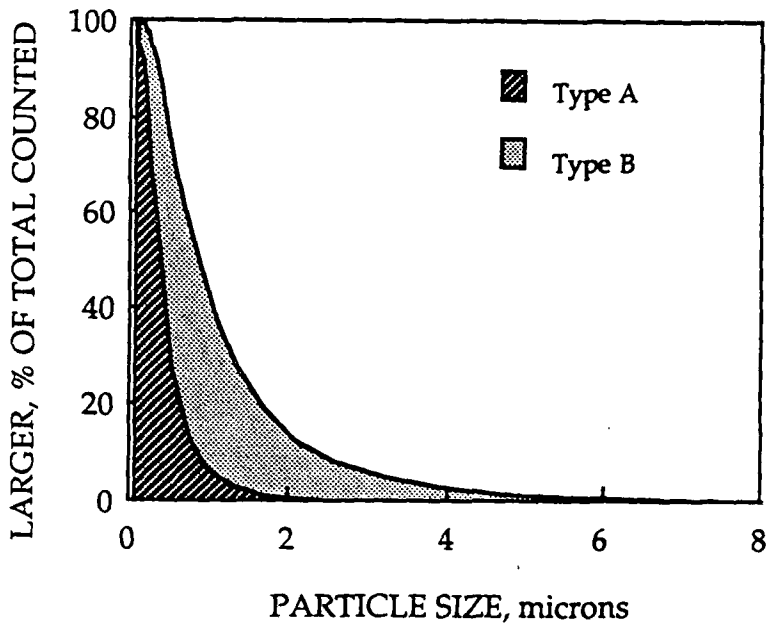

Figure 55. Results from measurements of particle size distribution for the two pigmentsused in this study. Size represents effective spherical diameter.

Both coating colors are shear thinning over the range of shear rates from 10^{-5} to 10^{6} sec^{-1}. Stress rheometer data illustrate that the shear-viscosity decreases by several orders of magnitude over the shear rate range of 10^{-4} and 10 sec^{-1}. Comparatively, the reference color shows a similar behavior but with viscosity values at least two orders of magnitude lower. This trend was also observed when measuring the plastic yield stress from rheograms. Although formulations with the type A pigment illustrated no measurable yield value in a typical Hercules rheogram, the problematic color (pigment type B) had substantial yield stress in the range from 5.0 to 6.4 10^5 dynes/cm^2 ($\pm$0.4 10^5 dynes/cm^2). Interestingly, however, the yield stress value decreased to 10^5 dynes/cm^2 after the color was subjected to high shear in the capillary viscometer. This suggests that structures in suspension which are responsible for the comparatively high low-shear viscosity and yield stress of the problematic color are sensitive to shear. Rheograms also indicated the time-dependence of viscosity in the form of a thixotropic loop. Thus the coating colors of interest demonstrated shear- and time-dependent structural viscosity.

The difference in the value of the apparent shear-viscosity between the two colors decreases substantially with increasing shear rates, as depicted from Brookfield, Hercules, and capillary data in the shear rate range of 10 to 10^6 sec^{-1}. Data from all four instruments do not fall on a single line probably because of differences in fluid temperature and in the measuring geometry between the viscometers. Linear regression of the combined Brookfield and Hercules data resulted in the following relationship for the power-law fluid model:

$$\mu = 1.04\,\gamma^{0.56} \tag{15}$$

The constant 1.04 represents the so-termed zero-shear-rate viscosity limit μ_o of the color, and 0.56 is the flow index N (the regression coefficient r is 0.90). The value of μ_o, equal to 1040 mPa sec, is numerically similar to μ_B, so that the apparent Reynolds number is roughly based on the zero-shear-rate viscosity of the color calculated with the procedure mentioned above. Thus, Re_a can be conveniently calculated from measurements with the two viscometers commonly used in practice. Constants μ_o and N for the reference color are 0.91 and 0.35, respectively. An outstanding difference between the reference and the problematic colors is in the flow index of the power-law fluid model. In addition to the high viscosity values observed with the stress rheometer, the problematic (type B) color has comparatively high flow index. However, the value of its flow index does not indicate shear-thickening, which is signified for N greater than one.

To review, rheological characteristics of a problematic color are: comparatively high shear-viscosity at shear rates below 10 sec^{-1}, high yields stress, steep reduction of viscosity with increasing shear rate, and apparent viscosity comparable to the reference color in the range of 10^3 to 10^6 sec^{-1}. Overall the coating color is shear rate thinning and thixotropic. It is should be pointed out, however, that the viscometric flows are steady and laminar. In the practical situation of their application coating colors are subjected to more complex hydrodynamic and other phenomena which may become dominant and influence the coating process.

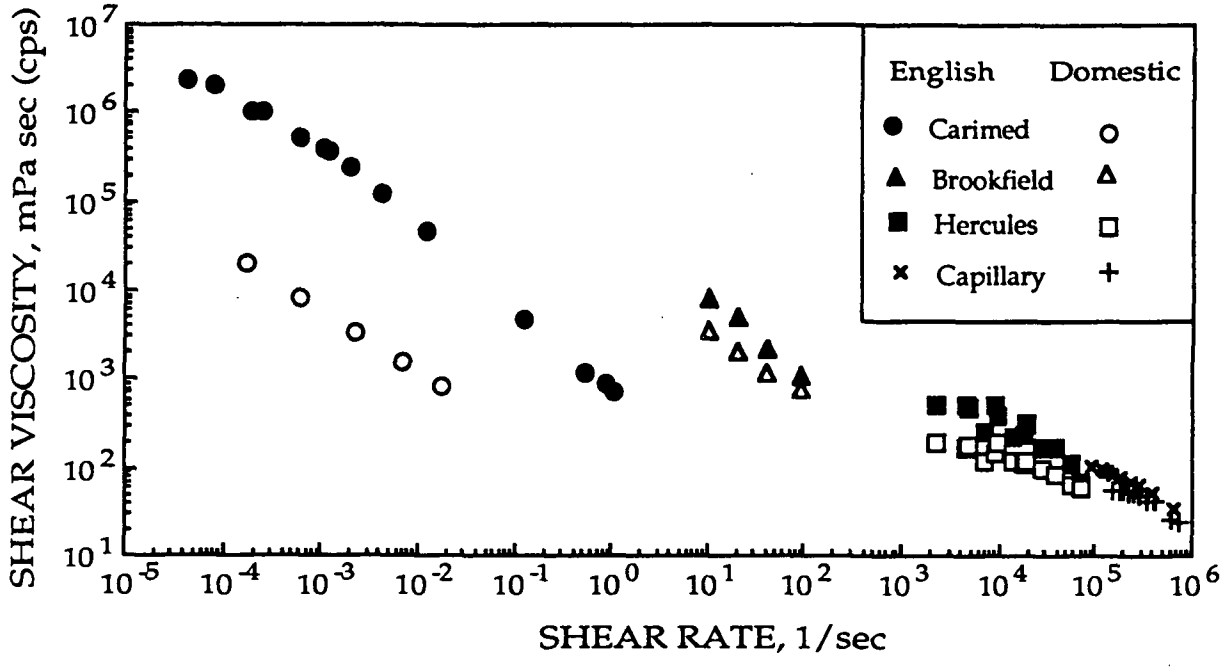

Figure 56. Rheological data of a problematic color used in pilot-plant trials and of the reference color. The first contains English China delaminated clay (type B), the second a Georgia kaolin (type A) delaminated grade. Thermostatic temperature of Carimed and Brookfield data was 25°C; temperature of Hercules data was 20°C, and of the capillary data 22°C.

RESULTS FROM TRIALS

Table 10 presents an overview of the results from the pilot-plant trials. These results should be analyzed and interpreted with caution. At first, it appears that the apparent Reynolds number of the pond, Re_a, is the only control parameter for the appearance of streaks. This may not be the case, as it is explained in the next section. The following paragraphs in this section report only results of the pilot-plant trials.

In both series of trials, the first occurrence of streaks appears for Re_a in the range between 550 and 750. After processing, the marginal case here shows at least one streak upon visual inspection of the web (Fig. 57). Such streaks are discontinuous narrow patches of 1-3 cm in width which run along the machine direction in an intermittent and periodic manner. This is referred to in Table 10 as marginal appearance of wet streaks.

As machine speed increases and the control parameter Re_a is raised, streaks grow both in width and frequency to eventually form almost continuous bands running along the machine direction for Re_a between 800 and 1000 (Fig. 57). In their severe form, low coat weight bands cover the full CD span of the web and become visible right after the blade during high speed operations. The width of individual bands varies between 3 and 8 cm, the widest of which appears with the formulation containing the platier clay particles, i.e., English China clay. About five to six bands are counted on a 40-cm wide web coated on the pilot SDC. At even higher speeds, the bands start a spatially oscillatory motion along the CD and, eventually, air inclusion induces skips. These nonuniformities cannot be corrected by adjusting the blade pressure (i.e., with the profile screws) across the machine line direction. Also, the problem could not be corrected by adjusting the baffle gap, the opening between the top edge of the overflow baffle and the surface of the backing roll. Figure 58 presents hydrostatic pressures from inside the feeding chamber and the pond of the pilot-plant SDC with the problematic color at different machine speeds but a constant through-flow rate of 132 L/min per meter width (or constant Re*). The pond pressure decreases with increasing machine speed for 3 and 5 mm baffle gaps, and increases for a baffle gap of 1.6 mm. This data implies that, as speed increases, a minimum gap is required to avoid a pressure drop and, consequently, air entrainment in the pond. Interestingly, wet streaks were eliminated when the solids content of the color was reduced from 58-56 % to 52%, corresponding to a Reynolds number change from Re=760-1000 to Re=1450-2380 (baffle set at 3 mm, machine speed constant at 1000 m/min).

Table 10. Visual observations from LWC papers coated in a pilot short-dwell coater (45° x 0.5 x 76 mm bevelled blade, 19 mm stick-out, 3 mm baffle gap, pond DAR=1:1, SAR=10:1).[a]

Trial Run No.	Color Viscosity[b] (mPa sec)	Machine Speed (m/min)	Reynolds Number Re_a	Appearance of Wet Streaks
	First Series (11 gsm, pump rate 166 L/min/m, English clay)			
1	1884	305	210	No
2	1428	760	690	Yes
3	1428	800	710	Yes
4	1428	820	740	Yes
5	1428	730	660	Yes; marginal
6	1412	610	560	No
7	980	640	840	Yes
8	980	670	880	Yes
9	980	700	920	Yes
10	1236	610	635	Yes; marginal
11	1236	700	730	Yes
12	1236	490	510	No
13	1236	550	570	Yes; marginal
14	1056	610	740	Yes
15	1056	1060	1300	Yes; severe
	Second Series (6-7 gsm, pump rate 166 L/min/m[c] Domestic clay)			
1	1268	700	790	Yes; sporadic
2[c]	1292	305	670	Yes; marginal
3	1268	760	850	Yes
4	1280	790	910	Yes
5	1292	820	1000	Yes
6	1224	730	1240	Yes
7[c]	904	305	480	No
8	1012	640	860	Yes
9	1052	1220	1650	Yes; severe
10[c]	1004	1340	1900	Yes; severe
11[c]	1104	370	470	No
12[c]	1120	430	540	No
13[c]	1156	490	600	Yes; marginal
14[c]	1160	550	670	Yes; sporadic
15[c]	1156	610	750	Yes

[a] The colors used had Brookfield viscosity of at least 900 mPa.s. Streaks do not appear at these Re values with formulations having lower viscosity.

[b] Brookfield viscosity, 100 rpm, no. 3 spindle.

[c] In this case the pumping flow rate was 200 L/min/m.

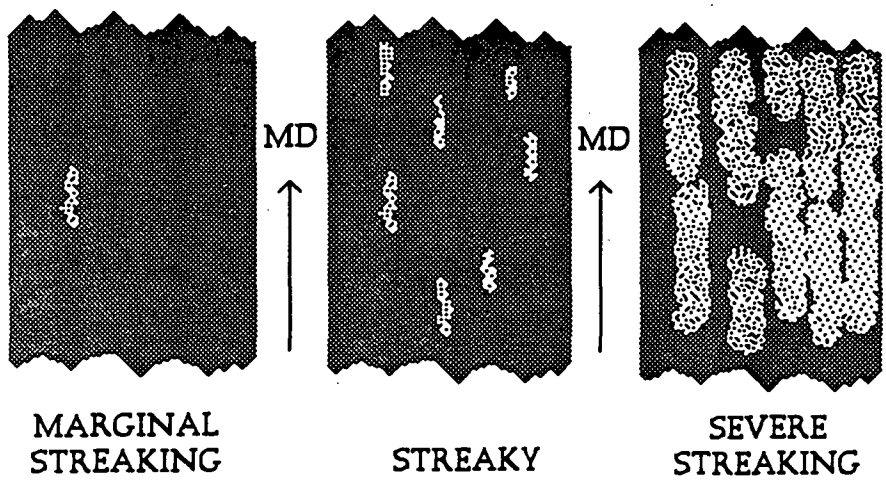

Figure 57. Schematic illustration of the appearance of wet streaks on LWC paper during pilot-plant trials.

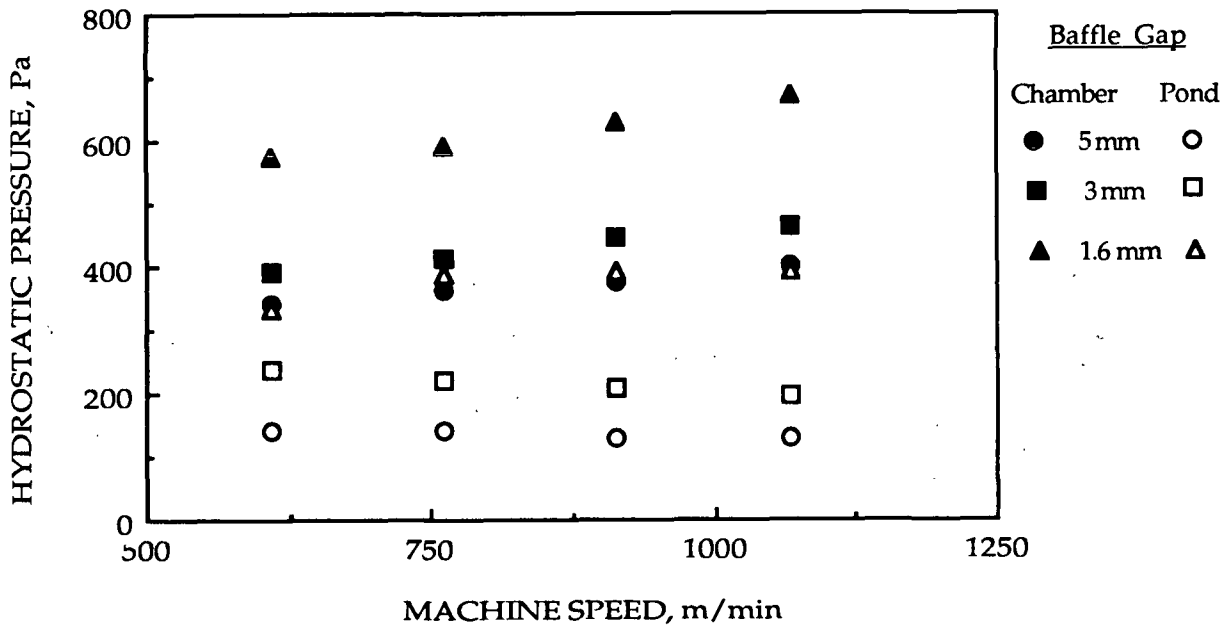

Figure 58. Pressure measurements as a function of machine speed for different SDC baffle settings during the production of LWC paper in the pilot-plant trials.

The above results suggest a connection between the appearance of streaks on the coated web and the Reynolds number, Re_a, for the range over which fluid viscosity and machine speed are varied. Generally, the Reynolds number decreases with reduced machine speed, but increases with lower fluid viscosity (from Eq. 1 and 14). Good examples of this are trials 6, 10, and 14 in the first series where constant machine speed at 610 m/min (2000 fpm) may or may not produce streaks depending on viscosity and the value of Re_a. This is also true irrespective of the type of clay pigment used, i.e., trial 15 in the second series. In the same manner, increasing machine speed while maintaining constant viscosity induces streaking, e.g., trials 4 and 6 in the first series. Thus, independent of how a certain value of Re_a is attained, streaks will appear if this value is above a critical range, such as in trials 2 and 14 in the second series where Re_a=670 represents the marginal case for appearance of streaks.

The range of Re_a over which streaks definitely occur for the first time, i.e., 550-750, is comparable with the values of Re for onset of three-dimensional flows in the experimental facility (Table 8). This is true within limits imposed by experimental uncertainty and differences in geometric dimensions, especially the spanwise aspect ratio. In general, endwalls (edges) and their proximity have a destabilizing effect on the state of flow by inducing steady state three-dimensional flows.[132] Flow in the pilot coater pond, therefore, is expected to be stable for greater values of the control parameter than in the experimental cavities. This, in combination with the shear-thinning rheology of the coating color which underestimates Re_a, can explain differences between the critical ranges of the two parameters Re and Re_a.

As the Reynolds number Re_a rises above 1000-1100, streaks fill the whole CD width and are visible to the naked eye even at production speeds. This range of Re_a is comparable to the critical value of Re (Table 8) for which violent spanwise oscillation of the flow is observed in the experimental cavity. These conditions probably signify onset of unsteady flow in the pond, very much like the appearance of mushroom-like structures in a lid-driven cavity flow with through-flow.

Hydrostatic pressure measurements (with a transducer mounted on the middle of the backing roll) indirectly indicate the existence of recirculating flows in SDC ponds. Figure 59 presents a typical profile with pressure values obtained for a wide range of color viscosities and operating conditions. Blade pressures are estimated from the literature [10] because their range exceeds the useful range of the transducer. Measurements under conditions of practical interest show that the pressure rises to 1-9 kPa (0.2-1.3 psig) right at the baffle, with the greater values corresponding to narrower baffle gaps. Inside the pond and closer to the blade, a pressure drop occurs which may cause the pressure to become subatmospheric, e.g., -2 to 4 kPa (-0.3 to 0.6 psig). This drop can be explained by the existence of recirculating flows in the

pond with the lowest point of pressure corresponding to the center of a vortex, something which was also confirmed qualitatively by numerical simulation. To obtain a quantitative correlation between the pressure profile inside the pond and the onset of streaks, it is necessary to measure spanwise pressure variations of the viscous layer which forms at the moving surface.

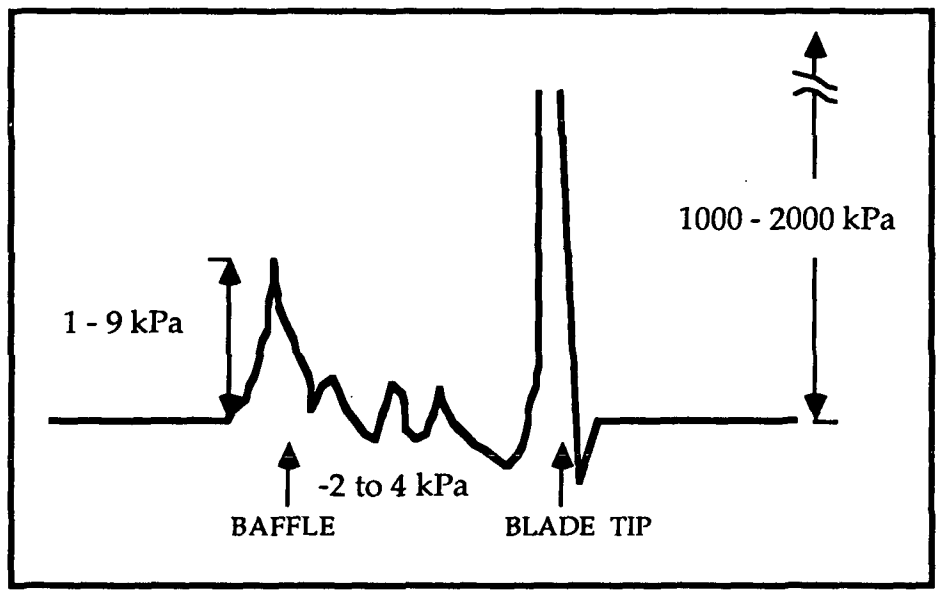

Figure 59. A typical profile of the hydrostatic pressure which acts normal to the web inside the SDC pond.

CHAPTER SEVEN

DISCUSSION AND IMPLICATION OF RESULTS

Operational differences between bevelled blade coating systems with an applicator roll and the short-dwell coater cannot only be explained by the low pressure and short contact time (between the color and the web) of the latter. The fluid dynamics upstream of the blade nip are qualitatively different in the two systems. In the case of a short-dwell coater, hydrodynamic phenomena in the pond can influence the local variation of color mass transport into the blade nip and the uniformity of momentum transfer across the machine direction. In addition, the hydrodynamic pressure across the blade may vary, depending on the state of flow in the pond. Such phenomena may not only determine the spatial and temporal uniformity of coat weight, but they can also affect orientation of inherently asymmetric pigment particles, thus explaining differences in the properties of the final coated sheet.

The connection between pond fluid dynamics and nonuniform coat weight is based on qualitative evidence. The hydrodynamics, however, are only part of a larger number of physical phenomena which describe this process and its complexity. The basic assumption that local and global flow phenomena, which are controlled by the two Reynolds numbers and pond dimensions, completely describe coatability in short-dwell coating is limiting. The evidence presented here does not exclude the possibility that wet-film thickness nonuniformities arise from air entrainment and destabilization of the moving contact line upstream, or from rheological phenomena of the coating color. For example, practical experience has shown that most of the problems in coating applications are caused by the comparatively high shear-viscosity of a color. Factors such as the solids level of a color and the shape of pigment particles introduce additional dimensionless parameters which can be correlated to nonuniformities. However, here the investigation concentrated only on the hydrodynamic aspects of flow which appears in pond-type systems for web modification.

The laminar flow in short-dwell ponds is characterized by recirculating flows wherein strong centrifugal forces arise from curvilinear streamlines. The basic state of flow consists of a main recirculating roll driven by the web, its tail-end sometimes described as a "rolling sausage" over the baffle stretching along the CD of the machine. Additional weaker (secondary) rolls appear at the corners of the pond depending on the specific geometry. This state of flow comprises the ideal case from the runnability standpoint, since there is a

uniformly stable mass of fluid delivered into the blade nip across the machine direction. However, this is not a uniquely defined state because it competes with other steady states, three of which have been identified experimentally to date. Multiple states of flow at the same Re indicate the sensitivity of hydrodynamic forces. Alternative states of flow feature three-dimensional structures which are stable to infinitesimal disturbances and, once established, do not switch to the basic steady state. Such behavior provides a possible explanation for the difficulty in predicting runnability in coating operations, and for the phenomenological differences between identical coaters. By analytically determining regions of attraction for each type of flow, it will be possible to set guidelines for desired operating states - useful information for production purposes.

As the fluid velocity increases, the flow rolls up into three-dimensional evolving structures. First in the form of localized corner vortices originating from viscous damping at the side endwalls. Second, as spanwise structures termed Taylor-Görtler-type vortices which dominate the global picture of the flow. These non-linear structures arise from the imbalance between centrifugal and pressure forces on the curved streamlines of the flow. Their appearance is conjectured by banded (or streaky) interfaces of faster- and slower-moving fluid in between the vortices. The source of such inherent fluid dynamic instabilities is internal to the system behavior. With axes parallel to the direction of web movement, counter-rotating vortices form regions of ingoing and outgoing fluid across the blade nip which, under certain circumstances, may cause uneven CD profile. Following a series of transitional modes, the pond flow eventually reaches complex unsteady states. Incidentally, the appearance of cellular structures in the pond does not signify the onset of turbulence.

Under the conditions investigated, the first appearance of low coat weight streaks running along the machine line direction relates to the expected onset of flow instabilities in the pond of a short dwell coater. The control parameter is the pond (apparent) Reynolds number, Re_a. In particular, the observation of severe streaking occurs when violent flow fluctuations set in along the span (cross machine direction) of the pond. It should be pointed out here that it is difficult to quantify the coat weight variations which are easily visible to the naked eye. A relatively convenient and quick technique is based on measuring the reflectance off the surface of the coated sheet which is directly proportional to variations of coat weight. In particular, spatial differences of coat weight are easily visualized if an ultraviolet dye is mixed in with the coating color and the sheet is observed under a UV light. Application of such a technique indicated that reflectance variations of less than 2% correspond to a streaked see-through appearance on LWC papers coated with 6-11 g/m^2 on one side.[133] This is indicative of how small variations in the uniformity of the coating lay can have a strong impact on the visual appearance of the coated sheet, especially at low coat weights.

The reported results correspond to viscous coating formulations with a Brookfield shear-viscosity of approximately above 900 mPa sec(@100 rpm). Rheological measurements on the problematic color illustrated that, like most coating colors, it is shear thinning thixotropic. A primary difference from colors without any runnability problems at high machine speeds is its unusually high viscosity at shear rates below 10 sec^{-1} and high yield stress. Consequently, its flow behavior does not only depend on the shear rate but also the nature of the flow field. In a fully-developed rectilinear flow driven by pressure, for example, a sheared mobile layer develops next to the walls and the rest of the fluid may move as an unsheared plug. In contrast, inside confined geometries, such as the one in a lubrication flow, movement occurs simultaneously everywhere as soon as the minimum required shear stress is reached over the entire flow field. The confined flow in a SDC pond is complicated, and is often made more so by viscosity and density stratification due to recirculating flows with curvilinear streamlines and the associated centrifugal forces.

Present qualitative evidence suggests that onset of hydrodynamic instabilities in the pond may be an adequate condition for occurrence of uneven CD profiles. In other words, whenever streaks are observed, the control parameter of the flow indicates unstable flows in the pond. However, it is possible for this parameter to be above its critical value, without the appearance of streaks. Practical experience in industrial and pilot-plant operations has shown that if shear-viscosity is low enough (e.g., reduced solids content or smaller pigment particles), the runnability window of short-dwell coating expands to greater machine speeds.

Thus it seems that the origin and evolution of streaks depends on more parameters than the ones which describe the flow in the pond. These parameters maybe related to physical phenomena such as air entrainment and instability of the moving contact line upstream, or to the characteristic time period required for particles' movement under a high degree of crowdedness in suspension. In addition, rheological effects arising from both the continuous (dispersing) phase and the dispersed particles make the picture more complicated. Such phenomena have not yet been studied.

To elucidate these effects, a mechanism can be proposed based on results from this study. Because of the recirculating flows in the pond, fluid elements and other components of coating colors that are only few millimeters away from the web move opposite to the machine direction. Only after these particles have penetrated the viscous layer, that forms on the moving web when the color contacts it upstream, do they experience the viscous drag of the substrate, at which point they are accelerated and convected downstream. In systems with an applicator roll, the outer layer of the which deflects down the blade is irrotational.[3] In contrast, the flow in short-dwell coaters contains recirculating eddies, which as demonstrated

above becomes unstable due to centrifugal forces and gives rise to time-periodic and three-dimensional flow patterns. Cellular structures in the pond cause differential orientation of pigment particles and, if there is not enough time for the particles to reorient, the structures can create unstable conditions in the nip. In addition, as pointed out by Gane, et al.,[134-135] orientation phenomena of clay particles upstream of the blade can also affect the final coating properties. Such effects are generally more pronounced in formulations containing highly asymmetric particles, e.g., delaminated clays, at relatively high solids content. They may not , however, be important when using pigments with small particle size, e.g., a no. 2 grade of clay. Thus, CD profile variations can be attributed the hydrodynamics in the pond coupled with color properties that are proportional to shear-viscosity. This scenario explains why below a certain solids concentration the streaks disappear, and it also explains the appearance of streaks with larger aspect ratio particles. Proof for this and other scenarios does not yet exist.

The dynamics of the flow at the blade are also important and should be considered. For example, based on the analysis by Higgins[14] and Guzy and Higgins,[46] a positive drop across the blade nip puts an upper limit on the final film thickness or coat weight that can be attained. Furthermore, they showed that, according to lubrication theory, below a certain film thickness the steady-state flow under the blade ceases to exist when the pressure gradient across the blade is positive. Variations of the hydrodynamic pressure across the span of a blade nip may also arise from flow instabilities, like the ones described above. Vortical flows in the pond are associated with pressure drops, the minimum pressure value corresponding to the center of a vortex.

Although this study does not provide explicit evidence of the precise mechanism for generation of streaks in SDC, it contributes to better understanding the hydrodynamics in pond-type application systems for web modification(such as coaters, size press, printing presses, etc.). The existence of multiple stable states of flow under the same operating conditions at a relatively low machine speed explains the experienced in practice difficulties in predicting the system behavior. Furthermore, this phenomenon justifies the inability to control such systems with schemes based only on a stochastic methodology. At high machine speeds, onset of hydrodynamic instabilities features structural flows which are characteristic of the inherent physics of the system. These flows are difficult to control and may influence the uniformity of the thin film applied onto the web, if the fluid rheology is formidable.

RECOMMENDATIONS

As the trend in the industry shifts toward higher machine speeds and lower coat weights, it should be recognized that film thickness imperfections put an upper limit on machine speed. This is especially important when using large, highly orientable pigment particles which give better print quality but their application is not conducive to high solids content (i.e., above 58%). Results from experimental studies presented here provide important information and insight regarding the dynamics of the flow in SDC ponds. The origin of CD profile unevenness, however, remains unclear. Further studies are required to pinpoint the physical origin of nonuniformities with a degree of rigor and confidence. To pinpoint the origin of nonuniformities requires (a) systematic pilot-plant trials to better document and clarify the exact conditions of streak appearance, and (b) a more fundamental and complete investigation of shear-driven cavity flows of Newtonian as well as non-Newtonian fluids.

Future pilot-plant trials with a short-dwell coater would concentrate on two aspects of data acquisition. First, a time-dependent property of the the flow in the pond need to be measured in order to construct high-resolution power spectra in which different dynamical regimes of the flow can be distinguished. Second, the periodicity of wet streaks on LWC paper should be thoroughly investigated over a long period of time by implementing Fast Fourier analysis (FFT) techniques. A comparison of the power spectra with the FFT graph would indicate the connection between what is going on in the pond and the nonuniformities on the coated web. Simultaneous pressure measurements at several points in the pond (i.e., with four transducers mounted on to the inner surface of the baffle) could be conveniently obtained, but caution should be exercised because pressure variations do not always relate directly to flow phenomena.

The present evidence suggests that wet streaks appear when the coating color attains a comparatively viscous character at low shear rates. However, a more comprehensive rheological analysis is required to identify which characteristic parameters of the fluid influence its runnability in the coater. This would include viscoelastic and transient shear measurements. Combination of this data with pilot machine documentation will contribute in establishing the operating widow of the short-dwell coating process.

In addition to flow instability in the pond, high-speed SDC systems have an another constraint - the air entrainment at the dynamic (moving) contact line between the color and

the substrate. The onset of air entrainment is characterized by the dynamic contact line approaching 180°, the exact value primarily depending on viscosity.[136] A destabilized contact line breaks into V-shaped structures, which grow with speed and eventually coalesce to release a bubble.[132] Although the fundamentals of dynamic wetting are still under investigation, it has been established that air entrainment puts a limit on the maximum processing speed in processes where a solid substrate comes in contact with a liquid, such as in a slide coater.[137] A systematic study of air entrainment in short-dwell coaters has not yet emerged.

Beyond the above work, more advancement is needed in the area of computer modelling to shed light in the complex physics of blade coating and to, at least partially, replace experiments which are tedious, time consuming and expensive. The numerical simulation presented here is limited due to software and hardware restraints. More powerful programs, like the one developed by Pranckh,[15] are needed to incorporate all relevant phenomena and fluid properties. In particular, the interest should concentrate on simulating three-dimensional flows containing free surfaces and assessing the non-Newtonian behavior of coating colors using model fluids.

CONCLUSIONS

Flow visualization in a lid-driven rectangular cavity with through-flow and finite dimensions, which experimentally simulates the short-dwell pond, reveals previously unknown aspects of such flows with both glycerine solutions and clay suspensions (i.e., coating colors). These are:

1. The basic primary ("two-dimensional") state, the ideal flow pattern for coating, competes with multiple steady states having three-dimensional flow structures. Three competing states have been identified to date. These are stable states in the sense that once established they do not switch into the basic primary state. The nonunique nature of steady flows can possibly be the cause of the difficulty in predicting runnability in many practical situations.

2. When the Reynolds number - the control parameter of the flow based on cavity width and fluid Brookfield viscosity (@ 100 rpm) - increases, centrifugal instabilities set in in the form of Taylor-Görtler-type vortices, pairs of counter-rotating rolls with axes parallel to the machine direction. The vortices meander along the span of the cavity, progressively oscillating, and eventually evolving into more complex states. There is little doubt that similar vortices appear in the pond of short-dwell coaters and other confined-flow geometries of size press equipment. It is suggested that regions between these vortices are characterized by differential mass transport and uneven momentum transfer into the blade nip. Critical values of the control parameter for onset of the various transitional modes of flow have been identified for square cavities with a span-to-width aspect ratio of 3 to 1.

Trials in a pilot-plant SDC facility with coating colors having problematic runnability showed the following:

1. Within the range over which the fluid viscosity was varied and for a specific type of pigment (i.e., delaminated English clay), appearance of streaks on LWC papers correlates well with expected onset of hydrodynamic instabilities in the pond. For a pilot coater having a span-to-width ratio of 10 to 1, streaks appear in their marginal form at $550<Re_a<750$ and in their severe form at Re_a greater than 1100. These results suggest that pond hydrodynamics constitute an important factor affecting runnability of high-speed SDC coaters.

2. However, these results are based on viscosity values of at least 900 mPa.s attained, for example, when processing formulations containing large proportions of delaminated clays at high solids content. These colors are shear thinning thixotropic, but demonstrate unusually high low-shear viscosity and yield stress. For colors having lower viscosities or solids content, the streaks actually disappear although the Reynolds number will be higher. Thus, onset of instabilities might constitutes an adequate condition for onset of streaks.

The results from this study do not provide enough information to completely pinpoint the origin of streaks and to explain the physics involved. Although a hypothesis has been stated for these coat weight nonuniformities, we will spare the reader until more concrete evidence can be produced. This study, however, increased the understanding of the problem and has proven, with concrete evidence, the existence of some new flow instability issues which may influence the operation of short-dwell coaters and other equipment for web modification with similar hydrodynamic characteristics.

ACKNOWLEDGEMENTS

I am sincerely indebted to my thesis advisor, Dr. Cyrus K. Aidun, for his guidance and the benefit of his in-depth knowledge in fluid dynamics. The incisive manner in which he posed questions and comments on my dissertation work has permanently changed my viewpoint on understanding the physics of fluid dynamic processes. I am also grateful to my former advisor, Dr. Ted Farrington, for letting me pursue this project. His encouragement and excitement were the driving forces at the beginning stages of my thesis. Also, I like to extent my appreciation to the rest of my committee, Dr. Jeff Lindsay and Jay Shands, for their indispensable advise and continuous stimulation. Finally, I like to thank Dr. Sergio Torza for supporting our original idea and assisting in the implementation of the experimental design.

I would like to express my deep appreciation to a number of people who made the completion of this work possible. Foremost, to Dennis Spencer, for his intuition in developing the flash x-ray radiographic techniques and building many parts of the experimental equipment. To John Schamell of Beloit Corp. and his group for designing and engineering the most crucial parts of the experimental equipment. To Gerry Kloth, Russ Tyler, Tom Hartman, and Glenn Winkler, for helping in setting up the experimental apparatus. To Lyle Vandenberg, Rich Mirabello, and Rod Lane for constructing the room of the experimental facility. To Mary Cronmiller for her help in the literature review. To Fred Sweeney, Don Beyer, and Bill Sommers for teaching me good photography and preparing slides for my presentations. To Zahed Sheikh and Kurt Fretz of Creare Inc. for their insights in computational fluid dynamics. To John Dean and Tom Parshall of Kaltec Scientific, Inc., and Pete Wheeler of Mitech Corp. for providing essential help in viscometric measurements. To Rick Huss of James River Corp., Neenah, WI, for helping me to prepare coating colors for this work. Finally, to Bruce Andrews and Tom Hughes for the lengthy discussions on the practical aspects of my results.

During my work at Beloit Corp. many people assisted me in one way or another. I would like to extent my sincere appreciation to Leroy (Pete) Busker for giving me the opportunity to complete my work at Rockton. The Coating Bay group of Gerry Garde, Mark Ryan, Trevor Porter, Glenn Johnson, and Pam Hynnek was indispensible when it came down to performing the actual pilot plant trials. It was my pleasure to work with them. Larry Sanford, Alfred Li, Sam Keller, and Jerry Emmanuel patiently tolerated my frustrations and helped me in many aspects of data acquistion and analysis techniques.

I am also grateful to a number of people for reasons not directly related to the completion of my thesis. Special thanks to all my fellow students, staff, and faculty at The (formly) Institute of Paper Chemistry for unknowingly helping to prolong my stay in the graduate school by making it more enjoyable.

This work was financially supported by The Institute of Paper Science & Technology and its member companies. Beloit Corporation provided expertises, donated the experimental apparatus, and financially supported parts of this work conducted at the Rockton Research Center. Their confidence in me is greatly appreciated.

Last, but no means least, a special thanks to my parents and grandmothers whose encouragement meant and continues to mean a lot to me. Without their emotional and financial support during my early years in The United States I would not have made it.

LITERATURE CITED

1. Unpublished data, Beloit Corporation, Rockton Research & Development Center, Beloit, WI, 1986-1989.

2. Eklund, D.E.; Strömberg, M. Das Strömungsbild beim Short-Dwell-Blade Strichauftrag. Wochbl. Papierfabr. 114(6):203-205(March 1986).

3. Eklund, D. E.; Norrdahl, P. C. The Flow Characteristics in a Short Dwell Coater. Coating Con -ference Proceedings. TAPPI Press, Atlanta, GA, 1986: 99-102.

4. Korpela, M.; Palsanen, J.; Pitkanen, S. Practical Experience with SDTA. Wochbl. Papierfabr. 114(8): 267-271(April 30, 1986).

5. Beisswanger, R. Coating Paper and Board, Practical Experience with the Short-dwell and Long-dwell Time Applicators. Blade Coating Seminar Notes. TAPPI Press, Atlanta, GA, 1986:137-143.

6. Baumeister, M. Experiences with Short-dwell Coating Aggregates. Coating 19(11): 384-387(Nov. 1986).

7. Ruckert, H.; Sommer, H. -P. Development of a Coating Device for Low Coating Weight at High Production Speed and High Solids Content. Wochbl. Papierfabrik. 114(5) :141-147(March 15, 1986).

8. Sommer, H. -P. Applicating Systems for Coating Ultra-lightweight Coated and Machine Finish Pigmentized Papers. Coating Conference Proceedings. TAPPI Press, Atlanta, GA, 1988:131-137.

9. Baumeister, M. European Coating Technology. Pulp Paper Can. 90(3):T100-T111(1989).

10. Sollinger, H.-P. Dynamic Coater -seine Auftrags- und Egalisiersysteme. Wochbl. Papierfabrik. 117(8):332-338(April 1989).

11. Triantafillopoulos, N.; Rudemiller, G.; Farrington, T.; Lindsay, J. Numerical Simulation of Short Dwell Pond Flows. Engineering Conference Proceedings, Book 1, TAPPI Press, Atlanta, GA, 1988, pp. 209-218.

12. Triantafillopoulos, N.; Rudemiller, G.; Aidun, C. Numerical Experiments of Short Dwell Coater Pond Flows, Int'l Symposium Pigment Coating Structure and Rheology. INSKO, Helsinki, Finland, Feb. 8-9, 1989.

13. Affes, H.; Conlisk, A.T.; Foster, M.R. The Steady Flow in a Short Dwell Coater. Coating Conference Proceedings. TAPPI Press, Atlanta, GA, 1990, pp. 299-307.

14. Higgins, B.G. Dynamics of Coating, Adhesion and Wetting, Status Report, Project 3328, PAC Meeting. The Institute of Paper Chemistry, Appleton, WI, Oct. 20, 1981, pp. 33-43.

15. Pranckh, F. R.; Scriven, L. E. Electrodrynamics of Blade Coating. AIChE J. 36(4):587-597 (1990).

16. Hydrodynamic Instabilities and the Transition to Turbulence. (H.L. Swinney, J. P.Gollub, Ed.) Topics in Applied Physics. Volume 45. Springer-Verlag, New York, 1981.

17. Eklund, D. E. Influence of Blade Geometry and Blade Pressure on the Appearance of a Coated Sur- face. Coating Conference Proceedings. TAPPI Press, Atlanta, GA, 1984: 37-41; Tappi, 67(5): 66-70 (1984).

18. Kuzmak, J. M. Bevelled-blade coating: Factors affecting coat weight. Coating Conference Proceedings. TAPPI Press, Atlanta, GA, 1985:

19. Eklund, D.E. Water Transport in the Blade Coating Process. Coating Conference Proceedings. TAPPI Press, Atlanta, GA, 1986:1-5.

20. Follette, W. J.; Fowels, R. W. Operating Variables of a Blade Coater. Tappi 43(11): 953-957 (Nov. 1960).

21. Böhmer, E. Shear Rates Developed in Trailing Blade Coaters. Svensk Papperstid. 67(9):347-355(May 1964).

22. Clark, N. O.; Windle, W.; Restall, C. A. The Heliocoater - A Novel Approach to a Study of the Problems of Blade Coating Machines. Paper Trade J. 15(38):49-54 (Sept. 16, 1966).

23. Böhmer, E. The Relationship Between Coating Weight and Other Variables During Blade Coating. Norsk Skogindustri :308-324(Nov. 1969).

24. Bliesner, W. C. Basic Mechanisms in Blade Coating. Tappi 54(10):1673-1679(Oct. 1971).

25. Modrak, J. P. Effect of Coating Color Rheology on the Blade Coating Process. Coating Conference Proceedings. TAPPI Press, Atlanta, GA, 1973:35-41; Tappi 56(10):70-73 (Oct. 1973); NAPS Document 02184.

26. Hayward, G. Factors Affecting the Metering Characteristics of a Blade Coater. Coating Conference Proceedings. TAPPI Press, Atlanta, GA, 1973:61-71.

27. Turai, L. L. Analysis of the Blade Coating Process. Tappi 54(8):1315-1318(Aug. 1971).

28. Ginn, R. F. A Fundamental Study of the Blade Coating Process. Project 3069, Report One, The Institute of Paper Chemistry, Appleton, WI, July 27, 1973.

29. Gartaganis, P. A.; Cleland, A. J.; Wairegi, T. Blade Mechanics of Extended Blade Coaters: Theory and Practice. Coating Conference Proceedings. TAPPI Press, Atlanta, GA 1977:145-155; Tappi 61(4):77-81(April 1978); Blade Coating Seminar. TAPPI Press, Atlanta, GA, 1982:5-14.

30. Ginn, R. F. High Shear Rheology in Blade Coater. Part I. A Mathematical Model. Part II. Experimental. J. Pulp Paper Sci. 109(4):J89-J98(July 1984).

31. Kuzmak, J. M. Bevelled-blade Coating. Tappi J. 69(2):72-75(Feb. 1986).

32. Kuzmak, J. M. Bevelled-blade coating: Factors Affecting Coat Weight. Blade Coating Seminar Notes. TAPPI Press, Atlanta, GA, 1986:72-75.

33. Böhmer, E.; Lute, J. A Laboratory Evaluation of Pigment Suspensions for Trailing Blade. SystemsSvensk Papperstindning 68(20):711-720(Oct. 31, 1965).

34. Böhmer, E.; Lute, J. Adhesive Migration and Water Retention with Reference to Blade Coating. Svensk Papperstindning 69(10):610-618(Sept. 30, 1966).

35. Windle, W.; Beazley, K.M.; Climpson, M. Liquid Migration from Coating Colors. Tappi 53(12):2232-2236(Dec. 1970).

36. Engström, G. Die Entwicklung des Feststoffgehaltes in der Strichschicht zwischen Auftrag und Blade. Wochbl. Ppaierfabr. 114(6):195-199(March 1986).

37. Luciani, M.; Galloni, M. Base Paper and Coating Colour in the Trailing Blade Process:Dependence of Coating Weight on Raw Stock Smoothness. Paper 190(4): 183-189((Aug. 12, 1978).

38. Slott-Moller, R. Coating Systems - A General Study. ATIP Rev. 33(4):153-169(April 1979).

39. Windle, W.; Beazley, K.M. The Role of Viscoelasticity in Blade Coating. Tappi 51(8):340-348 (Aug. 1968)

40. Batchelor, G.K. An Introduction to Fluid Dynamics. Cambridge University Press, Great Britain, 1967,pp. 219-222.

41. Hwang, S. S. Hydrodynamic Analyses of Blade Coaters. Chem. Eng. Sci. 34: 181-189(1979).

42. Hwang, S. S. Non-Newtonian Liquid Blade Coating Process. J. Fluid Eng., Trans. ASME, . 104:469-474(Dec. 1982).

43. Greener, Y.; Middleman, S. Blade-Coating of a Viscoelastic Fluid. Pol. Eng. Sci. 14(11):791-796 (1974).

44. Hsu, T. C.; Malone, M.; Laurence, R. L.; Middleman, S. Separating Forces in Blade Coating of Viscous and Viscoelastic Liquids. J. Non-Newtonian Fluid Mech. 18:273-294 (1985).

45. Sullivan, T.; Middleman, S.; Keunings, R. Use of a Finite-Element Method to Interpret Rheological Effects in Blade Coating. AIChE J. 33(12):2047-2056 (Dec. 1987).

46. Guzy, C. J.; Higgins, B. G. Viscous Pressure Across the Nip of a Blade Coater and its Effect on the Final Coated Film Thickness. Coating Conference Proceedings. TAPPI Press, Atlanta, GA. 1982: 63-71.

47. Higgins, B. G. Dynamics of Coating, Adhesion and Wetting. Status Report, Project 3328, PAC Meeting, Appleton, WI, The Institute of Paper Chemistry, Mar. 24, 1981, pp. 69-74.

48. Windle, W.; Beazley, K.M. The Mechanics of Blade Coating. Tappi 50(1):1-7(Jan. 1967).

49. Kahila, S. J.; Eklund, D. E. Factors Influencing the Coat Weight in Blade Coating with Bevelled Blades: Theory and Practice. Coating Conference Proceedings. TAPPI Press, Atlanta, GA,1978:13-25.

50. Kahila, S. J.; Eklund, D. E. Processes Occurring under the Blade During Blade Coating (1) Theory. Wochbl. Papierfabrik. 106(17):661-665(Sept. 15, 1978).

51. Kahila, S. J.; Eklund, D. E.; Obetko, D. Processes Occurring under the Blade During Blade Coating: (2) Practical Tests. Wochbl. Papierfabrik. 106(18):709-714(Sept. 30, 1978).

52. Pranckh, F. R.; Scriven, L. E. The Physics of Blade Coating of Deformable Substrate. Coating Conference Proceedings. TAPPI Press, Atlanta, GA, 1988:217-238.

53. Chen, K.S.A.; Scriven, L.E. On the Physics of Liquid Penetration into a Deformable Porous Substrate. Coating Conference Proceedings. TAPPI Press, Atlanta, GA, 1989: 93-106.

54. Ducey, M. J. New Short-dwell Coaters Reduce Raw Material Losses ans Downtime. Pulp Paper 58(5):102-104(May 1984).

55. Peiffer, R. Modern Blade Coaters. Blade Coater Seminar Notes. TAPPI Press, Atlanta, GA,1984:11-14.

56. Rautiainen, P. J.; Luomi, S. T. High Speed Coating Processes - Trends and Developments. Coating Conference Proceedings. TAPPI Press, Atlanta, GA, 1984: 121-128.

57. Thorndike, W. K., A Five-month Comparison of Applicator Roll and Short-dwell Blade Coaters. Blade Coating Seminar Notes. TAPPI Press, Atlanta, GA, 1984:47-49.

58. Brown, J. F. Commercial Experience with Short-dwell Coating on Light Weight Coated Paper. Coating Conference Proceedings. TAPPI Press, Atlanta, GA, 1984:71-75.

59. Dorr, R. S. Short-dwell Coaters' Operation. Paper Presented at the ME-NH TAPPI Meeting. Portland, Maine, Oct. 16, 1985.

60. Technical Information Sheet TIS 110.01. Blade Defects. TAPPI Press, Atlanta, GA, 1969.

61. Weigl., J.; Baumeister, M. Influencing Factors and their Effect on Coating Morphology, Deut. Papierwirt 3:147-162 (1980).

62. Maull, D. J.; East, L. F. Three-dimensional Flow in Cavities. J. Fluid Mech. 16:620-632 (1963).61.

63. Mills, R. D. On the Closed Motion of a Fluid in a Square Cavity. J. Royal Aeron. Soc. 69:116-120 (Feb. 1965).

64. Johnson, R. W.; Dhanak, A. M. Heat Transfer in Laminar Flow Past a Rectangular Cavity with Fluid Injection. J. Heat Transfer, Trans. ASME: 226-231 (May 1976).

65. Reiman, L. C.; Sabersky, R. H. Laminar Flow over Rectangular Cavities. Int. J. Heat Mass Transfer, 11:1083-1085 (1968).

66. Haugen, R. L.; Dhanak, A. M. Momentum Transfer in Turbulent Separated Flow Past a Rectangular Cavity. J. Appl. Mech, Trans. Series E. ASME 33(3): 641-646 (Sep. 1966).

67. Weiss, R. F.; Florsheim, B. H. Flow in a Cavity at Low Reynolds Number. Phys. Fluids, 8(9): 1631-1635 (Sep. 1965).

68. Roshko, A. Some Measurements of Flow in Rectangular Cut-out. NASA Technical Report 3488,1955.

69. Fox, J. Flow Regimes in Transverse Rectangular Cavities. In Heat Transfer and Fluid Mechanics. Stanford University Press, 1965, pp. 230-247.

70. Orlandi, P.; Ianetta, S. Laser Doppler Anemometer Flow Measurements in a Channel with a Wall Cut-out. 13th Biennial Fluid Dynamics Symposium, Kortowo, 1977.

71. Rockwell, D.; Knisely, C. Observations of the Three-Dimensional Nature of Unstable Flow Past a Cavity. Phys. Fluids 23(3):425-431(1980).

72. Neary, M.D.; Stephanoff, K.D., Shear-Layer-Driven Transition in a Rectangular Cavity. Phys. Fluids 30(10):2936-2946(Oct. 1987).

73. Mills, R. D. Numerical Simulation of the Viscous Flow Equations for a Class of Closed Flows. J. Royal Aeron. Soc. 69 :714-718(September, 1965).

74. Pan, F.; Acrivos, A. Steady Flows in Rectangular Cavities. J. Fluid Mech. 28(4): 643-655(1967).

75. Chashechkin, J. D. Experimental Studies of the Mixed Layer in Stratified Liquids. 2nd Int. Symp. Stratified Flows, Trondheim, Norway 2 : 783-790(June, 1980).

76. Koseff, J.R.;Street, R.L. Visualization Studies of Shear Driven Three-dimensional Recirculating Flow. Proc. Three Dimensional Turbulent Shear Flows Conf., ASME, St. Louis, June 7-11, 1982: 23-31.

77. Koseff,J. R. Momentum Transfer in a Complex Recirculating Flow. Doctoral Dissertation. The Department of Civil Engineering. Stanford University, CA, 1983.

78. Koseff,J.R., and Street,R.L. Visualization Studies of a Shear Driven Three-dimensional Recirculating Flow. J. Fluid Eng. 106(3):21-29(March 1984).

79. Rhee, H.S.; Koseff, J. R.; Street, R.L. Flow Visualization of a Recirculating Flow by Rheoscopic Liquid and Liquid Crystal Techniques. Exp. Fluids 2:57-64(1984).

80. Prasad, A.K.; Koseff, J.R., Reynolds Number and End-Wall Effects on a Lid-Driven Cavity Flow. Phys. Fluids A1(2):208-218(Feb. 1989).

81. Taylor, G.I. Stability of a Viscous Liquid Contained Between Two Rotating Cylinders. Phil. Trans. Royal Soc. London, Series A 223 :289-343(1923).

82. Görtler,H. Nachr. Akad. Wiss. Göttingen, Math. Phys. Kl. 2 (1940); translated as "On the Three Dimensional Instabilities of Laminar Boundary Layers on Concave Walls". Tech. Memorandum 1375, NACA, 1954.

83. Freitas, C.J., Non-Linear Transient Phenomena in a Complex Recirculating Flow: A Numerical Investigation. Doctoral Dissertation. The Department of Civil Engineering. Stanford University, CA, 1986.

84. Freitas, C.J.; Street, R.L., Non-Linear Transient Phenomena in a Complex Recirculating Flow: A Numerical Investigation. Int'l J. Num. Meth. Fluids, 8: 769-802(1988).

85. De Vahl Davis, G.; Mallinson, G. D. An Evaluation of Upwind and Central Difference Approximations by a Study of Recirculating Flow. Comp. Fluids 4 :29-43 (1976).

86. Tuann, S.; Olson, M.D., Review of Computing Methods for Recirculating Flows. J. Comput. Phys. 29:1-19(1978).

87. Goda, K., A Multistep Technique with Implicit Difference Schemes for Circulating Two- or Three-Dimensional Cavity Flows. J. Comput. Phys., 30:79-95(1979).

88. Gresho, P. M.; Chan, S.T.; Lee, R. L.; Upson, C.D. Solution of the Time-dependent, Three Dimensional Incompressible Navier-Stokes Equations via FEM. Proc. 2nd Int'l Conf. on Num. Meth. Lam & Turbl. Flow, 1981: 27-39.

89. Koseff, J.R.; Street, R. L.; Gresho, P. M.; Upson, C. D.; Humphrey, J. A. C.; To, W. -M. A Three Dimensional Lid-driven Cavity Flow: Experiment and Simulation. Proc. 3rd Int'l Conf. Num. Methods Lam. & Turbl. Flow, 1983: 564-581.

90. Freitas, C.J.; Street, R. L.; Findikakis, A. N.; Koseff, J. R. Numerical Simulation of Three Dimensional Flow in a Cavity. Int'l J. Num. Meth. Fluids 5 :561-575(1985).

91. Kim, J.; Moin, P. J. Application of a Fractional-Step Method to Incompressible Navier-Stokes Equations. Comp. Physics 59(2) :308- 323(1985).

92. Hwang, D.P.; Huygh, H.T. A Finite Difference Scheme for Three-dimensional Steady Laminar Incompressible Flow. Proc. 5th Int'l Conf. on Num. Methods Lam. & Turbl. Flow 5(1):244-260 (1987).

93. Ku,H.C.; Taylor, T.D.; Hirsh, R.S., Pseudospectral Methods for Solution of the Incompressible Navier-Stokes Equations. Comptures & Fluids, 15(2):195-214(1987).

94. Iwatsu, K.I.; Kawamura, T.; Kuwahara, Numerical Simulation of Three-Dimensional Flow Structure in a Driven Cavity. The Japan Society of Fluid Mechanics. Fluid Dynamics Research, 5:173-189(1989).

95. Hutchings, B.; Iannuzzelli, R. Mechanical Engineering, 109(5):72-76; (6):54-58; (7):60-63 (1987).

96. Boni, A.A.; Srinivasachars, S.J. J. Mech. Eng. Computing and Applications, 2(1):63-69 (Fall 1987).

97. Patankar, S.V. Numerical Heat Transfer and Fluid Flow. Hemisphere Publishing Corp., McGraw-Hill Book Co., New York, 1980.

98. FLUENT Manual. Version 2.9. Technical Note TN-369 Rev. 2.82. Creare Inc., Hannover, NH, 1987.

99. Sheikh, Z. Personal Communication, Creare, Inc., Hannover, NH, October 1987.

100. FLUENT User's Newsletter, 2(2):3,8 (1987).

101. Böhmer, E.; Lute, J. Svensk Pappestidning, 68(20):711-720(1965).

102. Czaban, S.; Parzonka, W.; Havlik, V. Non-Newtonian Behaviour of Kaolin Suspensions. Progress and Trends in Rheology II. Supplement to Rheologica Acta, 1988, pp. 325-328.

103. Hyman, W. A. Rheology of Power Law Fluids. I&EC Fund, 15:215-218 (August 1976).

104. Shands, J., Personal Communication, Beloit Corp., Spring 1987.

105. Aidun, C.K. Mechanics of Steady Isothermal Spinning of a Viscoelastic Liquid Film. Proc. Southern Conf. Theor. Appl Mechanics, 2:811-816(1986).

106. Saito, H.; Ishizuka, S.; Fuchigami, S. Instability of the Slide Coating Flow. Paper presented at the AIChE Meeting, International Symposium of Thin-film Mechanics, Orlando, FL, Feb 28 -Mar. 3, 1982.

107. Mueller, T.J. Flow Visualization by Direct Injection. In Fluid Mechanics Measurements. Chapter 7. (R.J.Goldstein, ed.) Hemisphere Publishing Corp., Washington, DC, 1985, pp. 354.

108. Quraishi, M.S.; Fahidy, T. Z. Techniques for Flow Pattern Studies. In Encyclopedia of Fluid Mechanics. Chapter 28. Vol. 3. (N. P. Cheremisinoff, ed.) Gulf Publishing Co., Houston, TX, 1986, pp. 811-840.

109. Gutoff, E. B.; Kendrick, C. E. Dynamic Contact Angles. AIChE 28(3):459-466(May 1982).

110. Catwell, B.; Coles, D.; Dimotakis, P. Structure and Entrainment in the Plane of Symmetry of a Turbulent Spot. J. Fluid Mech. 87:641-672(1978).

111. Gad-el-Hak, M. Visualization Techniques for Unsteady Flows: An Overview. J. Fluid Eng., Trans. ASME 110(3) :231-243(September, 1988).

112. Carbonnier, F. Nondestructive Testing Handbook: Flash Radiography. ASNT, Columbus, OH, 1983.

113. Bahl, K. L.; Vantine, H. C. A Flash Radiography Technique Applied to Fuel Injection Sprays. Proc. Flash Radiography Symp., (L. E. Bryant, ed.), ASNT, Columbus, OH, 1977, pp. 193-200 .

114. Farrington, T. E. Flash X-ray Imaging of Kraft Black Liquor Sprays. Tappi. 71(2): 89-92(Feb. 1988).

115. Triantafillopoulos, N.G.; Farrington, T. Flash X-ray Radiography Techniques for Visualizing Coating Flows. Proc. Coating Conference. TAPPI Press, Atlanta, GA, 1988, pp. 48-52.

116. Janet, F.; Thomer, G. Flash Radiography. Elsevier Publishing Co., Amsterdam, The Netherlands, 1976.

117. Kline, S. J. The Purpose of Uncertainty Analysis. J. Fluid Eng., ASME, 107 :153-160(June, 1985).

118. Moffat, R. J. Contributions to the Theory of Single-sample Uncertainty Analysis. J. Fluid Eng., ASME,107: 250-260(June,1982).

119. Abernethy, R. B.; Benedict, R. P.; Dowdell, R. B. Measurement Uncertainty. J. Fluid Eng., ASME, 107:161-164 (June, 1985).

120. Burggraf, O.R. Analytical and Numerical Studies of the Structure of Steady Separated Flows. J. Fluid Mech. 24(1):113-151 (1966).

121. Bozeman, J.D.; Dalton, C. Numerical Study of Viscous Flow in a Cavity. J. Comp. Physics 12:348-363(1973).

122. Nallasamy, M.; Krishna Prasad, K. On the Cavity Flow at High Reynolds Numbers. J. Fluid Mech. 79:391414(1977).

123. Pao, H-P. A Numerical Computation of a Confined Rotating Flow. J. Appl. Mech., ASME 37(E2):408-486(1970).

124. de Brederoede, V.; Bradsaw, P. Three Dimensional Flow in Nominally Two-Dimensional Separation Bubbles I. Flow Behind a Rearward Facing Step. I. C. Aero. Report. No. 72-19(Aug. 1972).

125. Aidun, C.; Triantafillopoulos, N. Global Stability Properties of Flow in a Short-dwell Blade Coater. Int'l Symposium of Thin-film Mecahnics, Spring National Meeting AIChE, Orlando, FL, 1990.

126. Wesfreid, J. E.; Zaleski, S. Cellular Structures in Instabilities. Springer-Verlag, New York, 1984, pp. 1-19.

127. Peerhossaini, H.; Wesfreid, J. E. Experimental Study of the Taylor-Görtler Instability. Proc. Propagation in Systems Far from Equilibrium, Springer-Verlag, Berlin, 1987, pp. 399-412.

128. Wortmann, F.X. Visualization of Transition. J. Fluid Mech. 38(3):473-480(1969).

129. Ito, A. Visualization of Boundary Layer Transition along a Concave Wall. In Flow Visualization III, (C. Vévet, ed.), Hemisphere Publishing Co., Washington, D. C., 1985, pp. 339-344.

130. Blackwelder, R.F. Analogies between Transitional and Turbulent Boundary Layers. Phys. Fluids 26(10):2807-2815 (Oct. 1983).

131. Kataoka, K. Taylor Vortices and Instabilities in Circular Couette Flows. In Encyclopedia of Fluid Mechanics. Chapter 9.,Vol. 1 (N. P. Cheremisinoff, ed.) Gulf Publishing Co., Houston, TX, 1986, pp. 261-265.

132. Aidun, C. Principles of Hydrodynamic Instability in Coating Systems. Coating Conference Proceedings, TAPPI Press, Atlanta, GA, 1990, pp. 275-308.

133. Li, A., Personal Communication, Rockton Research Center, Beloit Corp., September 1989.

134. Gane, P. A. C.; Coggon, L. Coating Blade Geometry: Its Effect on Coating Color Dynamics and Coated Sheet Properties. Coating Conference Proceedings. TAPPI Press, Atlanta, GA,1987: 7-18; Tappi J. 70(12):87-96 (Dec. 1987).

135. Gane, P. A. C.; Watters, P. Pigment Particle Orientation: An Analysis of the Opportunities for Optimizing Blade Coater Runnability and Coated Sheet Properties by Controlled Flow Geometry. Int'l Symposium Pigment Coating Structure and Rheology. INSKO, Helsinki, Finland, Feb. 8-9, 1989.

136. Burley, R.; Kennedy, B.S. An Experimental Study of Air Entrainment at a Solid/Liquid/Gas Interface. Chem. Eng. Sci. 31:901-911(1976).

137. Gutoff, E. B.; Kendrick, C. E. Low Flow Limits of Coatability on a Slide Coater. AIChE 33(1):141-145(Jan 1987).

APPENDIX A

SUPPLEMENTARY INFORMATION ON THE EXPERIMENTAL FACILITY FOR FLOW VISUALIZATION

This section provides detailed information about the experimental facility specifically designed for flow visualization in a roll-driven cavity with through-flow. Table 11 at the end of this section lists the important components of the system, the material that they are made out of, and their reference identification numbers on blueprint drawings.

Drive System and Support Structure

The system that drives the flow consists of a roll mounted on a set of roller bearings in pillow blocks supported by frame work (Fig. 60, 61 and 62). The hollow stainless steel roll, 60 cm in diameter, 202 cm in circumference, and 46 cm long , has a chrome plated surface (face only) polished to 100-microns microroughness to provide a smooth boundary for driving the flow. One end the roll shaft has a drive stick-out for a driving belt. This rubber belt is mounted onto the roll shaft with a 60-groove pulley and onto a motor with a 24-groove pulley, i.e., 2.5 speed reduction between the motor and the roll shaft. The motor is a variable speed Reliance D.C. motor with maximum output of 1750 rpm, corresponding to 1400 m/min peripheral roll speed.

The framework where the roll stands is solidly bolted on to the floor with stands grounded in concrete. The stands, which are located at each corner of the frame, have four hold-down bolts attached on the floor and four threaded leveling screws attached on to the frame. By adjusting each one of these screws individually during installation, the roll could be positioned properly onto the frame and balanced for speeds up to 1500 m/min. Dynamic balancing of the roll is critical because small deviations from its concentric rotation could have a substantial effect on the flow inside the cavity, especially in the transverse (spanwise) direction.

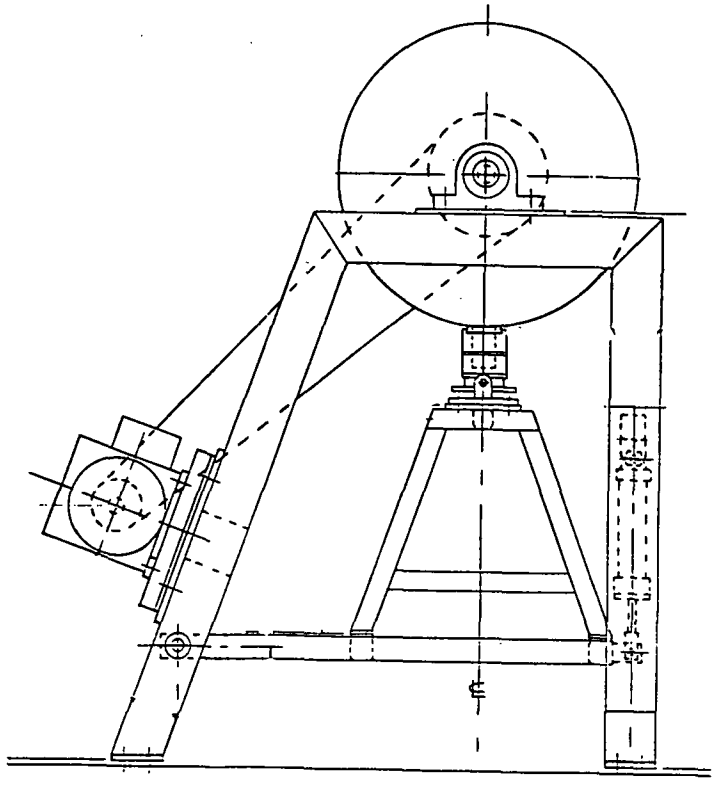

Figure 60. Schematic of laboratory coater; side-end view.

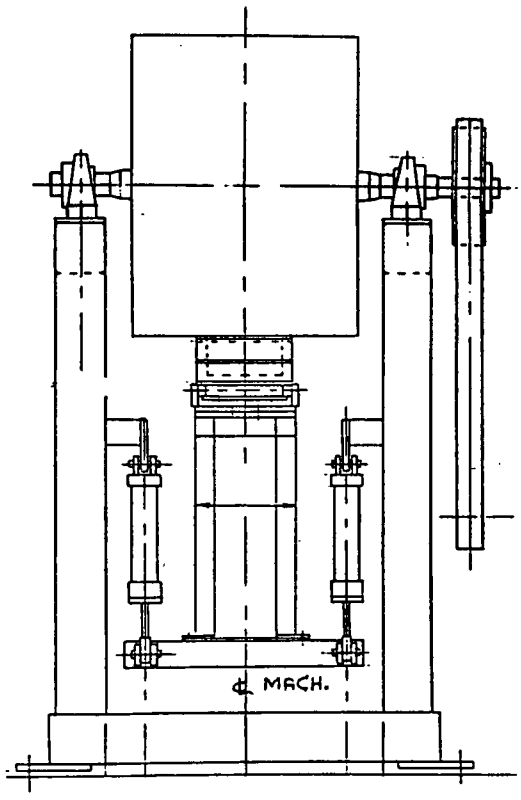

Figure 61. Schematic of laboratory coater; front-end view.

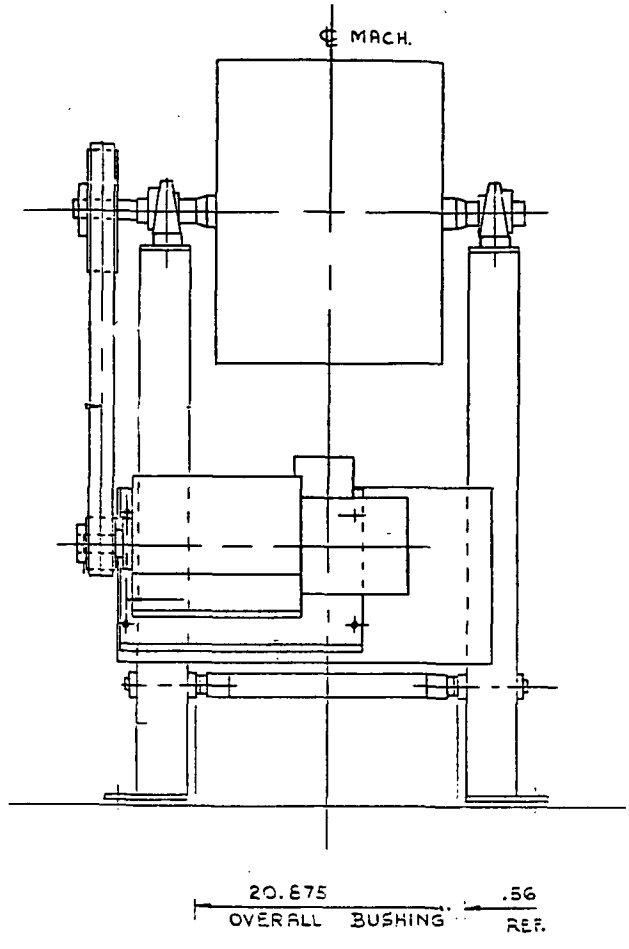

Figure 62. Schematic of laboratory coater; back-end view.

Cavities and Their Support Stand

The cavity assemblies consist of the (upper) observation cavity and the (lower) feeding chamber connected together with long threaded screws and separated by a plate having a feeding slot (3 cm wide) next to the upstream vertical wall of the cavity. A 1.0-cm thick Teflon collar fits in the cavity lip to reduce frictional losses from the contact with the roll surface. Both the collar and the plate are secured in their respective places with RTV rubber cement, which seals from leakage but it is also easily removable in case these parts need to be replaced.

Although the function of the perforated plate is to uniformly distribute the feeding fluid in to the observation cavity, this is not always successful, especially when the roll is moving at speeds above 150 m/min hence reverse flow occurs, i.e., in the direction from the top cavity in to the lower feeding chamber. Under these circumstances the separation plate interferes with flow structures in the (top) cavity and visualization results are not reliable. Evaluation of two plates with different diameter holes indicated that the one with the smaller holes (3.2 mm) is preferred because it allows for better control of the pressure in the cavity when the roll is moving. In addition, this perforated plate is covered with aluminum foil to form a partitioning wall between the top cavity and the lower chamber with only one row of holes remaining open next to the upstream vertical wall of the cavity (Fig. 22).Through this opening fluid is fed in to the cavity. Another set-up which is also possible is having a 100% open slot for feeding fluid into the cavity. A 1-cm wide slot is utilized in some of the experiments in this research, however, the perforated plate with 3.2 mm hole openings and 40% open area provides the best pressure control inside the cavity and, therefore, maintains uniform contact with the roll surface at peripheral roll speeds even above 250 m/min.

The cavity assembly is mounted on to an adjustable support plate with four threaded screws (Fig. 63 and 64). The plate is pivoted with a pair of screw pins on either side onto the loading stand. This type of pivoting allows for the cavity assembly to get its own center when loaded against the roll. As the roll rotates at various speeds, the cavity can seek its own center by slightly tilting forwards or backwards and, therefore, leveling itself. Such a self-adjusting mechanism is essential to ensure even loading in the transverse direction of the roll movement and avoid skewness of the the roll surface with respect to the lower (feeding) boundary.

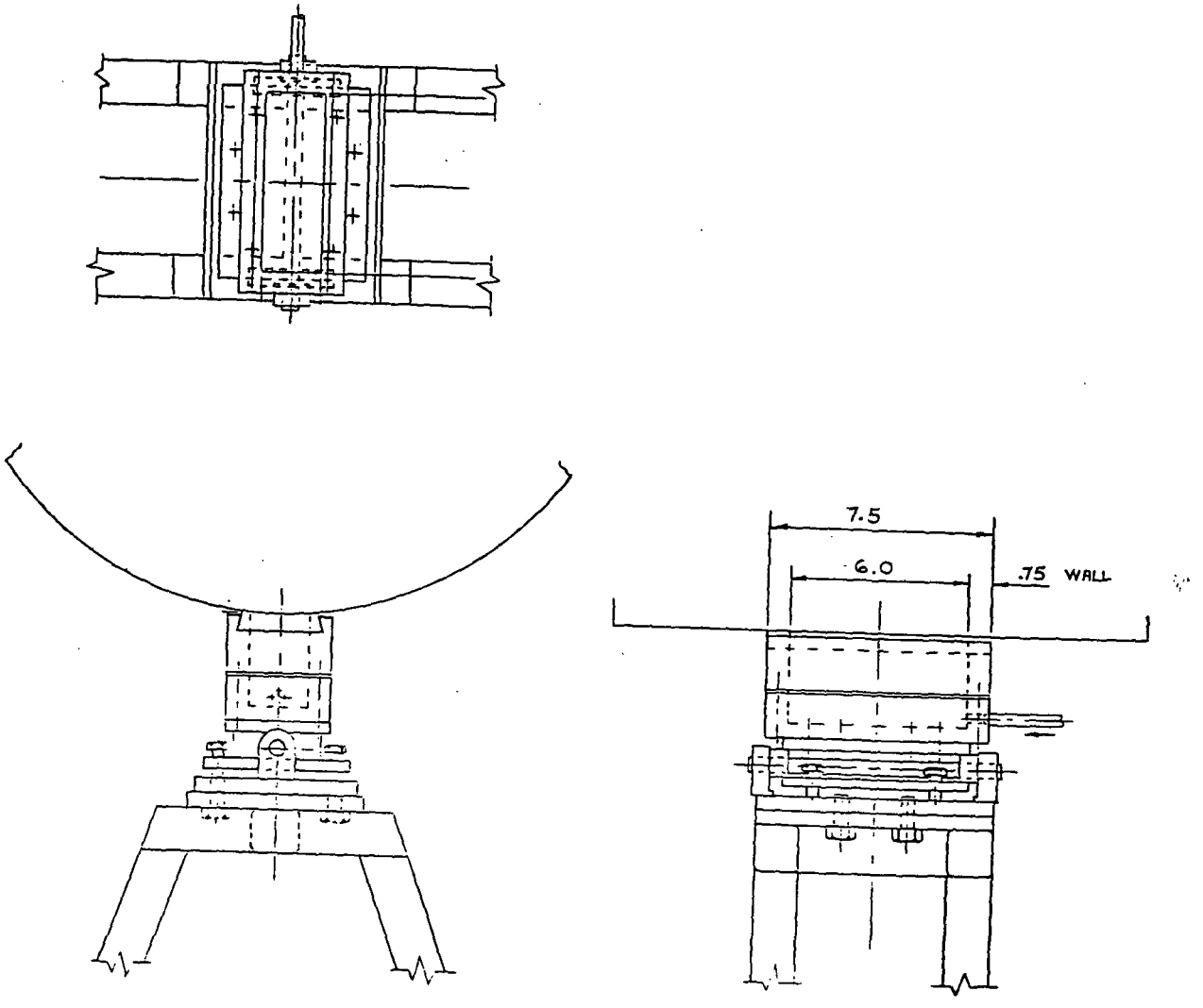

Figure 63. Schematic of large cavity and its arrangement.

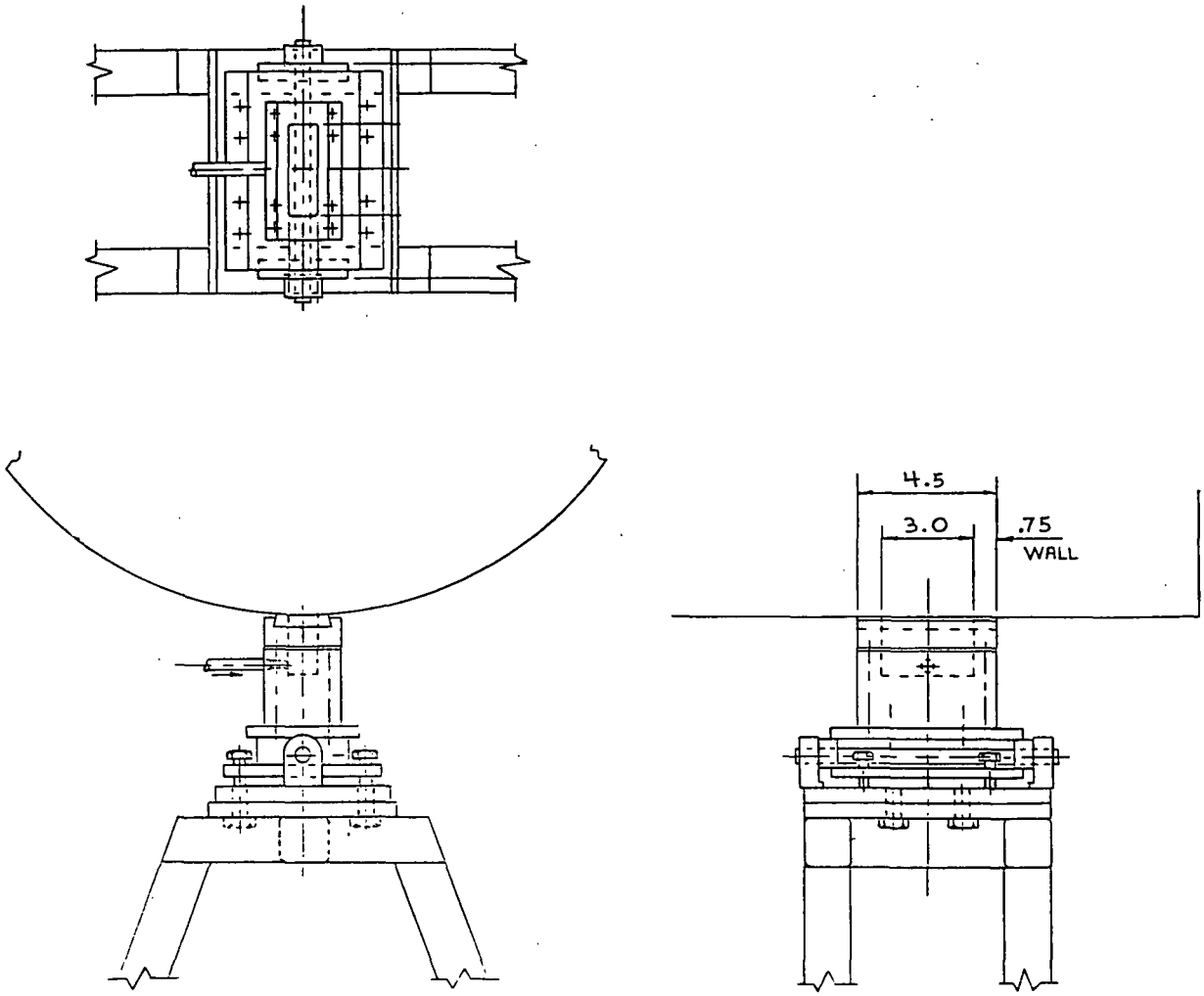

Figure 64. Schematic of small cavity and its arrangement.

Two air-pressurized cylinders raise the loading stand and keep the cavity in contact with the roll by applying hydraulic pressure P_h. This pressure can be externally regulated and is used to control the amount of fluid escaping onto the roll, therefore it determines the value of the through-flow Reynolds number, Re*. The other pressure, Pc, utilized as an operational parameter is a function of the feeding flow rate. As it is described in the flow characterization section, it takes adjustment of both these pressures to ensure that the cavity operates like an enclosed lid-driven system.

Auxiliary Equipment

A cylindrical container, 12.7 cm in diameter and 33.0 cm in height, is initially fabricated for supplying the cavity with fluid. About 2000 ml of fluid inside the container could be pressurized from 2 to 100 kPa with air entering through a flexible tube on the top. However, it was soon realized that this amount of fluid is not enough to operate the system continuously and without interruption. With installation of the 0.15 m^3 reservoir, to hold the supplied to the cavity fluid, the cylindrical container is connected on line with the feeding loop and serves the purpose of damping flow fluctuations induced by the pump. Flexible tubing in this loop has 6.35 mm ID. An on-off valve at the outgoing tubing from the container serves as an emergency shut-off.

An 12.0-cm high air-pressurized cylinder, made out of plexiglas, is utilized to hold up to 450 ml of the x-ray tracing fluid. Air entering through a solenoid valve can pressurize this cylindrical container from 70 to 345 kPa and control the injection speed of the tracing fluid (which also depends on fluid viscosity). At first, a T-shaped piece of plexiglas tubing was utilized to split the injecting stream into four flexible tubes (1.56 mm ID). The solenoid valve allows for initiating injection remotely, i.e., from the outside of the lead-shielded room surrounding the visualization facility. Usual procedure during flash radiography of the flow in the cavity includes (a) loading the cylinder and its injection tubing with the x-ray tracing fluid, (b) setting the air pressure desired, (c) placing the radiographic film behind the cavity, (d) getting outside the lead-shielded room and loading the x-ray unit to appropriate voltage, (e) turning on the solenoid valve for a predetermined period of time, and (f) activating the FXR unit to emit a burst of x-rays and, almost simultaneously, turn off solenoid valve.

Setup of Direct-tracer Injection System

Various setups were used in the course of research to develop a system for adequate injection of an x-ray tracing fluid into the flow field inside the cavity. The objective was to release a stream of tracing fluid which would not disturb the flow, remain coherent for few seconds, and give patterns of the flow. Nevertheless, this task is not always easy to achieve. Because three dimensional flow features were not known from the beginning, it was difficult to estimate where in the flow field injection would yield structures of interest. So, at the beginning most of the direct injection experiments were based on a trial and error method.

The cavity was filled with a typical (opaque) coating color having a total solids content of 60% by weight and including a clay pigment, a latex binder (17 parts per hundred styrenebutadiene emulsion), and 3 parts per hundred of a relatively low molecular weight sodium alginate as a thickener. The tracer was typically a 4% by weight solution of carboxymethylcellulose saturated with sodium tungstate. A detailed discussion about the choice and preparation of the tracing fluid is listed in a following Appendix. Here, however, a brief description of the different arrangements for the tracer injection is given.

Two different kinds of flexible tubing, having 1.56 mm ID and 2.38 mm ID respectively, were installed to vary the flow rate of the injected stream (at constant air pressure). The smaller diameter tubing was preferred due to its greater stream velocity. Using the T-shaped tube to split the flow into equal parts, four flexible tubings was inserted onto four holes of the, at least initially utilized, perforated plate. Thus, the injection streams entered the cavity from its bottom boundary, either flash to the upstream or downstream vertical walls. The idea was to inject the tracer at locations where, from previous experimental work, most of the activity was expected to take place. Results from radiographic studies with this set-up indicated that:

(a) individual lines of the tracing stream can be observed only at roll peripheral speeds above 240 m/min and air pressure in the tracer line of at least 170 kPa. It seems possible that at lower speeds the recirculating flow velocity is not high enough to carry the entering fluid into the bulk of the flow. (At high air pressures and low speeds, the injected streams disrupt the flow as this was determined visually from radiographs.)

(b) At least 3 seconds injection period is required, i.e., time that the solenoid valve remains open, for enough fluid to enter the cavity. Altering the time from 6 to 30 seconds at speeds of 240, 280, 480, and 820 m/min did not help but instead reduced radiographic contrast because of the large amount of tracing fluid present in the cavity.

(c) Line patterns can be detected visually on a radiographic film which have been deflected (in the spanwise direction) from the point of injection. The deflection was mostly towards the side end-walls. However, no coherent flow structures were observed.

(d) Low viscosity tracing fluid diffuses too fast into the bulk of the fluid inside the cavity. An attempt to introduce milk fat with the tracing solution to reduce diffusion rate did not help. Thus, there is a trade-off between diffusion and velocity of the fluid at the injection point.

(f) Plugging of the injection tubing occurs often, especially at high roll speeds. To avoid backflow into these tubes, a one-way plastic valve was installed on-line.

Major problem in these experiments was the diffusion of the x-ray tracing fluid before it would be possible for it to form characteristic structures of the flow. Excess of x-ray tracing fluid had the tendency to react with the coating color and destabilize the clay suspension. Also, possible three dimensional flows could make the problem worst by increasing mixing. Then, it was thought to inject the fluid along rather in the transverse direction of flow at the injection location (which was the cases above) and take a radiograph as soon as possible with minimum injection time (i.e., about 3 seconds). Actually, optimum would be to evenly inject a whole sheet of fluid along the span of the cavity.

A 12.7-cm in length brass tube was inserted in a slot engraved on the Teflon collar of a cavity flash to the downstream vertical endwall as depicted in Fig. (Fig. 22). Both circular and 6.35 mm square tubes were used. The inlet flow was at the middle of the tube, while for outlet various arrangements were tried the most successful being 0.8 mm in diameter (1.6 mm apart) holes drilled across the tube. This design had the advantage of using only one inlet tube (thus reducing pressure drop) and, by feeding in the middle, distributed the flow evenly. However, it was impossible to get a uniform "sheet" of tracer fluid emerging from the tube but only distinct lines emanating close to the center of the cavity (i.e., the middle of the injection tube). This was probably due to the high pressure drop at the first couple of holes, which did not allow for enough pressure to force fluid out of the rest. Thus, only single injection streams could be obtained.

Table 11. Description and references for main parts of experimental equipment used in flow visualization experiments.

Description	Part No.	Reference Drawing	Material
Roll (59.7 cm in diameter)	XP4-7241	XP6-7272	Chrome plated steel
Browning gear belt	--	XP6-7272	Rubber
Parker series heavy duty air cylinders	--	--	--
Roll stand	6XF-9857	XP6-7272	Mild steel
Support frame	3XF-9880	XP6-7272	Mild steel
Support pivoting	6XF9883	XP6-7272	Mild steel
Cavity assembly	--	XP6-7273	--
Cavity stand	--	XP6-7272	--
Adjustable cavity support plate	4XF9882	XP6-7273	Aluminum
Screw pin (removable)	2-XP9579M	XP6-7273	Brass
Cavity pivot	4XF9881	XP6-7273	Aluminum
Cross tie	2-XP6325M-2	XP6-7273	Mild steel
Cavity (2.54 x 2.54 x 7.62 cm)	4-XP9532M	XP6-7273	Clear acrylic Plexiglas (19.05 mm walls)
Feed chamber (2.54 x 2.54 x 7.62 cm)	4-XP9531M	XP6-7273	« «
Cavity (5.08 x 5.08 x15.24 cm)	4-XP9529M	XP6-7273	Clear acrylic Plexiglas (19.05 mm walls)
Feed chamber (5.08 x 5.08 x15.24 cm)	4-XP9528M	XP6-7273	« «
Collar (2.54 x 2.54 x 7.62 cm)	4-XP9533M	XP6-7273	Electrical grade Teflon (10.9 mm)
Collar (5.08 x 5.08 x15.24 cm)	4-XP9530M	XP6-7273	Teflon (10.9 mm)
Perforated plate (3.2 mm holes, 40% open)	--	--	Stainless steel
Perforated plate (6.5 mm holes, 58% open)	--	--	Stainless steel
IPC Cavity (5.08 x 5.08 x15.24 cm)	4-XP9529M	XP6-7273	Plexiglas window, Aluminum frame Teflon collar
Injection tube (11.0 cm length, 6.4 mm ID) with 0.8 mm holes spaced 1.6 mm apart	--	--	Brass
Injection tubing (2.4 mm ID, 5.6 mm OD)	--	--	Flexible plastic

APPENDIX B

FLASH X-RAY RADIOGRAPHIC TECHNIQUES

BACKGROUND

Flash X-ray Systems Characteristics

X-ray generating units for flash radiography (FXR) consist of two main parts: the x-ray tube and the pulsed high voltage source. Tubes for FXR produce relatively high peak current densities and effectively focus the electron beam by commonly utilized field emission technology.[1] When high voltage is applied between the cathode (the emitter) and the anode (the x-ray target), electron are "pulled" out of the metallic emitter by the extremely high electrical field created on its needle-like points (Fig. 65). Such a process leads to cathode surface vaporization and vacuum arc breakdown. Consequently, a maximum possible cathode emission occurs during the extremely short period of a pulse. The target is usually tungsten due to this element's high melting point, atomic number, and good electrical and thermal conductivities. A thin Beryllium window is used in front of the tube which allows for low energy soft x-rays (below 5 keV) to pass through, while Kovar windows can also be used to filter these rays.[2]

Several techniques have been utilized to generate the pulsed high voltage and to accommodate the high current, low impedance characteristics of flash x-ray tubes.[3] A common one is the Marx-Surge generator which consists of a bank of capacitors charged in parallel with a DC voltage and then discharge in series by means of cross-connected spark gaps. In more sophisticated systems, the capacitors are replaced by pulse-forming networks to produce a nearly rectangular output waveform which is more effective.[4] The whole pulser is surrounded by a pressure vessel filled with nitrogen gas, while the gap spacing and gas pressure are adjusted to optimize the output discharge characteristics.

The primary x-ray beam emerging from the tube window contains a wide range of energies, or equivalently wavelengths, described by a continuous spectrum, the so-called

Bremstrahlung. The spectrum contains hard (>50 keV), medium (20-50 keV), soft (10-20 keV), and ultrasoft (<10 keV) x-rays, with a peak at an energy level below 70 keV and an asymptotic approach to zero at higher energies. In general, softer energies allow for higher dosage and better image contrast, hence they are useful in imaging low density objects.[4] Hard x-rays, on the other hand, have greater penetrating power but produce lower contrast and , therefore, are useful in radiographing high density media.

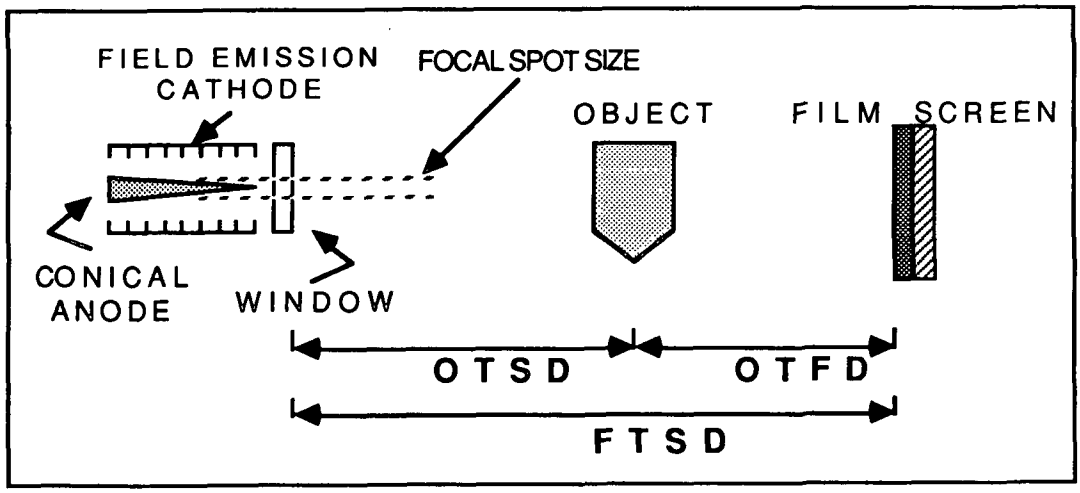

Figure 65. Schematic of a common tube type for flash x-ray radiography.

X-ray Interaction with Matter and Image Formation

Radiographic image contrast is determined by variations in x-ray intensity that reach a detector (film). When x-rays strike or penetrate an object, some pass through and excite the radiographic film, others are absorbed by matter, and some are scattered. The primary radiation transmitted through the object is the image-forming, while scattered (secondary) radiation is non-image forming that obscures details on the film. Absorption of x-rays by matter follows Beer's law:[5]

$$I = I_O \, e^{-(\mu_l x)}, \tag{B1}$$

where I_0 is the incident x-ray intensity, I is the intensity remaining after passing through thickness x of material, and μ_l is the linear absorption (also known as attenuation) coefficient characteristic of the material, its atomic number and density. In cases where the material comprises a mixture or chemical compound, the relationship takes the form:

$$\frac{\mu_l}{\rho} = \sum_i \left(\frac{\mu_l}{\rho} \right)_i Y_i , \tag{B2}$$

where μ_l/ρ represents the mass absorption coefficient, ρ is the density of the absorbing material, and Y_i is the mass fraction of element i. The mass absorption coefficient has the advantage of being independent of the physical or chemical state of the material. It is possible, therefore, to accurately calculate the attenuation of x-ray intensity through any material knowing its elemental composition and the initial x-ray spectrum. It is worth noting that Beer's law assumes a relatively narrow x-ray beam and monochromatic radiation. The primary x-ray beam produced by equipment of practical use, however, has different features. First, the beam forms a cone emerging from the tube window which expands as distance from the source increases. Secondly, the beam contains a wide range of wavelengths, each wavelength interacting in a different manner with intervening matter during the beam's travel. Atmospheric air, for instance, removes soft x-rays from the primary beam and shifts the beam to harder radiation. This is not always beneficial because hard x-rays are responsible for creating image noise, especially when the intention is to resolve low density objects.

The x-ray absorption coefficient, μ_l/ρ, is the sum of terms which define the interaction between x-rays and matter. It consists of two components which describe photoelectric absorption and Compton scattering.[5] As an x-ray beam passes through matter, high wavelengths of the radiation are removed by the photoelectric process. Photoelectric

absorption is dominant at x-ray energies below 100 keV and, because it depends on the atomic number, it is influenced by the elemental composition of the substances penetrated. Upon reaction between x-rays and the film emulsion, photons responsible for image formation are created with this process.[6] The Compton effect, on the other hand, scatters the beam and causes it to emerge (non-image forming radiation) at different angles behind an object. This process is dominant at energy levels above 100 keV and depends on the electron density of the elements composing the object. However, it is undesirable because scattered radiation creates film fogging which deteriorates image quality.[7] This is exactly the reason that relatively low energy FXR systems, as compared to the ones applied in studies of ballistic events, are adequate for the application considered here.

In addition to interaction with matter, propagation of x-rays through vacuum obeys the inverse-square law:

$$I(r) = \frac{I_o}{r^2}, \tag{B3}$$

where r is the distance from a point source, Io is the integrated intensity over the whole spectrum at the source, and I(r) is the intensity measured at distance r from the point source. A practical parameter measured is the dose, d, which is proportional to beam intensity and has units in Roentgen, R, which corresponds to radiation required to generate ions carrying 1 esu charge per 0.001293 g of air. Dosage is conveniently quantified with dosimeters which contain a material of calibrated radiation absorbancy. It is an important parameter because it determines the geometric arrangement required for exposing a film. A note of caution, however, is appropriate because radiographic work is rarely conducted in vacuum. As mentioned earlier, atmospheric air has the tendency to absorb ultrasoft x-rays so that attenuation can no longer be described by the inverse-square law. Instead, the power exponent becomes less than two, its precise value determined experimentally using materials of known absorbancy. This procedure will be described later.

Flash x-ray radiographic images are recorded on detectors (films) which serve the purpose of converting x-rays into optical photons. The x-ray photon energy spectrum will be changed by the presence of the object; the direct transmitted fluorescent beam will be hardened. For a uniformly intense beam, density and /or thickness variations of the object under observation absorb different amounts of x-rays, thus creating areas with variable grayness on the film. Sometimes intensifying screens can be used to enhance image quality by efficiently absorb

lower energy scattered radiation. They can be placed on the front or back of a film, but most commonly are positioned on on the backside to improve image quality by sensitizing the film. Screens are more effective with increasing radiation hardness but they have the tendency to reduce resolution.[8] Films are categorized as medical and industrial depending on the type of emulsion used, while screens can be made out of fluorescent or rare earth materials. Selection of film/screen combination depends on radiographic variables and the characteristic application under consideration.[7-9]

Radiographic images are essentially shadowgraphs where image quality is defined by contrast and definition. The former describes depth resolution and the later represents the lower limit of discernable details resolved on a film. Contrast depends on the thickness of the object to be imaged, scattering radiation, and the radiation quality (i.e., the beam hardness). Definition, on the other hand, depends on the geometric arrangement, focal spot size, and film mottle (graininess, blur, noise, etc.). An important aspect in FXR is the geometric arrangement of the source, object, film, and screen. Characteristic lengths defining geometric arrangement are the object-to-source distance (OTSD), object-to-film distance (OTFD), and film-to-source distance (FTSD) as depicted in Fig. 65. OTSD is manifested by the desired spatial resolution and contrast. Although shorter OTSD gives better penetration, it reduces spatial resolution. In general, OTFD should be kept as short as possible to minimize image magnification and blur due to scattered radiation. Finally, FTSD is determined by the intensity of the primary beam, the material of the absorbant, and the sensitivity of the film/screen used.

Due to practical considerations, x-ray sources in FXR systems have actually a finite size. This puts a lower limit on spatial resolution, which is essentially proportional to the focal spot size of the primary beam. Generally, there is a tradeoff between resolution and contrast, so that radiographic variables have to be optimized with priority to the parameter of interest. Details of selection procedures to optimize radiographic variables are included in standard books on radiography.[10-11]

FEASIBILITY STUDIES AND EXPERIMENTS

An extensive experimental program was undertaken to develop a FXR technique for visualizing through opaque coating fluids since optimization of radiographic parameters is specific to the application of concern. Coating colors, the main absorbant of interest here,

contains elements of relatively low atomic number and density, hence can be penetrated efficiently by low energy x-rays. Techniques developed for application in ballistic events or diagnosis are not applicable because they utilize sources of energy levels of several hundred keV to a few MeV. Thus, key variables which need to be determined are the source of x-rays, geometric arrangement, and film and screen combination. Constraints on the source and the penetrating thickness of colors are introduced because beam intensity increases penetration but at the expense of image contrast. Also, the source type and size are limited by unit availability.

Selection of Flash X-ray Unit for Radiography

All three flash x-ray sources available at The Institute of Paper Science & Technology, formerly The Institute of Paper Chemistry, were evaluated using static and dynamic tests for visualization through coating fluids. These were the two commercially available units manufactured by Hewlett-Packard, McMinnville Division, with 300 and 150 kV maximum tube voltages, respectively, and an experimental device build at our facilities based on know-how from Lawrence Livermore Laboratories (LLL) operating at approximately 136 kV. The first two devices employ Marx-Surge generators and soft x-ray tubes, having a tungsten anode and field-emission cathode, with a Beryllium window. The LLL device is basically utilizing a Blumlein line and has a razor-sharp anode edge that provides a small spot size and therefore good spatial resolution. The 150-kV unit produces a 70 nsec pulse of 150-keV with a dose of 40 mR at 20 cm away from the source. It has a nominal spot size of approximately 3 mm and contains a wide range of soft x-ray radiation. In contrast, the 300-kV unit has a harder beam with larger spot size (5 mm) but dose of 55 mR at 38 cm. Beryllium windows are used with both units in order to preserve the soft x-rays of the emerging beam, since such x-rays are more effective for imaging low density materials like the ones considered here.

At first, a study was conducted to determine the best x-ray source available by recording images of fine (50 and 100 microns in diameter) tungsten wires arranged vertically in a variable width wedge as illustrated in Fig. 66. Goal of experiments was to resolve the wires on radiographs which required not only good spatial resolution but also enough contrast. Tungsten was used as a demonstrative tracer for contrast because it is has high density and atomic number; hence its mass x-ray absorption coefficient is much higher than that of the coating color. In other words, if this material cannot be resolved in a radiograph, most other

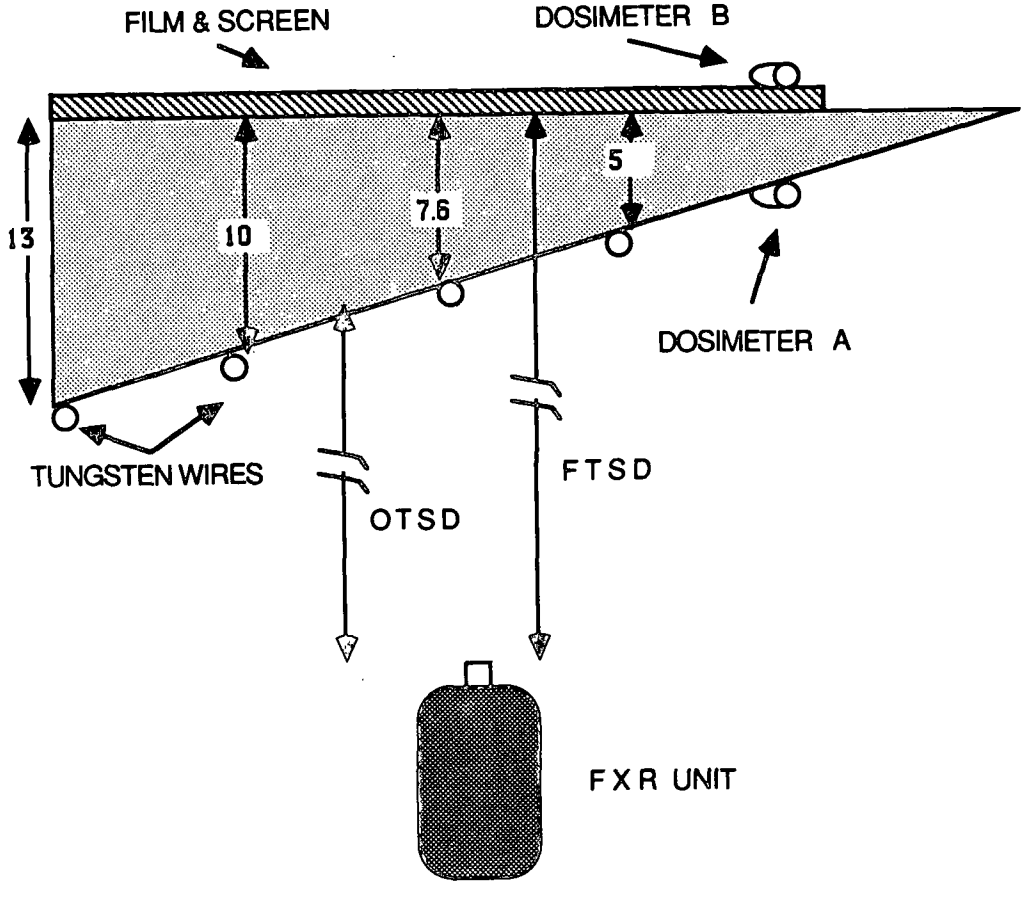

Figure 66. Schematic of setup for preliminary FXR experiments.

Results in Tables 14 and 15 present some characteristics of the x-ray beam emerging from the 150-kV FXR unit used in the experiments of this study. Data from Table 12 yields the following relationships for dosage d measured behind the material:

air $$d_x = \frac{14{,}040}{r^{1.95}} e^{-\mu_1 x} \quad \text{(B5)}$$

water $$d_x = \frac{10{,}270}{r^{1.84}} e^{-\mu_1 x} \quad \text{(B6)}$$

coating $$d_x = \frac{10{,}990}{r^{1.86}} e^{-\mu_1 x} \quad \text{(B7)}$$

where similarities between water and coating color are demonstrated. The exponent on distance r is less than 2 because of the attenuation of the x-rays through ambient air before reaching the object of interest. The difference on measured d_0 can be attributed to variable attenuation characteristics depending on wavelength since the beam is not monochromatic. In the same sense, mass x-ray absorption coefficients calculated from Equations B5-B7 for different r and x do not give the same values (Table 13).

Selection of Film and Screen

Various combinations of radiographic films and screens were evaluated at different FTSD using the setup in Fig. 65. The results are presented in Table 14. Image (tungsten wire) contrast and definition were the criteria for evaluation. Not enough contrast indicates cases where the wires were not visible although the film did not look over or under exposed. Industrial films were only tested because they are faster than medical films.[7] Attempts to use relatively fast medical films with small grains for resolution were unsuccessful. Industrial radiographic films evaluated were the X-OMAT AR (XAR), INDUSTREX AA and M, and the DEF (direct exposure film), all manufactured by Kodak. Lead sheets with various thicknesses and rare earth screens were utilized to reduce backscattering and enhance image contrast. Screens examined were: Optomix (MCI Optonix, Inc.), Optex (Kodak), and Rarex Blue III (MCI Optonix, Inc.). Selection of these films and screens was based on previous data compiled primarily for ballistic studies.[9]

Table 12. Characterization of x-rays attenuation through various fluids (150-kV FXR unit)

Thickness [a] (cm)	OTSD (cm)	Dosage (mR) [b]		
		Air	Water	Coating Fluid
12.70	16.70	43.80	5.84	1.95
12.70	19.24	38.90	1.95	1.95
12.70	24.32	38.90	1.95	1.95
12.70	29.40	29.20	1.95	1.95
12.70	34.48	17.50	0.97	0.97
12.70	39.54	15.60	0.97	0.97
12.70	44.64	12.70	1.95	0.50
10.16	16.70	46.70	8.80	4.90
10.16	19.24	43.80	8.80	2.92
10.16	24.32	32.10	5.80	1.50
10.16	29.40	27.20	3.90	1.50
10.16	34.48	19.50	3.90	3.90
10.16	39.54	17.50	3.90	0.50
10.16	44.64	15.60	0.97	1.95
7.62	16.70	64.20	17.50	7.78
7.62	19.24	50.60	11.70	5.80
7.62	24.32	33.10	10.20	3.90
7.62	29.40	29.20	7.80	3.90
7.62	34.48	24.30	8.80	3.90
7.62	39.54	16.50	4.90	2.90
7.62	44.64	16.50	8.80	1.95
5.08	16.70	73.90	25.30	15.60
5.08	19.24	63.20	20.40	10.70
5.08	24.32	45.70	14.60	7.80
5.08	29.40	31.10	11.70	5.80
5.08	34.48	26.30	10.70	5.80
5.08	39.54	16.50	9.70	4.90
5.08	44.64	16.50	16.80	1.95

[a] Equal to FTSD-OTSD.

[b] Readings corrected for nominal dosimeter values.

Table 13. Experimental linear x-ray absorption coefficients of various fluids (150-kV FXR unit).

OTSD (cm)	μ_l (cm^{-1})			
	Thickness of fluid penetrated, FTSD-OTSD, (cm)			
	12.70	10.16	7.62	5.08
			Air	
16.70	0.113	0.142	0.134	0.180
19.24	0.099	0.106	0.130	0.152
24.32	0.084	0.096	0.124	0.122
29.40	0.076	0.076	0.092	0.143
34.48	0.072	0.079	0.077	0.099
39.56	0.061	0.065	0.071	0.142
44.64	0.060	0.054	0.065	0.097
			Water	
16.70	0.445	0.717	1.046	1.642
19.24	0.519	0.689	0.956	1.544
24.32	0.398	0.633	0.880	1.390
29.40	0.371	0.570	0.779	1.252
34.48	0.293	0.504	0.778	1.224
39.56	0.275	0.480	0.670	1.140
44.64	0.313	0.323	0.720	1.056
			Coating Fluid	
16.70	0.113	0.614	0.947	1.558
19.24	0.099	0.637	0.891	1.471
24.32	0.084	0.475	0.759	1.275
29.40	0.076	0.441	0.713	1.148
34.48	0.072	0.506	0.675	1.091
39.56	0.061	0.280	0.605	1.010
44.64	0.060	0.394	0.525	0.787

Table 14. Preliminary radiographic experiments: Evaluation of films and screens.

FTSD (cm)	Dosage [a] (mR)	Film/screen Combination [b]	Image Quality Comments
		Hewlett-Packard 300-kV FXR unit	
183	3.0	XAR/Rarex Blue III	Not enough contrast; overexposed film
147	4.0	XAR/Rarex Blue III	Not enough contrast; overexposed film
91	8.0	DEF/Optex	Not enough contrast; underexposed film
76	11.0	DEF/Optex	Not enough contrast
74	10.0	XAR/Rarex Blue III	Overexposed film
61	8.0	DEF/Rarex Blue III	Overexposed film
61	10.0	DEF/Optex	Overexposed film
51	8.0	DEF/Rarex Blue III	Overexposed film
51	10.0	AA/Optex	Visible air bubbles through 10.2 cm
51	17.0	AA/Optamatic	Underexposed film
51	18.0	AA/Rarex Blue III	Not enough contrast
46	20.0	AA/Optex	Overexposed film
46	10.0	DEF/Optex	Overexposed film
46	13.0	AA/Rarex	Visible air bubbles through 10.2 cm
46	25.0	DEF/Optex	Overexposed film
46	18.0	AA/Rarex Blue III	Not enough contrast
41	30.0	AA/Rarex Blue III	Overexposed film
41 [d]	3.0	AA/Rarex Blue III	Underexposed film
41 [d]	3.0	AA/Optex	Underexposed film
31	25.0	DEF	Underexposed film
31	25.0	AA/Rarex Blue III	Overexposed film
31	20.0	DEF/Rarex Blue III	Overexposed film
31	18.0	DEF/Optex	Not enough contrast
25	30.0	DEF/0.25 mm Lead sheet	Not enough contrast
25	71.0	DEF	Not enough contrast
20	<1.0	DEF/0.13 mm Lead sheet	Not enough contrast; underexposed film
		Hewlett-Packard 150-kV FXR unit	
31	<1.0	AA/Rarex Blue III	Underexposed film
36	2.0	AA/Rarex Blue III	Overexposed film
36	1.0	DEF/Optex	Overexposed film
91	<1.0	AA/Optex	Underexposed film
137	1.0	XAR/Rarex Blue III	100-μ thick tungsten wires visible through 7.6 cm; marginally visible through 10.2 cm
122	1.0	XAR/Rarex Blue III	As above but lower contrast
		LLL device (136 kV, 12 mm Torr vacuum)	
81	5.0	XAR/Rarex Blue III	50-microns thick tungsten wires visible through 7.6 cm; 100-microns wire through 10.2 cm

[a] Dosage measured with a dosimeter placed along the emerging beam line behind the screen.

[b] All films are for industrial radiography and made by Kodak.

[c] The tube of the 300-kV unit excited up to 120 kV.

Results from these preliminary experiments suggest long FTSD and a combination of a fast film backed by a rare earth screen. Film-to-source distances of 110 to 130 cm are appropriate to resolve tungsten wires through several centimeters of coating colors using Kodak XAR film backed by a Rarex Blue III screen. The screen is required because, although it reduces both resolution and definition, the dosage transmitted over such FTSD and material thicknesses is small (about 1 mR from Fig. 66) to expose the film. However, because of the relatively long FTSD resolution improves. Thus, spatial resolution with the FTSD=122 cm and the above film/screen combination is limited to approximately 50 microns through 76 mm of coating, or 100 microns through 102 mm of coating color. Worth noting is that these values represent maxima because tungsten has unusually high x-ray absorption coefficients.

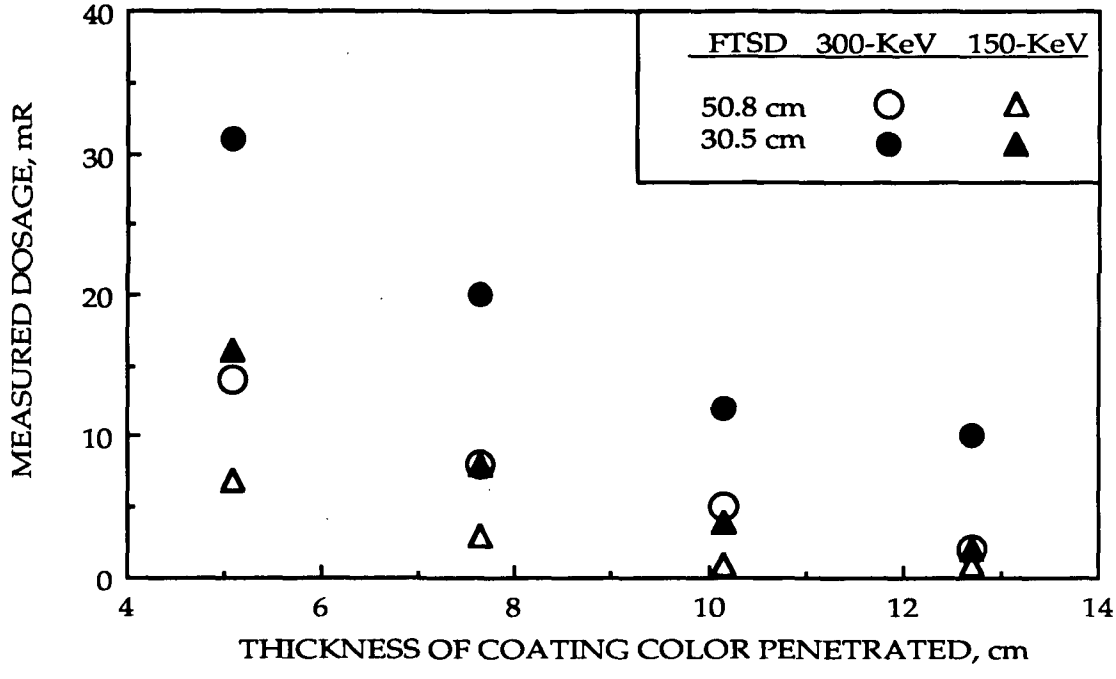

Figure 67. Measured x-ray dosages at various film-to-source distances penetrating different thicknesses of a coating color. The energy levels correspond to the Hewlett-Packard units for flash x-ray radiography.

Selection of an X-ray Tracer for Radiographing Coating Fluids Flows

This subsection describes the exploratory investigation undertaken to develop tracers for this first-time application of the flash x-ray radiography in studying the flow of opaque coating fluids. The technique is basically similar to the dye-injection method for flow visualization where the dye has been replaced by a fluid absorbing much more x-rays than the bulk fluid. Two key factors that need to be satisfied for developing the optimum x-ray liquid

tracer are: (a) the fluid should contain elements with high x-ray attenuation, like heavy metals which have relatively high atomic number and are dense, and (b) it also needs to have similar density and viscous behavior as typical coating colors. Although some of the tracers investigated proved to be inadequate for the specific application of interest here, they are listed because they might be useful for applying this visualization technique to study other types of dynamic phenomena.

First, a search was conducted to identify metal elements with high density which are good absorbants of x-rays and relatively easy to obtain. Data plotted in Fig. 68 represents values of mass x-ray absorption coefficients for three such elements obtained from standard Handbook Tables.[14] Lead, tungsten, and silver have similar absorption within the effective energy range 20-45 keV, the silver being slightly better than the other two.

Next step in this investigation was to identify compounds of the three elements which are soluble in liquid media matching the physical properties of the typical coating colors. Several compounds were picked based on their solubility in water and high content (by weight) of the x-ray absorbing element. These included sodium tungstate in powder (A.D. Mackay, Inc., Conn.) and crystallized forms (dihydrate, Aldrich Chemical Co., Inc., No. 22333-6); lead nitrate crystals and silver sulfate powder (Sargent Welch Scientific, Co., Ill.); and silver (I) fluoride (Aldrich Chemical Co., Inc., No. 22686-6). The following is a complete list of the liquid tracers tested (all percentages represent weight fractions):

Composition of Solution	Density (g/cc)	Active Element Content Based on Compound	Based on Solution
Carboxylmethyl Cellulose (CMC) (grade 7XL made by Hercules Inc.) approximately 3% solids content solution with sodium tungstate (50%)	1.45	62.6%	37.5%
Lead acetate (38%) in glycerol (99% pure)	1.51	63.7%	24.1%
Lead acetate (23.6%) and lead nitrate (20.3%) solution in water	1.50	63.0%	27.7%
Silver oxide (0.005%) in water	1.04	93.1%	0.004%
Silver sulfate (0.014%) in water	1.06	69.2%	0.77%
Silver nitrate (68.7%) in water	2.27	63.5%	43.6%
Silver fluoride (29%) in water	1.55	85.0%	25.0%

Figure 69 presents relative contrast of these tracers as they were radiographed by placing them in short 5-cm wide test tubes (XAR film/Rarex screen, 150-kV FXR unit, FTSD=122 cm). As it

will be discussed below, silver fluoride as well as pure sodium tungstate were abandoned because they cause phase separation whenever added in to coating colors. In general, classification of contrast agrees with the percent content of the active element present. Considering all the solutions containing silver as an example, silver nitrate (far right) gives the best contrast because of its relatively high silver content. In contrast, silver sulfate and oxide solutions have poor contrast due to low silver content. Overall, silver compounds give better contrast than substances based on lead or tungsten at comparable concentrations of active elements. This can be explained with the slightly higher mass x-ray absorption coefficient displayed by silver at the effective range of energy of the FXR source (Fig. 68). However, contrast is not the only parameter of concern to optimize the application.

Only the first two fluids from the above list had viscosities and densities comparable to coating colors, the rest having values similar to water. Rheology was difficult to match precisely at all shear rates (or rpm in a Brookfield viscometer), since coating colors are mostly shear-thinning thixotropic. A 3% solution of CMC containing approximately 50% by weight sodium tungstate ($Na_2WO_4 \cdot 2H_2O$) has, within experimental error, the same viscosity with a typical color at 100 rpm spindle speed(Fig. 70); the standard value of viscosity used in this study. Solutions of lead acetate in glycerol had viscosities about 30% lower than that of the color because glycerol was diluted with water to match the color's density.

Evaluation of tracing fluids was completed with dynamic flow visualization tests. A Couette device made out of Plexiglas was used for the purpose of these tests with the inner cylinder (93 mm in diameter) rotating and the outer (104 mm in diameter) remaining stationary. The annular gap (5 mm) was filled with coating color and the lower half of the device was radiographed with the film and screen, enclosed in a 13 x 18 cm protective cassette, placed in contact with the outer cylinder and on the opposite side from the x-ray source. Standard radiographic parameters were XAR film/Rarex screen, 150-kV FXR unit, and FTSD=122 cm. Tracing solutions were injected tangentially through a 1.6-mm-wide hole drilled on the outer cylindrical wall. This setup is depicted in the radiograph of Fig. 71.

Injection of the tracing fluids was achieved with an air pressure-driven cylinder which can deliver tracing solutions at velocities comparable to those of the coating color in the gap and up to about 1 m/sec. The velocity of the fluid at the injection point as a function of air pressure can be determined from measurements of flow rate and calculations based on tube-flow theory, like the data presented in Fig. 72. For constant rotational speed of the inner cylinder, air pressure varies depending on the viscosity of the tracer. For example, at 100 rpm

rotational speed , i.e., corresponding to about 50 cm/sec linear speed at the inner cylinder's surface, air pressures of 345 and 551 kPa were used for the first and second tracers, respectively, and approximately 14 kPa for the rest of the tracers.

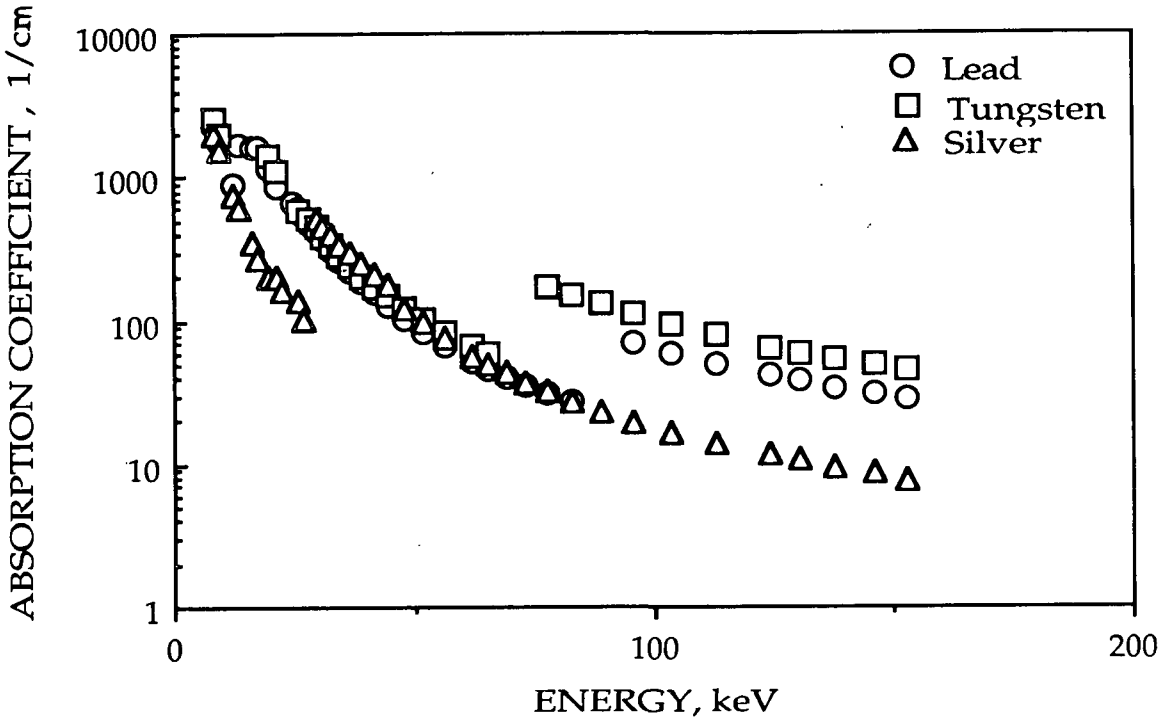

Figure 68. Linear absorption coefficients for different x-ray energies in materials of various metallic elements.

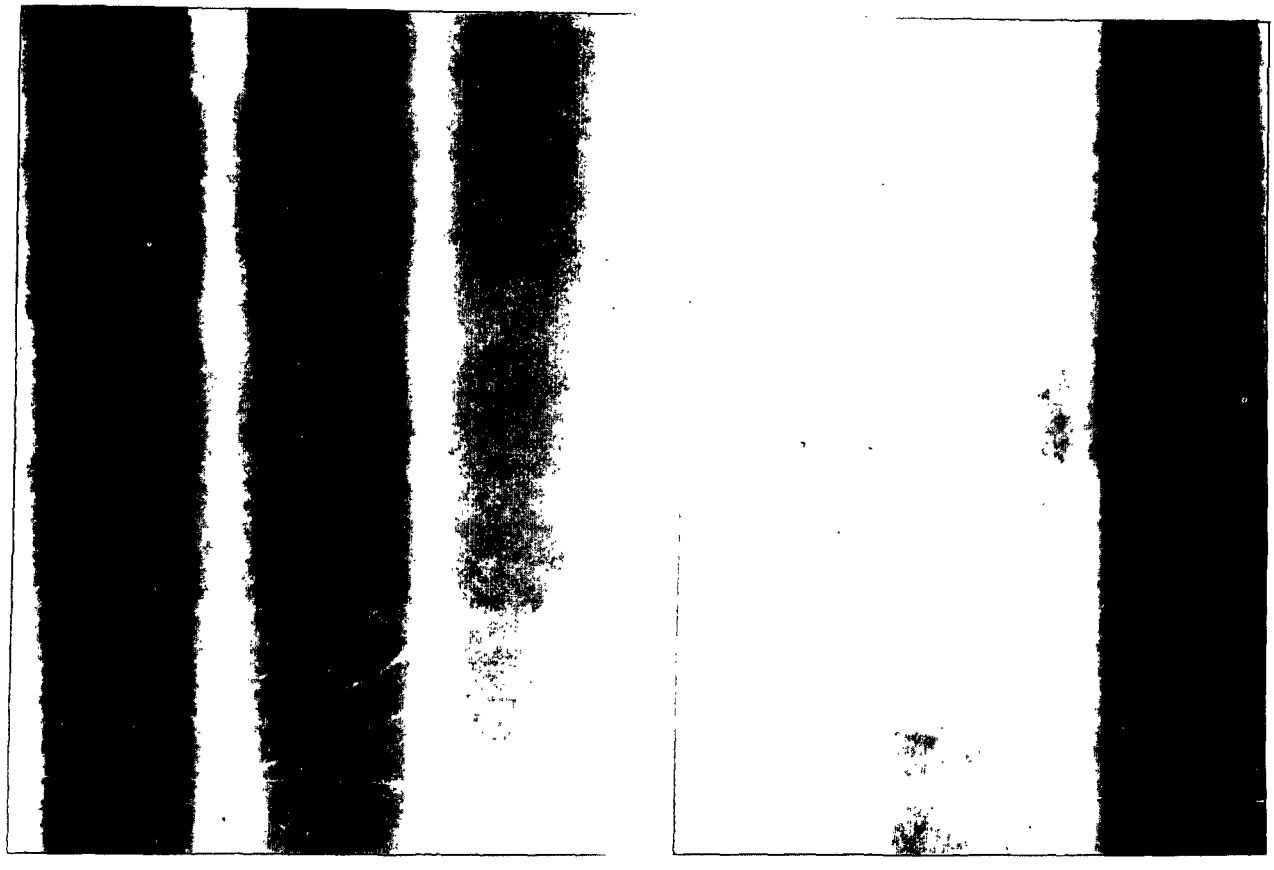

Figure 69. Relative contrast of liquid tracers evaluated. From left to right, in the order appearing in the text.

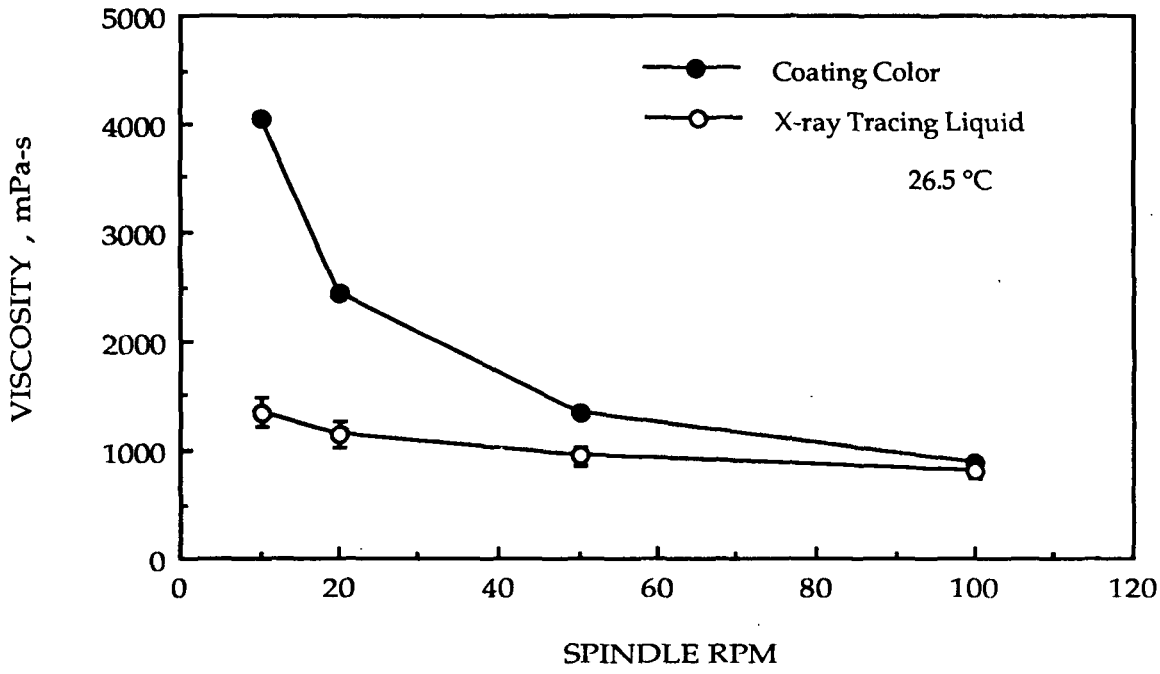

Figure 70. Measured shear-viscosities with a Brookfield viscometer at different rotational speeds (spindle no. 3). Color density 1.56 g/cc.

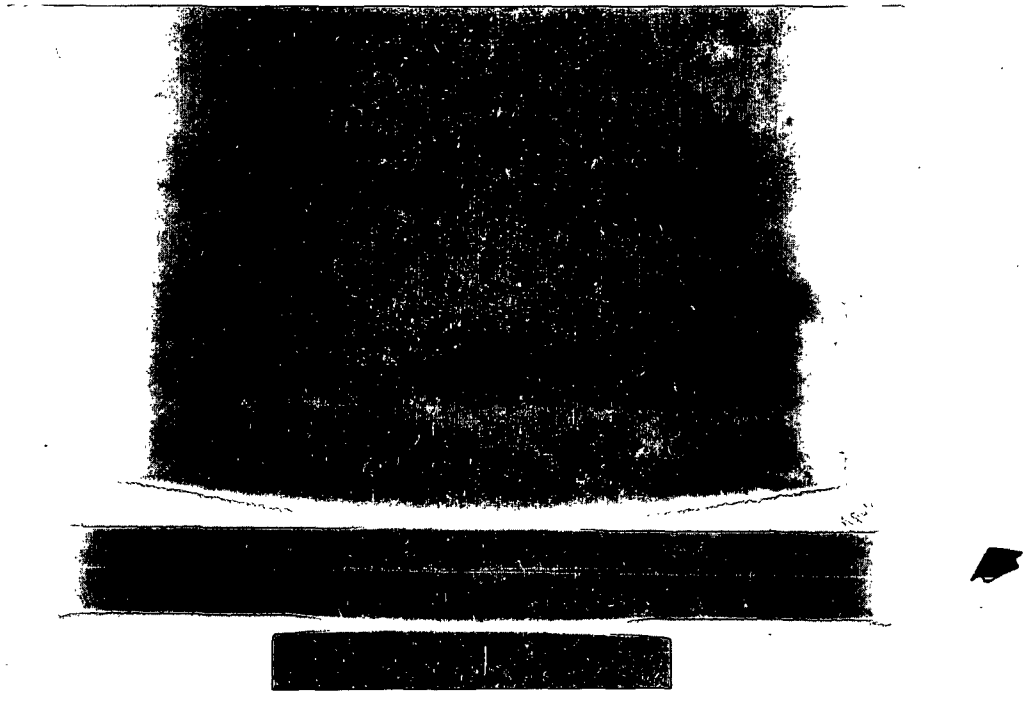

Figure 71. A radiograph of the lower section of the Couette device used for flow visualization with FXR. No fluid in the gap. The injection tube appears on the right.

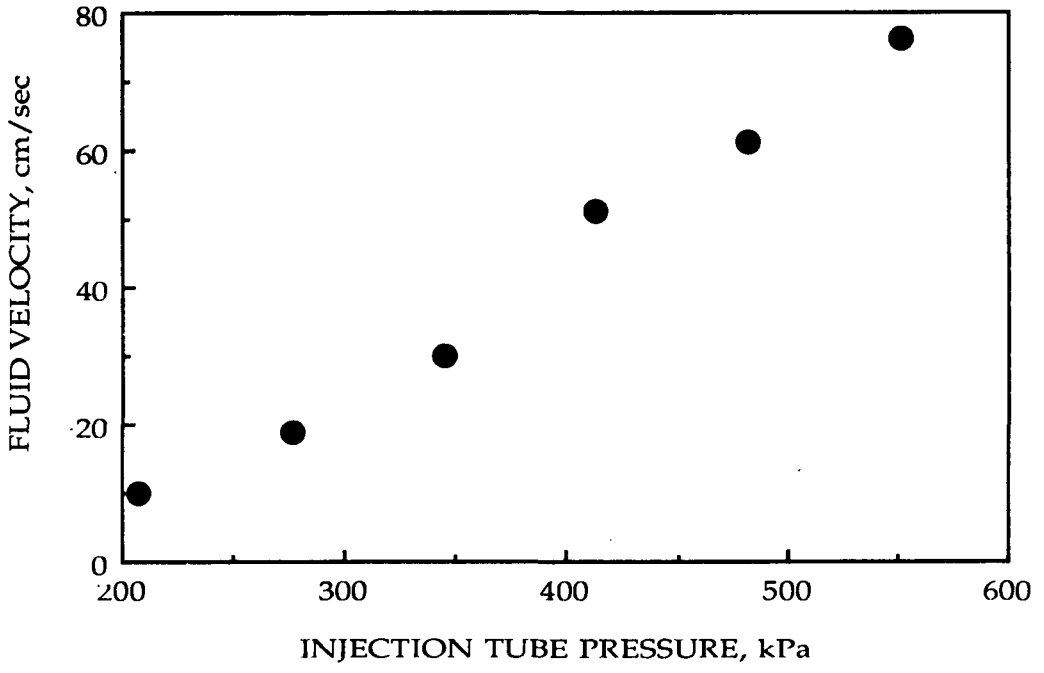

Figure 72. Calculated velocities at the exit of an injection tube as a function of pressure. (Calculations based on fully developed tube flow of a Newtonian fluid.)

Axisymmetric streamlines of the laminar Couette flow were unveiled with both the sodium tungstate solution in CMC (Fig. 73) and lead acetate in glycerol (Fig. 74). Maximum depth of absorbant (mostly color) penetrated at the middle of the radiographs was 11 cm. The coating color was similar to the one depicted in Fig. 70 and used in pilot plant trials for this study (890 mPa sec @ 100 rpm Brookfield). The injection time represents the period of time elapsed between pressurizing the injection tube and activating the FXR source. Its optimum value was estimated by trial-and-error. The swelling of the glycerol stream at the tip of the injection point can be possibly originate from differences in viscosity between this tracing fluid and the color. The rest of fluids did not give satisfactory results because of low contrast (silver oxide and sulfate) or separation of the suspended phase (pigment) from the coating color. Silver nitrate and fluoride, and the combination of lead acetate with nitrate caused clay particles to destabilize from the color suspension. A possible explanation in the case of silver compounds is that argentous ions (Ag^+) react with the dispersing agent (a pyrophosphate compound) to form complexes and, consequently, clay particles loose their stability in suspension.

The above results suggest that a CMC solution with sodium tungstate provides the best tracer for the application of interest. A typical procedure for preparing this solutions is as follows:

1. A 2-liters beaker is filled with 1000 ml of distilled water and placed on a hot plate (120-130°F). A mixer is used to continuously mix the water for uniform heating.

2. Up to 31.3 g of CMC (powder contains 4% water as moisture) are added slowly in to the beaker. Usually it takes about 2 g at a time. Wait until the powder is totally dissolved before adding next dosage. As content of CMC increases, mixer speed may also be increased.

3. After all CMC has been dissolved in to the water, up to 500 g of sodium tungstate can be added slowly. The addition rate is faster than before, e.g., 50 g per couple of minutes. Temperature of the plate can be reduced during this procedure to about 60-80°F. Heat helps to improve solubility of tungstate crystals. After all the amount of tungstate has been added in to the CMC solution, keep mixing for half an hour.

Tracing solid particles were also considered at the beginning of this study. Lead (200 mesh,PB 190) and tungsten metal (1-5 microns, WP 384) powders manufactured by Atlantic Equipment, Inc., New Jersey, and fine silver powder (325 mesh) made by A.D. Mackay, Inc., Conn., were tested as suspended particles in coating colors. However, there were several practical problems which made this technique inappropriate. First, the metal particles cannot readily dissolve in coating colors. Treatment with surface active agents may bring them in to solution, but will also change the physico-chemical characteristics of the color. Secondly, particles have to be at least 100 microns in size to be resolved, something which cannot be matched with the requirement for buoyancy as well as high density for mass x-ray absorption.

These feasibility studies and preliminary experiments generated a database useful in the application of flash x-ray radiographic techniques to opaque fluids flows and other dynamic phenomena than ballistics. Reference conditions for optimizing radiographic variables presented here correlate to radiographic imaging of low density materials. Results from the investigation presented in this section were used to set up the experimental procedure for the first-time visualization of cavity flows through opaque fluids.

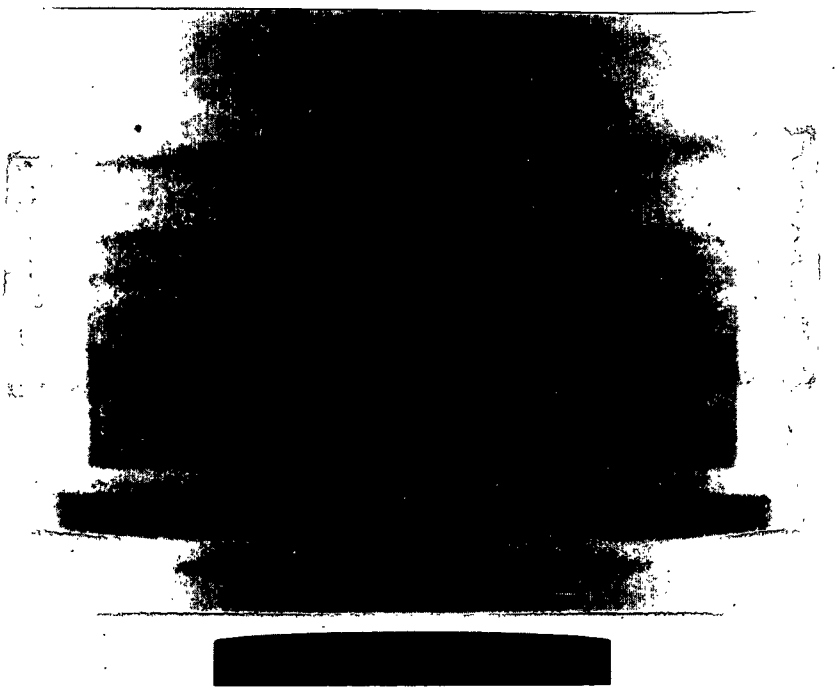

Figure 73. A radiograph of the lower section of the Couette device used for flow visualization with FXR. The gap is filled with a coating color. A stream of a CMC solution saturated with sodium tungstate injected in the direction of rotation (100 rpm, injection time 5 sec).

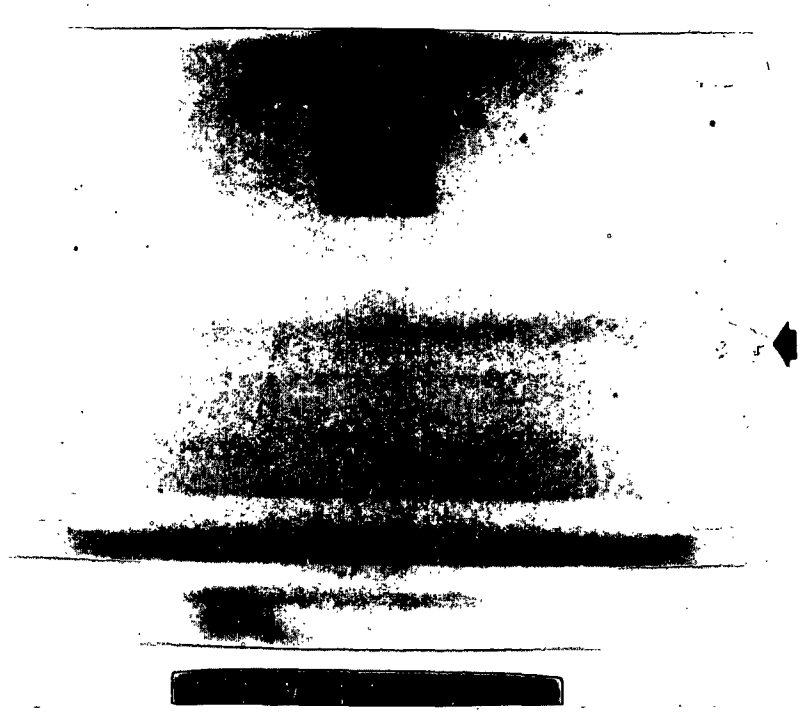

Figure 74. A radiograph of the lower section of the Couette device used for flow visualization with FXR. The gap is filled with a coating color. A stream of a lead acetate is been injected in the direction of rotation (100 rpm, injection time 5 sec).

Developing FXR Films: Procedures and Precautions

The fixer for films is the same as the one used for paper, but the developer has to be the kind proper for industrial radiography. To prepare 3800 ml (1 gal) of the developing solution for radiographic films, mix 946 ml (32 fl oz.) of part A from a Manual Developer and Replenisher fluid with 30 ml (1 fl oz.) of part B and add 2824 cc water, preferably softener. To make the same amount of the solution used for fixing, start with 1900 ml (0.5 gal) water, add 946 ml (32 fl oz.) of part A and 104 ml (3.5 fl oz.) of part B from a Rapid Fix with Hardener fluid, and pour into the solution an additional 850 ml (28 fl oz.) of water. Appropriate bath temperature of running water for processing FXR films is 20°C, with corresponding times 5 and 6 minutes in the developer and fixer fluids, respectively. If the temperature is different, add or subtract 1 minute per 1°C difference, i.e., longer times for lower temperatures, but under no circumstances the total time should exceed 8 minutes. The film needs to remained submerged in water for at least half an hour after fixing. A last wash with de-ionized water helps to avoid water droplets which tend to stain the film.

When the film is being submerged into the developing solution it turns black within seconds, an indication that it has been exposed. If it remains opaque white or delays to change color it means that it has been underexposed. If, on the other hand, overexposure is evident, developing time can be cut down to 3-4 minutes.While in the developer, the films need not to be agitated as it is common with paper. Vigorous agitation, however, is required during the first 15 sec in the fixer and after that time intermittent agitation for few seconds every minute is sufficient. It is possible to use a Stop Bath solution for rinsing the film before submerging it into the fixer, but no substantial benefit in doing this was observed. It is important to make sure that no excess solution drains into tank when removing the developed film and always wash it in running water for 30 seconds before fixing. After removing from the fixer, films need to be washed in running water for at least 20 minutes otherwise they have the tendency to fade away and loose contrast.

APPENDIX C

UNCERTAINTY ANALYSIS

This Appendix contains details on the methods used to calculate the uncertainty associated with measured and calculated parameters. Inaccuracies in measurements are determined by some kind of uncertainty analysis; a systematic methodology which provides the means to quantify uncertainty. Errors from each measurable variable are then propagated to the calculated parameters, such as the Reynolds number. The following describes the methods utilized to calculate uncertainty and gives details of sample calculations.

Methodology for Determining Uncertainty

Accuracy in determining the value of a certain parameter or measurand depends on the accuracy of the data used to obtain this value. For example, the accuracy in determining a fluid's density by weighing a constant volume is a function of both the weight and volume uncertainties. In general, uncertainty includes both a bias error and precision. Bias error (B) is estimated usually by identifying the systematic (read-off) error in a measurement and can be minimized by calibration. For viscometric measurements with a Brookfield instrument, errors arise from calibration with a silicone oil (100 mPa sec nominal viscosity @ 25 °C) and from limitation in reading the scale on the instrument dial.

Precision error is depicted by statistically treating a number of measurements of the same parameter. It is expressed as the precision index, a term used instead of standard deviation (S). The precision index (Sr) of the average of a set of N measurements, also known as standard error, is always less than that of an individual measurement as:

$$S_r = \frac{S}{\sqrt{N}} . \qquad (C1)$$

For a given parameter, total bias and precision are calculated independently with the root sum square method. If one assumes "n" sources of errors, then the bias error (B_r) is given by the sum of the bias errors arising from these sources:

$$B_r = \left(B_1^2 + B_2^2 + B_3^2 + \ldots + B_n^2\right)^{1/2}, \tag{C2}$$

and, similarly, for the precision error (Sr):

$$S_r = \left(S_1^2 + S_2^2 + S_3^2 + \ldots + S_n^2\right)^{1/2}, \tag{C3}$$

Finally, it is possible to combine all these errors in one parameter, namely the uncertainty (U). Then, the interval

$$X \pm U \tag{C4}$$

defines the band or range within which the true value of a parameter would lie for a specified confidence level. Levels of 95 or 99 percent can be achieved by combining B_r and S_r according to the additive (ADD) or the root square (RSS) methods, respectively:

$$U_{ADD} = B_r + tS_r, \tag{C5}$$

and

$$U_{RSS} = \sqrt{B_r^2 + (tS_r)^2}. \tag{C6}$$

The Student t value is a function of the degrees of freedom used in calculating S_r, but it is approximately equal to 2 for $N \geq 30$.

In nearly all experiments, uncertainty in the results is computed from the estimates of uncertainty in the measurands, or independent variables. Errors in a number of variables (P_i) propagate into a derived result (R) through the functional relationship between the result and its variables. Thus if $R = f(P_1, P_2, P_3, \ldots, P_n)$, then bias and precision errors can be calculated using the RSS method and are kept separate until the last step of computing the uncertainty of a result. The bias and precision errors of each independent parameter are defined as, respectively:

$$B_x = \left(\frac{\partial R}{\partial P_x}\right) B_{P_x}, \tag{C7}$$

and

$$S_x = \left(\frac{\partial R}{\partial P_x}\right) S_{P_x}, \qquad \text{(C8)}$$

At the final step, the total uncertainty in the result can be calculated with one of the two methods presented above, i.e., additive or RSS methods.

For the purpose of presenting details of how the analysis outlined above is utilized in this thesis, sample calculations are shown next. Typical computations which are included here present transfer functions, parameter values used, and the associated parameter uncertainties. Precision is based on the standard deviation value from thirty replications of a measurement with the same set-up, at the same day, and by the same operator. Total uncertainty is based on 95% confidence level, calculated with the additive method. An overview of the uncertainties associated with measured and calculated data appear in tabular form in the main text (Table 5).

Sample Calculations of Error Propagation

This subsection contains sample calculations of errors propagated in to the two main dimensionless parameters describing the flow in the lid-driven cavity with through-flow. The total uncertainty in the cavity Reynolds number is calculated with the procedure outlined above based on the uncertainties of each independent parameter:

$$\delta Re = \sqrt{\left(\frac{\partial Re}{\partial \rho} d\rho\right)^2 + \left(\frac{\partial Re}{\partial D} dD\right)^2 + \left(\frac{\partial Re}{\partial V} dV\right)^2 + \left(\frac{\partial Re}{\partial \mu} d\mu\right)^2}, \qquad \text{(C9)}$$

or

$$\frac{\delta Re}{Re} = \sqrt{\left(\frac{\delta \rho}{\rho}\right)^2 + \left(\frac{\delta D}{D}\right)^2 + \left(\frac{\delta V}{V}\right)^2 + \left(\frac{\delta \mu}{\mu}\right)^2}, \qquad \text{(C10)}$$

where bias and precision are calculated separately but combined at the end to obtain total uncertainty. Using data from the bias on estimating the cavity width and the density and viscosity of the fluid, the total systematic error on Re for different peripheral roll speeds is:

$$\frac{\delta Re}{Re} = \sqrt{\left(\frac{0.05}{1.4}\right)^2 + \left(\frac{0.05}{5.08}\right)^2 + \left(\frac{0.3}{V}\right)^2 + \left(\frac{1}{150}\right)^2}\,. \qquad \text{(C11)}$$

A similar procedure is followed for precision but using the standard error of thirty replicated measurements. The uncertainty on estimates of peripheral roll speed includes both interpolation errors from reading the tachometer and unsteadiness of the driving motor. Values were recorded when the fluid in the cavity was maintaining contact with the roll and after at least five minutes. Bias, precision, and total Re uncertainties are reported for four representative levels of speed:

Speed	Bias	Precision	Uncertainty (ADD, 95% conf.)	Uncertainty (RSS, 99% conf.)
18 m/min	0.035	0.08	17%	24%
46 m/min	0.031	0.04	10%	13%
73 m/min	0.031	0.03	8%	10%
270 m/min	0.030	0.03	8%	10%

Similarly, the uncertainty on the Reynolds number for through-flow is a function of the uncertainties of fluid parameters and the flow rate passing through the cavity:

$$\frac{\delta Re^*}{Re^*} = \sqrt{\left(\frac{\delta\rho}{\rho}\right)^2 + \left(\frac{\delta Q}{Q}\right)^2 + \left(\frac{\delta\mu}{\mu}\right)^2}, \qquad \text{(C12)}$$

where Q is the calculated flow rate from measurements of volume (V_t) and elapsed time (t). Representative calculations based on minimum and maximum values attained by the different measurable parameters are as follows:

	Bias	Precision
μ = 160 mPa sec	$(5/160)^2 = 10 \times 10^{-5}$	$(1/160)^2 = 4 \times 10^{-5}$
μ = 77 mPa sec	$(5/77)^2 = 84 \times 10^{-5}$	$(1/77)^2 = 17 \times 10^{-5}$
$\rho = 1.4$ g/cm^3	$(0.04/1.4)^2 = 81 \times 10^{-5}$	$(0.04/1.4)^2 = 20 \times 10^{-5}$
V_t= 95 cm^3	$(0.02/95)^2 = 0.004 \times 10^{-5}$	$(0.01/95)^2 = 0.001 \times 10^{-5}$
V_t= 6 cm^3	$(0.02/6)^2 = 1.1 \times 10^{-5}$	$(0.01/6)^2 = 0.27 \times 10^{-5}$
t = 7 sec	$(0.05/7)^2 = 5 \times 10^{-5}$	$(0.1/7)^2 = 20 \times 10^{-5}$
t = 90 sec	$(0.05/90)^2 = 0.03 \times 10^{-5}$	$(0.1/90)^2 = 0.12 \times 10^{-5}$

These numbers also give an assessment of the relative importance of different parameters to the computed variable. The above values give the following results for bias and precision maxima:

	Bias	Precision
V_t (cm^3)	0.01	0.02
t (sec)	0.05	0.10
Q (cm^3/sec)	0.008	0.045
Re*	0.013	0.015

The total uncertainty of Re* can be calculated from this data as (t-test for ν=10):

$$U_{0.95} = 0.013 + (1.81)(0.015) = 0.040.$$

APPENDIX D

SUMMARY OF OBSERVATIONS FROM FLOW VISUALIZATION EXPERIMENTS

A brief description of the observations recorded during flow visualization experiments and relevant data is given in this section. Visualization of the flow from the downstream vertical and a side end-walls was mainly based on the aluminum flake technique, except in one case where dyed glass fiber were used. The wavelength of flow structures was determined from visual inspection (±0.2 cm). Observations reported in the comments column do not necessarily imply onset of these phenomena at the corresponding Re, unless indicated otherwise. A summary of abbreviations used in the following Table is listed below:

GI	Gradual increase of roll speed	GD	Gradual decrease of roll speed
SS	Sudden start-up of the flow	PR	Basic primary state of flow
TP	Time-periodic flow	GöL	Görtler-like vortices
DSV	Downstream secondary vortex	USV	Upstream secondary vortex
λ	wavelength of secondary flow structures	L	Size of corner vortices
MC	Main recirculating cylinder	D*	Height of DSV at centerline
Gö	Görtler number based on wavelength		

Table 15. Summary of observations from flow visualization experiments in roll-driven rectangular cavities with through-flow (D/W=1:1, S/D=3:1).

μ (mPa sec)	V (m/min)	P_h (kPa)	P_c (kPa)	M (cm^2/sec)	Re*	Re	Comments
				Small Cavity (2.54 cm wide, water/glycerine fluid, ρ=1.28 g/cc)			
140	52	207	7	0.022	0.020	201	Visually estimated onset of DSV upon GI
140	70	207	7	0.022	0.020	271	GD; Five boxlike cells, λ=6.1 cm
140	76	207	7	0.153	0.140	201	Visually estimated onset of USV upon GI
140	128	207	7	0.153	0.140	496	GI; TP flow starts
140	137	207	7	0.153	0.140	531	GI; first observation of GöL vortices, Gö=73
				Large Cavity #1 (5.08 cm wide, water/glycerine fluid, ρ=1.28 g/cc)			
				Feed through a 3 mm wide perforated plate (3.2 mm Dia. holes, 40% open)			
400	18	483	90	0.019	0.006	50	GI; stable (basic) PR flow
400	38	517	90	0.031	0.010	102	GI; stable (basic) PR flow
400	49	483	117	0.035	0.011	132	GI; corner recirculating cells by endwalls
400	75	517	117	0.156	0.050	202	GI; corner recirculating cells by endwalls
400	88	483	117	0.024	0.008	240	GD; onset of (2) boxlike cells
400	102	483	117	0.034	0.011	278	GD; (2) boxlike cells
400	104	483	193	0.055	0.018	281	GD; (2) boxlike cells
400	107	483	117	0.039	0.013	289	GD; (2) boxlike cells
400	143	483	200	0.193	0.062	388	GD; (2) boxlike cells
400	168	483	200	0.182	0.0584	455	GI; visually estimated onset of GöL vortices
400	171	483	200	0.218	0.068	463	GI; GöL vortices, λ=1.91 cm,Gö=62
140	177	483	200	0.252	0.081	479	GI; GöL vortices, λ=1.91 cm,Gö=73
140	180	483	200	0.182	0.058	488	GI; GöL vortices, λ=1.91 cm,Gö=74
140	200	483	200	0.234	0.075	541	GI; GöL vortices, λ=1.91 cm,Gö=80
160	46	345	14	--	--	310	GD; boxlike cells (from video), λ=7.6 cm
160	61	345	14	--	--	413	GI; onset of GöL vortices, λ=1.88 cm, Gö=55

160	76	345	14	--	--	517	GI; unsteadiness,meandering of GöL,Gö=69
160	91	345	14	--	--	620	GI; migration of GöL from center to side walls
160	152	345	55	--	--	1033	GI; coherent structures cannot be visualized
160	213	345	97	--	--	1446	GI; chaotic motions set in
142	61	--	--	--	--	466	GD; appearance of GöL (from video)
142	58	--	--	--	--	442	GD; appearance of GöL (from video)
142	54	--	--	--	--	412	GD; appearance of GöLC (from video)
142	45	345	97	--	--	345	GD; appearance of GöL (from video)
142	37	--	--	--	--	279	GD; boxlike cells (from video), λ=7.6 cm
142	28	--	--	--	--	214	GD; boxlike cells (from video)
142	23	--	--	--	--	175	GD; boxlike cells (from video)
142	18	--	--	--	--	137	GD; boxlike cells (from video)

Large Cavity #2 (5.08 cm wide, water/glycerine fluid, ρ=1.28 g/cc)

Feed through a 3 mm wide perforated plate (3.2 mm Dia. holes, 40% open)

165	30	207	34	0.342	0.265	200	GD; 2 or 3 boxlike cells
155	84	414	69	0.469	0.387	591	GI;pair of GöLC at centerline,λ=2.0 cm,Gö=86
145	46	345	28	0.115	0.101	342	GI; corner vortices by side end-walls, L=2.8 cm
145	46	386	28	0.100	0.088	342	GI; corner vortices by side end-walls, L=2.5 cm
145	46	427	28	0.076	0.067	342	GI; corner vortices by side end-walls, L=2.4 cm
145	40	469	28	0.038	0.034	296	GI; corner vortices by side end-walls, L=2.3 cm
145	37	510	28	0.024	0.021	280	GI; corner vortices by side end-walls, L=2.0 cm
145	46	296	28	0.182	0.161	342	GI; corner vortices by side end-walls, L=2.8 cm
145	46	262	28	0.265	0.234	342	GI; corner vortices by side end-walls, L=2.8 cm
145	47	207	28	0.483	0.426	353	GI; corner vortices by side endwalls, L=2.8 cm
165	30	207	34	0.049	0.038	200	GD; (2) boxlike cells, L=3.5 cm
165	15	496	21	--	--	100	GI; corner vortices by side end-walls, L=2.7 cm
165	24	496	21	--	--	160	GI; corner vortices by side end-walls, L=2.5 cm
165	27	496	21	--	--	180	GI; corner vortices by side end-walls, L=2.4 cm
165	32	496	21	--	--	210	GI; corner vortices by side end-walls, L=2.3 cm
165	36	496	21	--	--	234	GI; corner vortices by side end-walls, L=2.2 cm
165	43	496	21	--	--	282	GI; corner vortices by side end-walls, L=1.9 cm
155	84	414	69	0.036	0.029	591	GI; two pairs of GöL at centerline, λ=2.0 cm
165	33	207	34	0.225	0.175	216	SS; stable (basic) PR flow

165	32	207	55	0.426	0.331	210	GD; (3) boxlike cells
165	32	207	34	0.273	0.212	210	GD; (3) boxlike cells
165	28	207	41	0.273	0.212	184	GD; (3) boxlike cells
165	34	207	31	0.219	0.170	220	GD; f(3) boxlike cells
165	34	207	17	0.182	0.142	220	GD; (3) boxlike cells
165	46	207	34	0.432	0.335	305	GD; (3) boxlike cells
165	40	483	34	0.043	0.034	260	Three (3) boxlike cells remain as Pc increases
165	26	483	21	0.018	0.014	170	Cells collapse to PR flow as Pc decreases
165	30	483	34	0.025	0.020	200	GI; PR flow after above sequence
165	33	207	34	0.252	0.196	214	GD; (2) boxlike cells
165	41	207	34	0.273	0.212	270	GD; (2) boxlike cells
165	26	483	34	0.007	0.006	170	SS; stable (basic) PR flow
165	20	483	21	0.013	0.010	132	SS; basic PR flow but no visible DSV
165	46	483	69	0.080	0.062	301	SS; basic PR flow with visible DSV

Large Cavity #2 (slightly shear-thinning fluid, ρ=1.10 g/cc)

Feed through a 3 mm wide perforated plate (3.2 mm Dia. holes, 40% open)

95	44	207	41	0.243	0.281	430	GI; basic PR flow
95	73	207	41	0.316	0.365	717	GI; horseshoe-shaped vortices in the DSV
95	127	207	38	0.395	0.458	1246	GI; mushroom-like forms inside the DSV
95	189	207	34	0.497	0.576	1856	GI; mushrooms are unsteady along the span
95	245	207	31	0.656	0.760	2402	GI; appearance/disappearance of mushrooms
95	305	207	28	0.756	0.863	2991	GI; appearance/disappearance of mushrooms
95	208	207	21	0.483	0.559	2044	SS or GI; eight (8) mushroom-like structures
95	40	207	14	0.252	0.292	388	GI; basic (stable) PR flow
95	69	414	69	0.400	0.463	672	GI; horseshoe-shaped vortices in the DSV
95	158	207	17	0.310	0.358	1545	GI; mushroom-like forms inside the DSV
95	203	207	17	0.382	0.442	1987	GI; mushrooms are unsteady along the span
95	222	207	17	0.437	0.507	2175	GI; eight (8) mushroom-like structures
95	330	207	14	0.469	0.543	3236	GI; appearance/disappearance of mushrooms
95	355	207	14	--	--	3478	GI; maximum speed with visible structures
95	167	207	28	0.283	0.328	1634	GI; eight (8) mushroom-like cells
95	165	207	28	0.283	0.328	1614	GI; eight (8) mushroom-like cells

Small Cavity #1 (2.54 cm wide, water/glycerine fluid, ρ=1.26 g/cc)

Feed through a 3 mm wide perforated plate (3.2 mm Dia. holes, 40% open)

95	96	207	7	--	--	539	GI; basic PR flow
95	99	207	7	--	--	556	GI; flow becomes TP inside the DSV
95	168	207	7	0.234	0.311	945	GI; eight horseshoe-shaped vortices, Gö=75
95	194	207	7	--	--	1090	GI; eight horseshoe-shaped vortices, Gö=86
95	23	207	7	--	--	128	GD; (2) boxlike vortices, λ=3.8 cm
95	26	207	7	--	--	144	GD; (3) boxlike vortices, λ=3.0 cm
95	30	207	7	--	--	171	GI; appearance of corner vortices, L=1.0 cm
95	30	207	7	--	--	166	GI; appearance of corner vortices, L=1.0 cm
95	34	207	7	--	--	188	GI; appearance of corner vortices, L=1.0 cm
95	28	207	7	--	--	159	GD; basic PR flow when max. Re<900

Large Cavity #1 (5.08 cm wide, water/glycerine fluid, ρ=1.26 g/cc)

Feed through a 3 mm wide perforated plate (3.2 mm Dia. holes, 40% open)

95	40	207	7	0.377	0.500	452	SS; stable (basic) PR flow
95	15	207	7	0.252	0.389	171	SS; stable (basic) PR flow
95	24	207	7	0.293	0.389	274	SS; stable (basic) PR flow
95	24	207	7	0.293	0.389	274	GD; Two (2) boxlike cells, λ=5.2 cm
95	21	207	7	0.252	0.335	233	GD; Two (2) boxlike cells
95	49	345	7	0.252	0.335	554	GI; GöL vortices appear
95	69	345	7	0.298	0.396	780	GI; GöL vortices appear
95	129	345	7	0.400	0.531	1448	GI; mushroom-like forms inside the DSV
95	56	207	7	--	--	633	SS; GöL vortices appear
95	27	207	7	--	--	308	GD; PR flow, speed reduced from above
95	15	207	7	--	--	171	GD; PR flow, speed reduced from above
95	69	207	7	--	--	770	SS or GI; eight (8) horseshoe-shaped vortices
95	76	207	7	--	--	856	SS or GI; eight (8) horseshoe-shaped vortices
95	30	207	7	--	--	342	GD from above; four boxlike cells
95	30	207	7	--	--	342	GD from Re=856 instantly; basic PR flow
95	15	207	7	--	--	171	GD from Re=856; four boxlike cells
95	15	207	7	--	--	171	GD from Re=856 instantly; basic PR flow
95	46	207	7	0.421	0.558	513	GD; Three (3) boxlike cells, λ=2.5 cm

95	15	207	7	0.335	0.444	301	GD; Two (2) boxlike cells
95	34	207	7	0.093	0.107	332	Start-up; basic (stable) PR flow, D*=1.5 cm
95	34	276	7	0.093	0.107	335	GI; basic (stable) PR flow, D*=1.6 cm
95	34	345	7	0.093	0.107	335	GI; basic (stable) PR flow, D*=1.7 cm
95	34	414	7	0.091	0.107	329	GI; basic (stable) PR flow, D*=1.8 cm
95	34	510	7	0.078	0.091	338	GI; basic (stable) PR flow, D*=1.9 cm
95	21	207	7	0.193	0.224	209	Start-up; basic (stable) PR flow, D*=1.5 cm
95	35	207	7	0.238	0.275	341	GI; basic (stable) PR flow, D*=1.7 cm
95	43	207	7	0.273	0.317	418	GI; basic (stable) PR flow, D*=1.8 cm
95	53	207	7	0.304	0.352	514	GI; basic (stable) PR flow, D*=1.9 cm
77	13	207	4	0.074	0.106	162	Start-up; basic (stable) PR flow, D*=1.4 cm
77	22	207	4	0.074	0.106	262	GI; basic (stable) PR flow, D*=1.5 cm
77	29	207	4	0.074	0.106	350	GI; basic (stable) PR flow, D*=1.7 cm
77	40	207	4	0.074	0.106	479	GI; basic (stable) PR flow, D*=1.8 cm
77	10	207	13	0.074	0.106	118	SS; basic (stable) PR flow, D*=1.5 cm
77	16	207	13	0.074	0.106	192	GI; basic (stable) PR flow, D*=1.6 cm
77	23	207	13	0.074	0.106	273	GI; basic (stable) PR flow, D*=1.8 cm
77	30	207	13	0.074	0.106	354	GI; basic (stable) PR flow, D*=1.8 cm
77	41	207	13	0.074	0.106	494	GI; basic (stable) PR flow, D*=1.8 cm
77	7	207	25	--	--	89	Start-up; basic (stable) PR flow, D*=1.4 cm
77	13	207	25	--	--	151	GI; basic (stable) PR flow, D*=1.5 cm
77	17	207	25	--	--	203	GI; basic (stable) PR flow, D*=1.6 cm
77	27	207	25	--	--	332	GI; basic (stable) PR flow, D*=1.7 cm
77	38	207	25	--	--	461	GI; basic (stable) PR flow, D*=1.8 cm
77	10	345	5	--	--	114	Start-up; basic (stable) PR flow, D*=1.5 cm
77	15	345	5	--	--	177	GI; basic (stable) PR flow, D*=1.6 cm
77	22	345	5	--	--	265	GI; basic (stable) PR flow, D*=1.7 cm
77	28	345	5	--	--	335	GI; basic (stable) PR flow, D*=1.8 cm
77	34	345	5	--	--	413	GI; basic (stable) PR flow, D*=1.8 cm
77	12	345	13	--	--	151	Start-up; basic (stable) PR flow, D*=1.5 cm
77	19	345	13	--	--	232	GI; basic (stable) PR flow, D*=1.7 cm
77	25	345	13	--	--	306	GI; basic (stable) PR flow, D*=1.8 cm
77	34	345	13	--	--	406	GI; basic (stable) PR flow, D*=1.8 cm
77	9	345	25	--	--	103	Start-up; basic (stable) PR flow, D*=1.4 cm
77	18	345	25	--	--	221	GI; basic (stable) PR flow, D*=1.6 cm

77	34	345	25	--	--	406	GI; basic (stable) PR flow, D*=1.8 cm

Large Cavity #1 (5.08 cm wide, water/glycerine fluid, ρ=1.26 g/cc, video of 6/14/89)

Feed through a 3 mm wide perforated plate (3.2 mm Dia. holes, 40% open)

95	38	207	7	--	--	428	Start-up; basic PR flow
95	52	207	7	0.328	0.435	582	GI; TP flow inside the DSV
95	52	207	8	0.656	0.870	582	GD; Four (4) boxlike cells
95	60	207	7	0.656	0.870	671	GI from Re=582; four boxlike cells
95	69	207	7	--	--	780	GI; sequential increase of speed hereafter
95	84	207	7	--	--	941	GI;
95	99	207	7	--	--	1112	GI
95	116	207	7	--	--	1301	GI; mushroom-like forms
95	138	207	7	--	--	1554	GI
95	154	207	7	--	--	1728	GI
95	165	207	7	--	--	1848	GI
95	180	207	7	--	--	2019	GI
95	198	207	7	--	--	2225	GI
95	213	207	7	--	--	2396	GI
95	256	207	7	--	--	2875	GI
95	276	207	7	--	--	3098	GI
95	312	207	7	--	--	3498	GI
95	338	207	7	--	--	3799	GI
95	27	207	7	--	--	308	Start-up; basic PR flow
95	57	207	7	--	--	643	GI from Re=308
95	30	207	7	--	--	332	GD from Re=643
95	86	207	7	--	--	962	GI from Re=332; basic PR flow
95	41	207	7	--	--	455	GD from Re=962; basic PR flow
95	98	207	7	--	--	1095	GI from Re=455
95	115	207	7	--	--	1290	GI from Re=1095
95	30	207	7	--	--	335	GD; from Re=1290
95	27	207	7	--	--	305	SS; basic PR flow
95	93	207	7	--	--	1047	GI from Re=305
95	27	207	7	--	--	301	GD; from Re=1047
95	24	207	7	--	--	274	Gradual start-up; basic PR flow

95	137	207	7	--	--	1540	GI from Re=274
95	35	207	7	--	--	394	GD from Re=1540
95	29	207	7	--	--	325	GD from Re=394
95	30	207	7	--	--	342	Start-up of flow; basic PR flow
95	125	207	7	--	--	1403	GI from Re=342
95	32	207	7	--	--	359	GD from Re=1403 slowly
95	27	207	7	--	--	301	GD from Re=359 slowly
95	22	207	7	--	--	246	GD from Re=301 slowly
95	18	207	7	--	--	205	GD from Re=205 slowly
95	74	207	7	--	--	835	GI from Re=205
95	23	207	7	--	--	257	GD from Re=835 slowly
95	111	207	7	--	--	1249	GI from Re=257
95	37	207	7	--	--	418	GD from Re=1249 slowly
95	22	207	7	--	--	246	GD from Re=418 slowly
95	36	207	7	--	--	404	Start-up of basic PR flow
95	83	207	7	--	--	928	GI from Re=404
95	30	207	7	--	--	342	GD from Re=928 abruptly
95	84	207	7	--	--	938	GI from Re=342
95	37	207	7	--	--	411	GD from Re=938 abruptly
95	132	207	7	--	--	1485	GI from Re=411
95	50	207	7	--	--	561	GD from Re=1485 abruptly
95	40	207	7	--	--	445	GD from Re=561 slowly
95	30	207	7	--	--	342	GD from Re=445 slowly
95	24	207	7	--	--	267	GD from Re=342 slowly
95	55	207	7	--	--	616	GI from Re=267
95	21	207	7	--	--	240	GD from Re=616
95	30	207	7	--	--	342	SS; basic PR flow
95	130	207	7	--	--	1455	GI from Re=342
95	23	207	7	--	--	257	GD from Re=1455
95	55	207	7	--	--	620	Start-up; basic PR flow
95	139	207	7	--	--	1561	Stop flow abruptly from this Re

Large Cavity #1 (5.08 cm wide, water/glycerine fluid, ρ=1.26 g/cc, video of 6/13/89)

Feed through a 3 mm wide perforated plate (3.2 mm Dia. holes, 40% open)

95	47	207	7	--	--	532	GI; onset of bright streaks (pair) in the DSV
95	51	207	7	--	--	579	GI; acceleration of bright streaks to endwalls
95	54	207	7	--	--	613	GI; acceleration increases
95	60	207	7	--	--	674	GI; irregular (wavy) MC and DSV interface
95	84	207	7	--	--	943	GI; spanwise oscillation of interfacial waves
95	47	207	7	--	--	532	GI; onset of bright streaks in the DSV
95	55	207	7	--	--	627	GI; bright streaks in the DSV (VHS-C)
95	78	207	7	--	--	889	GI; bright streaks in the DSV (VHS-C)
95	55	207	7	--	--	627	GI; bright streaks in the DSV (VHS-C)
95	41	207	7	--	--	465	GD; four stable cells along span (VHS-C)
95	330	207	7	--	--	3746	GI; maximum speed recorded (VHS-C)

Large Cavity #1 (5.08 cm wide, water/glycerine fluid, ρ=1.26 g/cc, video of 6/22/89)

Feed through a 1.5 mm wide slot

80	52	232	10	--	--	592	GI; onset of bright streaks (pair) in the DSV
80	60	232	10	--	--	688	GI; irregular (wavy) MC and DSV interface
80	77	232	10	--	--	888	GI; spanwise oscillation of interfacial waves
80	99	232	10	--	--	1136	GI; structures in mushroom-like forms appear
80	326	232	10	--	--	3736	GI; maximum speed recorded
80	36	232	10	--	--	416	After GD, boxlike (2) cells oscillate with GI
80	44	232	10	--	--	512	GI from Re=416; boxlike cells cease to exist
80	61	232	10	--	--	712	GI; onset of irregular MC and DSV interface
80	80	232	10	--	--	936	GI; spanwise oscillation of interfacial waves
80	81	232	10	--	--	944	GI; spanwise oscillation of interfacial waves
80	80	232	10	--	--	936	GI; spanwise oscillation of interfacial waves
80	44	232	10	--	--	520	GI from Re=180; boxlike cells cease to exist
77	37	483	8	--	--	450	SS; onset of TP flow in the DSV
77	30	241	35	--	--	368	GD from Re=1141; six boxlike cells
77	30	241	35	--	--	368	GD from Re=810; six boxlike cells
77	30	241	35	--	--	368	GD from Re=626; six boxlike cells
77	30	241	35	--	--	368	GD from Re=442; six boxlike cells
77	15	241	35	--	--	180	GD from Re=1583; six boxlike cells

Large Cavity #1 (5.08 cm wide, water/glycerine fluid, ρ=1.26 g/cc, video of 6/22/89)

Feed through a 3 mm wide perforated plate (3.2 mm Dia. holes, 40% open)

95	49	207	7	--	--	574	GI; onset of bright streaks (pair) in the DSV
95	60	207	7	--	--	698	GI; irregular (wavy) MC and DSV interface
95	43	207	7	--	--	507	GI; onset of bright streaks (pair) in the DSV
95	52	207	7	--	--	615	GI; irregular (wavy) MC and DSV interface
95	79	207	7	--	--	931	GI; spanwise oscillation of interfacial waves
95	95	207	7	--	--	1097	GI; structures in mushroom-like forms appear
95	101	207	7	--	--	1172	GI; appearance/disappearance of mushrooms
95	799	207	7	--	--	9227	GI; maximum speed attained
95	21	207	8	0.122	0.162	244	SS; basic (stable) PR flow
95	91	207	21	0.156	0.207	1057	GI from Re=244; mushroom-like forms
95	43	207	30	--	--	500	GD from Re=1057; Pc increases, PR basic flow
95	118	207	20	--	--	1372	GI from Re=500, then GD to Re=305; PR flow
95	22	207	8	--	--	256	GD from Re=1372, three (3) boxlike cells
95	26	207	8	--	--	303	Relieve Pc to 4 kPa; boxlike cells persist
95	24	207	1	--	--	280	Relieving Pc from above; PR basic flow
95	24	207	8	--	--	280	Increase Pc from above; PR basic flow
95	24	207	30	--	--	280	GI Pc; basic (stable) PR flow
95	26	345	8	0.050	0.067	303	GD from Re=1000; six (6) boxlike cells

Large Cavity #1 (5.08 cm wide, water/glycerine fluid, ρ=1.26 g/cc, #6141)

Feed through a 3 mm wide perforated plate (3.2 mm Dia. holes, 40% open)

95	47	207	7	--	--	546	GI; onset of bright streaks (pair) in the DSV
95	50	207	7	--	--	586	GI; onset of bright streaks (pair) in the DSV
95	59	207	7	--	--	694	GI; irregular (wavy) MC and DSV interface
95	80	207	7	--	--	943	GI; onset of GöL vortices

Small Cavity (2.54 cm wide, water/glycerine fluid, ρ=1.26 g/cc)

Feed through a 3 mm wide perforated plate (3.2 mm Dia. holes, 40% open)

95	47	207	7	--	--	556	GI; onset of bright streaks (pair) in the DSV
95	79	207	7	--	--	930	GI; spanwise oscillation of interfacial waves
95	80	207	7	--	--	943	GI; onset of GöL vortices

Feed through a perforated plate (3.2 mm Dia. holes, 40% open), video 2/88

Dyed glass fibers as tracers (1 mm long, 25 microns wide)

140	52	207	7	--	--	201	Visually estimated onset of DSV upon GI
140	76	207	15	0.153	0.140	295	GI, onset of USV; GD, five (5) boxlike cells
140	137	207	7	0.153	0.140	531	GI; DSV destabilizes to TP flow
400	48	517	83	0.019	0.006	132	GI; corner vortices by side end-walls
400	87	517	83	0.019	0.006	240	Visually estimated onset of (5) boxlike cells
400	167	517	83	0.019	0.006	455	GI; GöL vortices inside the DSV, Gö=147
161	75	344	20	--	--	507	GI; recorded footage of PR and DSV
140	64	275	20	--	--	496	GI; appearance of TP flow structures
140	70	275	20	--	--	543	GI; appearance of TP flow structures
140	76	275	20	--	--	590	GI; steady GöL vortices, visualize USV
140	45	275	20	--	--	354	GI; oscillation of boxlike cells spanwise
140	52	275	20	--	--	401	GI; visualize DSV
140	128	275	20	--	--	992	GI; meandering of GöL vortices spanwise
140	131	275	20	--	--	1015	GI; meandering of GöL vortices spanwise

APPENDIX E

INDUSTRIAL PILOT COATER TRIALS

Details of the short-dwell coater trials conducted at the Rockton Research Center of Beloit Corp. are included in this section. The scope was to identify as precisely as possible the critical speed, and Re at which wet streaks first appear and collect paper samples for further analysis. Two rotogravure formulations, coded as ER and UR, were applied on LWC stock during trials at two different days. Basic difference between the two colors was the kind of delaminated clays used, i.e., English China and Georgia kaolin for trials 8/25/89 and 9/25/89, respectively. Table 16 presents the conditions and some results from all of the trial runs.

A bevelled stiff blade was utilized to apply the coating colors onto uncalendered LWC papers. These papers had basis weight of 49 gsm, run 0 of 8/25/89 and all of 9/25/89, and 62 gsm, runs 1-15 of 8/25/89. Blade stickout represents the distance between the tip and the point where the loading tube makes contact with the blade. Chamber here means the pressurized feeding enclosure that supplies coating color to the pond. Viscosities correspond to values obtained with a Brookfield viscometer (spindle no.5, 100 rpm) and a Hercules Hi-shear viscometer (bob E, spring set 400,000 dynes cm/cm) for high- and low-shear measurements, respectively. Densities of colors were obtained with a pychnometer. The Reynolds number Re is based on the distance between the tip of the blade and the overflow baffle.

Composition of coating colors based on by weight parts per hundred (pph) of pigment:

Color ER for trials of 8/25/89

Delaminated English China clay - type A	77%
Delaminated English China clay - type B	33%
Dispersant (tetrasodium pyrophosphate)	0.35 pph
Lubricant (sodium stearate)	0.50 pph
Latex (styrenebutadiene emulsion)	4.5 pph
Thickening agent (alkali-swellable emulsion)	0.26 pph
800 ml Ultraviolet dye (Tinopal SCP)	
200 ml NaOH to control pH to 9.0	

Color UR for trials of 9/25/89

Delaminated Georgia kaolin clay	100%
Dispersant (tetrasodium pyrophosphate)	0.35 pph
Lubricant (sodium stearate)	0.50 pph
Latex (styrenebutadiene emulsion)	4.5 pph
Thickening agent (alkali-swellable emulsion)	0.26 pph
800 ml Ultraviolet dye (Tinopal SCP)	
200 ml NaOH to control pH to 9.0	

Table 16. Details from pilot-plant short-dwell coater trials.

Parameters	Trial Runs

Standard Conditions

Blade Bevel (degrees)	45
Blade Length (mm)	76
Blade Thickness (mm)	0.5
Blade Stickout (cm)	1.9
Head Angle (degrees)	54
Baffle Gap (mm)	3

First Trial (8/25/89)

Sample Code	0	1	2	3	4	5	6	7	8
Coat Weight (gsm)	11	11	11	11	11	11	11	11	11
Coating Formulation	ER	ER	ER	ER	ER	ER	ER	ER	ER
Total Solids (% by weight)	58.1	58.1	56.6	56.6	56.6	56.6	57.6	55.6	55.6
Reel Moisture (%)	4.5	4.5	4.5	4.5	4.5	4.5	4.5	4.5	4.5
Tube Pressure (kPa)	207	90	131	138	152	138	97	90	97
Feed Pump Rate (L/min/m)	166	166	166	166	166	166	166	166	166
Chamber Pressure (kPa)	–	10	10	10	10	10	9.5	9.5	9.5
Machine Speed (m/min)	1070	305	762	793	823	732	305	640	671
Color Viscosity (mPa sec)									
Low-shear	1884	1884	1428	1428	1428	1428	1412	980	980
High-shear	73	73	66	66	66	66	63	49	49
Color Temperature (°C)	26.7	26.7	28.9	28.9	28.9	28.9	33.3	27.8	27.8
Reynolds Number, Re	729	207	687	714	742	659	556	841	881
Comments	Severe Streaks	No Streaks	Streaky	Streaky	Streaky	Streaky	No Streaks	Streaky	Streaky

First Trial (continue)

Sample Code	9	10	11	12	13	14	15
Coat Weight (gsm)	11	11	11	11	11	11	11
Coating Formulation	ER	ER	ER	ER	ER	ER	ER
Total Solids (% by weight)	55.6	57.1	57.1	57.1	57.1	56.3	56.3
Reel Moisture (%)	4.5	4.5	4.5	4.5	4.5	4.5	4.5
Tube Pressure (kPa)	104	110	117	97	104	104	173
Feed Pump Rate (L/min/m)	166	166	166	166	166	166	166
Chamber Pressure (kPa)	9.5	9.5	9.5	10	10	10	10
Machine Speed (m/min)	701	610	701	488	549	610	1067
Color Viscosity (mPa sec)							
Low-shear	980	1236	1236	1236	1236	1056	1056
High-shear	49	58	58	58	58	56	56
Color Temperature (°C)	26.7	28.9	28.9	28.9	28.9	27.8	27.8
Reynolds Number, Re	921	635	730	507	571	743	1300
Comments	Streaks	Streaks	Severe Streaks	No Streaks	Sporadic Streaks	Streaks	Severe Streaks

Second Trial (9/25/89)

Sample Code	1	2	3	4	5	6	7	8	9
Coat Weight (gsm)	6.2	6.4	6.4	6.2	6.2	6.8	6.5	6.3	7.0
Coating Formulation	UR	UR	UR	UR	UR	UR	UR	UR	UR
Total Solids (% by weight)	59.6	59.6	59.6	59.6	59.6	59.6	59.6	59.6	59.6
Reel Moisture (%)	–	3.6	4.4	4.7	5.3	5.9	2.5	3.3	5.9
Tube Pressure (kPa)	221	200	200	200	200	214	152	159	207
Feed Pump Rate (L/min/m)	166	200	166	166	166	166	200	166	166
Chamber Pressure (kPa)	9.5	10	10	10	10	10	8.0	9.0	9.0
Machine Speed (m/min)	701	305	762	793	823	732	305	640	671
Color Viscosity (mPa sec)									
Low-shear	1268	1292	1268	1280	1292	1224	904	1012	1052
High-shear	62.5	–	–	–	–	–	–	–	–
Color Temperature (°C)	25.6	25.6	25.6	25.6	25.6	25.6	25.6	25.6	25.6
Reynolds Number, Re	790	670	850	910	1000	1240	480	860	1650
Comments	Severe Streaks	No Streaks	Streaky	Streaky	Streaky	Streaky	No Streaks	Streaky	Streaky

Second Trial (continue)

Sample Code	10	11	12	13	14	15
Coat Weight (gsm)	6.3	6.5	6.0	6.2	6.7	6.3
Coating Formulation	UR	UR	UR	UR	UR	UR
Total Solids (% by weight)	59.6	59.6	59.6	59.6	59.6	59.6
Reel Moisture (%)	5.4	2.6	2.7	3.1	3.9	4.4
Tube Pressure (kPa)	221	159	159	145	145	145
Feed Pump Rate (L/min/m)	200	200	200	200	200	200
Chamber Pressure (kPa)	10	10	10	10	10	10
Machine Speed (m/min)	1340	366	428	488	549	610
Color Viscosity (mPa sec)						
Low-shear	1004	1104	1120	1156	1160	1156
Color Temperature (°C)	24.4	24.4	24.4	24.4	24.4	24.4
Reynolds Number, Re	1900	471	542	600	673	750
Comments	Severe Streaks	No Streaks	Streaky	Streaky	Streaky	Streaky

APPENDIX F

REFERENCES TO THE APPENDICES

1. Jamet, F.; Thomer, G. F. Flash Radiography. Elsevier Publishing Co., Amsterdam, The Netherlands, 1976.

2. Flash Radiography. Technical Bulletin B-23. Hewlett-Packard, McMinnville Division, McMinnville, OR, 1973.

3. Früngel, F. B.A. High Speed Pulse Technology: Capacitor Discharge Engineering, Vol. 3. Academic Press, New York, NY, 1976.

4. Carbonier, F. Nondestructive Testing handbook: Flash Radiography. ASNT, Columbus, OH, 1983.

5. Bertin, E. P. Principles and Practices of X-ray Spectrometric Analysis. Plenum Press, 3rd Edition, New York, NY, 1979, pp. 51-68.

6. Vinegar, H. J.; Wellington, S. L. Tomographic Imaging of Three-phase Flow Experiments. Rev. Sci. Instrum. 58(1):96-107 (1987).

7. White, K. J.; McCoy, D. G. Influence of Scattering and Image Enhancement Technique for Flash X-ray Ballistic Events. Proc. Flash Radiography Symp. ASNT, Columbus, OH, 1984, pp. 88-99.

8. Bryant, J. E.; Lucero, J. P. Film/Screen Study for Flash X-ray. Proc. Flash Radiography Symp., (L. E. Bryant, ed.), ASNT, Columbus, OH, 1984, pp. 15-23.

9. Bryant, L. E.; Lucero,J. P.; Fresquez, S.S. Film/Screen Study for Flash X-ray. Los Alamos National Laboratory, Report LA-UR-88-779, 1988.

10. Flash X-ray Seminar Notes. Hewlett-Packard, McMinnville Division, McMinnville, OR, June 1987.

11. Quinn, R.A.; Sigl, C.C. Radiography in Modern Insdustry. Eastman Kodek Co., Rochester, NY, 4th Edition, 1980.

12. Triantafillopoulos, N.G.; Farrington, T. Flash X-ray Radiography Techniques for Visualizing Coating Flows. Proc. Coating Conference, TAPPI Press, Atlanta, GA, 1988, pp. 48-52; IPST Technical Paper Series No. 274, 1988.

13. Farrington, T. Unpublished Data, October 1986.

14. International Critical Tables, vol. 1. Mc-Graw-Hill Co., New York, NY, 1928, pp. 8-15.